Thermal, Structural and Luminescent Properties of Long After-Glow $MAl_xO_y:Eu^{2+},Dy^{3+}$ (M: Sr, Ba) Phosphors

By

Barasa Daniel Bem

A thesis submitted in partial fulfillment of the requirements for the degree

Doctor of Philosophy (Ph.D.)

in the

Department of Physics

Faculty of Natural and Agricultural Sciences

at the

University of the Free State

Republic of South Africa

Promoter:	Prof. F.B. Dejene
Co-promoters:	Prof. H.C. Swart
	Prof. A.S. Luyt

November 2010

Research institutions

The research described in this thesis was carried out at various institutions: The University of the Free State [Qwa Qwa and Bloemfontein campuses], the Council for Scientific and Industrial Research (CSIR)–Pretoria, and the Nelson Mandela Metropolitan University (NMMU)–Port Elizabeth. The project was financially supported by the National Research Foundation (NRF)–South Africa and the University of the Free State. Special acknowledgement goes to Kenyatta University, Nairobi, Kenya, for the award of the study leave.

To my parents

Ellam Wekhwela Nambuwani, my father, and Rhodah Nyangweso, my mother, – my ultimate role models. Obe le bophelo bo botle, lerato le thabo dilemong tsohle.

Acknowledgements

I wish to express my heartfelt gratitude to the following people:

- Prof. Dejene, F.B. my promoter; for his support and particularly for being instrumental in making it happen.
- Prof. Swart, H.C. my co-promoter; for his continuous support, guidance and special understanding of my circumstances.
- Prof Luyt, A.S. my co-promoter; for his encouragement, inspiration and willingness to go the extra mile for his students.
- Staff of the Department of Physics, University of the Free State. For the positive interactions and support: Mrs Cronje, K. Mr Dolo, J.J. Ms Lebeko, K.M. Dr Mothudi, B.M. Dr Msomi, J.Z. Mrs Pretorius, E. Dr Ocaya, R.O. to mention but a few.
- Fellow researchers: Mr Ahmad, E.M. Mr Ali, A.G. Dr Coetsee, E. Dr Dlamini, M.S. Mrs Duvenhage, M.M. Miss Foka, K.E. Mr Koao, L.F. Miss Lephoto, M.A. Miss Mofokeng, J.P. Mr Mokhoto. Mr Motloung, J.S. Dr Kebede, M. Dr Molefi, J.M. Dr Ngaruiya, J.M. Mr Nsimama, P. Dr Roro, R. (NMMU), Mr Sefadi. Miss Tshabalala, M.A. among others.
- Prof Van Wyk, P.W.J. and Janecke, B. of the Centre of Microscopy for their support and advice during SEM measurements. Ms Lombard and Ms Huibrie (HCF) Joubert, Department of Geology (UFS), for their assistance with XRD measurements. Prof. J.R. Botha, for permission to use his PL system.
- My family: My wife, Mary – for the absolute sacrifice and selflessness; my children; Ruth, Ken, Fiona, and Oscar – I am setting the lower threshold. My brothers: Moses, David and Peter, and my sister, Alice.

I am grateful for the financial support from the South African National Research Foundation, and the University of the Free State as well as Kenyatta University for the grant of study leave.

I bow before Almighty God for giving me the strength and courage to pursue this study

Abstract

The optimization of properties for new and potentially useful materials becomes a continuous and sometimes a lifelong process if future applications are anticipated. Research on luminescent materials is a good example of this statement and rare earth-doped alkaline earth aluminates is at the epicentre of this focus due to the anticipated superior qualities, vis a vis those of classical sulphide phosphorescent materials. The focus in these developments has been to produce a phosphor with high emission intensity, high colour purity, longer afterglow and that is safe and chemically stable. To address some of the issues in these efforts, this study had three major aims: (1) The investigation of the surface morphology, crystallinity, particle size, luminescence, and thermal properties of commercial phosphors by various techniques. (2) The preparation and characterization of two types of phosphors by standard techniques. (3) The preparation and characterization of phosphor/polymer composites.

The first commercial phosphor was a green-emitting aluminate phosphor. The properties of this phosphor as well as those of LDPE/phosphor and PMMA/phosphor composites were studied. Polymer/phosphor composite samples were prepared with phosphor concentrations ranging from 1 to 5 volume% and subsequently hot-melt-pressed. Sharp and broad XRD peaks were observed for the LDPE and PMMA composites respectively, reflecting configuration characteristics similar to those of the respective pure polymers. TEM micrographs show a transition from nanosized particles to cluster formation with increase in phosphor concentration. PL was observed in the composites of both polymers for phosphor volume concentrations above 1.0% for PMMA and above 0.5% for LDPE. For each of these samples, a broad PL peak at about 505 nm wavelength was observed after excitation at 350 nm with a xenon lamp. For the LDPE composites, the DSC results show that the presence of the phosphor in the polymer had no major influence on either the melting temperature or enthalpy values of the polymer. LDPE/phosphor composite samples, based on blue-emitting commercial aluminate phosphor, were similarly prepared and characterized for structural, luminescent and thermal properties. XRD analysis revealed the presence of the $Sr_4Al_{14}O_{25}$ phase in the composites. PL spectra have two sets of peaks, major broad bands peaking at about 486 nm and minor ones between 412 nm and 418 nm, attributed to the 4f–5d transition of Eu^{2+}. DSC and TGA results show that the introduction of the

phosphor in LDPE matrix caused a slight reduction in the crystallinity of LDPE but a strong increase in the stability of the composites.

$SrAl_xO_y:Eu^{2+},Dy^{3+}$ phosphor was synthesized by a combustion method and characterized for luminescent and thermal properties. Phosphor nanocrystallites with high brightness were obtained. The average crystallite sizes, calculated from the Scherrer equation ranged between 34 and 43 nm. Emissions arising from transitions between the 5d and 4f orbital gaps of Eu^{2+} are manifested in the broad-band excitation and emission spectra with major peaks at 360 and 515 nm, respectively. The decay curves and half-life times show a clear trend in the influence of the phosphor in the improvement of the initial brightness and the afterglow times, which are ascribed to the presence of shallow and deep traps. Thermal results indicate that the phosphor nanoparticles acted as nucleating agents and improved the overall crystallinity in the LDPE/ $SrAl_xO_y:Eu^{2+},Dy^{3+}$ phosphor system.

The temperature-dependence of the structural and luminescent properties of sol-gel derived $SrAl_xO_y:Eu^{2+},Dy^{3+}$ phosphor was investigated. Calculations based on XRD results, by means of the Scherrer equation showed the average crystallite sizes increasing from about 42 to 47 nm. Reflections corresponding to both $SrAl_2O_4$ and $Sr_2Al_3O_6$ phases were observed at the various annealing temperatures but with a diminishing contribution from the $Sr_2Al_3O_6$ phase. PL characterization also shows temperature-dependence through variation of both the peak position and intensity, which indicate emission at low and high annealing temperatures originating from Eu^{2+} and Eu^{3+} ions respectively.

$BaAl_xO_y:Eu^{2+},Dy^{3+}$ was the second phosphor synthesized by a combustion method. PL results indicate that the LDPE/$BaAl_xO_y:Eu^{2+},Dy^{3+}$ interface, which is considered to have an influence on the composite behaviour, did not significantly change the spectral positions of the phosphor materials, whose major emission peaks occurred at about 505 nm. The improved afterglow results for the composites are probably due to morphological changes due to the increased surface area and defects. Thermal results indicate that the BaAlxOy:Eu^{2+},Dy^{3+} particles acted as nucleating centres and enhanced the overall crystallinity in the LDPE nanocomposite while preventing lamellar growth, hence reducing the crystallite sizes in LDPE.

Key words

Alkaline earth aluminates

$BaAl_xO_y:Eu^{2+},Dy^{3+}$

Combustion method

Composites

DSC

LDPE

Long-afterglow

Phosphorescence

Photoluminescence

Rare earth ions

Sol- gel method

$SrAl_2O_4:Eu^{2+}Dy^{3+}$

$Sr_4Al_{14}O_{25}:Eu^{2+}Dy^{3+}$

$SrAl_xO_y:Eu^{2+},Dy^{3+}$TGA

Acronyms

AFM	Atomic Force Microscopy
CB	Conduction Band
CCD	Charge Coupled Device
$BaAl_xO_y$	Barium aluminate
$BaMgAl_{10}O_{17}$	Barium magnesium aluminate
BeO	Beryllium oxide
BN	boron nitride
Ce	Cerium
CERN	European Organization for Nuclear Research (French: `*Organisation Européenne pour la Recherche Nucléaire*)
Co	Cobalt
CO_2	Carbon dioxide
CRT	Cathode Ray Tube
CTS	Charge Transfer States
CTAB	Cetyl TrimethylAmmonium Bromide
Cu	Copper
DSC	Differential Scanning Calorimetry
Dy	Dysprosium
EDS	Energy Dispersive Spectroscopy
Eu	Europium
Fe	Iron
FED	Field Emission Display
FWHM	Full Width at Half Maximum
H_2O	Water
He-Cd	Helium Cadmium laser
HRTEM	High Resolution Transmission Electron Microscopy
LED	Light Emitting Diode
LHPG	Laser Heated Pedestal Growth
LDPE	Low Density Polyethylene
$Mg_4(F)GeO_6$	Magnesium Fluorogermanate

MgTe	Magnesium Telluride
MRI	Magnetic Resonance Imaging
NaCl	Sodium Chloride
Nd	Neodymium
NdP_5O_{14}	Neodymium phosphate
Ni	Nickel
PL	Photoluminescence
PMMA	Poly(methylmethacrylate)
QD	Quantum Dot
QE	Quantum Efficiency
QY	Quantum Yield
RE	Rare earth
SEM	Scanning Electron Microscopy
$Sr_xAl_yO_z$	Strontium aluminate
$Sr_xMgSi_yO_z$	Strontium magnesium silicate
STM	Scanning Tunneling Microscopy
Tb	Terbium
TEM	Transmission Electron Microscopy
TGA	Thermogravimetric Analysis
TiO_2	Titanium dioxide
Tl	Thallium
TL	Thermoluminescence
TSL	Thermally Stimulated Luminescence
UV	Ultraviolet
VB	Valence Band
Xe	Xenon
XRD	X-Ray Diffraction
Y_2O_2S	Yttrium orthosulphide
Y_2O_3	Yttrium oxide
$Y_3Al_5O_{12}$	Yttrium aluminate
YVO_4	Yttrium orthovanadate

ZnO	Zinc oxide
Zn_2SiO_4	Zinc silicate
ZnS	Zinc Sulphide

Contents

List of Figures

List of Tables

Chapter 1
Aims and Outline of Thesis

1.1 General background

According to the US Department of Energy [1], illumination accounts for 14% of the total energy used in the United States and 21% of the electricity consumed in the building sector. With the emphasis on reducing lighting energy use and concurrently reducing pollution from fossil fuel power plants, there is an interest in improved general purpose illumination technologies.

The goal to produce efficient phosphors for lighting applications has been a long standing one for researchers working on luminescent materials. The quantum efficiencies of the phosphor coatings in current ‘‘state-of-the-art’’ fluorescent lamps generally exceed 90%. Further major improvements in fluorescent lighting efficiency may be sought in the development of more efficient means of generating visible photons from phosphors. The development of practical multiphoton-emitting phosphors, which produce more than one visible photon per incident ultraviolet photon using a controlled photon cascade process, can significantly improve the overall energy conversion of fluorescent lamps.

Potential applications of phosphors are numerous, especially in the areas of safety improvement and energy saving. These applications may be broadly classified as: (1)

light sources represented by fluorescent lamps, (2) display devices represented by cathode-ray tubes, (3) detector systems represented by x-ray screens and scintillators, and (4) other applications, such as luminous paint with long persistent phosphorescence; nanophosphors of ZnO and TiO_2 in cosmetics, which have increased absorption of ultraviolet rays from the sun; bacteria-mediated delivery of nanophosphors and cargo into cells of live animals; use of nanophosphors as new contrast agents for tumour imaging, etc [2,3]. Research and development on these materials requires the use of a number of fields in science and technology such as physical and inorganic chemistry, solid-state physics, electronics, illuminating, and image engineering. Therefore, research and technology in phosphors require a unique combination of interdisciplinary methods and techniques, which forms a fusion of the above mentioned fields. The focus in these research efforts has been to seek to understand the mechanisms underlying the luminescent processes such as trapping and de-trapping, in order to develop more efficient phosphorescent materials for various applications. Of special attraction are phosphors prepared on the nanometre scale, in which case the method of synthesis becomes an important aspect, since variations in the synthesis process conditions can create a significant change in the morphological, structural, optical, and other properties of nanomaterials. The special functionality of materials on the nano scale has been known for some time.

1.2 An overview of past Phosphor research

The scientific research on phosphors has a long history going back more than 100 years. A prototype of the ZnS-type phosphors, an important class of phosphors for television tubes, was first prepared by Théodore Sidot, a young French chemist, in 1866 rather accidentally. It seems that this marked the beginning of scientific research and synthesis of phosphors [1].

From the late 19^{th} century to the early 20^{th} century, Philip E.A. Lenard and co-workers in Germany performed active and extensive research on phosphors, and achieved impressive results. They prepared various kinds of phosphors based on alkaline earth

chalcogenides (sulfides and selenides) and zinc sulfide, and investigated their luminescence properties. They established the principle that phosphors of these compounds are synthesized by introducing metallic impurities into the materials by firing. Lenard and co-workers tested not only heavy metal ions but various rare-earth ions as potential activators.

P. W. Pohl and co-workers in Germany investigated Tl^{+}-activated alkali halide phosphors in detail in the late 1920s and 1930s. They grew single-crystal phosphors and performed extensive spectroscopic studies. In co-operation with F. Seitz in the U.S. they introduced the configurational co-ordinate model of luminescence centres and established the basis of present-day luminescence physics.

Humbolt Leverenz and co-workers at Radio Corporation of America (U.S.) also investigated many practical phosphors with the purpose of obtaining materials with desirable characteristics to be used in television tubes. Detailed studies were performed on ZnS type phosphors.

Since the end of World War II, research on phosphors and solid-state luminescence has evolved dramatically. This has been supported by progress in solid-state physics, especially semiconductor and lattice defect physics. Advances in the understanding of the optical spectroscopy of solids, especially that of transition metal ions in general and rare-earth ions in particular, have also helped in these developments.

The concept of the configurational coordinate model of luminescence centres was established theoretically. Spectral shapes of luminescence bands were explained on the basis of this model. The theory of excitation energy transfer successfully interpreted the phenomenon of sensitized luminescence. Optical spectroscopy of transition metal ions in crystals clarified their energy levels and luminescence transition on the basis of crystal field theory. In the case of trivalent rare-earth ions in crystals, precise optical spectroscopy measurements made possible the assignment of complicated energy levels and various luminescence transitions.

Advances in studies of band structures and excitons in semiconductors and ionic crystals contributed much to the understanding of luminescence properties of various phosphors using these materials as hosts. The concept of direct and indirect transition types of semiconductors helped not only to find efficient luminescence routes in indirect type semiconductors, but also to design “efficient” materials for light-emitting diodes and semiconductor lasers. The concept of donor-acceptor pair luminescence in semiconductors was proposed and used to produce luminescence semiconductor phosphors of better efficiency.

1.3 The novelty and issues in nanostructured luminescent systems

In a narrow sense, the word phosphor is used to mean inorganic luminescent materials, usually those in powder form and synthesized for the purpose of practical applications. Phosphors with one dimension less than 100 nm are called nanophosphors and may be described as nanostructured, inorganic, insulating solid materials that efficiently emit light under energetic particle and electromagnetic radiation.

Though the investigation of nanophosphors is a nascent field [2-6] there is observably a growing interest in the investigation, design and manufacturing of nanostructured materials. The first report on the effects of nanostructuring on the optical properties of materials dates from 1990, when strong visible luminescence emission from porous Si was announced [7]. Since then, an intense research effort to investigate and explore these effects has been in progress, mostly focused on semiconductor nanostructures (quantum dots). These materials possess properties, such as optical, magnetic, and structural properties, among other characteristics, that are often uniquely different from those exhibited by their macroscopic counterparts. This change in behaviour is partly attributed to perturbations of the electronic distribution induced by reduced dimensionality, i.e. the large increase in the surface-to-volume ratio, i.e. the relative dominance of surface atoms and thus the enhanced role of the surface energy [8]. Apart from surface influences, the change in the electronic structure of a material, due to quantum confinement effects play another significant role in changing properties. As the

particle size decreases, the quantum confinement effects begin to occur [9,10]. These alterations can be explored to create materials with new properties tailored for specific applications that offer superior performance to existing ones.

A recent development, which has further stimulated research on luminescent materials is the use of phosphors as the light-emitting components in flat panel displays (FPDs) such as field emission displays (FEDs). Unlike conventional phosphor particles, luminescent nanostructured materials are attractive for field-emission display (FED) applications because their small size allows complete penetration by the low-voltage electrons for efficient material utilization [11]. However, unlike cathode ray tube (CRT) displays, which use highly energetic electrons and substantial beam currents to excite phosphor emission, design constraints in flat panel displays severely limit the amount of excitation power available to excite phosphors. Consequently, the emission efficiency of phosphor materials becomes an issue of major concern in the design of flat panel displays. Unfortunately, the emission efficiency of rare-earth-activated phosphors appears to be limited by concentration quenching of activators [12] and other effects [13]. The quenching effects are aggravated when low-voltage electrons are used for excitation [14].

Compared to microscale particles, the main drawback of nanoscale phosphors is their lower quantum efficiency. This is attributed to the large surface area, which amplifies quenching processes. Therefore, research activities aiming at the application of these materials concentrate on the deactivation of surface quenching, which might be achieved by coordinating the surface to ligands having low-phonon frequencies or by the application of a passivating shell. It is, therefore, important to understand the mechanisms of quenching in phosphors in order to design effective methods to overcome quenching limitations of phosphor efficiency.

From a more fundamental standpoint, the lanthanide dopant can serve as a sensitive probe of the chemistry and structure of its host. Nanostructured materials can provide model systems to study surfaces using tools such as photoluminescence (PL) spectrometry whose utility is derived from its unique sensitivity to discrete electronic

states, many of which lie near surfaces and interfaces. The high surface-to-volume ratio of nanocrystalline particles results in a significant fraction of all atoms in the particle being at or near a surface. Consequently, doping lanthanide ions in nanocrystals of these dimensions places a sensitive probe at the particle surface. In contrast to nanostructured materials, it is difficult to study the luminescence of dopant ions located at the surface of micron-sized particles because the large signal from ions in the interior of the particles obscures any signal from ions at the surface.

Investigating and understanding nanoscale host materials will be important for optimizing their emissive properties for technological applications in future lighting, communication and display devices. Preparing optically active nanostructures has the potential for discovering and investigating materials that exhibit unexpected and unique optical phenomena, such as possible enhanced coupling of the localized centres to electromagnetic radiation [15] or other confinement effects [16]. Preparing lanthanide-doped nanostructures also provides a new method to develop and study transparent composite materials. The reduced optical scattering of nanometre-sized particles allows the preparation and use of nanocrystals embedded in an amorphous matrix in applications such as lasers and amplifiers, which usually require high-quality crystals or glasses [17]. Using nanostructured composites (nanocomposites) in optical applications could simplify material preparation or allow the use of new host materials for which good crystals cannot be grown.

1.4 The novelty and issues in nanocomposite structures

Recent technological breakthroughs and the desire for new functions generate an enormous demand for novel materials. On their own, many of the well-established materials cannot fulfill all technological desires for the various new applications. Scientists and engineers realized early on that mixtures of materials can show superior properties compared with their pure counterparts. One of the most successful examples is the group of composites which are formed by the incorporation of a basic structural

material into a second substance. Most of the resulting materials show improved properties and a well-known example is inorganic/polymer composites.

Composite materials consisting of inorganic/organic components, of which one of the phases is present in dimensions that are nanoscale or smaller [18] are of considerable interest. Significant variations in the properties of these materials, which can differ greatly from the components in their pure form or from composites in which both of the phases have macroscopic dimensions, are expected. For example, in the case where silica constitutes the inorganic phase, many of these studies have focused on the dramatic enhancement in mechanical properties that is realized for organic polymers in which silicate nanoparticles have been dispersed [19]. Another example is the enhanced stability imparted in magnetic recording media from the distribution of magnetic nanoparticles in a diamagnetic matrix [19,20].

A key aspect of applying nanomaterials in technological applications is protecting them from degradation. The high surface area of nanocrystals compared with micrometre-size particles results in high reactivity and accelerated rates of reaction with water, oxygen, and CO_2. For instance, approximately 50% reduction in the luminescence intensity of Y_2O_3:Eu^{3+} nanocrystals has been observed over a period of several months when stored in a laboratory desiccator. Similarly, the luminescence of many sulfide and selenide quantum dots have been observed to decrease rapidly if they are not capped or protected to prevent oxidation [17]. Passivating the surfaces of nanoparticles can be accomplished by using chemical reactions to coat or disperse the particles in a polymer or glass matrix.

1.5 The persistent luminescence phenomenon: Issues and perspectives

Persistent luminescence is a phenomenon where the material is emitting, usually in the visible range, for hours after the excitation source has been switched off [21]. The excitation used may be visible light or UV, x-ray, or gamma radiation. Persistent luminescence has been and still is, unfortunately in a misleading manner, called

phosphorescence because of the long emission time. Phosphorescence may be an appropriate term to be used in the context of luminescence from organic compounds involving triplet-to-singlet transitions. These are forbidden with a long decay time but are otherwise perfectly natural. The long decay time of persistent luminescence, however, is due to the storage of the excitation energy by traps and is released from them with thermal energy. Thus the term thermally stimulated luminescence (TSL) is appropriate.

Although the quest for new persistent luminescent materials has now resulted in several blue and green emitting persistent phosphors that remain visible for many hours, practically nothing, neither in understanding the phenomenon nor in developing new materials, took place before the mid 1990s. The expectation for the discovery of new and even better persistent luminescent materials was heightened following the discovery of $SrAl_2O_4:Eu^{2+},Dy^{3+}$ and $Sr_2MgSi_2O_7:Eu^{2+},Dy^{3+}$. The brightness and lifetime of these two phosphors completely overshadows that of their most important predecessor, ZnS:Cu,Co. However, a survey of the output in the past 16 years, of the research done on luminescent materials, shows that only a handful of phosphors are bright enough to consider their use

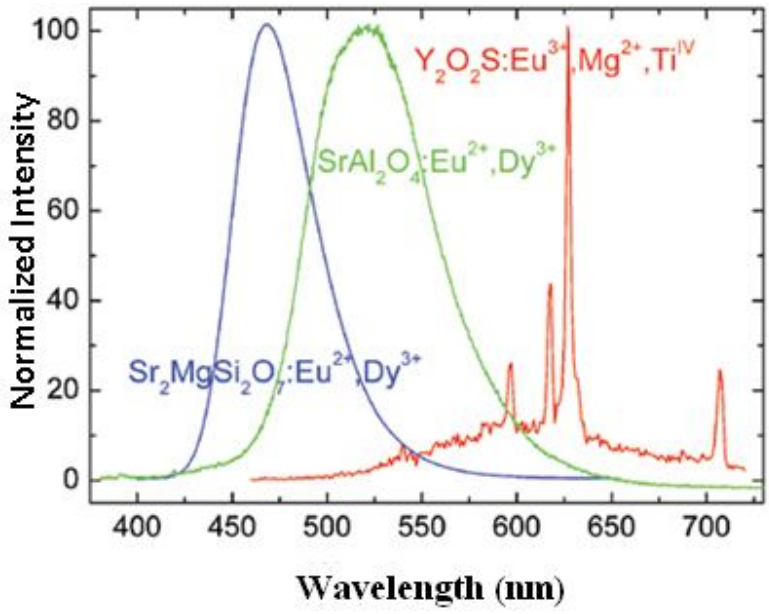

Figure 1.1: The luminescence spectra of the blue-emitting $Sr_2MgSi_2O_7:Eu^{2+},Dy^{3+}$, green emitting $SrAl_2O_4:Eu^{2+},Dy^{3+}$ and red emitting $Y_2O_2S:Eu^{3+},Mg^{2+},Ti^{IV}$ phosphors after UV excitation [22].

in practical applications. And yet the ultimate goal in the search for lighting phosphors would be the production of white light. The idea of making a white-emitting persistent light source by combining the three individual blue-, green-, and red-emitting phosphors, in a way similar to the tri-colour fluorescent tubes, seems possible when the emission spectra of these phosphors are considered separately (Fig. 1.1). The feasibility of this novel idea lies in the ability to synchronize the duration of the three colours. The luminescent characteristics of rare earth ions can go a long way in the achievement of this goal since many radiative electronic transitions in these ions occur in the visible region. This phenomenon, once understood, opens up the possibility to tailor the emissions to specific requirements.

Besides lighting applications, there are other attractive current and potential phosphor applications. These include the use of phosphors as sensors, examples of which include temperature sensing and also the sensing of changes in pressure (on airplane wings, for example). The use of nanoparticulate persistent luminescence materials for biomedical applications with direct in situ imaging sounds both interesting and feasible. Though not as exciting, the use of persistent luminous paints adds a great deal to the inspiration in this research area that is increasingly being commercialized.

1.6 Motivation

Commercially available phosphors are proprietary materials and hence the exact composition and phase responsible for their luminescent characteristics such as intensity and persistence time are not known. These conventional phosphors are usually obtained by the solid state sintering method, whose products are normally in micrometre scale and are characterized by strong light scattering at grain boundaries leading to a reduction in light output as well as a lower concentration quenching threshold due to non-uniform doping. Alternative synthesis techniques such as the conventional sol-gel methods are expensive due to the low solubility of metal alkoxides and the large amounts of vapour produced by the organic solvents may also be a source of environmental problems.

Consequently, it is necessary to identify a more appropriate synthesis procedure, which avoids these negative aspects while optimizing phosphor production.

Ideally the requirement for obtaining high photoluminescence nanophosphor particles should involve the absorption of large amounts of excitation energy by the activator ions followed by the simultaneous return of excitons to the ground state by the radiative process. To achieve these processes, experimental investigations should address the key material parameters required to understand, control, and correlate material properties with optical performance. These parameters include the average particle diameter, and particle-size distribution, surface morphology, concentration quenching, crystallinity, as well as the underlying phosphorescence mechanisms. Although the elaboration of persistent luminescence mechanisms has been advancing at a rapid pace, the refinement of the details is still needed.

On the other hand, phosphor nano-composites can potentially be used to produce low-energy consumption and high efficiency illumination for long hours. Progress in these areas depends on the ability to selectively and controllably deposit nano-particles, and to uniformly disperse the phosphors in a host matrix, to create a strong and stable three dimensional network.

Finally, although research in nanostructured materials is beginning to produce a clear picture of these materials, the current theories and experimental databases are inadequate for a full understanding of the optical properties of luminescent nanostructures. It is therefore imperative to build an elaborate theoretical and experimental data base to facilitate the synthesis of tailor-made luminescent materials (phosphors). The alternative approach, which seems to largely inform the current investigations, is to adopt a laborious, inefficient, ‘trial and error’ approach that is not cost-effective and that is reliant on luck for advancement.

1.7 Description of the research problem

The alkaline earth aluminates, doped by divalent europium (Eu^{2+}), have the potential to be a class of materials with persistent luminescence and high quantum efficiency in the visible region [23], which can provide durable properties with ultraviolet irradiation [24]. However, their very low persistence luminescence inhibits further progress in their applications [25]. Similarly, although the Eu^{2+},R^{3+} (R: rarae-earth ion) co-doped barium aluminates as $BaAl_xO_y$:Eu^{2+},Dy^{3+} have been studied only infrequently, they have the potential for persistence luminescence. The reasons may be due to its rather complicated structural chemistry as well as the considerable size mismatch between the Ba^{2+} ion and the activator (Eu^{2+}) cations.

Generally, aluminate phosphors have widely been investigated due to their several advantages over other phosphors. In particular, rare earth ions co-doped strontium aluminate ($SrAl_2O_4$:Eu^{2+},Dy^{3+}) phosphors have been extensively researched and developed following their invention in 1993 [26]. Due to their properties, this class of phosphors are commercially used in a broad range of applications for which ZnS:Cu,Co phosphors cannot. In spite of the extensive investigations there is a paucity of work done on phosphor hosts, particularly for outdoor applications, an area that is finding increasing applications for these materials. For example, though a lot of effort has been devoted to the development of the syntheses [27-31] and mechanisms [32-35] of phosphorescence of these phosphors, little attention has been paid to the well-known drawback of weak resistance to water. Hence, the degradation of these phosphors due to weak resistance to water or even moisture remains an unresolved issue. Approaches that have been employed so far, [36-42] involve complex processes that require elaborate equipment, but still tend to compromise the luminescence intensity of the phosphors. Therefore, cheaper and more effective intervention techniques are needed.

1.8 Aims of the research

- Generation of a broad impact on nano-particle fabrication, with a wide application potential by making high energy-efficient rare earth doped strontium and barium aluminate nano-phosphors, which will significantly improve the energy efficiency of various applications including lighting sources as well as detector and display systems.
- Identification of a polymer matrix that will enable the creation of a strong and stable three dimensional network when it acts as a host for the phosphor particles. This is intended to extenuate the moisture-induced degradation, which has continued to characterize phosphors. The lower density of polymers, compared to metals and ceramics, as well as resistance to atmospheric and other forms of corrosion, informed their choice.
- Investigation of the morphology, structure, photoluminescence intensity, and afterglow characteristics of the as-prepared phosphors, as well as the composites of the phosphors with the PMMA and LDPE polymers, based on SEM imaging, EDS spectra, TEM imaging and diffractometry, x-ray diffraction, luminescence spectroscopy as well as DSC and TGA analyses on the composites.

1.9 Research objectives

To:

- Investigate the morphological, compositional, structural and photoluminescent properties of commercially prepared, green-emitting, $SrAl_2O_4:Eu^{2+},Dy^{3+}$ phosphor powder.
- Uniformly disperse the commercially prepared, green-emitting, $SrAl_2O_4$: Eu^{2+},Dy^{3+} phosphor into matrices of LDPE and PMMA polymers, in order to create a strong and stable three dimensional network and to subsequently investigate the mixing conditions, luminescence as well as thermal properties of the resultant composites. The characterization of the properties was intended to

elucidate information to identify suitable materials to hybridize with luminescent materials in order to minimize their moisture-induced degradation rates.

- Investigate the morphological, compositional, structural and photoluminescent properties of commercially prepared, blue-emitting, $Sr_4Al_{14}O_{25}:Eu^{2+},Dy^{3+}$ phosphor powder.
- Introduce the commercially produced, blue-emitting, $Sr_4Al_{14}O_{25}:Eu^{2+},Dy^{3+}$ phosphor into the LDPE polymer matrix and to characterize the structural, luminescence and thermal properties of the resultant polymer/phosphor composites.
- Prepare nanophase $SrAl_xO_y:Eu^{2+},Dy^{3+}$ phosphor powders by means of a combustion technique at a relatively low temperature and to study the morphological, structural and photoluminescent properties of the powder products.
- Introduce the combustion-synthesized $SrAl_xO_y:Eu^{2+},Dy^{3+}$ phosphor powders in the LDPE polymer and to investigate the morphological, structural, photoluminescent and thermal properties of the polymer/phosphor composite system as a precursor to the determination of a strong and stable composite network, with a view to addressing negative environmental effects, such as moisture that compromise phosphor potency.
- Use the sol-gel method to synthesize nanophase $SrAl_xO_y:Eu^{2+},Dy^{3+}$ phosphor powders and to study the influence of annealing temperature on the crystallinity, phase composition and luminescence properties of the phosphor material.
- Prepare powders of $BaAl_xO_y:Eu^{2+},Dy^{3+}$ materials with different Eu^{2+} and Dy^{3+} concentrations, by the combustion method and to study the influence of concentration on the structure, homogeneity, persistent luminescence as well as phase stability.
- Prepare $BaAl_xO_y:Eu^{2+},Dy^{3+}$/LDPE composites of well-defined composition and to study their photoluminescent and thermal properties.

1.10 Thesis outline

A summary of the contents in each chapter of this thesis is provided below.

Chapter 1

In this chapter the background information, overview of research contributions on classical phosphors, rationale and aims of the research project are given. The issues, perspectives and general advantages of nanostructured as well as inorganic/organic nanocomposite systems are briefly discussed. Finally, a summary of the subjects treated in the succeeding chapters of this thesis, is presented.

Chapter 2

In this chapter, the theoretical basis of the luminescent phenomenon is provided. A concise description of the key terminology employed in discussing luminescence is given, with emphasis on the sensitization, concentration quenching as well as transient characteristics of luminescence. This is followed by a summary of the physical principles involved in the luminescence process. Finally, descriptions of the mechanisms underlying the phenomenon are given, ending with a discussion of the factors, which determine the emission colour in luminescent materials.

Chapter 3

This chapter is dedicated to a detailed assessment of the relevant literature, which is divided into two parts: (i) The review of the literature on the synthesis and characterization. (ii) An analysis of some of the prominent mechanisms, which have been proposed for the photoluminescence phenomenon, particularly long afterglow luminescence.

Chapter 4

This is also a two-part chapter devoted to the discussion of the experimental techniques: (i) The presentation of the relevant characterization techniques, with emphasis on those that were employed in this study. (ii) The description of the two

synthesis procedures, i.e. the sol-gel process and the combustion reaction method, that were used in this work.

Chapter 5

In this chapter investigations of the morphological, compositional, structural and photoluminescent properties of the commercially prepared, green-emitting, $SrAl_2O_4:Eu^{2+},Dy^{3+}$ phosphor are described both for the as-prepared powder and for the composites of the phosphor in PMMA and LDPE polymers. A discussion of the thermal properties of the composites, based on DSC and TGA results, is also given.

Chapter 6

The investigations on the effects of adding the commercial blue-emitting $Sr_4Al_{14}O_{25}:Eu^{2+},Dy^{3+}$ phosphor in low-density polyethylene are described in this chapter.

Chapter 7

This chapter considers the characteristics of the europium and dysprosium co-doped strontium aluminate green phosphor, which was synthesized by a combustion method using urea as reducer and fuel. The results of the characterization of the morphology, particle size and structure, by the usual techniques, are presented. Further, the same properties, including thermal stability, are also discussed for the composites of the phosphor when it acts as a filler in the LDPE polymer.

Chapter 8

The strontium aluminate system exists in various crystalline phases. In particular, the $SrAl_2O_4$ phase is known to have two crystallographic polymorphs: monoclinic and hexagonal, which exist at low and high temperatures, respectively. The polymorphic behaviour in phosphors have an implication on their properties. These characteristics and the issues revolving around them, are discussed in this chapter, on the basis of the sol-gel synthesized $SrAl_xO_y:Eu^{2+},Dy^{3+}$ phosphor.

Chapter 9

In this chapter, the characterization of the luminescent and thermal properties of the blue-green $BaAl_xO_y:Eu^{2+},Dy^{3+}$ phosphor, synthesized by a combustion reaction method, as well as those of composites of the phosphor with the LDPE polymer, are discussed. An analysis is provided of the morphology, particle size, phase structure and thermal stability of the products, which were characterized by the usual standard techniques.

Chapter 10

The conclusions of the work described in the previous chapters of this thesis are summarized and compared with the project aims, in this chapter. In addition, several issues and perspectives, which can be useful in the design, synthesis, and application of phosphors, are mentioned.

1.11 References

1. Srivastava, A.M. Ronda, C.R. *Luminescence from Theory to Applications.* Ronda, C. (Ed.), Wiley-VCH, Germany, Chap. 4, (2008).
2. Cooke, D.W. Lee, J. K. Bennett, B.L. Groves, J.R. Jacobsohn, L.G. McKigney, E.A. Muenchausen, R.E. Nastasi, M. Sickafus, K.E. Tang, M. Valdez, J.A. *App. Phys. Lett*., **88:** 103, (2006).
3. Erdei, S. Roy, R. Harshe, G. Juwhari, H. Agrawal, D. Ainger, F.W. White, W.B. *Mater. Res. Bul*., **30:** 745, (1995).
4. Goldburt, E.T. Kulkarni, B. Bhargava, R.N. Taylor, J. Libera, M. *J. Lumin*., **72–74:** 190, (1997).
5. Meltzer, R.S. Feofilov, S.P. Tissue, B. Yuan, H.B. *Phys. Rev. B.*, **60:** R14012, (1999).
6. Chander, H. *Mat. Sci. and Eng*., **R49:** 113, (2005).
7. Canham, L.T. Wire *Appl. Phys. Lett*., **57:** 1046, (1990).
8. Edelstein, A.S. Cammarata, R.C. (Eds.) *Institute of Physics Publishing*, Bristol, Chap. 2, (1996).
9. Navrotsky, A. *Geochem. Trans.*, **4:** 34, (2003).
10. Chen, X.Y. Zhuang, H.Z. Liu, G.K. Li, S. Niedbala, R. *J. Appl. Phys.*, **94:** 5559, (2003).
11. Schwoebel, P.R. Brodie, I.*J. Vac. Sci. Technol. B.*, **13**(4)**:** 1391, (1995).
12. Ozawa, L. Mechanisms. *J. Electrochem. Soc.*, **126**(1)**:** 106, (1979).
13. Vater, U. Kunzler, G. Tews, W. *J. Fluores.*, **4:** 79, (1994).
14. Seager, C.H. Tallant, D.R. *J. Appl. Physics*., **87:** 4264, (2000).
15. Bhargava, R.N. *J. Lumin*., **70:** 85, (1996).
16. Tissue, B.M. Bihari, B. *J. Fluores*., **8**(4)**:** 289, (1998).
17. Barber, D.B. Pollock, C.R. Beecroft, L.L. Ober, C.K. *Opt. Lett*., **22**(16)**:** 1247, (1997).
18. Mackenzie, J.D. *Hybrid Organic-Inorganic Composites*; American Chemical Society: Washington, DC, **585:** 226. Chap. 17, 226, (1995).
19. Mark, J.E. *Polym. Eng. Sci*., **36:** 2905, (1996).

20. Moser, A. Takano, K. Margulies, D.T Albrecht, M. Sonobe, Y. Ikeda Y. Sun S.H. *J. Phys. D-App. Phys*., **35**(19)**:** R157, (2002).
21. Harvey, E.N. A. *Amer. Phil. Soc*., Philadelphia, 305, (1957).
22. Holsa, J. *The Electrochemical Society Interface*, 42, (2009).
23. Zuoling, F. Shihong, Z. Yingning, Y. Siyuan, Z. *Chem. Phys. Lett.,* **395:** 285, (2004).
24. Yamamoto, H. *Fundamentals of Luminescence*. CRC Press: New York, Chap. 2, (2007).
25. González, R.M.L. González-Calbet, J.M. Vallet-Regí, M. Cordoncillo, E. Escribano, P. Carda, J. B. Marchal, M. *J. Mater. Chem.,* **12:** 1128, (2002).
26. Yen, W.M. Shionoya, S. Yamamoto, H. *Phosphor Handbook*, CRC Press, Boca Raton, 790, (2006).
27. Matsuzawa, T. Aoki, Y. Takeuchi, N. Murayama, Y. *J. Electrochem. Soc*., **143**(8)**:** 2670, (1996).
28. Katsumata, T. Sakai, R. Komuro, S. Morikawa, T. Kimura, H. *J. Cryst. Growth*., **198/199**(I): 869, (1999).
29. Liu, Y. Xu, C.N. *J. Phys. Chem. B.*, **107:** 3991, (2003).
30. Ye, C.H. Bando, Y. Shen, G.Z. Golberg, D. *Chem.,* **118:** 5044, (2006).
31. Han, S.D. Singh, K.C. Cho, T.Y. Lee, H.S. Jakhar, D. Hulme, J.P. Han, C.H. Kim, J.D. Chun, I.S. Gwak, J. *J. Lumin.,* **128:** 301, (2008).
32. Yamamoto, H. Matsuzawa, T. *J. Lumin.,* **72–74:** 287, (1997).
33. Aitasalo, T. Hölsä, J. Jungner, H. Lastusaari, M. Niittykoski, J. *J. Lumin.,* **94–95:** 59, (2001).
34. Clabau, F. Rocquefelte, X. Jobic, S. Deniard, P. Whangbo, M.H. Garcia, A. Mercier, T.L. *Mater.,* **17:** 3904, (2005).
35. Clabau, F. Rocquefelte, X. Jobic, S. Deniard, P. Whangbo, M.H. Garcia, A. Mercier, T.L. *Solid State Sci.,* **9:** 608, (2007).
36. Han, S.D. Singh, K.C. Cho, T.Y. Lee, H.S. Jakhar, D. Hulme, J.P. Han, C.H. Kim, J.D. Chun, I.S. Gwak, J. *J. Lumin*., **128:** 301, (2008).
37. Glasser, F.P. Glasser, L.S.D. *J. Am. Ceram. Soc*., **46**(8)**:** 377, (1963).
38. Masumi, I. Hidehiko, K. Takuya, O. Tomoya, S. *JP. Patent.*, **316:** 433, (1997).

39. Lu, X.D. Zhong, M.J. Shu, W.G. Yu, Q.M. Xiong, X.Q. Wang, R.Q. *Powder Technol*., **177:** 83, (2007).
40. Guo, C.F. Luan, L. Huang, D.X. Su, Q. Lu, Y.H. *Mater. Chem. Phys*., **106:** 268, (2007).
41. Wu, S.L. Zhang, S.F. Liu, Y. Yang, J.Z. *Mater. Lett*., **61:** 3185, (2007).
42. Zhu, Y. Zeng, J. Li W. Xu, L. Guan, O. Liu, Y. *Appl. Surf. Sci.*, **255:** 7580, (2009).

Chapter 2
An Overview of the Theoretical Background on Luminescent Materials

2.1 Introduction

In a broad sense, the word phosphor is synonymous with a solid luminescent material, i.e., a material that converts absorbed energy into visible light, without undergoing incandescence. In a narrow sense the word simply refers to inorganic luminescent materials. As already mentioned, phosphors with one dimension less than 100 nm are called nanophosphors and may be described as nanostructured, inorganic, insulating solid materials that efficiently emit light under energetic particle and electromagnetic radiation [1]. Light emission from a phosphor is referred to as either fluorescence or phosphorescence. Light emission during the time when a substance is exposed to the exciting radiation is called fluorescence, while the after-glow if detectable by the human eye after the cessation of excitation is referred to as phosphorescence. However, in organic molecules, the two terms are distinguished by whether the transition

to emit light is allowed or forbidden by spin selection rules. Light emission due to an allowed transition is called fluorescence, while that due to a forbidden transition is called phosphorescence [2]. The term luminescence, which includes both fluorescence and phosphorescence, is used to describe the non-equilibrium emission of radiation. Three processes are involved in the luminescence process: excitation, energy transfer and radiative transition of the electrons. When light is absorbed as the excitation, the luminescence process is called photoluminescence (PL).

An overview of the terminology employed in characterizing luminescent properties is given below.

2.2 Characteristics of luminescence

The most important characteristics of luminescence are; power, emission and excitation spectra, polarization, rise and decay time, light sum, energy/quantum efficiency. A brief description of these and other terms follows.

2.2.1 Luminescence power

Luminescence power refers to the amount of radiant energy of luminescence released by matter per unit time. If the unit volume of the substance is taken into account, one speaks of the specific power of luminescence. The spectral density $W_l(\nu)$ and the luminescence power W_l are related by the equation [3],

$$W_l = \int_0^\infty W_l(\nu) d\nu \qquad (2.1)$$

where the integration is carried out over the entire spectrum of luminescence. If the radiation spectrum consists of one band or line, then instead of Eq. (2.1) one can write $W_l = W_l(\nu)\Delta\nu$, where $\Delta\nu$ is the effective bandwidth. By definition, only the part of spontaneous radiation specific power W_{sp} that exceeds the thermal emission background pertains to luminescence.

2.2.2 Luminescence spectrum

Graphs showing the dependence of luminescence power on the wavelength, frequency, or energy of radiation quanta are called luminescence spectra. The dependence of photoluminescence power on the frequency or wavelength of exciting light $W_l(\nu)$ with its constant intensity at all frequencies is referred to as the excitation spectrum.

2.2.3 Luminescence polarization

As with other kinds of radiation, the polarization of luminescence consists of anisotropy of the electromagnetic oscillation distribution in the plane perpendicular to the beam [3].

2.2.4 Optical indicatrix

The graph of the dependence of the electromagnetic radiation energy flux on the direction of its propagation is called the radiation indicatrix [3], and it is used mainly for describing elementary radiators.

2.2.5 Stokes' and anti-Stokes' shift

Stokes' law states the fact that the energy of absorption in luminescent materials, is higher than that of emission in most cases. The energy difference between the two is called the Stokes' shift [2]. Phosphors that show an emission with a large Stokes' shift usually exhibit a low quenching-temperature, which is disadvantageous for many applications [4]. Luminescent materials based on lanthanide ions circumvent this problem because the actual luminescent process is largely independent of its environment.

Anti-Stokes' luminescence refers to luminescent radiation whose wavelength is shorter than that of the exciting light [3]. This phenomenon is used in infrared ray counters and light-emitting diodes for obtaining radiation in the visible region [5,6].

Several reasons may be advanced to explain the occurrence of the anti-Stokes' phenomenon [3]:

- Due to energy exchange with other particles or with the crystal lattice, the electron that has been promoted to an excited state under the action of the light quantum $h\nu_{ex}$ can receive additional energy and move to a higher level (Fig. 2.1). The transition of the electron from this level back to its original state leads to the light quantum $h\nu_e > h\nu_{ex}$.

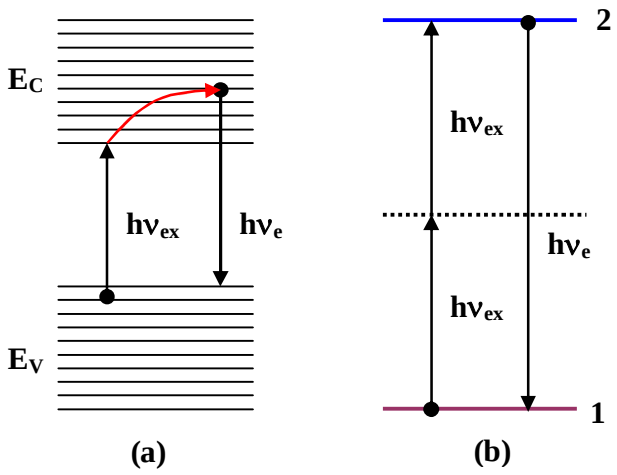

Figure 2.1: Two mechanisms responsible for anti-Stokes' luminescence: (a) After being excited from the valence band E_v to the conduction band E_c, an electron receives additional energy as a result of its interaction with the crystal lattice. (b) An electron is excited to the high-energy level 2 by two-photon absorption [3].

- When the transition of electrons to higher states originates from an excited, rather than the usual ground state, this may lead to a cascade of transitions to levels whose energies are considerably greater than $h\nu_{ex}$ [7].
- At large excitation densities a nonlinear optical process of two-photon absorption is possible. The substance is excited to levels whose energy is equal to $2h\nu_{ex}$.
- An accumulation of absorbed energy in one centre may take place as a result of the interaction between the excited centres.

2.2.6 Luminescence rise and decay

Usually, for non-persistent phosphors, a two level model can be used to explain the luminescence process (Fig. 2.2(a)) [8]. Fig. 2.2(b) is the three-level model illustrating long persistent phosphorescence, which includes a ground state, an excited state and a metastable trapping state for the active electron. The ground state electrons are pumped up to the excited state at a rate R_{ex}, and then decay back to the ground state with a transition rate R_{em}. C_t and C_d are trapping and detrapping rates respectively.

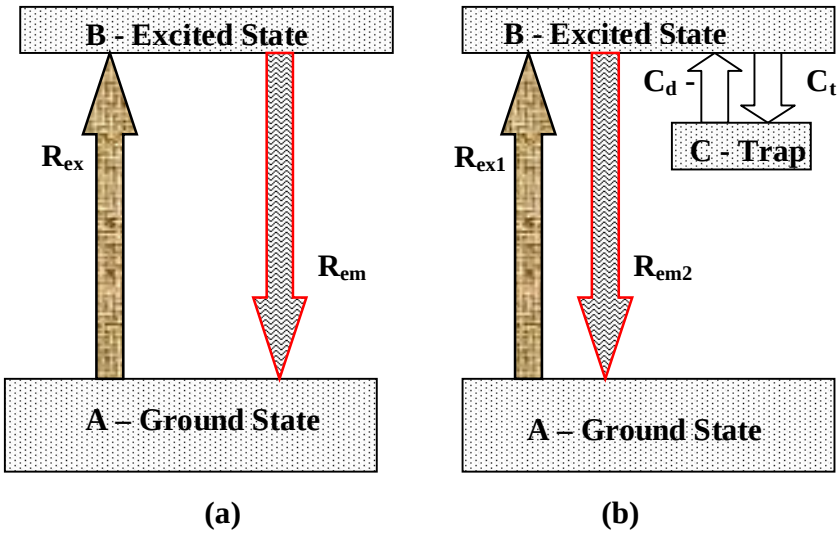

Figure 2.2: (a) Two-level model for non-persistent materials. (b) Three-level model for long persistent materials [8].

Increases in the luminescence intensity with time I(t) occur in accordance with certain laws. In the simplest case of a two-level system, I(t) is given by the equations [9],

$$I(t) = I_l^{st}\left[1 - \exp\left(-\frac{t}{\tau}\right)\right], \qquad 0 \le t \le t_1 \qquad (2.2)$$

$$I(t) = I_1(t_1)\exp\left[-\frac{(t - t_1)}{\tau_0}\right] = I_l^0 \exp\left(-\frac{t}{\tau_0}\right), \qquad t \ge t_1 \qquad (2.3)$$

where I_l^{st} is the luminescence intensity in a stationary regime, t = 0 and t = t_1 are the moments of switching on and off of the time-invariant intensity of excitation. The

parameters τ and τ_0 determine the mean time of luminescence rise and decay; τ decreases with increasing excitation energy density.

2.2.7 Light sum

Light sum (Σ) is defined as the number of light quanta N(t) emitted by a crystal phosphor after the illumination has ceased and is given by the equation [3],

$$\sum = \int_0^\infty N_l(t)dt . \qquad (2.4)$$

The afterglow of crystal phosphors partially compensates for the deficiency of luminescence quanta Σ_d in the luminescence rise portion as compared with the steady-state regime. The ratio Σ/Σ_d depends on the excitation intensity and can be greater or less than unity because of the change in the quantum yield of luminescence that takes place during the excitation process.

2.2.8 Thermoluminescence

When the stimulation of an electron from a metastable level to the conduction band, to facilitate recombination with a hole, is achieved by warming, then the process is referred to as thermoluminescence. Thermoluminescence is important since the study of the temperature dependence of the afterglow intensity and spectrum permits one to draw conclusions about the depths at which impurity levels lie in solids [10,11].

2.2.9 Phosphor efficiency

Phosphor efficiency may be expressed either in terms of energy or quantum yield. Energy efficiency (yield) of luminescence is the ratio of the luminescence energy to the absorbed excitation energy [3] while quantum efficiency is the ratio of the number of luminescence quanta to the number of absorbed quanta [12]. The concept of the luminescence yield was introduced into the literature by Vavilov [13]. The theory of injection luminescence distinguishes between internal and external quantum of luminescence. The internal yield is equal to the ratio of the number of emitted radiation

quanta to the number of recombinations of electrons and holes [3]. The external yield takes into account only those radiation quanta that are emitted by, say, the light-emitting diode and can be recorded by a detector. As a rule, due to the small angle of total internal reflection at the crystal-air boundary and the higher absorption coefficient of edge luminescence, the external quantum yield of injection luminescence is much smaller than the internal quantum yield. Since recombination radiation propagates in all directions, a major portion of it is reflected back from the crystal surface and is absorbed in the device [3].

2.2.10 Transient characteristics of luminescence

Light emission from solids has been studied mainly for two reasons: (1) As a technique for investigating the energy levels giving rise to radiative transitions and the corresponding transition probabilities. (2) As a way of developing light emitters for many practical applications. The main focus of investigations has been in two directions:

(i) The spectral response under various temperatures and intensities of excitation.
(ii) The time dependence of the decay of luminescence.

Of these two, the time dependence of luminescent relaxation has received the least rigorous treatment [14], both as regards the range of times investigated and as regards the theoretical interpretation of the observed behaviour.

Phosphorescence is a transient luminescent phenomenon, i.e. a time-dependent emission process that is related to a quasistable state in a luminescent centre or an electron or hole trap. The classical law governing the decay in a monomolecular recombination process, for example that involving an excited free carrier and a bound centre, is an exponential time dependence of the form [14],

$$L(T) \propto \exp\left(-\frac{t}{\tau}\right) \qquad (2.5)$$

where τ is a suitable time constant. Consequently, there is a tendency to anticipate exponential processes. For a bimolecular process, the expected classical law is of the form [14],

$$L(T) \propto (t + t_0)^{-2} \qquad (2.6)$$

where t_o is a characteristic time constant. However, it is accepted by several workers [14,15] that the prevailing form of time dependence in response to excitation of duration short in comparison with the time of measurement is a power law of the form,

$$L(T) \propto t^{-5} \qquad (2.7)$$

and those workers plot their results in the log L-log *t* representation which brings out these relations. The prevalence of power laws in the context of luminescence becomes especially interesting in the light of the fact that very similar power laws are known to be very generally applicable to dielectric relaxation [16] and are also known in recombination in semiconductors and semi-insulators 17]. The fact that many different materials show luminescence decays which are well described by power laws strongly suggests the applicability of some very general common principles. However, the validity of power laws in the interpretation of luminescence decay still requires to pass the universality test.

2.3 Non-radiative transitions

In addition to the radiative emissions from an excited luminescent centre, there is the possibility of non-radiative de-excitation processes taking place. A discussion of some of these processes follows.

2.3.1 The decay of luminescence

The general representation of the emission decay process of the luminescence intensity $I(t)$ after the termination of excitation is an exponential function of the form [18],

$$I(t) = I_0 \exp\left(-\frac{t}{\tau}\right), \qquad (2.8)$$

where τ is the decay time constant of the emission, although the emission decay curve of non-localized centres, is not always represented in the exponential form of this equation. Since the emission intensity is proportional to the number of excited luminescence centres in a unit volume, the decay time of the after-glow in Eq. 2.8 is equal to the lifetime of the centre and may be expressed as,

$$\tau = \left(W_R + W_{NR}\right)^{-1} \tag{2.9}$$

where W_R and W_{NR} are the radiative and nonradiative transition probabilities, respectively. Consequently, it can be shown that the luminescence efficiency of the centre is given by,

$$\eta = \frac{W_R}{W_R + W_{NR}} \tag{2.10}$$

The non-radiative transition probability W_{NR} is generally ruled by thermal relaxation processes. However, it can also be increased by the effect of resonant energy transfer between optical centres.

2.3.2 Relaxation processes

2.3.2.1 Thermal activation

The thermal relaxation in a luminescence centre can be divided into two types of mechanisms as shown by the two configurational coordinate diagrams (a) and (b) in Fig. 2.3 [18]. In the first type (a), the centre is thermally activated from point A, the point of the lowest energy on the excited state II, to the crossing point C where the electronic states of the excited and ground states are intermixed, and then thermally released from C to B on the ground state I. The energy ε necessary to excite the centre from A to C is called the thermal activation energy. The probability that the centre will make the transition from state II to state I by thermal activation via point C is generally given by:

$$a = s\exp\left(-\frac{\varepsilon}{kT}\right). \tag{2.11}$$

Therefore, the nonradiative transition probability by thermal activation is given by,

$$W_{NR} = s\exp\left(-\frac{\varepsilon}{kT}\right), \qquad (2.12)$$

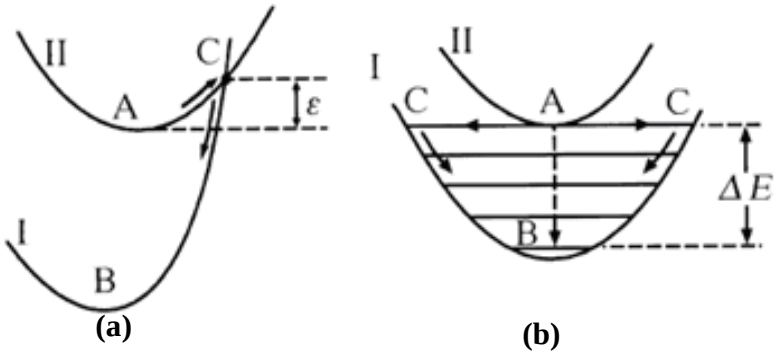

Figure 2.3: Configurational coordinate models of nonradiative relaxation processes: (a) Thermal activation type. (b) Multiphonon type. [19]

where s is the frequency factor and *k* is the Boltzmann constant. This type of non-radiative transition is strongly dependent on temperature, resulting in thermal quenching, that is, the decrease of emission efficiency and shortening of the emission decay time at high temperature, as may be deduced from the equations, $\tau = (W_R + W_{NR})^{-1}$ and $\eta = W_R(W_R + W_{NR})^{-1}$ for the lifetime and luminescence efficiency of the centre, respectively.

2.3.2.2 Multiphonon emission

The second type of nonradiative transition is a multiphonon process shown in Fig. 2.4(b). This is the most important non-radiative de-excitation process that competes with radiative de-excitation and is often observed in the relaxation between the 4*f* excited levels of rare-earth ions [18], where no cross-point exists between curves I and II in the configuration coordinate diagram because of the similarity of the electronic states. The transition between states I and II occurs at point A, where an energy gap ΔE exists between the states: namely, the transition from the pure electronic state of II to the electron-phonon-coupled state of I, with *n* phonons, takes place at A, which is followed by the instantaneous transfer to point C and relaxation to B. The nonradiative transition

probability is, therefore, dependent on ΔE or n, the number of phonons necessary to fill the energy gap, since $\Delta E = n\omega_p$, where ω_p is the largest phonon energy. The nonradiative multiphonon transition probability is then given by [20],

$$W_{NR}(\Delta E) = W_{NR}(0)e^{-\alpha\Delta E} \qquad (2.13)$$

where α depends on the character of the phonon (lattice vibration). Since the process is mainly due to the spontaneous emission of phonons, the temperature dependence of the probability is small.

2.3.3 Energy transfer

Energy transfer is the migration of the excitation energy between pairs of luminescent centres. The ions involved can either be identical or of different species. The excitation residing in an ion can migrate to another identical ion that is in the ground state as a result of resonant energy transfer when they are located close to each other [21]. Energy migration processes increase the probability that the optical excitation is trapped at defects or impurity sites, enhancing non-radiative relaxation. However, in some compounds such as NdP_5O_{14}, the lattice sites occupied by Nd are separated from each other by a relatively large distance (5.6 Å), and a high luminescence efficiency is achieved even when all the sites are occupied by activator ions (Nd) [22]. The energy transfer between different ion species can also take place when they have closely matched energy levels. The energy transfer results either in the enhancement (e.g., $Ce^{3+} \rightarrow Tb^{3+}$) or in the quenching (e.g., $Eu^{3+} \rightarrow Nd^{3+}$) of emission. Energy transfer between 4f levels has been shown to originate from the electric-dipole electric-quadrupole interaction using glass samples [21]. Besides the energy transfer arising from the interaction between ions, the process can also occur from a host crystal to activators leading to host-excited luminescence [21].

2.3.4 Sensitization of luminescence

The term sensitized luminescence in crystalline phosphors refers to the phenomenon whereby an impurity (activator or emitter) is enabled to luminesce upon the

absorption of light in a different type of centre (sensitizer, or absorber) and upon the subsequent radiationless transfer of energy from the sensitizer to the activator. Energy transfer processes are often used in practical phosphors in order to enhance the emission efficiency [18]. While the energy transfer from a donor to an emitting centre causes sensitization of luminescence, the transfer from an emitting centre to a nonradiative centre causes the quenching of luminescence. A very small amount (~10 ppm) of Fe, Co, and Ni in ZnS phosphors, for example, appreciably quenches the original emission as a result of this type of energy transfer [23]. Although these ions (referred to as killer or quencher ions) are normally undesirable, they are, in some phosphors, intentionally added for the purpose of reducing the emission decay time, thereby obtaining a fast-decay phosphor at the expense of emission intensity [24].

2.3.5 Concentration quenching

Concentration quenching of luminescence is the reduction in the emission of a phosphor when the activator concentration surpasses a certain critical value as shown in Fig. 2.4. The origin of this effect is thought to be one of the following [18]:

- Cross-relaxation between the activators results in the loss of excitation energy from the emitting state.
- Increased activator concentration facilitates migration of excitation energy to remote killers.
- The pairing or coagulation of activator ions converts them into quenching centres.

The emission colour of a phosphor can change with the increase in activator concentration when the concentration quenching due to cross-relaxation occurs on a particular level among several emitting levels. An example is provided by Tb^{3+}-activated phosphors. At concentrations below 0.1%, the emission colour of these phosphors is blue-white due to mixing of blue emission from the $^5D_3$ emitting level and green emission from the $^5D_4$ level. At concentrations above 0.1%, the colour changes to green. This

change is attributed to cross-relaxation [18] between the $^5D_3$ and $^5D_4$ emitting levels, which diminishes the population of Tb^{3+} ions in $^5D_3$ state while increasing the ions in the $^5D_4$ state.

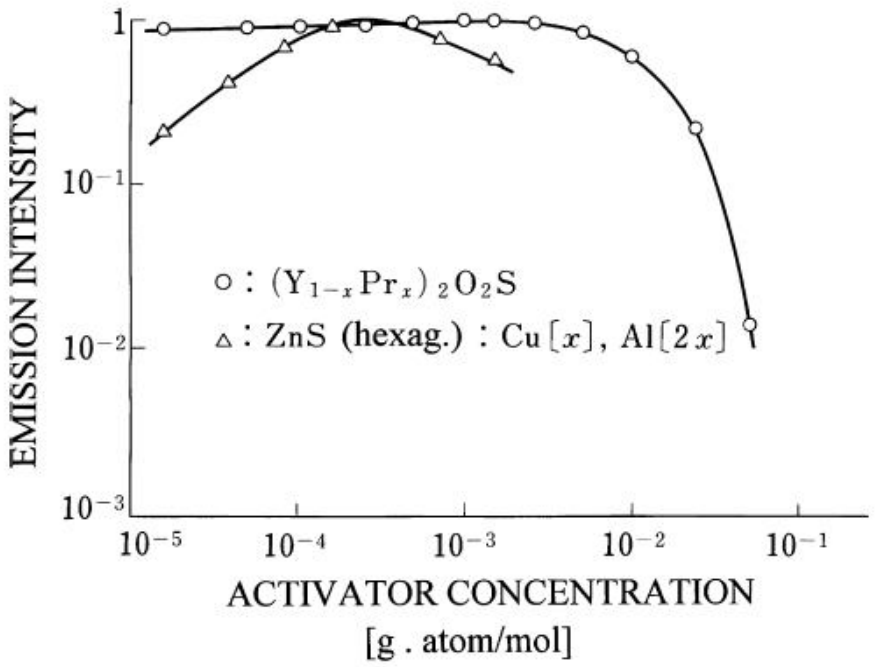

Figure 2.4: Activator concentration dependence of the cathode-luminescence intensities of $Y_2O_2S:Eu^{3+}$ and ZnS:Cu [25].

2.3.6 Quenching traps

Impurities can either improve or reduce the luminescence efficiency of a host matrix. For example, the luminescence efficiency of ZnS phosphors has been known to be drastically reduced by contamination with very small amounts of the iron group elements [23]. Ions that cause this quenching effect are referred to as killers or quenching traps of luminescence and may be defined as defects caused by incidental impurities or that are inherent to the lattice. The kind and quantity of the ions that change phosphor characteristics differ from one phosphor to another [26]. Consequently, it is very important to remove such impurities and defects, from host lattices, in the manufacturing processes of phosphors. There are two proposed mechanisms for the occurrence of this phenomenon; (1) the killers may give rise to deep levels in the forbidden band, which act

as nonradiative recombination centres for free electrons in the conduction band and holes in the valence band or, (2) the excitation energy absorbed by the luminescence centre is transferred nonradiatively to the killer ions [27].

2.3.7 Luminescence quantum yield and quenching processes

Due to the energy loss processes, which take place in luminescent materials, not all phosphors have a quantum efficiency of one. In addition, the degradation processes in luminescent materials do occur quite frequently during the operation of devices utilizing phosphors. The influence of these processes on device performance can be considerable; 30-50% loss in the case of cathode ray tubes [28]. The energy efficiency of these processes is given by [28]:

$$\eta = \frac{(1-r)(h\nu)}{\xi \eta_t \eta_{act} \eta_{esc}} \qquad (2.14)$$

in which r is the backscatter coefficient, hν is the mean energy of the photons emitted, ξ is the energy needed to generate a thermalized electron-hole pair, η_t is the transfer efficiency of electron-hole pairs to activators or sensitizers, η_{act} is the quantum efficiency of the activator ions and, η_{esc} is the escape probability. Eq. (2.14) can be used to deduce loss processes [28] when,

- the absorbed energy does not reach the luminescent ions (η_t),
- the absorbed energy reaches the luminescent ions but there are nonradiative channels to the ground state (η_{act}),
- the luminescence generated is absorbed by the luminescent material (η_{esc}).

2.4 Physical principles of luminescence

2.4.1 Basics of luminescence

The phenomena of fluorescence and phosphorescence are best explained with the help of the Jablonski energy-level diagram (Fig. 2.5). For any particular molecule, there

are a combination of singlet (S) and triplet (T) states. Excitation (e.g. S_0 to S_1, S_2) involves the absorption of sufficient energy to raise a molecule's electrons into electronic states of S_1 or S_2. However, excitation is not a continuous process and the energy absorbed by the molecule has to ultimately be released, which may occur by one or a combination of the following events [29];

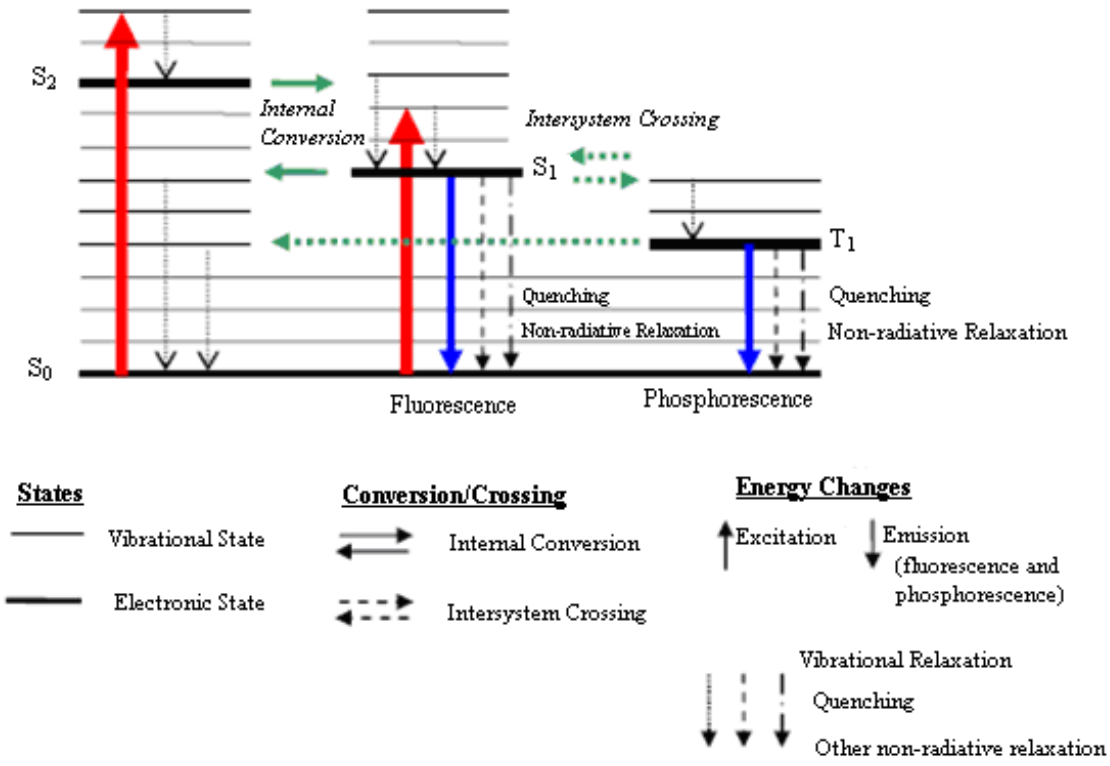

Figure 2.5: Jablonski energy level diagram showing the luminescence process [30]

- emissions of photons equal to the energy-level difference
- energy transfer via quantized vibrational exchange (phonons) in the material
- other complex energy transfer mechanisms

These energy transfers are further classified as, vibrational relaxation, internal conversion, quenching, intersystem crossing, and delayed fluorescence.

The above descriptions give the impression that every atom has the potential to exhibit luminescence. According to Sant and Merienne [31] practically all existing materials are luminescent. However, luminescent behaviour depends on relative probabilities of alternative processes by which excited atoms can return to the ground state. Further, according to Heyes [32] the persistence of phosphorescence implies that electrons occupy excited energy levels for extended periods. This allows interactions between excited atoms and the surroundings to have an influence on the nature of the emission.

2.4.2 Luminescence in phosphors

The configurational coordinate diagram (Fig. 2.6) can be used to explain the influence on the processes of absorption and emission in a phosphor. Though simple, the model can illustrate several physical phenomena including Stokes' shift, absorption and emission band widths and can assist in understanding thermal quenching [30].

After excitation, electrons occupying an upper vibrational level of an excited state (B) will relax to the ground vibrational level of that state (C) losing energy via the release of phonons [32]. Following radiative emission, the electrons reaching a higher vibrational level of the ground state (D) will further lose energy (phonons) on their return to their ground state equilibrium (A). The difference in excitation and emission energy levels can be seen in the diagram illustrating Stokes' shift (Fig. 2.1) [30].

A non-radiative emission may occur if the temperature is high enough. In such a condition, electrons in the excited state can intersect the ground state curve (E) allowing vibrational relaxation via phonon release to the ground state. Ranson [33] describes this as the absorption of thermal energy (phonon) from point C, which excites the electrons to the intersection point E. Since non-radiative processes can now also take place, the observed luminescence intensity from a large quantity of excited ions will diminish. An increase in temperature will result in electrons spreading over a number of vibrational levels in the excited state. Since radiative transitions can take place between any of the

vibrational states in the excited and ground states, a broadening of the emission lines is expected [32].

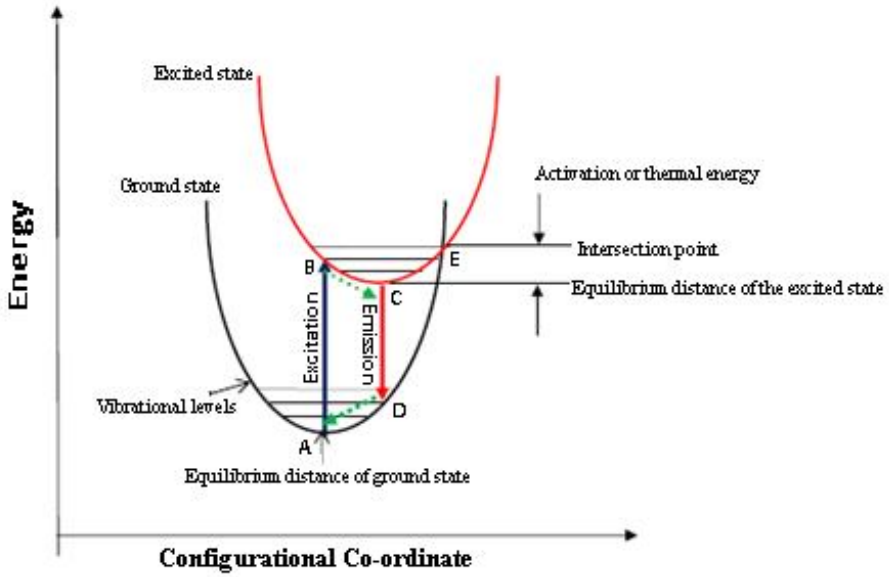

Figure 2.6: Configuration coordinate diagram [30].

2.5 Electronic processes leading to luminescence

2.5.1 4f Energy levels and relaxation

In contrast to other transition metal ions, the 4f electronic energy levels of lanthanide ions are not heavily affected by the environment or crystal electric field because the 4f electrons are shielded from external electric fields by the outer $5s^2$ and $5p^6$ electrons [22]. Due to the crystal field, the Stark effect splits each level into a number of sublevels as determined by the symmetry of the crystal field surrounding the rare-earth ion.

In a luminescent material, the excited states relax either by light or phonon emission. The rate of phonon emission, ω, depends on the number of phonons emitted simultaneously to bridge the energy gap and is expressed as [22],

$$\omega \propto \exp\left(-k\frac{\Delta E}{h\nu_{\max}}\right), \qquad (2.15)$$

where ΔE is the energy gap to the nearest lower level and $h\nu_{max}$ is the maximum energy of phonons coupled to the emitting states. The following information can be deduced from equation 2.15:

(1) The rate of phonon emission, ω, decreases rapidly with an increase in ΔE, so that the competitive radiative process becomes dominant [34].
(2) Large values of $h\upsilon_{max}$ quench light emission. This is demonstrated by the fact that luminescence of Eu^{3+} in aqueous solution is almost quenched, but begins to appear if H_2O is replaced by D_2O [35].

2.5.2 $4f^{n-1}5d^1$ States and charge-transfer states (CTS)

Two additional kinds of electronic states exist in the energy region spanned by 4f levels. These states have different characters from 4f levels [22]. They are the $4f^{n-1}5d^1$ states and the charge transfer states (CTS). In the former, one of the 4f electron(s) is transferred to a 5d orbital and, in the latter case, electrons in the neighbouring anions are transferred to a 4f orbital. Both of these processes are allowed and result in strong optical absorptions. They are observed as broadband excitation spectra around 300 nm [22]. Optical absorptions due to f-d transitions are found for Pr^{3+} and Tb^{3+}; those due to a charge-transfer transition are found in Eu^{3+}. Luminescence due to the transition from CTS has also been reported for Yb^{3+} [36].

Unlike the energies of 4f states, the energies of the $4f^{n-1}5d^1$ and CTSs are more dependent on their environments. However, the relative order of energies of these states are found to be the same for the whole series of rare-earth ions in any host materials [22].

2.5.3 Electronic transitions involved in europium luminescence

Europium ions play an important role in phosphors for the lighting and display industry [28]. Fig. 2.7 displays the energy level diagram of these ions. An understanding

of the spectral properties associated with the emission spectra is crucial for phosphor development. In the diagram, the energy axis is representative of ions in oxidic lattices. Horizontal lines represent narrow energy states of 4f levels. Shaded areas represent broad charge transfer states in the case of Eu^{3+} and $4f^6 5d^1$ states for Eu^{2+}. Triangles indicate

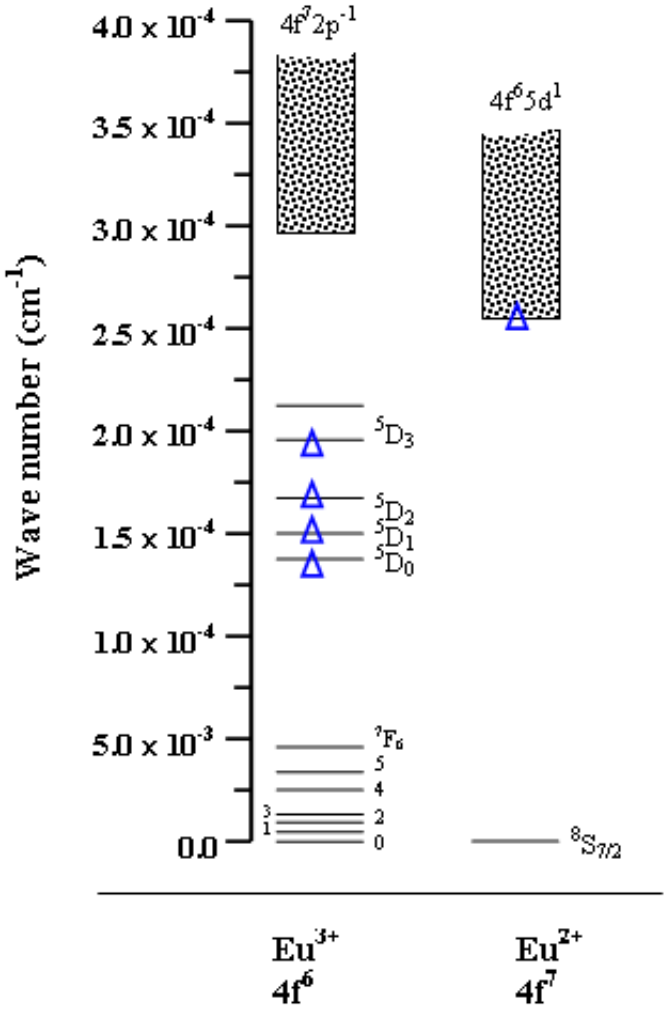

Figure 2.7: Energy level diagram of Eu^{3+} and Eu^{2+} [28]

levels from which radiative transitions can occur. For Eu^{2+} the 5d band covers almost all 4f levels, leading to a broad emission spectrum. The emission wavelength is determined by the position of the 4f $^6 5d^1$ levels, which is a function of the crystal field [28].

2.6 Luminescence of transition metal ions

2.6.1 Introduction

The electronic configuration in transition metal ions consists of optically active unfilled outer 3d shells, while that in rare earth ions has unfilled optically active 4f electrons screened by outer electronic filled shells. The unfilled shells cause the ions to present quite unique features.

The ionic radii of divalent transition metal ions with $3d^n$ electron configurations are close to those of the cations of IIb-VIb compounds [28]. Hence, these transition metal ions can be easily introduced into IIb-VIb compounds. In contrast to divalent ions, trivalent rare-earth ions are difficult to introduce into IIb-VIb compounds in high concentrations. This is because the valence of the trivalent ions is different from the host cations and the chemical properties are also quite different [37]. This is one of the reasons that bright luminescence from trivalent rare-earth ions in ZnS is rather difficult to obtain, though exceptionally bright and highly efficient luminescence has been observed in $ZnS:Tm^{3+}$. This phosphor shows bright blue luminescence under cathode-ray excitation [37].

2.6.2 Luminescence of some rare earth ions

2.6.2.1 Introduction

The rare earth ions, either in their divalent or trivalent charge states, form a very important class of luminescence activators in phosphors and single crystals [38]. The activator ions in phosphors are usually derived from these atoms. In spite of their scarcity and difficulty in obtaining, the rare earths are highly valued for their unique properties, especially as optically active elements in their ionized state. The atomic structure of rare earth ions in the lanthanide series and transition metal ions of the iron group are shown in Fig. 2.8. All lanthanide ions are characterized by a Xe core, an unfilled $4f$ shell, and

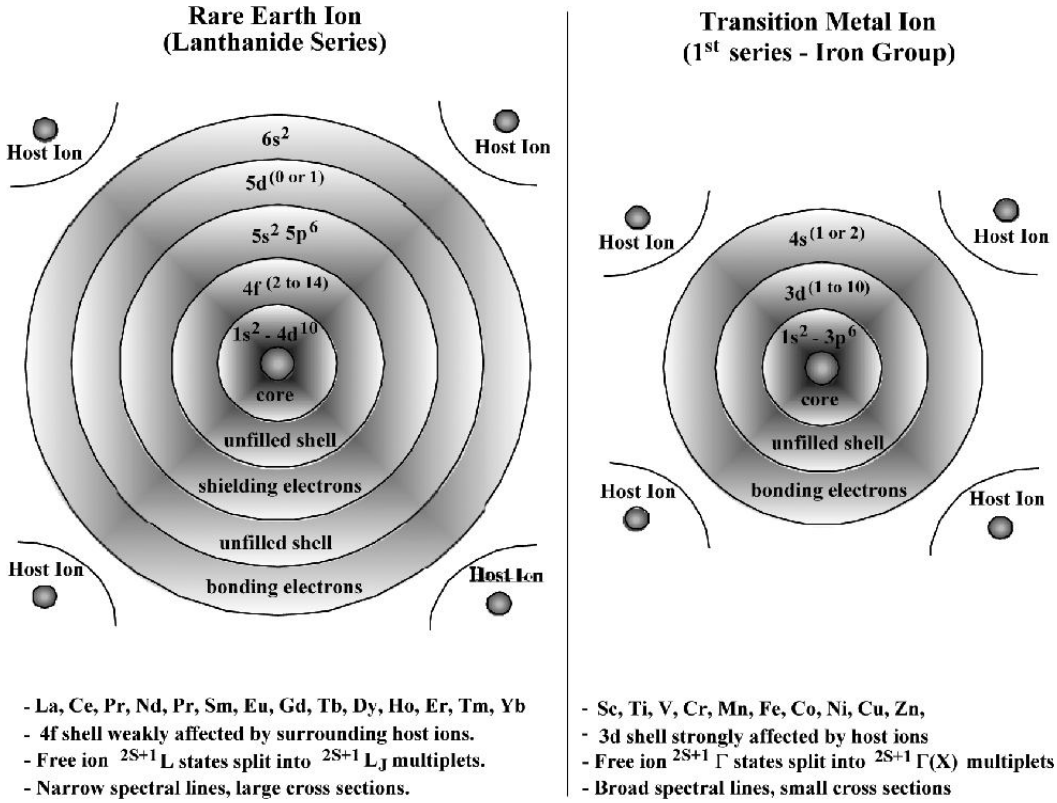

Figure 2.8: Rare Earth and Transition metal ion atomic structure [39].

some outer shells that screen the 4*f* shell from outside perturbing influences [39]. This screening effect protects the optically active electrons to some extent from the influence of the crystal field, giving the lanthanides their characteristic sharp and well defined spectral features. In other words they are very similar to free ion spectra. This is in contrast to other transition metals where the unfilled 3d shell is not as well screened due to only a single outer shell.

2.6.2.2 The f-f transition of Eu^{3+}

The outer electronic configuration in trivalent lanthanide ions is $5s^2 5p^6 4f^n$, where *n* indicates the number of electrons in the unfilled 4f shell while the $4f^n$ electrons are the valence electrons that are responsible for the optical transitions [40].

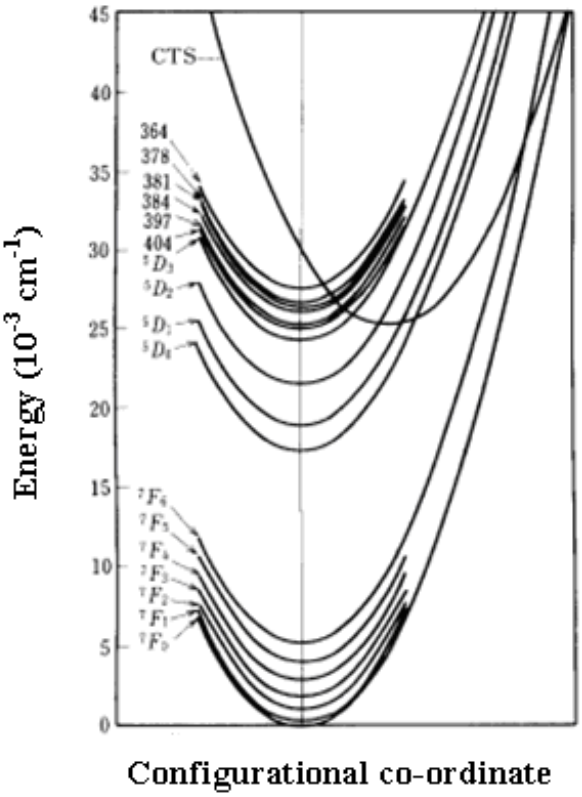

Figure 2.9: Configurational co-ordinate model of $Y_2O_2S:Eu^{3+}$ [41]

The luminescence from Eu^{3+} usually consists of narrow lines in the red spectral range. Most of the lines belong to transitions from the $^5D_0$ level to the ^7F_J (J = 0, 1, 2, 3, 4, 5, 6) levels, although transitions from other 5D-levels are frequently observed [22]. The $^5D_0 \rightarrow {}^7F_J$ transitions are ideally suited for determination of the lattice site symmetry. For a position with inversion symmetry, electric dipole transitions between the 4f levels are strictly forbidden. Without inversion symmetry, electric dipole transitions become allowed and some transitions with $\Delta J = 0, \pm 2$ appear and dominate the spectrum for even small deviations from inversion symmetry [28].

Eu^{3+} emission is characterized by quenching, magnetic, and electric dipole transitions, respectively. The emissions from $^5D_2$ and $^5D_1$ are quenched, with an increase in the Eu^{3+} concentration due to a cross-relaxation process, $(^5D_J \rightarrow {}^5D_0) \rightarrow ({}^7F_0 \rightarrow {}^7F_J)$ [22]. The emission in the vicinity of 600 nm is due to the magnetic dipole transition $^5D_0 \rightarrow {}^7F_1$,

which is insensitive to the site symmetry. The emission around 610–630 nm is due to the electric dipole transition of ($^5D_0 \rightarrow {}^7F_2$), induced by the lack of inversion symmetry at the Eu^{3+} site, and is much stronger than that of the transition to the $^7F_1$ state.

The configurational co-ordinate model shown in Fig. 2.9, can be used to explain the luminescence process in $Y_2O_2S:Eu^{3+}$. The excitation of Eu^{3+} takes place from the bottom of the $^7F_0$ curve, rising along the straight vertical line, until it crosses the charge-transfer state (CTS). Relaxation occurs along the CTS curve [41]. Near the bottom of the CTS curve, the excitation is transferred to ^5D_J states. Relaxation to the bottom of the ^5D_J states is followed by light emission downward to ^7F_J states.

2.6.2.3 The d-f transition of Eu^{2+}

Similar to the trivalent (RE^{3+}) ions, divalent rare earth (RE^{2+}) ions have an outer electronic configuration of $4f^n$. However, unlike that of RE^{3+} ions, the $4f^{(n-1)}5d$ excited configuration of RE^{2+} ions is not far from the $4f^n$ fundamental configuration [40]. As a

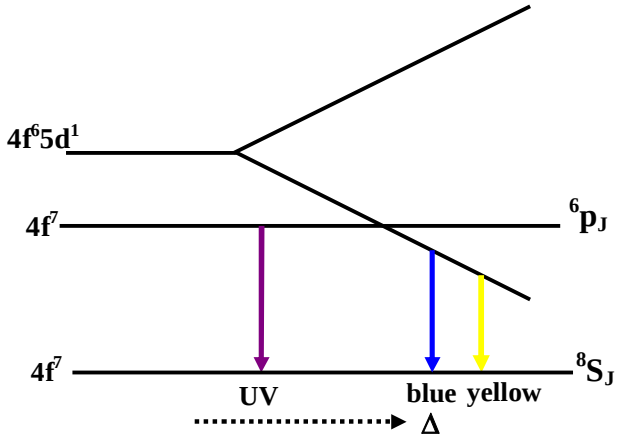

Figure 2.10: Schematic diagram of the energies of $4f^7$ and $4f^65d^1$ levels in Eu^{2+} influenced by crystal field Δ [42]

result, $4f^n \rightarrow 4f^{(n-1)}5d$ transitions can possibly occur in the optical range for divalent rare earth ions. They lead to intense (parity-allowed transitions) and broad absorption and emission bands.

The emission bands of Eu^{2+} are usually broad due to f-d transitions [22]. The wavelength positions of the emission bands depend very much on hosts, changing from the near- UV to the red. This dependence is interpreted as due to the crystal field splitting of the 5d level, as shown schematically in Fig. 2.10 [42]. With increasing crystal field strength, the emission bands shift to longer wavelength. The luminescence peak energy of the 5d-4f transitions of Eu^{2+} and Ce^{3+} are affected most by crystal parameters denoting electron-electron repulsion; on this basis, a good fit of the energies can be obtained [43].

2.6.2.4 The f-h transition of Dy^{3+}

Dy^{3+} emits in two spectral regions: (1) 470 to 500-nm region due to the $^4F_{9/2} \rightarrow {}^6H_{15/2}$ transition. (2) 570 to 600-nm region due to the $^6F_{15/2} \rightarrow {}^6F_{11/2}$ transition [44]. However, the direct UV excitation of this ion is not effective due to the relatively large energy of both the charge transfer as well as the $4f^8 5d^1$, states. Excitation by means of host complex ions may be achievable by an energy transfer process [45].

2.7 Excitation mechanisms of luminescence centres

2.7.1 Introduction

Inorganic phosphors are composed of a host lattice doped with a small amount of impurity ions that activate luminescence (Fig. 2.11) [28]. The absorption of energy, which is used to excite the luminescence, takes place by either the host lattice or the doped impurities. In most cases the emission takes place on the impurity ions, which when they also generate the desired emission are called activator ions. Hence, the luminescence processes of a phosphor can be divided into the processes mainly related to the host and those that occur around and within the activator [28].

The activator ions possess energy levels that can be populated either by direct excitation or indirectly by energy transfer. Generally, two types of activator ions can be

distinguished. In the first type the energy levels of the activator ion involved in the emission process show only weak interactions with the host lattice [4]. The second type of activator ions strongly interact with the host lattice. The strong coupling of the electronic states with vibrational modes of the lattice mainly leads to more or less broad bands in the spectrum [4].

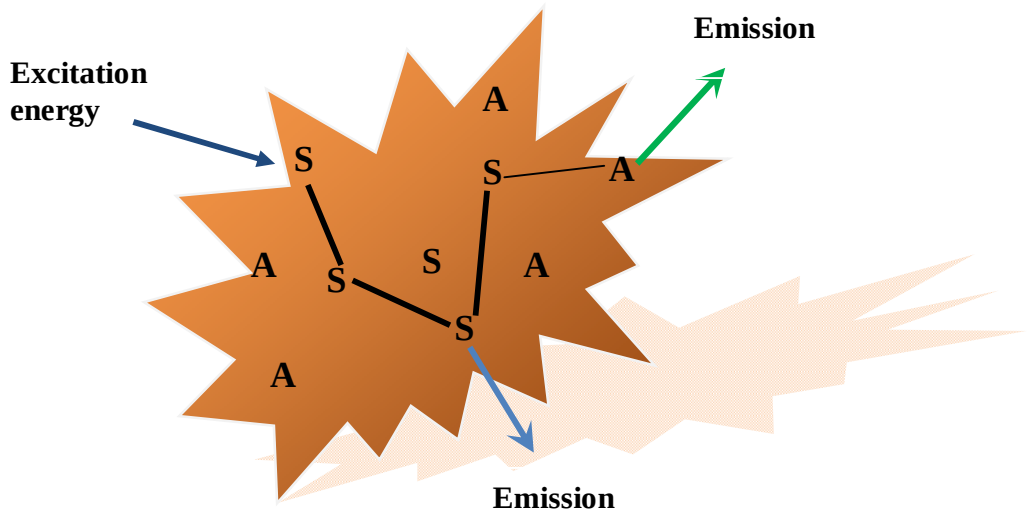

Figure 2.11(a): Luminescent material containing activator ions A and sensitizing ions S. Redrawn from [28].

The absorption efficiency of an activator can be increased by adding a second kind of impurity (sensitizer). A sensitizer is a foreign ion incorporated into a host lattice and that is capable of transferring its energy of excitation to a neighbouring ion (activator), thus inducing luminescence (Fig. 2.11(b)) [4].To avoid the occurrence of the transient decay processes such as concentration quenching, which diminish the efficiency of the luminescence process, the impurity concentrations used are usually low.

The luminescence of inorganic solids can be traced to two mechanisms: luminescence of localized centres and luminescence of semiconductors [47,47]. A brief account of the mechanisms involved in these luminescence processes is given below.

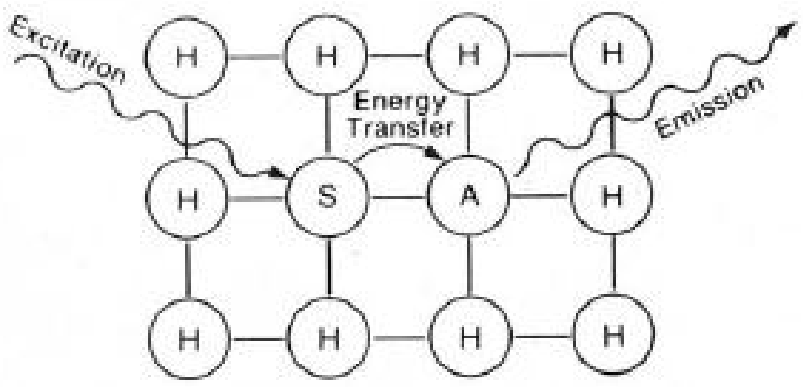

Figure 2.11(b): Diagrammatic representation of the role in the luminescence process of a sensitizer (S) and its relationship to an activator (A) and the host lattice (H) [4].

.2.7.2 Centre luminescence

In this mechanism, the emission is generated on an optical centre, in contrast to, e.g., emission, which results from optical transitions between host lattice band states or from a transition between two centres [28]. The resulting characteristic luminescence occurs in the visible part of the electromagnetic spectrum and may consist of either sharp or broad emission bands [28]. Sharp bands arise from purely electronic transitions while broad bands originate from the simultaneous transitions of both electronic and vibrational systems [48]. Broad bands are observed when the character of the chemical bonding, in the ground and excited states, differs considerably. This goes hand in hand with a change in equilibrium distance between the emitting ion and its immediate chemical environment and is commonly explained with the configuration coordinate diagram shown in Fig. 2.12 [49]. In the diagram,

- r_g and r_e represent the metal-ligand distances in the ground and excited states, respectively.
- E_a and E_e are the energies at which the absorption and emission bands have their maximum intensity, respectively.

- Δ is the energy of the so called zero phonon line; this transition involves completely relaxed excited and ground states, and no excited phonon states are involved – hence the name of this kind of transitions.
- $\hbar\omega_g$ and $\hbar\omega_e$ give the phonon frequencies in the ground and excited states, respectively.

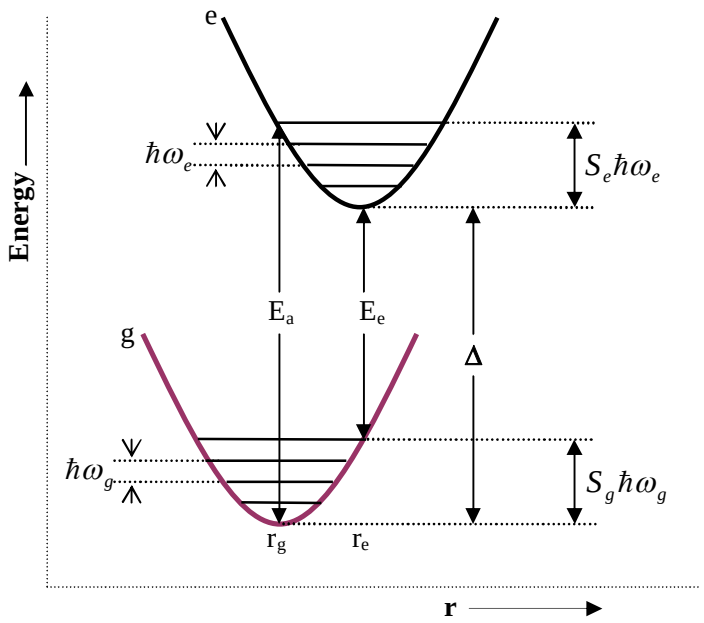

Figure 2.12: Potential energy curves illustrating an electronic transition from the ground to the excited state. The Stokes' shift comprises of the terms $S_e\hbar\omega_e$ and $S_g\hbar\omega_g$. Redrawn from [4].

- S_e and S_g are the Huang-Rhys factors in the ground and excited states, respectively. They give the mean number of phonons involved in the absorption and emission processes, respectively.

2.7.3 Charge transfer luminescence

The optical transition in the charge transfer process takes place between different kinds of orbitals or between electronic states of different ions [28]. This kind of excitation has a very strong influence on the charge distribution on the optical centre.

Hence, there is considerable change in the chemical bonding and the corresponding emission spectra are expected to be very broad.

2.7.4 Donor-acceptor pair luminescence

The luminescence transitions in this mechanism involves electron transfer from the excited state of donors to the ground state of acceptors. This mechanism was recognized earlier on [50] as a basis for understanding semiconductor luminescence. The

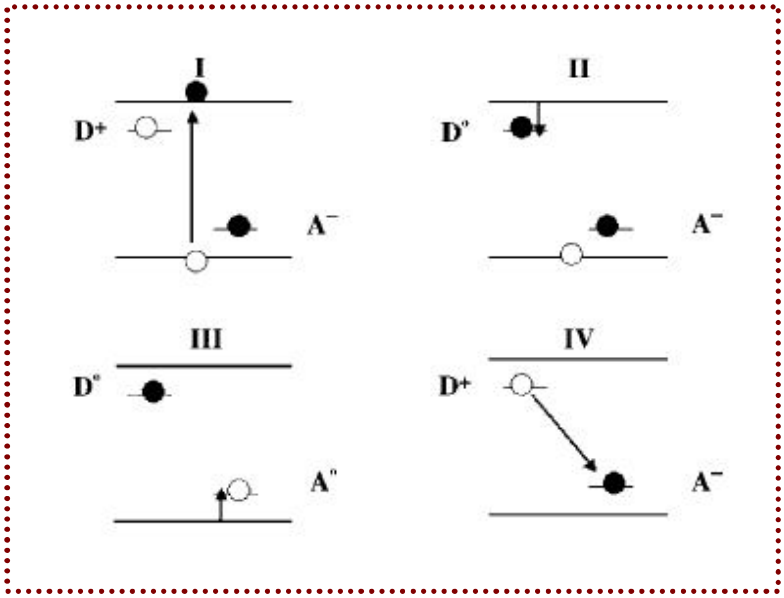

Figure 2.13: Processes leading to donor-acceptor pair luminescence [28]

model illustrated in Fig. 2.13 depicts the excitation of electrons into the conduction band. The electrons are in turn captured by ionized donors, while the resulting holes in the valence band are captured by ionized acceptors. Electron transfer between neutral donors and neutral acceptors leads to emission. The final state (with ionized donors and acceptors) is Coulomb stabilized. Therefore, the spectral position of the emission generated on a donor-acceptor pair depends on the distance between the donor and the acceptor in a pair [28]. The energy (E) involved in the overall luminescence process may be expressed as [28],

$$E = E_g - (E_A - E_D) + \frac{e^2}{4\pi\varepsilon_0\varepsilon R}, \qquad (2.16)$$

in which E_g is the band gap energy, E_A is the energy required for neutralization of the ionized acceptor, E_D is the energy required for neutralization of the ionized donor, and R is the distance between the donor and acceptor involved in the emission process. The Coulomb term originates from the electrostatic interaction between ionized donor and acceptor.

2.8 Traps and phosphorescence

2.8.1 Introduction

A trap can be considered as a localized electronic state which captures charge carriers. One of the main properties of traps is their depth, i.e. the activation energy needed to release a captured charge carrier. Shallow traps (with a depth lower than around 0.4 eV) [51] are fully emptied at low temperatures, and do not actively take part in processes at room temperature. Very deep traps (around 2 eV or deeper) [52], on the other hand, require more energy to be emptied than is available at room temperature. To observe persistent luminescence at room temperature, the traps should have an appropriate activation energy somewhere between these two extremes (a trap depth around 0.65 eV is considered to be optimal) [53]. Trap processes may cause phosphorescence when charge carriers are thermally reactivated into the conduction band (valence band) and then radiatively recombined at an emitting center [18].

2.8.2 Trap processes

Unlike the band levels that extend throughout the whole crystal, the trap levels exist only in relatively small regions of space around the trap potential. If the state is highly localized so that an electron bound to the trap potential has a wavefunction that extends only as far as the nearest neighbours, the uncertainty in location is small. Such a trap potential is known as a deep trap. The energy level for a deep trap in an *E* vs *k*

diagram, therefore, extends over a wide range of *k* values. For shallow traps, the uncertainty in location is large, and therefore the corresponding uncertainty in momentum is small. Such localized trap potentials may be caused by imperfections in the material, surface related states or self-trapped states [54].

- **Imperfections:** In general, there are three types of imperfections; point imperfections due to defects, point imperfections due to impurities, and large structural imperfections such as imperfection complexes, dislocation or grain boundaries [54].
- **Surface-related states:** The high surface-to-volume ratio of nanostructured materials means that the surface properties should have a significant role on their optical properties. Surface-related states are energetically positioned within the band gap of the materials [55,58]. These surface traps are associated with surface reconstruction in the atomic positions, stoichiometric defects, dangling bonds, external adatoms (like oxygen) associated with contamination or chemical/physical changes in the exposed surface and interfacial defects due to lattice mismatch [57].
- **Self-trapped states:** A charge inside a dielectric matrix produces a polarization in the dielectric as a consequence of its Coulomb field [58]. In turn, the polarized surroundings will produce a reaction field at the location of the charge. The interaction of the charge with this reaction field stabilizes the charge in the dielectric matrix. This is known as self-trapping. Self-trapped states have been employed to explain trapping in size-quantized systems in which the carriers are considered to be most likely trapped in the states localized at the quantum dot/matrix interface [59,60] or outside the quantum dot in the surrounding matrix [61,62]. The self-trapped states are significant when trapping of carriers in the surrounding matrix, for example polymers occurs. Charges injected into polymers induce localized acceptor states. These acceptor states are characterized by atomic and electronic relaxations of the molecular moiety on which the charge is localized and of the polymer matrix surrounding the charge. These kinds of energetically relaxed states are not the intrinsic states of a neutral polymer.

The crucial parameters describing the process of localization and trapping is the relation between the spatial overlap of the electron/hole wavefunction with that of trap potential as well as the depth of local potential fluctuations. The trapping process decreases the overlap of the electron/hole wavefunction and therefore increases the recombination time. Apart from changing the recombination process, trapping can also cause lattice distortion, alternate the potential barrier or active chemical reaction [63].

2.8.3 The decay rate equation

Two scenarios may be encountered in deriving the decay rate equation of a phosphor. The first one presumes the existence of only one kind of trap and leads to the development of the simple model shown in Fig. 2.14, and consequently the deduction of

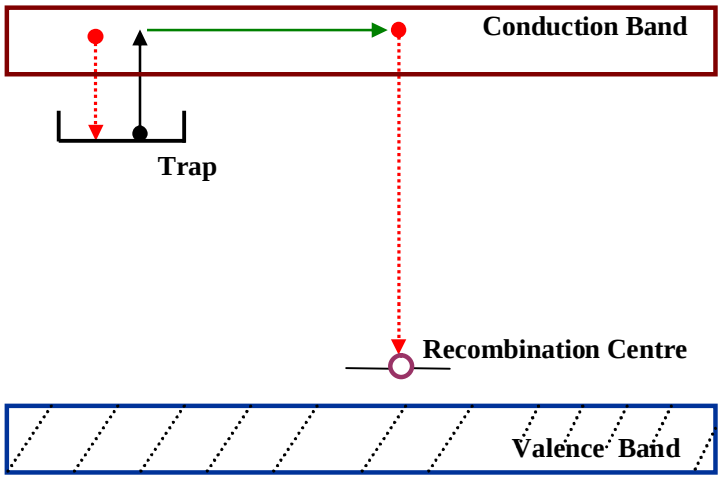

Figure 2.14: Luminescence after-glow process via a trap in an energy band scheme [18]

the decay rate equations for two reaction types; monomolecular and bimolecular. The second scenario considers the more realistic situation of the presence of more than one type of trap in a phosphor.

For the one trap condition the parameters are defined as follows; N is the trap concentration, n_c and n_t are the number of electrons per unit volume in the conduction band and trap states, respectively, p is the number of holes and is equal to $(n_c + n_t)$. Then, the rate equation representing the decaying processes of the concentration of electrons and holes after the termination of excitation is [18],

$$\frac{dn_t}{dt} = -an_t + b(N - n_t)n_c \tag{2.17}$$

$$\frac{dp}{dt} = -rpn_c \tag{2.18}$$

where a is the probability per second for a trapped electron to be thermally excited into the conduction band, b and r are the probabilities that a free electron in the conduction band will be captured by a trap or will recombine with a hole. It is supposed that the number of the electrons n_c in the conduction band in the after-glow process is so small that $p \approx n_t$ and $dp/dt \approx dn_t/dt$. Then, the above two equations give [18],

$$\frac{dn_t}{dt} = \frac{-an_t^2}{n_t + \left(b/r\right)(N - n_t)} \tag{2.19}$$

Equation 2.19 can be solved analytically for two cases: $b << r$ and $b \approx r$ to yield the final two equations.

- For $b << r$, which presumes that the electrons once released from traps are not re-trapped in the after-glow process, Eq. 2.19 can be simplified to,

  $$\frac{dn_t}{dt} = -an_t \tag{2.20}$$

  Since the emission intensity is given by $I(t) \propto dp/dt$ and $dp/dt \cong dn_t/\mathrm{dt}$, then the exponential decay of after-glow is given by the equation,

  $$I(t) = I_0 \exp(-at)\,. \tag{2.21}$$

  Equation 2.21 is referred to as the first-order or monomolecular reaction equation.

- In the case $b \cong r$, which means that the traps and emitting centres have nearly equal capturing cross-sections, Eq. 2.19 can be simplified to,

$$\frac{dn_t}{dt} = -\frac{a}{N} n_t^2 \qquad (2.22)$$

and then the number of trapped electrons per unit volume is given by,

$$n_t = \frac{n_{t_0}}{1 + \left(N / a n_{t_0} \right) t}. \qquad (2.23)$$

Approximating $I(t) \propto dn_t/dt$ as before, the decay curve of the after-glow is obtained as [18],

$$I(t) = \frac{I_0}{(1 + \gamma t)^2}, \qquad \left(\gamma = N / a n_t \right). \qquad (2.24)$$

This form is called the second-order or bimolecular reaction type, where the decay curve is changed by excitation intensity as well as by temperature.

However, the real phosphors may have several kinds of traps of different depths. For example, in $SrAl_2O_4:Eu^{2+}$, Dy^{3+}, there are three kinds of traps; 0.57, 0.41 and 0.19 eV [64]. The three traps represent defect-related shallow traps such as Sr–vacancy defects, and deep traps such as Dy^{3+} related hole-traps [64]. Therefore, in many real cases, the after-glow decay curve is not represented simply by a monomolecular or bimolecular reaction curve. In the second scenario, the decay curves are often fitted with equations of the form,

$$I(t) = \frac{I_0}{(1 + \gamma t)^n}, \qquad (2.25)$$

where n ranges between 0.5 and 2 [18].

2.9 Factors determining the emission colour

The colour of the emitted light in rare-earth doped luminescent materials depends on the activator species as well as host composition. For example, using UV or VUV as the excitation source, the following results have been obtained in phosphor materials used for practical applications:

- Red phosphor can be obtained by doping Y_2O_3 cubic structure with europium [65,66].
- Green colour is generated when Zn_2SiO_4 is doped with Mn [67,68].
- Blue emission is derived from Eu-doped $BaMgAl_{10}O_{17}$ [69,70].
- Ce-doped $Y_3Al_5O_{12}$ produces yellow light [71,72].

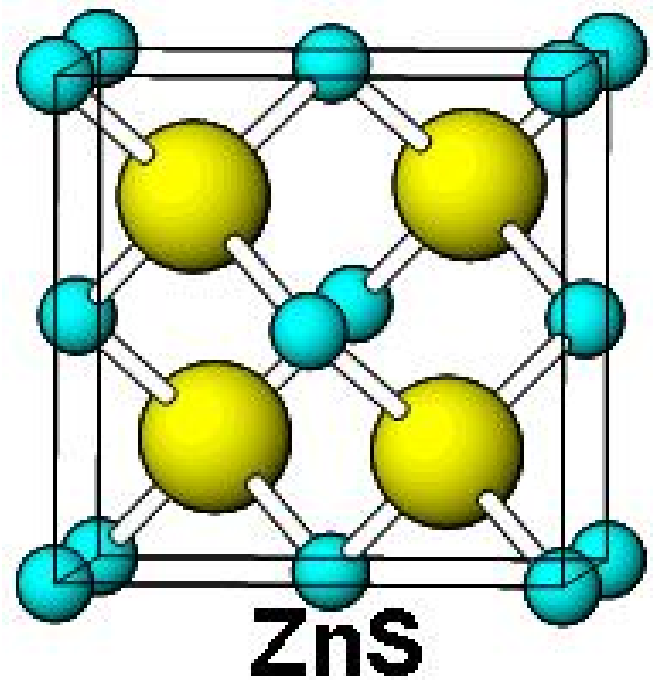

Figure 2.1 5(a): Zinc-blende structure

The dependence of the emission colour on the two factors originates in the crystal structure adopted by IIa-VIb compounds. Except for MgTe, which crystallizes in the zinc-blende structure (Fig. 2.15(a)) and BeO, which favours the wurtzite lattice (Fig. 2.15(b)), most of the IIa-VIb family have NaCl-type structures (Fig. 2.15(c)) [73]. The compounds in the NaCl-type structure can form solid solutions in a wide range of compositions. As a consequence, the emission colour can be varied by changing the host composition as well as the activator species and concentration. Such diversity is one of the advantageous features of the IIa-VIb compounds. For the rare earth ions, many radiative electronic transitions occur in the visible region while retaining their atomic-like

spectra in a wide range of host materials. This phenomenon, once understood, opens up the possibility to tailor the emission colour to specific applications.

In the specific case of the aluminate phosphors, the phosphorescence from the aluminates is believed to be caused by the 4*f*–5*d* transition of the Eu^{2+} ions in the crystals [52,74,75]. This electron transition has been reported to be affected by the electrical environment around the Eu^{2+} ions. Therefore, the colour of the phosphor is expected to vary with the crystal structure of the mother phases.

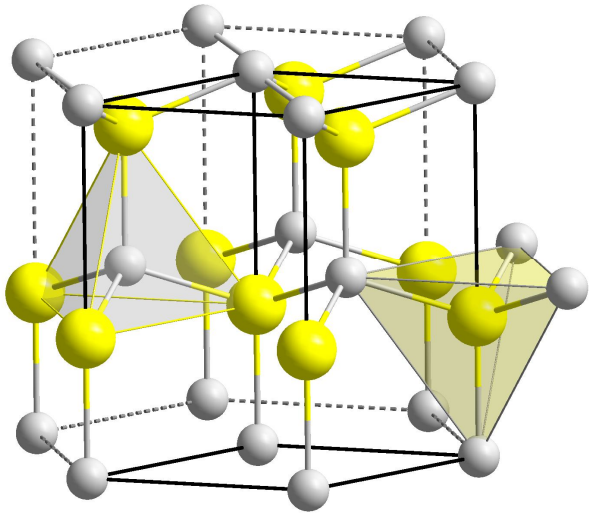

Figure 2.15(b): Wurtzite structure

In cases where at least one of the electronic states is involved in the chemical bonding, the coupling to the lattice has to be taken into account. This situation is encountered for many transition metal ions, for the s^2 ions, and for rare-earth ions showing d→f emission. In Fig. 2.16, this situation is illustrated for d→f optical transitions on Eu^{2+}. Other rare-earth ions showing d→f emission are Ce^{3+}, Pr^{3+}, Nd^{3+} and Er^{3+} [49].

The energy difference between the d- and f-electrons is modified by the covalence of the Eu^{2+}-ligand bond and the crystal field strength. An increase of the covalence of the

Eu^{2+}-ligand bond results in a lower energy difference of the 4f-5d energy separation (due to the nephelauxetic effect). This treatment considers the shift of the centre of gravity

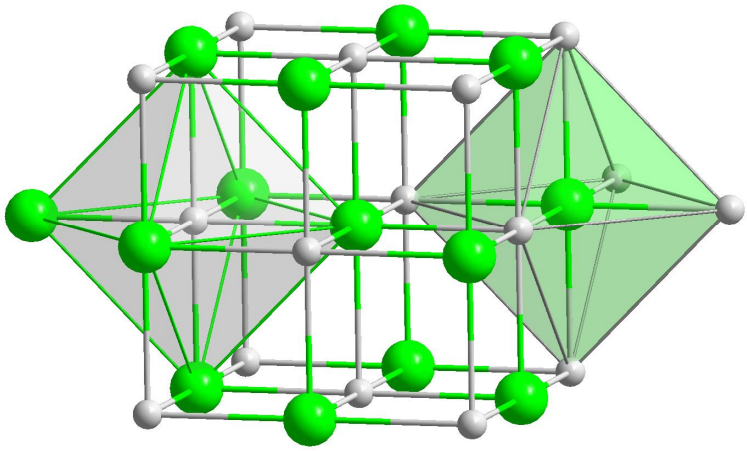

Figure 2.15(c): NaCl structure

(also called barycenter) of the d-electron level (also called centroid shift), i.e. any splitting is not yet taken into account [76]. The extent to which the crystal field interaction splits the d-level depends on the symmetry and the strength of the crystal field. In this way, e.g., for Eu^{2+}, emission can be obtained extending from the UV part of the optical spectrum to the red part [76]. Both are easily accessible by choosing appropriate host lattices, and for this reason broad-band emitters can in general be tuned within a large spectral range and can be adapted to the application needs.

The spectral position of the emission lines due to transitions between f-electronic states does not vary very much on changing the host lattice. However, the relative emission intensity of the several possible optical transitions does vary considerably. In general, it can be stated that in cases where the rare-earth ion occupies a site with inversion symmetry, the selection rule states: $\Delta J = 0, 1$. In cases where $\Delta J = 0$, any transition to another state with $J = 0$ is forbidden as well. In such a case, $\Delta|J|$ is necessarily [76]. These are all magnetic dipole transitions. In lattices without inversion symmetry there is also electric dipole emission.

For these transitions, the selection rule is: $\Delta \left| J \right| \leq 6$. Here again, for initial or final states with J = 0, other selection rules are operative. In such a case, for electric dipole transitions, $\Delta| J | = 2, 4,$ or 6. It is observed that the presence of an inversion centre opens up the possibility to tune the emission spectrum to a small extent. For Eu^{3+} with excited state $^5D_0$, the emission can be tuned from orange (590 nm, with inversion symmetry,

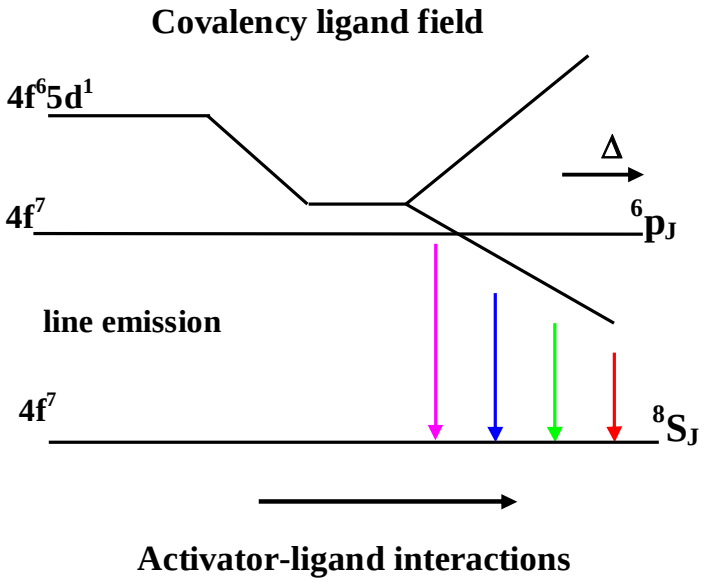

Figure 2.16: The effect of crystal field strength on the energy levels and emission colour of the Eu^{2+} ion in solid state. The arrows indicate different emission colours [76]

$^5D_0 \rightarrow {}^7F_1$ transition) to red (610 nm, without inversion symmetry, $^5D_0 \rightarrow {}^7F_2$ transition). A more general description of these effects is provided by the Judd-Ofelt theory [77,78].

As has already been stated, in the donor-acceptor pair luminescence mechanism, both the donors and the acceptors and the magnitude of the band gap strongly influence the spectral position, and hence the emission colour to be obtained. This characteristic is adequately illustrated by the blue- and green-emitting ZnS:Ag and ZnS:Cu,Au phosphors, respectively [78].

2.10 References

1. Shionoya, S. *Phosphor Handbook*. CRC Press, Boca Raton, Chap.1, (2007).
2. Yamamoto, H. *Fundamentals of luminescence*. CRC Press: New York, Chap. 2, (2007).
3. Gribkovskii, V.P. *Theory of Luminescence.* Plenum Press, New York, (1998)
4. Justel, T. Nikol, H. Ronda, C. *Angew. Chem. Int. (Ed.)*, WILEY-VCH Verlag GmbH, D-69451 Weinheim, **37**: 3084, (1998).
5. Galginaitis, S.V. *Met. Trans.*, **2**(3)**:** 757, (1971).
6. Bergh, A.A. Dean P.J. *Proc. IEEE*, **60:** 156, (1972).
7. Auzel, F. Chen, Y, Meichenin, D. *J. Lumin.*, **60-61:** 692, (1994).
8. Jia, D. *Opti. Mater.*, **22:** 65, (2003).
9. Stepanov, B.I. Gribkovskii, V.P. *Theory of Luminescence*. ILIFFE Books, London. (1963).
10. Levshin, V.L. *Photoluminescence of Solid and Liquid Substances*. GITTL, Moscow, Leningrad, (1959).
11. Henisch, H.K. *Electroluminescence*. Pergamon, Oxford, (1962).
12. Adachi, C. Tsutsui, T. *Fundamentals of Luminescence*. CRC Press, Taylor & Francis Group, LLC, Chap. 2. (2007)
13. Levshin, V.L. *J. Sov. Phys.*, **4(**5): 747, (1962).
14. Jonscher, A.K. Polignac, A.*J. Phys. C: Solid State Phys.*, **17:** 6493, (1984).
15. Debye, P.J. Edwards, J.D. *J. Chem. Phys.*, **20:** 236, (1952).
16. Jonscher, A.K. *J. Mater. Sci.*, **16:** 2037, (1983).
17. Jonscher, A.K. Li, J-R. *J. Phys*. C: *Solid State Phys.*, **16**(32)**:** L1159, (1983).
18. Nakazawa, E. *Fundamentals of Luminescence*. CRC Press: New York, Chap. 2, (2007).
19. Nakazawa, E. *J. Lumin.*, **18/19**(1)**:** 272, (1979).
20. Pelle, F. Auzel, F. *J. Alloys Comp.*, **300–301:** 131, (2000).
21. Nakazawa, E. Shionoya, S. *J. Chem. Phys.*, **47:** 3211, (1967).
22. Kano, T. *Principal Phosphor Materials and Their Optical Properties*. CRC Press: New York, Chap. 3, (2007).

23. Tabei, M. Shionoya, S. *Jpn. J. App. Phys.*, **14:** 240, 240, (1975).
24. Suzuki, A. Yamada, H. Uchida, Y. Kohno, H. Yoshida, M. *Tech. Digest Phosphor Res. Soc.* 197th Meeting, (1983).
25. Kuboniwa, S. Kawai, H. Hoshina, T. *Jpn. J. Appl. Phys.*, **19:** 1647, (1980).
26. Narita, K. *Practical Applications of Phosphors*. Yen, W.M. Shionoya, S. Yamamoto, H. (Eds.), CRC Press: New York, Chap. 1, (2006).
27. Godlewski, M. Skowronski, M. *Phys. Rev. B.*, **32**(6)**:** 4007, (1985).
28. Ronda, C. R. *Luminescence from Theory to Applications*. Ronda, C. R. (Ed.). Chap. 1. Willy-VCH, Germany, (2008).
29. Allison, S.W. Gillies, G.T. *Review of Scientific Instruments.* **68**(7)**:** 2615-2650, (1997).
30. Khalid, A.H. Kontis, K. *Principles, Current State of the Art and Recent Applications* of *Sensors.* **8**: (2008).
31. Sant, Y.L. Merienne, M.C. *Aerospace Sci. Technol.*, **9**(3)**:** 285, (2005).
32. Heyes, A.L. *Advanced Measurement Techniques for Aeroengines and Stationary Gas Turbines*. Von Karmen Institute for Fluid Dynamics. March 1, (2004).
33. Ranson, R.M., *PhD Thesis*. Nottingham Trent University, (1999).
34. Riseberg, L.A. Moos, H.W. *Phys. Rev.*, **174**(2)**:** 429, (1968).
35. Kropp, J. L. Windsor, M.W. *J. Phys. Chem.*, **71**(3)**:** 477, (1967).
36. Turro, N.J. *Modern Molecular Photochemistry*. Benjamin/Cummings, Menlo Park, CA, (1978).
37. Hoshina, T. Imanaga, S. Yokono, S. *J. Lumin.*, **15:** 455, (1977).
38. Blasse, G. Grabmaier, B.C. *Luminescent Materials*. Springer-Verlag, Berlin, (1994).
39. Walsh, B.M. *Advances in Spectroscopy for Lasers and Sensing.* Bartolo, B.D. Forte, O. (Eds.), Springer, Netherlands, (2006).
40. Sole, J.G. Bausa, L.E. Jaque, D. *An Introduction to the Optical Spectroscopy of Inorganic Solids.* John Wiley & Sons Ltd. The Atrium, Southern Gate, Chichester, West Sussex, England, Chap. 6, (2005).
41. Struck, C.W. Fonger, W.H. *J. Lumin.*, **1-2:** 456, (1970).

42. Blasse, G.: *Luminescence of Inorganic Solids*. DiBartolo, B., Plenum Press, 457, (1978).
43. Van Uitert, L.G. *J. Lumin.*, **29:** 1, (1984).
44. Sommerdijik, J.L. Bril, A. *J. Electrochem. Soc*., 122, 952, (1975).
45. Sommerdijik, J.L Bril, A. Hoex-Strik, F.M.J.H. *Philips Res. Rept.*, **32:** 149, (1977).
46. Blasse, G. Grabmaier, B.C. *Luminescent Materials*. Springer-Verlag, Berlin, (1994).
47. Blasse, B. Bril, A. *Philips Tech. Report*, **10:** 370, (1970)
48. Martienssen, W. Warlimont, H. *Handbook of Condensed Matter and Data Materials*. Springer, USA, (2005).
49. Dexter, D.L. A *J. Chem. Phys.*, **21:** 836, (1953).
50. Prener, J.S. Williams, F.E. *J. Electrochem. Soc.*, **103**: 342, (1956).
51. Chen, R. McKeever, S.W.S. *World Scientific*: Singapore; **xiii:** 559, (1997).
52. Dorenbos, P.*J. Electrochem. Soc.* **152:** H107, (2005).
53. Matsuzawa, T. Aoki, Y. Takeuchi, N. Murayama, Y. *J. Electrochem. Soc*., **143:** 2670, (1996).
54. Bube, R.H. *Electrons in solids, 2nd Ed*. Academic Press, San Diego, (1987).
55. Hache, F. Klein, M.C. Ricard, D. Flytzanis, C. *J. Opt. Soc. Am. B*, **8**(9)**:** 1802, (1991).
56. Lueth, H. *Solid Surfaces, Interfaces and Thin Films*. Springer-Verlag, Berlin, (2001).
57. Nemec, P. Maly, P. *J. Appl. Phys.*, **87:** 3342 (2000).
58. Tian, Y. Wu, C. Fendler, J.H. *J. Phys. Chem*., **98:** 4913, (1994).
59. Wang, Y. *J. Phys. Chem*., **95:** 1119, (1991).
60. Zhang, J.Z. O'Neil, R.H. Roberti, T.W. McGowen, J.L. Evans, J.E. *Chem. Phys. Lett.,* **218:** 479, (1994).
61. MacDonald, R.L. Lawandy, N.M. *Phys. Rev. B.,* **47:** 1961, (1993).
62. Woggon, U. Rückmann, I. Kornack, J. Müller, M. Cesnulevicius, J. Petrauskas, M. Kolenda, J. *J. Cryst. Growth*., **117:** 608, (1992).
63. Kaschke, M. Ernsting, N.P. Müller, U. Weller, H. *Chem. Phys. Lett.,* **168**(6)**:** 543, (1990).

64. Yuan H. Ph.D. *Thesis,* University of Georgia, 73, (1998).
65. Konrad, A. Fries, T. Gahn, A. Kummer, F. Herr, U. Tidecks, R. Samwer, K. *J. Appl. Phys.,* **86**(6)**:** 3129, (1999).
66. He, C. Guan, Y. Yao, L. Cai, W. Li, X. Yao, Z. *Mater. Res. Bull.,* **38:** 973, (2003).
67. Morimo, R. Matae, K. *Mater. Res. Bull.,* **24:** 175 (1989).
68. Miyata, T. Minami, T. Saikai, K. Takata, S. *J. Lumin.,* **60-61:** 926, (1994).
69. Jung, K.Y. Kang, Y.C. *Mat. Lett.,* **58:** 2161, (2004).
70. Chang, H. Lenggoro, I.W. Ogi, T. Okuyama, K. *Mat. Lett.,* **59:** 1183, (2005).
71. Rosario, G.D. Ohara, S. Mancic, L. Milosevic, O. *App. Surf. Sci.,* **238:** 469, (2004).
72. Kottaisamy, M. Thiyagarajan, P. Mishra, J. Rao, M.S.R. *Mat. Res. Bul.* **43:** 1657, (2008).
73. Krebs, H. *Fundamentals of Inorganic Crystal Chemistry*. McGraw-Hill, London, 159, (1968).
74. Pallila, F.C. Levine, A.K. Tomkus, M.R. *J. Electrochem. Soc.,* **115:** 642, (1968).
75. Abbruscato, V. *J. Electrochem. Soc.,* **118:** 930, (1971).
76. Meijerink, A. Nuyten, J. Blasse, G. *J. Lumin.,* **44:** 19, (1989).
77. Ofelt, G.S. *J. Chem. Phys.,* **37:** 511, (1962).
78. Judd, B.R. *Phys. Rev.*, **127:** 750, (1962).

Chapter 3
Literature Review

3.1 Introduction

Luminescent materials are mostly solid inorganic materials consisting of a host lattice, usually intentionally doped with impurities [1]. Most of these materials are oxides, sulfides, fluorides, halides, and oxysulfides doped with transition metal ions or rare-earth ions. They are generally characterized by the emission of light with energy beyond thermal equilibrium [2]. Recently, with the advent of solid-state lighting technologies as well as the development of plasma and field emission display panels, a great number of traditional phosphors cannot meet the requirements for new applications, for example; (1) excitation by near-ultraviolet (UV) or visible light, (2) efficient emission of appropriate colours and (3) survival in adverse environments. Therefore, novel phosphors with superior luminescent properties are being sought.

Quite a number of unresolved problems may be identified even among the so called classical phosphors. Hence, this will be a good starting point in this review. The term classical may be used to refer to luminescent materials which are applied in classical applications, i.e. applications which have been known for a long time. Examples of such applications include x-ray imaging, luminescent lighting and cathode-ray tubes

(television). This category roughly includes the tungstates (MWO_x), vanadates (MVO_x), trivalent antimony (Sb^{3+}), red bismuth ganate ($Bi_4Ge_3O_{12}$), and copper (Cu^{+}).

3.2 Synthesis

3.2.1 Tungstates

Following Rontgen's invention of x-rays, a search for phosphors which were able to absorb x-rays and to convert the absorbed energy efficiently into light was started [3]. As early as 1896, Pupin proposed calcium tungstate **(**$CaWO_4$) for this purpose. In spite of having served for more than 90 years in x-ray intensifying screens, there are still issues regarding the nature of the emission transition and the quenching temperature of the luminescence in this material.

3.2.2 Vanadates

The nowadays overwhelming role of rare-earth ion luminescence in commercial phosphors [3], started in 1964 with the successful proposition of europium-doped yttrium vanadate (YVO_4:Eu^{3+}) as a red phosphor for colour television tubes and later also for luminescent lamps [4]. While the luminescence of Eu^{3+} in YVO_4 has been investigated thoroughly and satisfactorily understood, the vanadate VO_4^{-3} group luminescence is less well understood. On the whole, this class of materials is yet to be satisfactorily understood.

3.2.3 Trivalent antimony (Sb^{3+})

The Sb^{3+} luminescence is fairly well understood. It can be described in terms of transitions between the $5s^2$ ground configuration and the 5s5p excited configuration, as shown by Oomen *et al.* [5] using the halide elpasolites as a model host lattice. The Sb^{3+} ion in apatite: $Ca_5S(PO_4(F,Cl))$:Sb^{3+},Mn^{2+} [3] was the best lamp phosphor for decades. However, the high efficiency of the Sb^{3+} emission in apatite has not yet been well understood. The Stokes' shift is some 19,000 cm^{-1}, half of the value of the first excitation

band maximum [6]. According to an old criterium by Dexter *et al.* [7], this means that the emission cannot be efficient. Though this material has been applied for decades in many millions of luminescent lamps, the constitution of the Sb^{3+} centre in apatite [3] is not yet clear.

3.2.4 **Red bismuth luminescence** ($BaSO_4$:Bi)

The efficient red luminescence for bismuth doped barium sulphate ($BaSO_4$:Bi) was reported in 1886. However, it was not until half a century later that this was confirmed, while a satisfactory explanation came another half century later [8].

3.2.5 **Bismuth ganate ($Bi_4Ge_3O_{12}$)**

Due to its excellent scintillation properties, the compound $Bi_4Ge_3O_{12}$ has been put to various applications, the most prominent of which is in the electromagnetic calorimeter of CERN (Geneva) [3]. However, the nature of the emission transition in this material is still unclear. It has a very large Stokes' shift, which for many years was considered to be a $6s^2 \rightarrow 6s6p$ Bi^{3+} transition. It took quite some time for the proposition to be made that the emission originated in the D level, which is essentially a charge transfer level [9]. The difficulty in understanding the emission is attributed to the complicated nature of the composition of the emitting level in $Bi_4Ge_3O_{12}$.

3.2.6 **Copper (Cu^+)**

The Cu^+ ion ($3d^{10}$ configuration) is known to emit efficiently in many host lattices. The emission is usually ascribed to a $3d^9 4s \rightarrow 3d^{10}$ transition. However, optically detected paramagnetic resonance on NaF:Cu^+ shows that in the emitting state the spin density in the Cu 4s orbital is very small [10]. This implies that also here the emitting state is more complicated than originally thought.

3.2.7 Silicates ($M_2M_gSi_2O_7$)

The most widely studied persistent luminescent silicates consist of the materials $M_2MgSi_2O_7$ (M = Ca,Sr,Ba), that play a role similar to that of MAl_2O_4 in the aluminate group. Of these, the best known compound is $Sr_2MgSi_2O_7:Eu^{2+},Dy^{3+}$, first reported by Lin *et al*. in 2001 [11]. The most common method for preparation of these materials ($M_2MgSi_2O_7$) is the solid-state reaction technique at 1200–1400 °C. Other methods that have recently been successfully employed include sol-gel [12], co-precipitation [13], and combustion [14,15]. A huge enhancement of the afterglow in nearly all co-doped aluminates and silicates has usually been observed. For example, $Sr_2MgSi_2O_7:Eu^{2+},Dy^{3+}$ [16] and $Ba_2MgSi_2O_7:Eu^{2+},Tm^{3+}$ [17] have a much brighter and longer afterglow than their non-co-doped variants. However, contrary results were reported by Hölsä and co-workers who found that, with the exception of Tb^{3+}, which had a weak positive influence, the afterglow in $Ca_2MgSi_2O_7:Eu^{2+}$ was significantly reduced upon addition of trivalent rare-earth ions [18]. Another remarkable observation of $Ca_2MgSi_2O_7:Eu^{2+}$ was in disagreement on the emission spectrum. Blasse [19] and Hölsä [18] found an emission maximum around 535 nm, whereas Mao and co-workers reported an emission band centred around 515 nm when co-doping with Dy and Nd [20,21,22]. Using a sol-gel method, Wang *et al.* [23] prepared $Sr_2ZnSi_2O_7:Eu^{2+},Dy^{3+}$. By applying different synthesis temperatures, they were able to obtain grains of various sizes and they showed that a smaller grain size enhanced both the brightness and lifetime of the afterglow.

3.2.8 Aluminates

The group of compounds consisting of Eu^{2+} doped and rare-earth (R^{3+}) co-doped alkaline earth aluminates ($MAl_2O_4:Eu^{2+},R^{3+}$; M: Ca, Sr, Ba) are by far the most studied family of persistent luminescent materials and are considered the first generation of the modern persistent luminescence materials [24]. This classification was a culmination of the developments emanating from the breakthrough reported in the article by Matsuzawa *et al.* on $SrAl_2O_4:Eu^{2+},Dy^{3+}$ [24]. Since then the aluminates have been at the centre of attention in persistent luminescent research. Some of the specific outstanding

achievements of this era include the bright green luminescence of the monoclinic [25] $SrAl_2O_4:Eu^{2+}$, which was discovered in 1966 [26] and described by Blasse and Bril two years later, together with that of $CaAl_2O_4:Eu^{2+}$ and $BaAl_2O_4:Eu^{2+}$ [27].

The promising results exemplified by these phosphors led to a search for a method to synthesize co-doped $MAl_2O_4:Eu^{2+}$ in an efficient, cheap and simple way. The methods include, solid-state reaction combustion [28-32], Pechini [28], microwave [33], laser heated pedestal growth (LHPG) [34], and sol-gel [35-38], which have been used to varying degrees of satisfaction. These investigations revealed that not all the techniques lead to identical crystallographic and luminescent properties. For example, $SrAl_2O_4:Eu^{2+},Dy^{3+}$ prepared by microwave synthesis shows a decreased initial brightness of the afterglow, together with a small blue shift of the emission spectrum, possibly due to the small grain size [33]. A similar blue shift has been reported for sol-gel prepared $SrAl_2O_4:Eu^{2+},Dy^{3+}$ [36-38]. During the preparation of $CaAl_2O_4$ by combustion or a sol-gel method, Hölsä and co-workers obtained an unusual hexagonal crystal structure instead of the expected monoclinic one [28,35]. Other researchers have been able to create grains with orthorombic structure [31]. These observations imply that care should be taken when comparing luminescence of compounds prepared using different procedures. Similarly, the exact composition of the starting mixture has important consequences for the afterglow behaviour. A deficit of alkaline earths has been found to enhance the afterglow [39], while an excess of barium in $BaAl_2O_4:Eu^{2+},Dy^{3+}$ has been observed to completely annihilate the persistent luminescence in the phosphor [40].

The influence of the borate (B_2O_3) on $SrAl_2O_4:Eu^{2+},Dy^{3+}$ has been the subject of interest to various researchers. Though this material is usually added to the starting mixture as a fluxing agent [24], it has been observed to have other influences. For example, samples prepared without borate showed only very weak [36,41] or no persistent luminescence at all [42] even though perfect $SrAl_2O_4$ phase formation was achieved. A probable explanation for this effect is that the boron is incorporated in the host as BO_4, where it forms substitutional defect complexes with Dy^{3+} [42]. This

decreases the depth of the charge traps in $SrAl_2O_4$ from 0.79 eV to 0.65 eV, making it suitable for persistent luminescence at room temperature [41].

The aluminate phase $Sr_4Al_{14}O_{25}:Eu^{2+},Dy^{3+}$, is a blue-emitting persistent phosphor with emission around 490 nm and an afterglow that has been reported to remain visible for over 20 hours [43,44]. A small deficit of strontium enhances the persistent luminescence [43,44], and preparation without borate strongly reduced the afterglow [41]. The addition of silver (Ag^+) ions in this phosphor has been observed to have a positive effect on the afterglow, and has been attributed to an increase in the trap density [45].

Other interesting results on aluminates involve the $Sr_3Al_2O_6:Eu^{2+},Dy^{3+}$ phase. The emission colour from the triboluminescence [47] and photoluminescence [48] measurements on this phosphor is bright green with a spectrum peaking around 510 nm. However, when the same material was prepared using either microwave or sol-gel processes [49,50], red Eu^{2+}-emission around 612 nm was observed. These conflicting reports have led to the emission colour of $Sr_3Al_2O_6:Eu^{2+},Dy^{3+}$ being indicated as 'disputed'.

3.2.9 Sulfides

Sulfide phosphors are among the oldest classes of luminescent materials as exemplified by the ZnS-type phosphors [51]. ZnS-type phosphors have played a very important role in cathode-ray tubes and have a history of more than 130 years. Despite their long history, progress in understanding the fundamental physical properties for these phosphors has been quite slow. This has been attributed to two main reasons: (1) These materials are hygroscopic and produce toxic H_2S when placed in contact with moisture. (2) Their luminescence properties are sensitive to impurities and nonstoichiometry, which make it difficult to obtain controlled reproducibility in performance [52].

The hygroscopic nature of these sulfide materials makes them less stable (due to H_2S production) compared to silicates and aluminates [52]. Sulfides generally show an increased red shift compared to their oxide counterparts, enabling emission at longer wavelength, in the yellow, orange or red region of the visible spectrum. This increased red shift is mainly determined by a larger centroid shift for sulfides than oxides, which is due to a larger covalency between the anion and the Eu^{2+} ion [53]. CaS is a well known phosphor host, and upon doping with Bi^{3+}, blue persistent luminescence is obtained [54]. However, Jia *et al*. obtained a red afterglow when doping with Eu^{2+} and Tm^{3+} [55,56]. Additionally, they proved that traces of Ce^{3+} further enhanced the lifetime and brightness of the afterglow [57].

3.2.10 Phosphates

Phosphates, together with aluminates, silicates, and borates, constitute the materials from which most commercial phosphors are derived [58]. They (phosphates) are another class of materials with the possibility of exhibiting afterglow. Persistent luminescence in two similar orthorhombic pyrophosphate compounds, α-$Ca_2P_2O_7$:Eu^{2+} and α-$Sr_2P_2O_7$:Eu^{2+}, co-doped with Y^{3+} ions, has recently been reported by Pang *et al.* [59,60]. $Ca_2P_2O_7$:Eu^{2+},Mn^{2+} had already drawn some attention as a possible conversion phosphor in white LEDs due to the presence of both a blue Eu^{2+}-based and an orange Mn^{2+}-based emission band [61]. Pang *et al.* found that by co-doping with Y^{3+}-ions, the blue europium emission remained visible for over six hours in $Ca_2P_2O_7$:Eu^{2+},Y^{3+} and over eight hours in $Sr_2P_2O_7$:Eu^{2+},Y^{3+}.

The foregoing account demonstrates that a variety of issues still persist in the synthesis of phosphors. In particular, broad-band luminescence in inorganic systems is a phenomenon that requires more investigation for a better quantitative and in many cases even a qualitative understanding. Efforts to find solutions to these problems may partly be ascribed to the complicated nature of the emitting states, and partly to the fact that most researchers have tended to mostly focus on narrow-line luminescence of the rare-earth ions, where it has been easier to obtain useful results [3].

3.3 Persistent luminescence mechanisms

3.3.1 Introduction

Knowledge of inorganic luminescent materials can be traced to approximately the tenth century in Japan and China as well as since the end of the middle edges in Europe [62,63]. The first scientifically documented observation of the persistent luminescence phenomenon associated with these materials dates back to the beginning of the 17^{th} century [64] when the Italian shoemaker, V. Casciarolo, observed strong luminescence from the famous Bologna stone. In the 20^{th} century, applications of this phenomenon were put to use [65], in spite of the lack of a satisfactory explanation. A renewed search for the underlying mechanisms was spurred by the discovery of the persistent luminescent properties of $SrAl_2O_4:Eu^{2+},Dy^{3+}$ by Matsuzawa *et al.* [24]. It was generally agreed that after excitation, charge carriers can be captured by traps, then gradually released followed by a return to the activators while simultaneously producing the luminescence [66]. A significant amount of research has also been done on thermoluminescence glow curves and how to extract information about trap depth from them [67]. However, details such as the nature and origin of the traps and the charge carriers are still unclear. Since 1996, different mechanisms have been suggested, ranging from very basic conceptual models to complex systems with multiple charge traps of various types and depths [66,67]. In particular, a mechanism of persistent luminescence that was proposed in 1996 for $SrAl_2O_4:Eu^{2+};Dy^{3+}$ has been widely adopted to explain afterglow in many Eu^{2+} and Dy^{3+} co-doped aluminates and silicates. The mechanism involves the thermally activated release of a hole from Eu^{2+} in its excited 5d state to the valence band which is subsequently trapped by Dy^{3+}. However, the true mechanism in the persistent luminescence of these phosphors is still a disputed matter. To arrive at plausible mechanisms or to discard implausible ones, it is necessary to know the absolute energy level locations [68]. Following is a concise overview of some of the prominent luminescence mechanisms, which have been proposed.

3.3.2 The Matsuzawa model

Following their discovery of the $SrAl_2O_4:Eu^{2+},Dy^{3+}$ phosphor, Matsuzawa *et al.* [24] also proposed a mechanism to explain the origins of the extraordinary persistent luminescence. The mechanism relies largely on the photoconductivity study of powder $SrAl_2O_4:Eu^{2+}$ samples [69]. A schematic picture of their model is shown in Fig. 3.1. In this model, holes are assumed to be the main charge carriers. This assumption is based on earlier measurements by Abbruscato on non codoped $SrAl_2O_4:Eu^{2+}$, which also shows a weak afterglow. From his results obtained by Hall measurements, Abbruscato concluded that holes in the valence band had to be the main charge carriers [69]. He suspected that Sr^{2+} vacancies acted as traps for these holes. Additionally, Matsuzawa *et al.* performed non-uniform illumination photoconductivity measurements, which also suggested that holes are the main charge carriers [24].

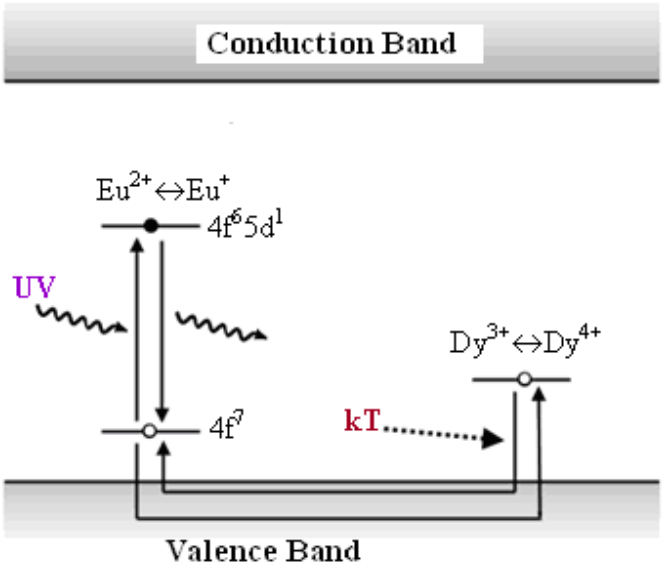

Figure 3.1: Phosphorescence mechanism proposed by Matsuzawa *et al.* for $SrAl_2O_4:Eu^{2+},Dy^{3+}$ [24].

The Matsuzawa model modified Abbruscato's assumptions in order to explain the influence of rare earth co-doping. When an Eu^{2+} ion is excited by an incident photon, there is a possibility that a hole escapes to the valence band, thereby leaving behind a Eu^{+} ion. The hole is then captured by a trivalent rare earth ion, such as Dy^{3+}, thus creating a Dy^{4+} ion.

$$Eu^{2+}\left(4f^{7}\right)+h\nu \rightarrow Eu^{2+*}\left(4f^{6}5d^{1}\right)$$

$$Eu^{2+*}\left(4f^{6}5d^{1}\right)\rightarrow Eu^{2+}\left(4f^{7}\right)+h\nu'$$

$$Dy^{3+}\ (4f^{9}) + h^{+} \rightarrow Dy^{4+}\ (4f^{8})$$

After a while, thermal energy causes the trapped hole to be released into the valence band again. From there it can move back to a Eu^{+} ion, allowing it to return to the Eu^{2+} ground state with emission of a photon [24]. In their mechanism, Matsuzawa *et al.* made two crucial assumptions: (1) The fundamental level of the $4f^{7}$ configuration of Eu^{2+} is close in energy to the top of the valence band. (2) The Eu^{2+} ion, excited by irradiation, becomes an excited Eu^{+*} ion upon electron capture, Eu^{2+*} $(4f^{6}5d^{1})$ + $e^{-} \rightarrow Eu^{+*}$ $(4f^{7}5d^{1})$. The Matsuzawa model quickly gained recognition [40,42,70], and was frequently used to explain observed phosphorescence behaviour in newly discovered compounds [20,43,71]. Various thermoluminescence [34,72,73,74], photoconductivity [70], and electron paramagnetic resonance [66] measurements were performed to confirm the validity of the model. However, the results of these experiments were often inconclusive and no hard evidence for the model could be found. For example, the generation of the Eu^{+*} and Dy^{4+} species, under a UV or visible excitation was considered to be highly unlikely. Furthermore, electronic band structure calculations carried out for $SrAl_2O_4$:Eu^{2+} had shown that the Eu d-block bands lie just below the conduction band bottom [76].

3.3.3 The Aitasalo model

The phosphorescence mechanism of Aitasalo *et al.* proposed in 2003 for $CaAl_2O_4$:Eu^{2+},Nd^{3+} differed considerably from the Matsuzawa model [68]. The mechanism (Fig. 3.2) is based on the realization that the formation of the highly unstable species Eu^{+*} under UV or visible irradiation is highly unlikely. The reduction of Eu^{3+} into Eu^{2+} in oxides already requires a high energy (~3.7 eV), and the further reduction of Eu^{2+} should require a much higher energy [3]. To retain the hole trapping process suggested from the photoconductivity experiments, Aitasalo *et al.* assumed the occurrence of energy transfer to Eu^{2+} and proposed that the UV excitation promotes an electron from the valence band to a discrete level of unknown origin, while the hole created in the valence band is trapped by an alkaline earth vacancy level V_{Ca}. Then, Aitasalo *et al.*

assumed that the thermal energy allows the transfer of the electron from the discrete level of unknown origin to an oxygen vacancy level V_O, from which a recombination takes

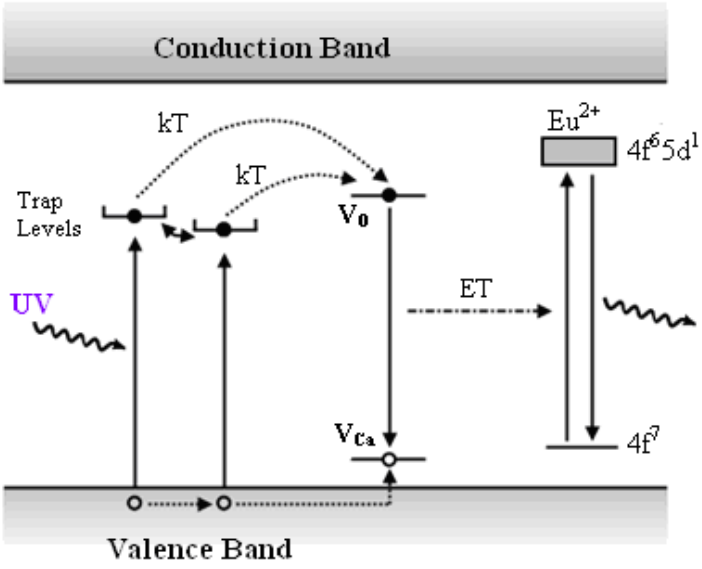

Figure 3.2: Phosphorescence mechanism proposed by Aitasalo *et al.* for $CaAl_2O_4$: Eu^{2+},Nd^{3+} [68].

place toward the V_{Ca} level. The energy released is then transferred to an Eu^{2+} ion, which is excited and then is de-excited instantaneously. However, EPR measurements of $SrAl_2O_4$:Eu^{2+},Dy^{3+}, which showed that the concentration of Eu^{2+} decreases during the UV excitation and increases when the excitation is stopped until the extinction of phosphorescence [43], seem to contradict this assertion. This observation indicates that Eu^{2+} ions participate in the trapping process and, hence, do not support the idea of energy transfer to Eu^{2+} after the trapping, as suggested by Aitasalo *et al*. In this mechanism, Nd^{3+} co-doping is considered to serve the role of increasing the number of cation vacancies.

3.3.4 The Dorenbos model

The Dorenbos mechanism is basically the same as the Matsuzawa model but it does not require the existence of Eu^{+} and RE^{4+}(RE = tetravalent rare earth ions). Hence, it is in agreement with the Aitasalo model with regard to the improbable existence of Eu^{+} and Dy^{4+} ions (in aluminate and silicate compounds) [68]. Dorenbos pointed out that the

assumed hole on the ground state of Eu^{2+} after excitation is based on faulty reasoning, since in contrast to the Bloch states of the valence and conduction band, which are delocalized, the energy levels of the rare earth ions are localized. Hence, the 4f state of europium after the excitation should not be interpreted as a 'real hole' that can accept an electron. He was also not convinced by the observation of hole conduction by Abbruscato and Matsuzawa, and noted that more detailed research was required to shed more light on this aspect [68]. As a result of the inadequacy of the Matsuzawa model to address these problems, Dorenbos was motivated to present a different model (Fig. 3.3) in 2005.

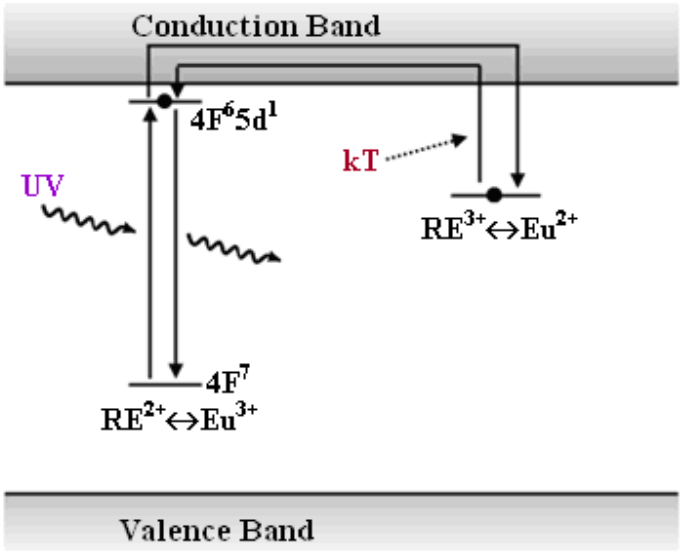

Figure 3.3: Phosphorescence mechanism proposed by Dorenbos *et al*. for aluminate and silicate compounds [68].

Similar to the Matsuzawa model, electrons are considered to be excited in Eu^{2+} ions. Since the 5d level of these ions lies very close to the conduction band [68], the excited electrons can easily be released into the conduction band and subsequently caught by a trivalent rare earth co-dopant, creating a divalent ion. Thermal energy can then release the trapped electron, followed by a recombination upon reaching a luminescent centre [68,77].

On the basis of the enormous research effort put into the determination of the location of rare-earth energy levels in inorganic compounds [78] the Dorenbos model

could be used to make two significant explanations: (1) His infererence that the energy level of Dy^{2+} (*i.e.*, Dy^{3+} after capture of an electron) in $SrAl_2O_4$ lies approximately 0.9 eV below the conduction band [68]. This value is of the same order as the trap depth found in $SrAl_2O_4$:Eu^{2+},Dy^{3+} [24,72,79]. (2) The model can be used to explain why Sm^{3+} and Yb^{3+} ions strongly reduce the afterglow. Previous work by Dorenbos had revealed that the relevant levels of Sm^{2+} and Yb^{2+} are located much lower than those of the other divalent rare-earth ions such as Dy^{2+} and Nd^{2+} [80]. Hence, the resulting traps are too deep to be emptied at room temperature. The existence of intrinsic persistent luminescence in non-codoped materials can however not be explained by this model.

3.3.5 The Clabau model

The model by Clabau *et al.* is probably one of the most comprehensive mechanisms proposed for the persistence luminescence phenomenon in rare-earth-doped aluminate phosphors. Fig. 3.4 depicts the schematic illustration of the mechanism, which

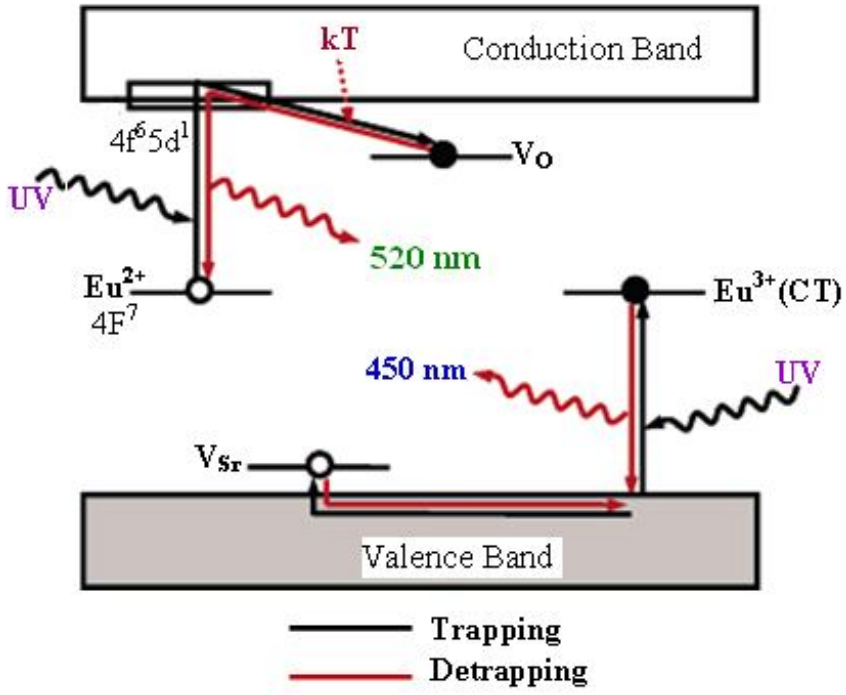

Figure 3.4: Phosphorescence mechanism proposed by Clabau *et al.* for $SrAl_2O_4$: Eu^{2+},Dy^{3+},B^{3+} [67].

was proposed for $SrAl_2O_4:Eu^{2+},Dy^{3+},B^{3+}$. Its deduction was based on three facts: (1) The d orbitals of Eu^{2+} are located near the conduction band bottom of the host $SrAl_2O_4$. (2) The Eu^{2+} concentration decreases under UV excitation. (3) The phosphor samples always have a small quantity of remnant Eu^{3+} ions because it is impossible to reduce all Eu^{3+} ions into Eu^{2+} ions under the synthetic conditions employed [67].

The model proposes that under UV irradiation electrons are promoted from the occupied 4f levels of Eu^{2+} to the empty 5d levels and from the valence band top to the unoccupied 4f levels of residual Eu^{3+} (i.e., charge transfer). The electrons promoted to the 5d levels can be trapped at the V_O defects located in the vicinity of the photogenerated Eu^{3+} cations while the holes created in the valence band can be trapped either at the V_{Sr} or V_{Al} levels. Due to these trapping processes, Eu^{2+} is oxidized to Eu^{3+}, while residual Eu^{3+} is reduced to Eu^{2+}. The thermal energy at ambient temperature causes the detrapping of the trapped electrons directly to the 5d levels of Eu^{3+}, hence leading to the $4f^6 5d^1 \rightarrow 4f^7$ green phosphorescence. The 450 nm blue emission, observed only at low temperatures (below 150 K), is attributed to the charge transfer from the fundamental level of the $4f^7$ configuration of Eu^{2+} to the valence band and is associated with a hole de-trapping mechanism [67]. This model is similar to the Dorenbos model, but differs on some important points. The first difference arises from the assertion that there is no migration of electrons through the conduction band. The transport of electrons between the traps and the luminescent centres is believed to occur through direct transfer, which requires close proximity between the europium ions and the lattice defects [67]. Clabau *et al.* arrived at this conclusion on the basis of analysis of results from measurements of the temperature-dependence of photoconductivity as well as thermoluminescence (TL), which indicate that detrapped electrons do not migrate in the conduction band. This observation is reinforced by results of their evolution of TL curves of the alkaline-earth aluminate (AAl_2O_4) series (A = Ca, Sr, Ba), which suggest that electron detrapping, from the oxygen vacancy levels, occurs towards the 5d orbitals of Eu^{2+} rather than to the conduction band [67].

The second difference is based on the nature of the traps. By comparing glow curves of nonco-doped and Dy^{3+}-co-doped $SrAl_2O_4:Eu^{2+}$, Clabau *et al.* noticed that the relevant peaks differed in size and location, but were very similar in shape. From this, they concluded that the chemical nature of the trap was not influenced under co-doping. This led them to the idea that lattice defects, namely oxygen vacancies, must act as traps in $SrAl_2O_4:Eu^{2+},RE^{3+}$ [81]. The influence of the rare-earth ions as co-dopants is explained by their stabilizing influence on the oxygen vacancies. The ionization potentials of the rare-earths can be used as a measure of the extent of this stabilization, since a lower ionization potential will cause the codopant to attract oxygen vacancies more strongly, thereby increasing the trap depth [82]. It has actually been observed that when $SrAl_2O_4:Eu^{2+}$ is co-doped with different rare earth ions, with an increasing ionization potential, the duration of the afterglow is shortened [67].

3.3.6 Revised models

The 2005 model by Clabau *et al.* attributed the two observed Eu^{2+} emissions to the Eu^{2+} ions occupying the two Sr^{2+} sites in the $SrAl_2O_4$ lattice. This assertion was challenged by Ngaruiya *et al.* [83] on account of the chemical indistinguishability of the two sites as well as their similarity in abundance. In 2008, they postulated the preferential alignment

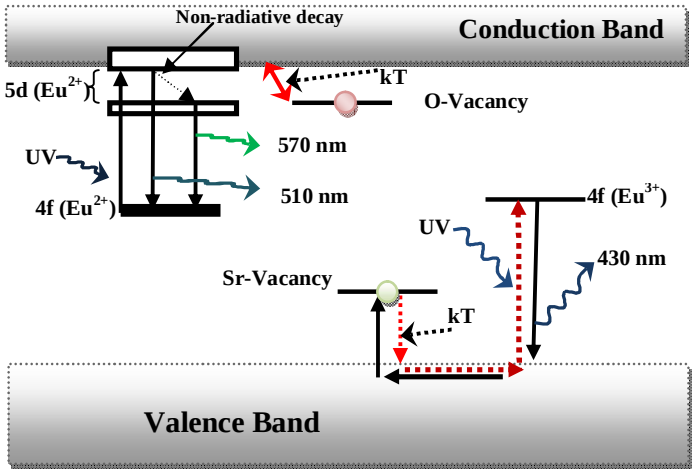

Figure 3.5: Clabau's *et. al.* [67] phosphorescence mechanism as modified by Ngaruiya *et al.* [83]

of one of the 5d-orbitals of the Eu^{2+} ion to modify the Clabau *et al.* model (Fig. 3.5). The crux of the revision is on alignment as one of the factors that influence Eu^{2+} emissions. Ba and Sr ions are reported to form linear chains in the lattices of $BaAl_2O_4$ and $SrAl_2O_4$ [84]. An Eu^{2+} ion in these chains experiences, in addition to the negative charges of the nearest anion neighbours, positive charges due to cation neighbours in the chain direction. The positive charges can orient one d-orbital preferentially, thereby lowering its energy and therefore result in Eu^{2+} emitting at longer wavelengths [83].

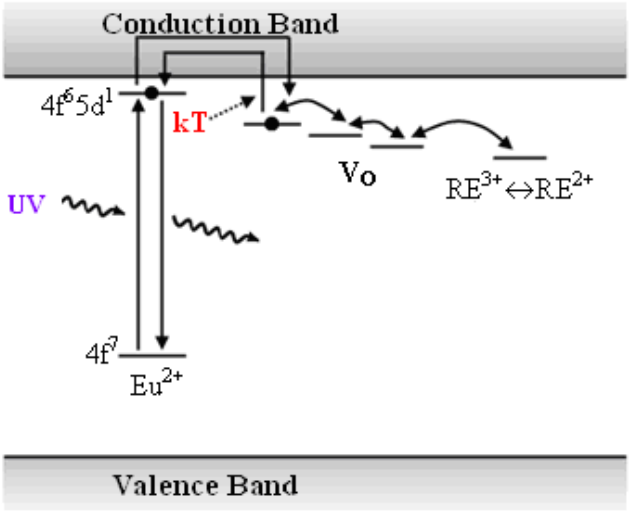

Figure 3.6: Phosphorescence mechanism proposed in 2006 by Aitasalo *et al.* for $CaAl_2O_4:Eu^{2+},Dy^{3+}$ [57].

Fig. 3.6 shows the model by Aitasalo *et al.* [57], which was developed in 2006 by incorporating ideas from both the Dorenbos and Clabau models. In the new mechanism, electrons that are excited in the Eu^{2+} luminescent centres can easily escape into the conduction band. Both oxygen vacancies and trivalent codopant ions introduce trap levels. The captured electrons can escape again into the conduction band and recombine in a luminescent centre when enough thermal energy is made available. However, the exact nature of the traps was not clarified from the reasoning that the defects involved can interact with each other and form complex aggregates [57].

3.4 The $SrAl_2O_4$ phase

As mentioned earlier, the alkaline earth aluminates MAl_2O_4 (M = Ca,Sr,Ba) are by far the most studied family of persistent luminescent materials. Of these, $SrAl_2O_4$ has received the most attention due to its various potential benefits.

3.4.1 Structural characteristics of $SrAl_2O_4$

$SrAl_2O_4$ has two polymorphisms: the low temperature monoclinic structure and the high temperature hexagonal one [85]. A reversible phase transformation between the two crystallographic forms has been observed to occur at about 650°C [86]. The structure of the low-temperature phase is well established [87], but that of the high-temperature phase is not [86]. The structure of the low-temperature phase has a three-dimensional network of corner-sharing AlO_4 tetrahedra, which has channels in the a- and c-directions

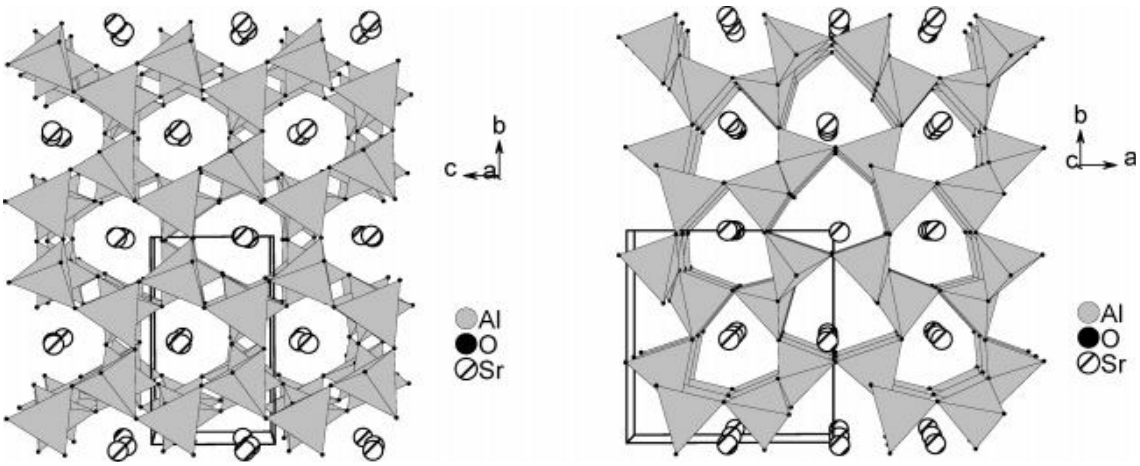

Figure 3.7: Schematic views of the monoclinic phase of $SrAl_2O_4$ along the a- and c-directions [67].

where the Sr^{2+} ions are located (Fig. 3.7). There are two crystallographically different sites for Sr^{2+} (Wyckoff position 2a), which have identical co-ordination numbers (i.e., 6 + 1), similar average Sr-O distances (i.e., 2.695 Å and 2.667 Å) and similar individual Sr-O distances. The two environments differ only by a slight distortion of their "square planes". on the oter hand, the Sr^{2+} and Eu^{2+} ions are very similar in their ionic size (i.e.,

1.21 and 1.20 Å, respectively). Consequently, when occupied by Eu^{2+} ions, the two different Sr^{2+} sites will have a quite similar local distortion, so that the Eu^{2+} ions located at the two different Sr^{2+} sites will have very similar local environments. The phosphorescence in the monoclinic phase of the $SrAl_2O_4$:Eu^{2+} phosphor has been observed when prepared in the form of a thin layer [88] or a crystal [89,90], by solid-state reactions (at 1300 °C during few hours) [24], a sol-gel route (at 1150 °C) [38], a microwave route [90], and a combustion method [91]. Europium is usually introduced in the reaction mixture in its oxidized state Eu^{3+} (Eu_2O_3), and phosphorescence appears only after a reducing treatment (in situ or afterwards) [92]. Luminescence measurements show that after this reducing treatment, europium is mainly present in the reduced form Eu^{2+} [24], but Mossbauer measurements have shown that there remains roughly 5 to 10% of Eu^{3+} [76].

3.4.2 Dopant and co-dopant sites

The sites of the dopants and co-dopants of $SrAl_2O_4$ are dictated by their ionic radii. The Eu^{2+} (1.20 Å), Eu^{3+} (1.01 Å), and Dy^{3+} (0.97 Å) ions can readily occupy the Sr^{2+} (1.21 Å) ion sites, as confirmed by EPR measurements [93]. The two crystallographically different Sr^{2+} sites are very similar, so it is expected that the luminescent ions (Eu^{2+}) are present at both sites. This expectation is corroborated by EPR measurements [94]. The fact that Sr^{2+} and Eu^{2+} ions have very close ionic radii explains why Eu^{3+} ions introduced in the Sr^{2+} sites of $SrAl_2O_4$ are easily reduced to Eu^{2+} [92].

3.4.3 Probable vacancies

The formation of the by-product $Sr_3Al_2O_6$ during the synthesis of $SrAl_2O_4$ [92] as well as the thermoluminescence (TL) measurements carried out for the stoichiometric and nonstoichiometric samples of $SrAl_2O_4$: Eu^{2+} [69] indicate that $SrAl_2O_4$ tends to have strontium vacancies (V_{Sr}), and hence oxygen vacancies (V_O) due to the requirement of charge neutrality. Aluminum vacancies (V_{Al}) might exist as well, but would be energetically unfavourable to form because the Al-O bonds are short and strong.

3.5 References

1. Ronda, C.R. *Luminescence from Theory to Applications*. Wiley-VCH, Germany, 3, (2008).
2. Feldmann, C. Justel, T. Ronda, C.R. Schmidt, P.J. *Functional Materials.* **13**(7)**:** WILEY-VCH, Verlag GmbH & Co KGaA, Weinheim, (2003)
3. Blasse, G. Grabmaier, B.C. *Luminescent Materials.* Springer, Berlin, (1994).
4. Folkerts, H.F. Blasse, G. *Chem. Mater.,* **6**(7)**:** 969, (1994).
5. Oomen, E.W.J.L. Dirksen, G.J. Smit, W.M.A. Blasse, G. *J. Phys., C* **20**(8)**:** 1161, (1987)**.**
6. Oomen, E.W.J.L. Smit, W.M.A. Blasse, G. *Mat. Chem. Phys.,* **19**(4)**:** 357, (1988).
7. Dexter, D.L. Klick, C.C. Russell, G.A. *Phys. Rev.,* **100:** 603, (1955).
8. Hamstra, M.A. Folkerts, H.F. Blasse, G.*J. Mater. Chem.,* **4:** 1349, (1994).
9. Folkerts, H.F. Ghianni, F. Blasse, G. *J. Phys. Chem. Solids.,* **57:** 1659, (1996).
10. Van To1, J. Van der Waals, J.H. *Chem. Phys. Lett.,* **194**(4-6)b**:** 288, (1992).
11. Lin, Y. Tang, Z. Zhang, Z. Wang, X. Zhang, J. *J. Mater. Sci. Lett.,* **20:** 1505, (2001).
12. Ji, H. Xie, G. Lv, Y. Lu, H. *J. Sol-Gel Sci. Technol.,* **44:** 133, (2007).
13. Pan, W. Ning, G. Zhang, X. Wang, J. Lin, Y. Ye, J. *J. Lumin.,* **128:** 1975, (2008).
14. Song, F. Donghua, C. Yuan, Y. *J. Alloy. Compd.,* **458:** 564, (2008).
15. Xu, Y. Chen, D. *Ceram. Int.,* **34:** 2117, (2008).
16. Toda, K. Imanari, Y. Nonogawa, T. Miyoshi, J. Uematsu, K. Sato, M. *J. Ceram. Soc. Jpn.,* **110:** 283, (2002).
17. Aitasalo, T. Hölsä, J. Laamanen, T. Lastusaari, M. Lehto, L. Niittykoski, J. Pellé, F. *Ceram.-Silikáty.,* **49:** 58, (2005).
18. Aitasalo, T. Hölsä, J. Kirm, M. Laamanen, T. Lastusaari, M. Niittykoski, J. Raud, J. Valtonen, R. *Radiat. Meas.,* **42:** 644, (2007).

19. Blasse, G. Wanmaker, W.L. Ter Vrugt, J.W. Bril, A. *Philips Res. Rep*., **23:** 189, (1968).
20. Jiang, L. Chang, C. Mao, D. *J. Alloy. Compd.*, **360:** 193, (2003).
21. Fei, Q. Chang, C. Mao, D. *J. Alloy. Compd.*, **390:** 133, (2005).
22. Jiang, L. Chang, C. Mao, D. Feng, C. *Opt. Mater.*, **27:** 51, (2004).
23. Wang, X.J. He, Z.Y. Jia, D. Strek, W. Pazik, R. Hreniak, D. Yen, W.M. *Microelectron. J.*, **36:** 546, (2005).
24. Matsuzawa, T. Aoki, Y. Takeuchi, N. Murayama, Y. *J. Electrochem. Soc*., **143:** 2670, (1996**).**
25. Chander, H. Haranath, D. Shanker, V. Sharma, P. *J. Cryst Growth*., **271:** 307, (2004).
26. Lange, H. *US patent* **3**, 294, 699, (1966).
27. Blasse, G. Bril, A. *Philips Res. Rep.*, **23:** 201, (1968).
28. Aitasalo, T. Hölsä, J. Jungner, H. Lastusaari, M. Niittykoski, J. Parkkinen, M. Valtonen, R. *Opt. Mater.*, **26:** 113, (2004).
29. Chen, R. Wang, Y. Hu, Y. Hu, Z. Liu, C. *J. Lumin.*, **128:** 1180, (2008).
30. Peng, T. Yang, H. Pu, X. Hu, B. Jiang, Z. Yan, C. *Mater. Lett.*, **58:** 352, (2004).
31. Qiu, Z. Zhou, Y. Lü, M. A. Zhang, Ma, Q. *Acta Mater.*, **55:** 2615, (2007).
32. Zhao, C. Chen, D. *Mater. Lett.*, **61:** 3673, (2007).
33. Geng, J. Wu, Z. *J. Mater. Synth. Proces*., **10:** 245, (2002).
34. Jia, W. Yuan, H. Lu, L. Liu, H. Yen, W.M. *J. Cryst. Growth*., **200:** 179, (1999).
35. Aitasalo, T. Hölsä, J. Jungner, H. Lastusaari, M. Niittykoski, J. *J. Alloy. Compd*., **341:** 76, (2002).
36. Chen, I.C. Chen, T.M. *J. Mater. Res*., **16:** 644, (2001).
37. Peng, T. Huajun, L. Yang, H. Yan, C. *Mater. Chem. Phys.*, **85:** 68, (2004).
38. Tang, Z. Zhang, F. Zhang, Z. Huang, C. Lin, Y. *J. Eur. Ceram. Soc.*, **20:** 2129, (2000).
39. Katsumata, T. Nabae, T. Sasajima, K. Komuro, S. Morikawa, T. *J. Electrochem. Soc.*, **144:** L243, (1997).
40. Sakai, R. Katsumata, T. Komuro, S. Morikawa, T. *J. Lumin.*, **85:** 149, (1999).
41. Nag, A. Kutty, T.R.N. *Mater. Res. Bull.*, **39:** 331, (2004).

42. Nag, A. Kutty, T.R.N. *J. Alloy. Compd.*, **354:** 221, (2003).
43. Lin, Y. Tang, Z. Zhang, Z. *Mater. Lett.*, **51:** 14, (2001).
44. Lin, Y. Tang, Z. Zhang, Z. Nan, C.W. *Appl. Phys. Lett.*, **81:** 996, (2002).
45. Suriyamurthy, N. Panigrahi, B.S. *J. Lumin.*, **128:** 1809, (2008).
46. Yuan, Z. Chang, C. Mao, D. Ying, W. *J. Alloy. Compd*., **377:** 268, (2004).
47. Akiyama, M. Xu, C. Nonaka, K. Watanabe, T. *Appl. Phys. Lett.*, **73:** 3046, (1998).
48. Chang, C. Li, W. Huang, X. Wang, Z. Chen, X. Qian, X. Guo, R. Ding, Y. Mao, D. *J. Lumin*., **130:** 347, (2010).
49. Zhang, P. Xu, M. Zheng, Z. Sun, B. Zhang, Y. *Mater. Sci. Eng. B Solid State Mater. Adv. Technol.*, **136:** 159, (2007).
50. Zhang, P. Li, L. Xu, M. Liu, L. *J. Alloy. Compd.*, **456:** 216, (2008).
51. Lenard, P., Schmidt, F., and Tomascheck, R. *Handb. Exp. Phys.*, **23**, Akadem. Verlagsges, Leipzig, (1928).
52. Shionoya, S. *Phosphor Handbook*, Yen, W.M. Shionoya, S. Yamamoto, H. (Eds.), CRC Press, Boca Raton, Chap.3, (2007).
53. Dorenbos, P. *J. Lumin.*, **104:** 239, (2003).
54. Jia, D. Zhu, J. Wu, B. *J. Lum*., **91:** 59, (2000).
55. Jia, D. Jia, W. Evans, D.R. Dennis, W.M. Liu, H. Zhu, J. Yen, W.M. *J. Appl. Phys.*, **88:** 3402, (2000).
56. Jia, D. Zhu, J. Wu, B. *J. Electrochem. Soc*., **147:** 386–389, (2000).
57. Jia, D. *J. Electrochem. Soc*., **153:** H198, (2006).
58. Jia, W. Jia, D. In: *Phosphor Handbook*, Yen, W.M. Shionoya, S. Yamamoto, H. (Eds.), CRC Press, Boca Raton, Chap.4, (2007).
59. Pang, R. Li, C. Shi, L. Su, Q. *J. Phys. Chem. Solids*., **70:** 303, (2009).
60. Pang, R. Li, C. Zhang, S. Su, Q. *Mater. Chem. Phys.*, **113:** 215, (2009).
61. Hao, Z. Zhang, J. Zhang, X. Sun, X. Luo, Y. Lu, S. Wang, X. *Appl. Phys. Lett*., **90:** 261113, (2007).
62. Shionoya, S. Yen, W. *Phosphor Handbook*; CRC Press: New York, (1999).
63. Harvey, E. N. *Amer. Phil. Soc*., Philadelphia, 18, (1957).

64. Murayama, Y. *Phosphor Handbook*, Shionoya, Y. Yen, Y. (Eds.), CRC Press, Boca Raton (1999).
65. Holsa, J. *The Electrochemical Society Interface*., 42, (2009).
66. Eeckhout, K.V.D. Smet, P.F. Poelman, D. *Mater.*, **3**: 2536, (2010)
67. Clabau, F. Rocquefelte, X. Jobic, S. Deniard, P. Whangbo, M.H. Garcia, A. Le Mercier, T. *Chem. Mat.*, **17**, 3904, (2005).
68. Dorenbos, P. *J. Electrochem. Soc.*, **152**, H107, (2005).
69. Abbruscato, V. *J. Electrochem. Soc.*, **118:** 930**,** (1971).
70. Yuan, H.B. Jia, W. Basun, S.A. Lu, L. Meltzer, R.S. Yen, W.M. *J. Electrochem. Soc.*, **147:** 3154, (2000).
71. Lin, Y. Zhang, Z. Tang, Z. Wang, X. Zhang, J. Zheng, Z.*J. Eur. Ceram. Soc.*, **21:** 683, (2001).
72. Nakazawa, E. Mochida, T. *J. Lumin.*, **72–74:** 236, (1997).
73. Kato, K. Tsutai, I. Kamimura, T. Kaneko, F. Shinbo, K. Ohta, M. Kawakami, T. *J. Lumin.*, **82:** 213, (1999).
74. Yamamoto, H. Matsuzawa, T. *J. Lumin.*, **72–74:** 287, (1997).
75. Nakamura, T. Kaiya, K. Takahashi, N. Matsuzawa, T. Ohta, M. Rowlands, C.C. Smith, G.M. Riedi, P.C. *Phys. Chem. Chem. Phys.*, **3:** 1721, (2001).
76. Clabau, F. *Thesis*. Universite´ de Nantes, Nantes, France, (2005).
77. Dorenbos, P. *Phys. Status Solidi B-Basic Solid State Phys.*, **242:** R7, (2005).
78. Dorenbos, P. *J. Lumin.*, **108:** 3015, (2004).
79. Aitasalo, T. Hölsä, J. Jungner, H. Krupa, J.C. Lastusaari, M. Legendziewicz, J. Niittykoski, J. *Radiat. Meas.*, **38:** 727, (2004).
80. Dorenbos, P. *J. Phys.-Condens. Matter.*, **15:** 8417, (2003).
81. Clabau, F. Rocquefelte, X. Jobic, S. Deniard, P. Whangbo, M.H. Garcia, A. Le Mercier, T. *Solid State Sci.*, **9:** 608, (2007).
82. Clabau, F. Rocquefelte, X. Le Mercier, T. Deniard, P. Jobic, S. Whangbo, M.H. *Chem. Mater.*, **18:** 3212, (2006).
83. Ngaruiya, J.M. Nieuwoudt, S. Ntwaeaborwa, O.M. Terblans, J.J. Swart, H.C. *Mater. Lett.*, **62:** 3192, (2008).

84. Poort, S.H.M. Reijnhoudt, H.M. Van der Kuip, H.O.T. Blasse, G. *J. Alloys Compd.*, **241:** 75, (1996).
85. Lee, J.S. Kim, Y.J. *Thin Solid Films*., **518:** 149, (2010)
86. Jia, W. Yuan, H. Lu, L. Liu, H. Yen, W.M. *J. Lumin.*, **76-77:** 424, (1998).
87. Schulze, A. Mueller-Buschbaum, H.Z. *Anorg. Allg. Chem.*, **475:** 205, (1981).
88. Kato, K. Tsutai, I. Kamimura, T. Kaneko, F. Shinbo, K. Ohta, M. Kawakami, T. *J. Lumin.*, **82**(3)**:** 213, (1999).
89. Katsumata, T. Nabae, T. Sasajima, K. Matsuzawa, T. *J. Cryst. Growth*, **183:** 361, (1998).
90. Geng, J. Wu, Z. *J. Mater. Synth. Proc.*, **10:** 245, (2002).
91. Peng, T. Yang, H. Pu, X. Hu, B. Jiang, Z. Yan, C. *Mater. Lett.*, **58:** 352, (2004).
92. Beauger, C. *Thesis*. University of Nice, Nice, France, (1999).
93. Nakamura, T. Kaiya, K. Takahashi, T. Matsuzawa, T. Ohta, M. Rowlands, C. Smith, G. Riedi, P. *Chem. Phys.*, **3:** 1721, (2001).
94. Kaiya, K. Takahashi, N. Nakamura, T. Matsuzawa, T. Smith, G. Riedi, P. *J. Lumin.*, **87-89:** 1073, (2000).

Chapter 4
Characterization and Synthesis Techniques

4.1 Introduction

The key material parameters required to understand, control, and correlate material properties with optical performance include the average particle diameter and particle-size distribution, crystallinity and material shape or morphology. Characterizing particle or feature size for nanocrystals and nanostructures is done routinely using scanning transmission electron microscopy (STEM), high-resolution transmission electron microscopy (HRTEM), scanning electron microscopy (SEM), scanning tunneling microscopy (STM), and atomic force microscopy (AFM) [1]. TEM methods usually require dispersion of the particles, but, of all the microscopy methods listed here, HRTEM can provide the best spatial resolution of better than 0.2 nm [2]. Furthermore, the high resolution imaging can identify defects and surface structures. An important aspect of the direct imaging methods is that they will reveal the shapes of nanomaterials, which can affect the optical characteristics of many types of materials [3]. AFM is being used more frequently, although preparing atomically thin AFM tips to image particles or features less than 10 nm can be very difficult. AFM has the potential to provide spatially resolved chemical information [4]. The main advantage of SEM, STM, and AFM methods is that they can be used to study the morphology of as-prepared nanoparticles and nanocomposites. Direct size measurements obtained from images are often used in conjunction with other measurements such as powder x-ray diffraction (XRD).

For a complete picture of the crystal phase, average particle diameter, particle-size distribution and the morphology of the samples, it is necessary to combine diffraction and imaging characterization tools. Crystal phase confirmation and purity can be obtained by using powder XRD [5] and selected-area electron diffraction (SAED). SAED can analyze single nanoparticles that are 10 nm and larger [6]. Similarly, using electron diffraction patterns in TEM or the interference fringes in HRTEM images can also confirm the crystal phase of individual nanoparticles. In some cases, it is possible to correlate the phase and structural information obtained from microscopy and diffraction measurements with the optical properties [7].

The complete characterization of a whole material requires elemental analysis, which is often performed in an electron microscope using energy-dispersive x-ray spectrometry (EDXS) or by surface analytical techniques such as x-ray fluorescence, Auger electron spectroscopy (AES), and x-ray photoelectron spectroscopy (XPS). XPS, extended x-ray absorption fine structure (EXAFS), and electron energy loss spectroscopy (EELS) can provide further details about the surface chemistry, structure, and local environment [8]. Elemental and qualitative analytical techniques are also necessary to identify intentional adsorbates or unintentional contaminants on a particle surface. Molecular spectroscopy such as Raman spectroscopy and Fourier transform infrared (FTIR) spectroscopy can characterize materials and help identify any surface contaminants or intentional capping agents.

Luminescence is an appropriate tool for characterizing the structures and performance of phosphors due to the strong optical emission of these materials. Optical spectroscopy can provide a sensitive measure of particle size, size distribution, and particle shapes for quantum dots and metals. Complementary information for characterizing multiple phases, defects, quenching, and environmental effects can be obtained from lifetime measurements [9]. Luminescence spectra, lifetimes, and quantum-efficiency measurements can be made with laboratory-scale spectrometers utilizing optical photons, electrons or x-rays, as excitation sources. However, detailed studies using vacuum-UV excitation may require sophisticated excitation sources. Optical

spectroscopic measurements are quite important to determine colour purity and quantum efficiency of phosphor materials.

In the case of inorganic/organic composites, the range of characterization methods used in the analysis of the composition, the molecular and nanometre structure as well as the physical properties of these materials is quite large. Many of the methods are specific for particular material compositions [10]. Compared with classical inorganic materials, hybrids are often amorphous so well-established characterization techniques such as x-ray diffraction are limited. Many methods used are more related to the characterization of amorphous organic polymers. The heterogeneous nature of these materials means that generally a variety of analytical techniques has to be used to get a satisfactory answer to structure– property relationships.

4.2 Scanning electron microscopy (SEM) and energy dispersive x-ray spectroscopy (EDXS)

Scanning electron microscopy is an imaging technique, which is capable of producing high resolution images of a sample surface. SEM images have a characteristic three-dimensional appearance and are useful for judging the surface structure of a sample [11]. Electron microscopy became one of the most important techniques to characterize the materials morphology on the nanometre and nowadays even on the atomic scale [12]. Electron microscopy takes advantage of the wave nature of rapidly moving electrons. In the microscope, a beam of electrons is generated in a vacuum. The beam is collimated by electromagnetic condenser lenses, focused by an objective lens, and then scanned across the surface of the sample by electromagnetic deflection coils. The primary imaging method is by collecting secondary electrons that are released by the sample. The electrons are detected by a scintillation material that produces flashes of light from the electrons. The light flashes are then detected and amplified by a photomultiplier tube. By correlating the sample scan position with the resulting signal, an image can be formed that is strikingly similar to what would be seen through an optical microscope [13].

Beside the emitted electrons, x-rays are also produced by the interaction of electrons with the sample. These x-rays are characteristic of the elements present in the sample and can be detected in a scanning electron microscope coupled with an x-ray analyzer such as the energy dispersive x-ray spectrometer (EDXS) [14]. Different

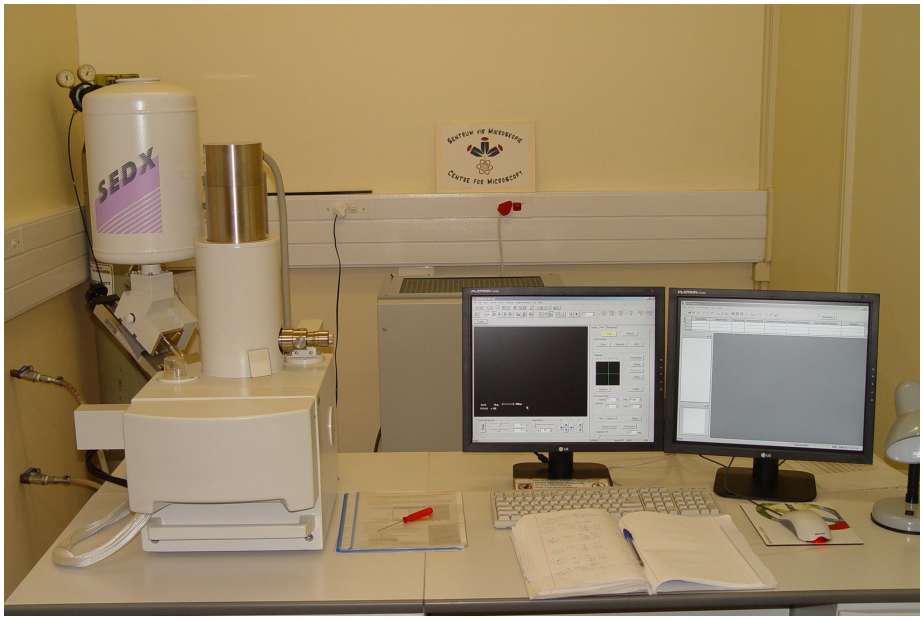

Figure 4.1: The SEM equipment coupled with EDS: SHIMADZU Superscan model SSX-550

detection modes can be applied such as the detection of backscattered electrons or the electron backscatter diffraction (EBSD) which gives crystallographic information about the sample. SEM is very versatile in having many other imaging modes available that provide specialized information. However, in the analysis of SEM micrographs, one has to be aware of some limiting aspects such as [13]:

- ✓ All specimens are in high vacuum and probably have another shape in a liquid or gel-like surrounding.
- ✓ The images reveal only a small fragment of the whole sample raising the possibility that the region analyzed may not be characteristic of the whole sample.
- ✓ The high energy electron beam incident on the sample may probably change it.

In general electron microscopy results should always be confirmed by other techniques.

In this study, the surface morphology and elemental composition of the phosphor powders were investigated using a Shimadzu Superscan SSX-550 electron microscope (SEM) coupled with an energy dispersive x-ray spectroscope (EDS). For SEM measurements, the probe size was 3.0 nm, the probe current 0.02 nA, and the accelerating voltage 5.0 keV. The probe size for EDS analysis was 4 nm, specimen current 1.00 nA, and accelerating voltage 15.0 keV. The set up used in this work is shown in Fig. 4.1.

4.3 X-ray diffractometry (XRD)

The object of x-ray diffractometry is in two main areas; fingerprint characterization, and the determination of structural properties of crystalline materials. Hence, this technique, which is nondestructive, is suitable for identifying major constituents of a mixture and is also an effective tool for determining the phase,

Figure 4.2: The X-ray diffractometer used in this study is a Bruker AXS Discover diffractometer

crystallinity, and purity of samples prepared under various conditions. It has a detection limit of 5 percent [15].

When the positions and intensities of the diffraction pattern of a sample are taken into account, the pattern is unique for a single substance. The x-ray pattern is like a fingerprint and mixtures of different crystallographic phases can be easily distinguished by comparison with reference data. Usually electronic databases such as the International Centre for Diffraction Data (ICDD) are employed for this comparison. The major information one gets from this method is the crystalline composition and the phase purity. In the case of semicrystalline or amorphous materials, broad humps are observed in the diffractogram. Therefore the degree of crystallinity can be qualitatively estimated. If the crystallites of the powder are very small the peaks of the pattern will be broadened. From this broadening it is possible to determine an average crystallite size by the Debye–Scherrer equation,

$$d = \frac{k\lambda}{\cos\theta\sqrt{\beta^2 - \beta_0^2}} \qquad (3.1)$$

where d denotes the average size of the crystallites, k is a factor which is usually set to 0.9, θ is the Bragg angle, β is the broadening of the diffraction line measured at half of its maximum intensity (radians), β_0 represents the scan aperture of the diffractometer, and λ is the x-ray radiation wavelength. An error for the crystallite size by this formula can be up to 50% [15]. The system employed in this study (Fig. 4.2) is a Bruker D8 (Bruker Corporation of Germany) x-ray diffractometer in which the source of the x-ray radiation is CuK_α with a wavelength of 1.5406 Å and was operating at 40 kV and 40 mA, with a scan step of 0.02° in 2θ and a scan speed of 4°/min. The divergence slit (DS) was set equal to the scatter slit (SS) at a value of 1°, while the receiving slit (RS) was 0.15 mm.

4.4 Transmission electron microscopy (TEM)

Transmission electron microscopy is an imaging technique in which a beam of electrons is focused onto a specimen causing an enlarged image to either appear on a

fluorescent screen or layer of photographic film, or to be detected by a CCD camera [16]. Fig. 4.3 shows the basic construction of a transmission electron microscope as well as a photograph of the system employed in this work.

The source radiation is generated using an electron gun and the resulting beam of electrons is focused into a tight, coherent beam by multiple electromagnetic lenses and apertures. The lens system is designed to eliminate the loss of electrons as well as to control and focus the electron beam. The corrected beam is then focused onto the

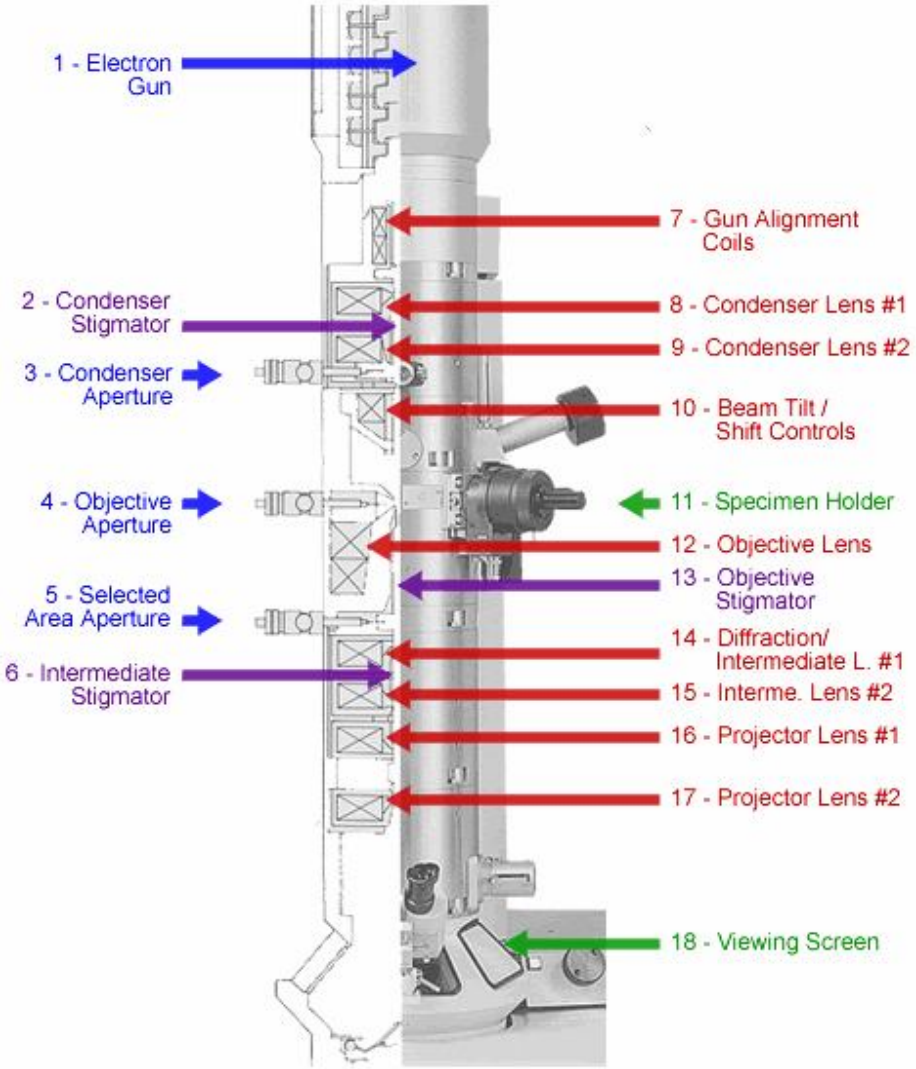

Figure 4.3(a): Schematic diagram of a transmission electron microscope [18]

sample. The beam has enough energy for the electrons to be transmitted through the sample. The transmitted electron signal is greatly magnified by a series of electromagnetic lenses. The magnified transmitted signal may be observed in either an electron diffraction mode or direct imaging mode. Data is accumulated from the beam after it passes through the sample. The electron diffraction mode is employed for crystalline structure analysis, while the image mode is used for investigating the microstructure, e.g. the grain size and lattice defects [17]. A modern high-resolution TEM goes down to a resolution <100 pm.

Figure 4.3(b): JEOL JEM-2100 model transmission electron microscope

While the ability to get atomic-scale resolutions from transmission electron microscopy is of great advantage, TEM is a relatively expensive equipment. It requires extensive sample preparation, which makes it a relatively time-consuming technique with a low throughput of samples.

The TEM results in this project were obtained using a JEOL JEM-2100 transmission electron microscope operating at 200 kV. The system is available at the Council for Scientific and Industrial Research (CSIR), nanomaterials laboratory. Sample preparation involved suspending particles in ethanol by ultrasonification and drying a drop of the suspension on a carbon-coated copper grid.

4.5 Photoluminescence spectroscopy (PL)

The luminescence properties of a phosphor can be characterized by its emission spectrum, brightness, and decay time [19]. Additional information pertaining to both the basic luminescence mechanisms and their practical application can be obtained from the absorption and reflectance spectra.

The photoluminescence technique is a nondestructive and contactless spectroscopic method of probing the electronic structures of materials [20]. The excitation energy and intensity are chosen to probe different regions and excitation

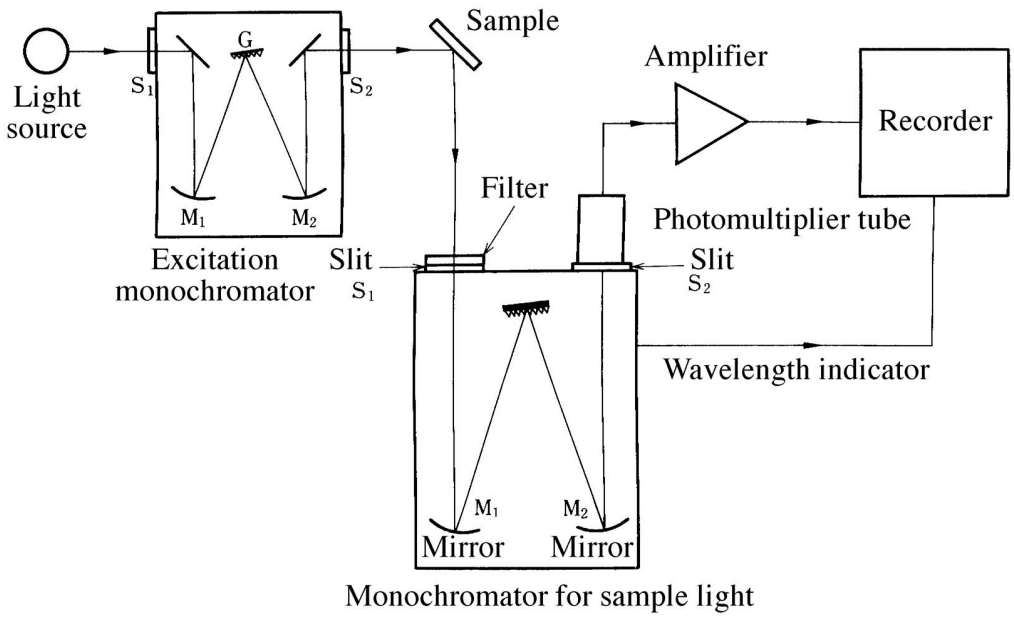

Figure 4.4: Typical experimental set up for PL measurements [21]

concentrations in the sample. The light emitted in PL can be collected and analyzed to yield a wealth of information about the photoexcited material. The PL spectrum provides the transition energies, which can be used to determine the electronic energy levels [20]. The spectrum is obtained using a monochromator equipped with an appropriate light detector. A typical PL set-up is shown in Fig. 4.4. A detailed description of its operation can be found elsewhere [21].

The PL intensity and spectral content is a measure of various important material properties such as chemical composition, structure, impurities, kinetic processes and energy transfer [21]. Variation of the PL intensity with external parameters like

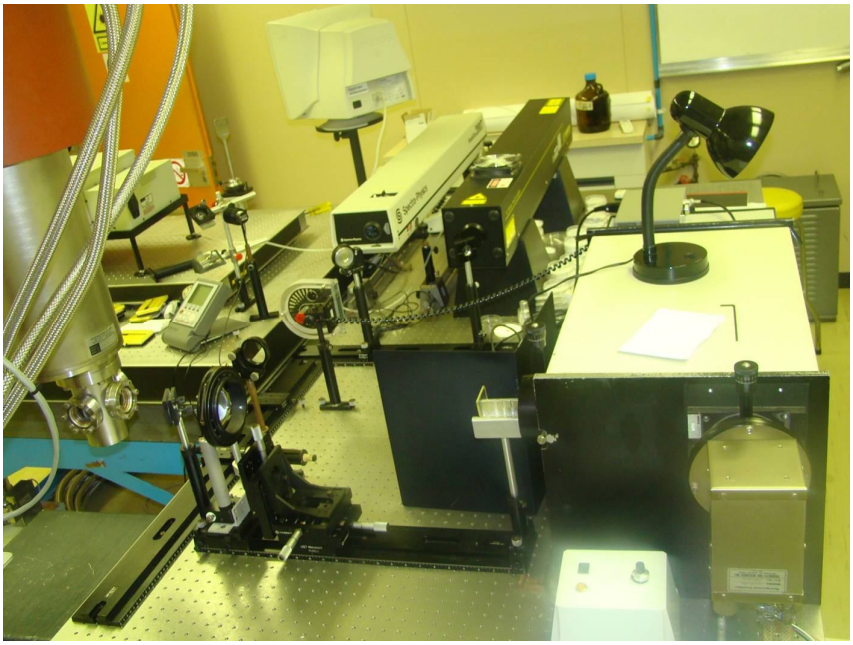

Figure 4.5(a): The He-Cd laser equipment

temperature and applied voltage can be used to characterize further the underlying electronic states and bands [19]. Additionally, one of the characteristics of PL is that it has a unique sensitivity to discrete electronic states. Since many of these states lie near surfaces and interfaces, PL becomes an important tool for obtaining detailed information about the nature of the states. When the states serve as long-lived traps, the depth of the

traps can be determined by observing thermal activation in temperature-dependent PL [20].

Compared with other optical methods of characterization like reflection and absorption, the PL technique has various advantages: It is simple, versatile, nondestructive and the measurement does not rely on electrical excitation or detection, so

Figure 4.5(b): The Cary Eclipse fluorescence spectrophotometer system

that sample preparation is minimal. PL can be used to study virtually any surface in any environment. The main drawback of PL analysis is that the sample under investigation must emit light and the difficulty in estimating the density of interface and impurity states constitutes another shortcoming [20].

In this study, two systems were employed for PL characterization; a SPEX 1870 0.5m spectrometer system, equipped with a He–Cd laser lamp as the excitation source and a Cary Eclipse fluorescence spectrophotometer (Model: LS 55). Samples for the laser system were excited at 325 nm and emission observed in the wavelength range 400 to

600 nm at room temperature. The Cary Eclipse spectrophotometer is equipped with a 150 W monochromatic xenon lamp as the excitation source and a grating to select a suitable wavelength for excitation. Each sample was loaded into a circular holder and excited with 340 nm radiation from the pulsed xenon lamp. The emission spectra were scanned in the range of wavelengths from 360 to 750 nm. To measure the excitation spectra, the analyzer monochromator was set to the maximum wavelength of the emission spectra and then an excitation monochromator was scanned in the range of 250 to 450 nm. The same system (Cary Eclipse) was used to investigate the phosphorescence decay curves of the phosphors in air at room temperature. The two systems are shown in Fig. 4.5.

4.6 Thermal analysis (TA) techniques

The term thermal analysis (TA) refers to a variety of analytical experimental techniques in which a property of a sample is continuously measured as the sample is programmed through a predetermined temperature profile. Fig. 4.6 shows a schematic of a TA instrument. Among the most common TA techniques are differential scanning calorimetry (DSC) and thermal gravimetric analysis (TGA).

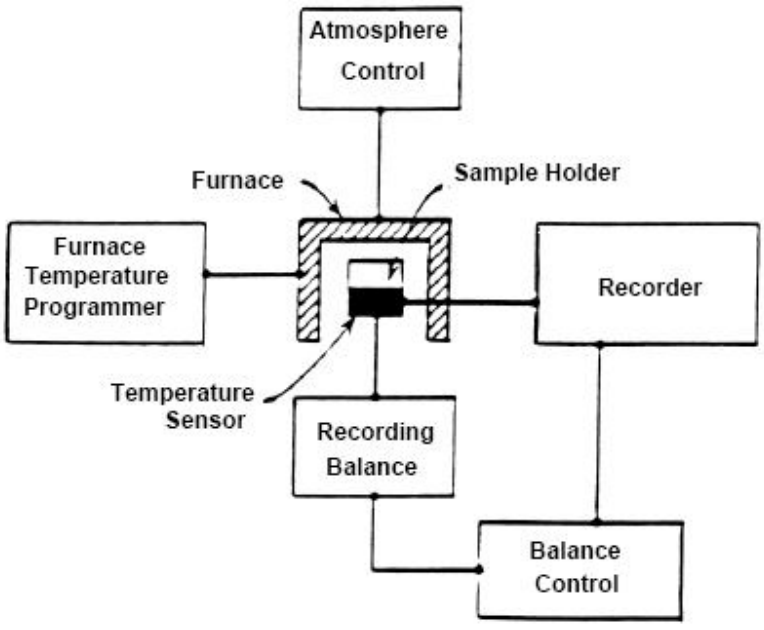

Figure 4.6: Typical components of a TA instrument

4.6.1 Differential scanning calorimetry (DSC)

Differential scanning calorimetry is a thermoanalytical technique, which measures the heat flow associated with thermally induced transitions in polymeric materials [22]. The measurement is carried out by comparing the difference in the amount of heat required to increase the temperature of a sample and a reference, whose heat capacity is well defined over the range of temperatures to be scanned. The DSC can give thermodynamic information about properties such as glass transitions, phase changes, melting, crystallization, product stability, and oxidative stability [23].

The basic principle underlying this technique is that when the sample undergoes a physical transformation such as a phase transition or thermal decomposition, more or less heat is required, compared with the reference, to maintain both at the same temperature. Whether more or less heat must flow to the sample depends on whether the process is exothermic or endothermic. An exothermic or endothermic event in the sample results in a deviation between the two heat flows and results in a peak in the DSC curve (plot of heat flow against temperature/time). The difference in heat flow between the sample and reference also delivers the quantitative amount of energy absorbed or released during such transitions. The experiments can be carried out under oxygen and other atmospheres such as an inert gas [24]. Two widely used DSC designs are the quantitative DTA (Heat-Flux DSC) and the power compensation DSC.

4.6.1.1 Quantitative DTA (Heat-Flux DSC)

The term heat-flux differential scanning calorimeter is widely used by manufacturers to describe commercial quantitative DTA instruments [25]. In quantitative DTA, the temperature difference between the sample and reference is measured as a function of temperature or time, under controlled temperature conditions. The temperature difference is proportional to the change in the heat flux (energy input per unit time). The structure of a quantitative DTA system is shown in Figure 4.7(a). The conformation of the sample holder assembly is different from that in a classical DTA set-

up. The thermocouples are attached to the base of the sample and reference holders. A second series of thermocouples measures the temperature of the furnace and of the heat-sensitive plate. During a phase change heat is absorbed or emitted by the sample, altering the heat flux through the heat-sensitive plate. The variation in heat flux causes an incremental temperature difference to be measured between the heat-sensitive plate and the furnace. The heat capacity of the heat-sensitive plate as a function of temperature is measured by adiabatic calorimetry during the manufacturing process allowing an estimate

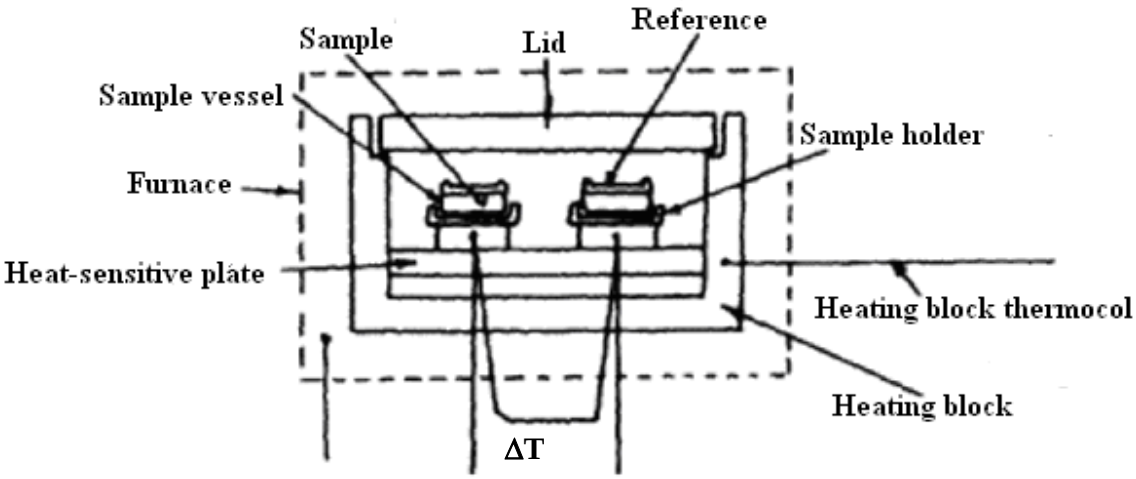

Figure 4.7(a): The structure of a quantitative DTA system [Seiko Instruments design] [25]

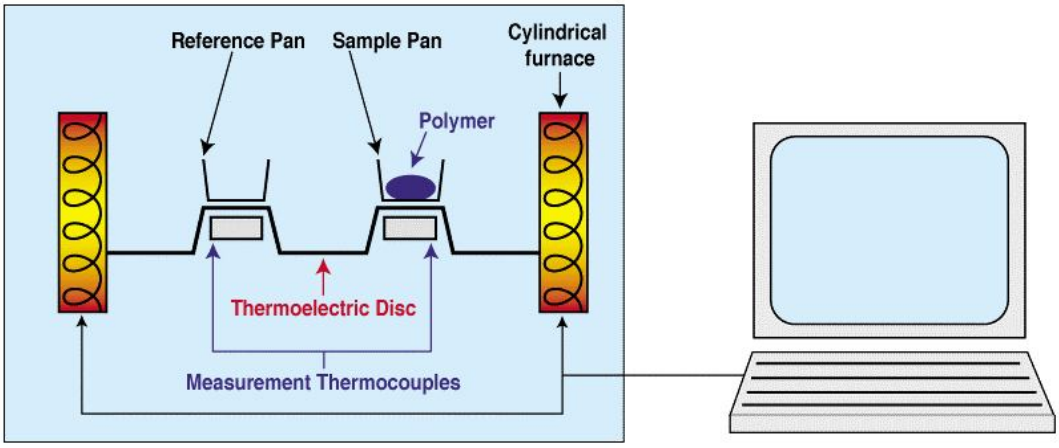

Figure 4.7(b): Schematic of a heat-flux DSC Cell [18]

of the enthalpy of transition to be made from the incremental temperature fluctuation. The sample and reference materials are placed in sample vessels and inserted into the sample and reference holders. For optimum performance of a quantitative DTA system the sample should weigh less than 10 mg, be as flat and thin as possible and be evenly placed on the base of the sample vessel. The maximum sensitivity of a quantitative DTA instrument is typically 35 μW [25]. In the most popular design, two separate pans sit on a pair of identically positioned platforms connected to a furnace by a common heat flow path (Fig. 4. 7a). A sample is placed in one of the pans while the other one is left empty and serves as a reference. The instrument furnace, which is computer-operated, is switched on and in turn heats the two pans at a specific rate, usually anywhere between 5-20 ^{o}C per minute. The instrument makes absolutely sure that the heating rate stays exactly the same throughout the experiment. But more importantly, it makes sure that the two pans are heated at the same rate so that both are maintained at nearly the same temperature.

4.6.1.2 Power compensation differential scanning calorimetry (DSC)

The structure of a power compensation-type DSC instrument is shown in Fig. 4.7(b). Its operating principle is different from that of DTA systems. The base of the sample holder assembly is placed in a reservoir of a coolant. The sample and reference

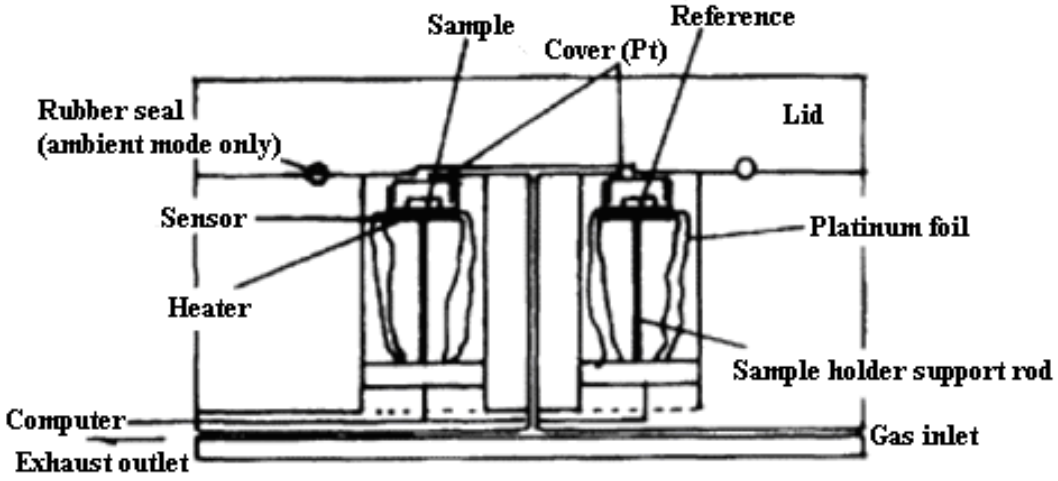

Figure 4.7(c): Schematic diagram of power compensation DSC system [25]

holders are individually equipped with a resistance sensor, which measures the temperature of the base of the holder, and a resistance heater. If a temperature difference is detected between the sample and reference, due to a phase change in the sample, energy is supplied until the temperature difference is less than a threshold value, typically less than 0.01 K. The energy input per unit time is recorded as a function of temperature or time. A simplified consideration of the thermal properties of this configuration shows that the energy input is proportional to the heat capacity of the sample. The maximum sensitivity of this instrument is 35 μW [25].

The temperature range of a power compensation DSC system is between 110 and 1000 K depending on the model of sample holder assembly chosen. Some units are only designed to operate above 290 K, whereas others can be used over the entire temperature range. The heater of a power compensation type DSC instrument is smaller than that of a quantitative DTA apparatus, so that the temperature response is quicker and higher

Figure 4.7(d): The Perkin-Elmer DSC7 thermal analyzer used in this study

scanning rates can be used. Instruments display scanning rates from 0.3 to 320 K/min on heating and cooling. The maximum reliable scanning rate is 60 K/min. Isothermal experiments, annealing (single- and multi-step) and heat capacity measurements can be

performed more readily using the power compensation-type instrument. Maintaining the instrument baseline linearity is a problem at high temperatures or in the sub-ambient mode. Moisture condensation on the sample holder must be avoided during sub-ambient operation.

In both DTA and compensation techniques, a plot is made as the temperature increases. Generally, the temperature program for the DSC analysis is designed such that the sample holder temperature increases linearly as a function of time. In this work, a compensation type (Perkin-Elmer DSC 7) differential scanning calorimeter, under flowing nitrogen, was employed for the DSC analyses. The system was interfaced to a computer, which was used for calculations by means of the Pyris Software. Calibration of the system was based on the onset temperatures of melting of indium and zinc standards, as well as the melting enthalpy of indium. Samples of masses ranging from seven to ten milligrams were sealed in aluminium pans and heated from 25 to 160 °C at a heating rate of 10 °C min^{-1}, and immediately cooled at the same rate to 25 °C. For the second scan, the samples were heated and cooled under the same conditions. Peak temperatures of melting and crystallization, as well as melting and crystallization enthalpies, were determined from the second scan. Three measurements, from which average temperature and enthalpy values were calculated, were performed on each sample.

4.6.2 Thermogravimetric analysis (TGA)

Thermogravimetric analysis is an analytical technique used to determine the thermal stability and the fraction of volatile components in a material by monitoring the weight change that occurs as a specimen is heated [26]. The measurement is normally carried out in air or in an inert atmosphere, such as helium or argon, and the weight is recorded as a function of increasing temperature. The measurement is occasionally performed in a lean oxygen atmosphere, of 1 to 5% O_2 in N_2 or He, to slow down oxidation. TGA instruments can be divided into two general types: vertical and horizontal balance. Vertical balance instruments generally have a single specimen pan hanging from the balance or located above the balance on a sample stem. Calibration of these

instruments is necessary in order to compensate for buoyancy effects due to the variation in the density of the purge gas with temperature, as well as the type of gas. Unlike vertical balance instruments, horizontal balance TGA instruments normally have two pans for the sample and reference, respectively, and can therefore also perform DTA and DSC measurements. They are considered free from buoyancy effects but require calibration to compensate for differential thermal expansion of balance arms.

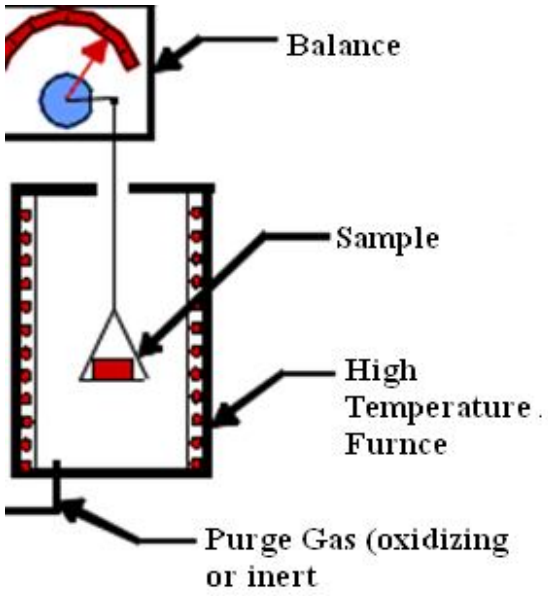

Figure 4.8(a): Schematic of a TGA furnace [18]

In the present work, the vertical type TGA instrument was used. The schematic diagram and photograph of the instrument used in this analysis are shown in Fig. 4.7. The instrument is a Perkin-Elmer TGA7 thermogravimetric analyzer. The samples, each having a mass between 6 and 10 mg were placed into a sample pan which is attached to a sensitive microbalance assembly, as shown in Fig. 4.7(a). The sample holder portion of the TGA balance assembly was subsequently placed into a high temperature furnace. The samples were subsequently heated from 25 to 600°C at a rate of 10°Cmin^{-1} in a flowing nitrogen atmosphere (flow rate 20 mL min^{-1}). The balance assembly measures the initial sample weight at room temperature and then continuously as the temperature increases. The samples lost weight as species decomposed or evaporated. These changes were

detected by the analytical balance from which the samples were suspended. The data were plotted with weight percent on the y-axis and temperature on the x-axis.

Figure 4.8(b): Image of the TGA apparatus used in this project

4.7 Synthesis techniques

4.7.1 Sol-gel

The sol-gel method is one of the traditional wet chemical techniques for producing metal oxide nanoparticles through chemical processes; hydrolysis, gelation, followed by drying, and finally thermal treatment [27,28]. In general, the sol is defined as colloidal particles suspended in a liquid solvent from which a gel can be formed. On the other hand, a gel is a three dimensionally interconnected rigid network, having submicrometre pores and a polymeric chain whose average length is of the order of microns. In sol-gel processing, metal alkoxides are used as a reactive metal precursor and hydrolyzed with water. By adding appropriate reagents, homogeneous gels from the mixture of alkoxides can be produced through the processes of hydrolysis and gelation. After gelation, the precipitate is subsequently washed, dried, and then sintered at an

elevated temperature to obtain crystalline metal oxide nanoparticles [27,29]. The advantages of the sol–gel method include easier composition control, better homogeneity and a lower reaction temperature which is better suited to synthesizing high purity, fine powders. In addition, the particle size of the final product can be easily controlled by changing the initial concentration of the starting sols and intermediate processing conditions such as gelation, drying, calcination, and rates of cooling. Although the sol-gel method can be used to produce nanophosphors or metal-oxide nanoparticles [30,31], this technique has some significant disadvantages. These include; (1) the requirement for the drying and annealing processes to be deliberately slow to avoid the formation of cracks and striations, (2) the difficulty in removing the residual hydroxyls, making it necessary to anneal the samples at high temperatures (above 1000°C), which may result in undesirable side effects.

4.7.2 Combustion synthesis

Rare-earth doped phosphors are mainly synthesized by the solid-state reaction method. This technique has several shortcomings such as prolonged reaction time, larger

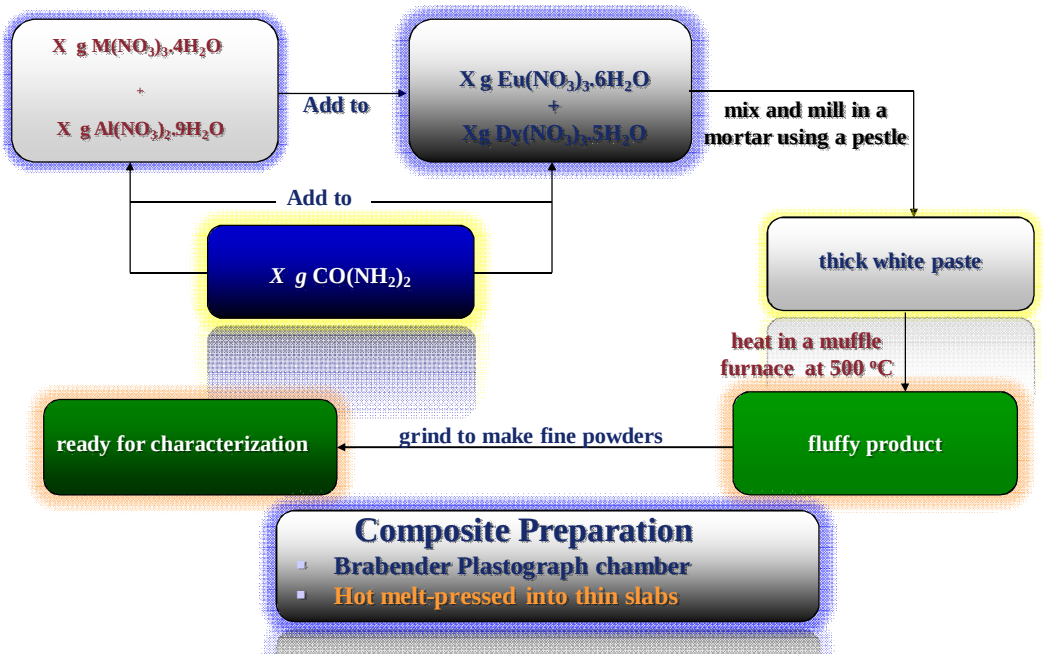

Figure 4.9: Sequence of events during combustion synthesis

grain growth, poor homogeneity, and it could be mitigated by alternate routes offered by wet-chemistry. Sol-gel methods have also been employed to synthesize nanophosphors by many researchers [30-33]. However, the as-prepared powders obtained from the sol-gel method have low crystallinity and often require post-treatment at high temperature, which results in severe agglomerations.

Combustion synthesis has emerged as an important technique for the synthesis and processing of various types of materials, which include nanomaterials [34]. It is based on the concept that once initiated locally by means of a thermal source of short-term service, highly exothermic reactions can become self-sustaining in the form of a combustion wave and yield the final product progressively without requiring additional heat. For any combustion reaction to take place, a fuel and an oxidizer are necessary. Different fuels may be used but they all serve two purposes [35]: (i) They are the source of C and H, which on combustion form CO_2 and H_2O and liberate heat. (ii) They form complexes with the metal ions, facilitating homogeneous mixing of the cations in solution. When the mixture of fuel and oxidizer is heated, the mixture grows into a frothy foam which may occupy the entire reaction vessel and then gets self-ignited followed by combustion. It is an exothermic reaction that occurs with evolution of heat. Once ignited the energy necessary for combustion reaction is then supplied from the reaction itself, hence it is referred to as self-propagating high temperature synthesis. The combustion method of preparing nanocrystalline materials, although it appears to be a breaking down (physicist's approach) process, is in fact, a building-up (chemist's approach) process as the product nuclei are formed initially and then grow [35].

Phosphors prepared by the combustion method have low density and appear fluffy. Ultra fine particles are produced through this process due to the evolution of gases. As more gases are released the agglomerates are either not formed or they are disintegrated into fine particles. Combustion synthesis processes are characterized by high-temperatures, fast heating rates, and short reaction times. These features make combustion synthesis an attractive method for the manufacture of technologically useful materials at lower costs compared to conventional ceramic processes. Some other

advantages of this method are; (a) use of relatively simple equipment, (b) formation of high-purity products, (c) stabilization of metastable phases and, (d) formation of products of virtually any size and shape.

The sequence of events in the combustion process used in this work is shown in Fig. 4.8.

4.8 References

1. García, M.F. Arias, A.M. Hanson, J.C. Rodriguez, *J. AChem. Rev.*, **104:** 4063, (2004).
2. Smith, D.J. *Rep. Prog. Phys.*, **60:** 1513, (1997).
3. E. Hao, G.C. Schatz, Hupp, J.T. *J. Fluoresc.*, **14**, 331, (2004.)
4. Wan, J.X. Wang, Z. Chen, X. Mu, L. Qian, Y. *Eur. J. Inorg. Chem.*, **20:**, 4031, (2005).
5. Zhang, H.Z. Banfield, J.F. *J. Phys. Chem. B.*, **104:** 3481, (2000).
6. Liu, J.Y. *J. Electr. Micros.*, **54:** 251, (2005).
7. Dinsmore, A.D. Hsu, D.S. Qadri, S.B. Cross, J.O. Kennedy, T.A. Gray, H.F. Ratna, B.R. *J. Appl. Phys.*, **88**(9)**:** 4985, (2000).
8. Tao, Y. Zhao, G. Ju, X. Shao, X. Zhang, W. Xia, S. *Mater. Lett.*, **28:** 137-140, (1996).
9. Wegh, R.T. Meijerink, A. Lamminmäki, R-J. Hölsä, J. *J. Lumin.*, **87–89:** 1002, (2000).
10. Kickelbick, G. *Hybrid Materials. Synthesis, Characterization, and Applications*. Kickelbick, G. (Ed.) Wiley-VCH Verlag GmbH & Co. KGaA, Weinheim, (2007).
11. Kalaitzidis, S. Christanis, K.*Int. J. Coal Geo.*, **54**(1-2)**:** 69, (2003).
12. Ebert, M. Inerle-Hof, M. Weinbruch, S. *Atmospheric Environment*, **36**(39-40)**:** 5909, (2002).
13. Goldstein, J.I. *Scanning Electron Microscopy and X-ray Microanalysis*. Plennum Press, New York, (1981).
14. Yacobi, B.G. Holt, D.B. Kazmerski, L.L. *Microanalysis of Solids*. New York, Plenum Press, (1994).
15. Cullity, B.D. Stock, S.R. *Elements of X-Ray Diffraction*. 3rd Edition, Prentice-Hall Inc. New Jersey. (2001)
16. Kuno, M. *Introduction to Nanosciene and Nanotechnology*: A Workbook. Notre Dame, (2005)

17. Kohler, M. Fritzsche, W. *Nanotechnology: An Introduction-Nanostructuring Techniques*. Wiley-VCH, (2003).
18. Giunta, P.R..*PhD Dissertation*. The Florida State University of Arts and Sci. (2005).
19. Yen, W. M. Shionoya, S. Yamamoto, H. *Measurement of Phosphor Properties*. CRC Press, Taylor & Francis Group, LLC, Chap. 1, (2007).
20. Gfroerer, T.H. *Encyclopedia of Analytical Chemistry*. R.A. Meyers (Ed.), John Wiley & Sons Ltd, Chichester, 9209, (2000).
21. Yoshioka, T. Ogawa, M. *Measurements of luminescence properties of phosphors.* CRC Press: New York, Chap. 14, (2007).
22. Danley, R.L. *Thermochimica Acta*., **395**(1-2)**:** 201, (2002).
23. Pabdn, C.V. Frutos, P. Lastres, J.L Frutos, G. *J. Pharm. and Biom. Anal.*, **15:**131, (1996).
24. Maria, G. Heinzle, E.*J. Loss Prev. Proc. Indus.*, **11:** 187, (1998).
25. Hatakeyama, T. Quinn, F.X. *Thermal Analysis: Fundamentals and Applications to Polymer Science.* ,John Wiley & Sons Ltd. Baffins Lane, Chichester, West Sussex PO19 IUD, England, Chap. 2, (1999)
26. Galíková, A. Pola, J. *Thermochimica Acta.*, **473**(1-2)**:** 54, (2008).
27. Yen, W.M. Weber, M.J. *Inorganic Phosphors*. CRC Press, Boca Raton, (2004).
28. Elliot, S. *The Physics and Chemistry of Solids.* John Willey and Sons, New York, (1998)
29. Gogotsi, Y. *Nanomaterials Handbook*. CRC Press, Boca Raton, (2006).
30. Fadlalla, H.M.H. Tang, C.C. Elssfah, E.M. Shi, F. *Mater. Chem. Phys.*, **109**(2-3)**:** 436, (2008).
31. Lin, C.C. Lin, K.M. Li, Y.Y.*J. Lumin.*, **126**(2)**:** 795, (2007).
32. Hsu, W.H. Sheng, M.H. Tsai, M.S. *J. Alloys Compd.*, **467:** 491, (2009).
33. Zhou, L. Yan, B. *J. Phys. Chem. Sol.*, **69:** 2877, (2008).
34. Patil, K.C. Aruna, S.T. Ekambaram, S. *Curr. Opin. Solid State Mater. Sci.*, **2:** 158, (1997).
35. Patil, K.C. Aruna, S.T. Mimani, T. *Curr. Opin. in Solid State and Mater. Sci.* **6:** 507, (2002)

Chapter 5

Properties of the Green Commercial $SrAl_2O_4:Eu^{2+},Dy^{3+}$ Phosphor in LDPE and PMMA Polymers

5.1. Introduction

The recognition of the size-dependence of the physical properties of materials has led to vigorous exploration of nanophase materials [1-4]. Nanophase materials are materials in the 1 to 100 nm range and exhibit greatly altered properties compared to their normal, large-grained counterparts with the same chemical composition. Phosphors constitute one of the categories of materials that show promising properties when synthesized in the nanophase. Strontium aluminate ($SrAl_2O_4$–Fig. 5.1) is a solid, odourless, nonflammable pale yellow powder. When activated with a suitable dopant,

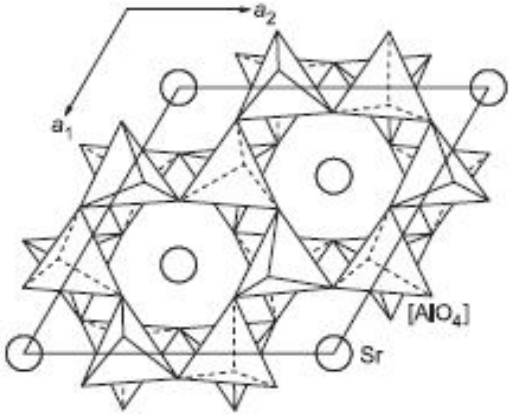

Figure 5.1: Crystal structure of $SrAl_2O_4$ at 1073 K, viewed along (001) [5]

e.g. europium or neodymium, it acts as a photoluminescent material with long persistence of phosphorescence. Europium-activated strontium aluminate is a vastly superior phosphor than its predecessor, copper-activated zinc sulphide; it is about 10 times brighter, 10 times longer glowing, but 10 times more expensive than ZnS:Cu. The material is very hard, causing abrasion to machinery handling it; coating the particles with a suitable lubricant is usually used when strontium aluminate is added to plastics.

These phosphors find a wide range of applications such as in defence, domestic, commercial as well as in the scientific domains. These include use in luminous paints, as safety indicators in emergency cases, and in display devices (e.g. field emission displays and toys). Green-emitting $SrAl_2O_4$ phosphors co-doped with europium (Eu) and dysprosium (Dy) have been focused on as high brightness and long afterglow characteristic materials.

Various mechanisms have been developed in an effort to explain the trapping and de-trapping mechanisms in these materials. A mechanism based on hole trapping created by Dy^{3+} ions co-doped into the host was developed on the long afterglow characteristics [2-5]. On the basis of some incompleteness in the prediction of certain experimental and theoretical phenomena, Clabau *et al.* [8] have more recently proposed a model of phosphorescence in terms of trapping of electrons only. Phosphor nano-composites can potentially be used to produce low-energy consumption and high efficiency illumination for long hours. Progress in each of these areas depends on the ability to selectively and controllably deposit nano-particles, and to uniformly disperse the phosphors in the host matrix, to create a strong and stable three dimensional network. Though rare-earth ion-doped alkaline earth aluminate phosphors have been extensively investigated [1,6,7], there is a lack of work done on phosphor hosts, particularly for outdoor applications, an area that finds increasing use for these materials. Exposure to moisture and other environmental factors have the potential to cause accelerated degradation in luminance.

This chapter deals with the mixing conditions, luminescence as well as thermal properties of the newly developed $SrAl_2O_4:Eu^{2+},Dy^{3+}$ phosphor introduced into two

polymer matrices, namely poly(methylmethacrylate) (PMMA) and low-density polyethylene (LDPE). The characterized properties are also discussed. The lower density of polymers, compared to metals and ceramics, as well as resistance to atmospheric and other forms of corrosion, render them more suitable for these applications.

5.2. Experimental

5.2.1 Materials

Commercially produced strontium aluminate powder from Phosphor Technology in the UK was used. It has a density of 3.67 gcm^{-3} and a melting point of 1200 ºC. PMMA has a melt flow index (MFI) of 0.8 g/10 min, a melting point of 135 ºC, and a density of 1.19 gcm^{-3}. LDPE has an MFI of 2.0 g/10 min, a melting point of 110 ºC, and a density of 0.922 gcm^{-3}. LDPE was supplied by Sasol Polymers, South Africa.

5.2.2 Sample preparation

The preparation of $SrAl_2O_4$:Eu phosphor has already been reported elsewhere [9,10]. Polymer-phosphor composites were produced by melt-mixing the green-emitting strontium aluminate phosphor into poly(methylmethacrylate) and low-density polyethylene, respectively at volume ratios ranging from 0.05% to 5% calculated from the equation,

$$M_f = V_c \rho_f \left[1 - \frac{1}{\left(V_f / V_m + 1 \right)} \right] \qquad (5.1)$$

where V_c = volume of the mixing chamber (50 cm^3), ρ_m = density of the matrix (polymer = 1.19 gcm^{-3}), and ρ_f = density of the filler (phosphor = 3.67 gcm^{-3}). Samples were weighed according to the required ratios and mixed using a volume of 50 cm^3 in a Brabender Plastograph mixing chamber at a speed of 30 rpm for 15 minutes. The mixing was carried out at 160 °C and 180 °C for PMMA and LDPE, respectively. The samples,

whose average thickness was 0.43 ± 0.08 mm, were extruded at 200 °C and 250 °C for PMMA and LDPE, respectively.

5.2.3 Morphology and structural analysis

The microstructure and elemental composition of the samples were investigated using a scanning electron microscope (SEM) (Shimadzu model ZU SSX–550 Superscan) coupled with an energy dispersive X-ray spectrometer (EDS). The as-prepared samples were directly cut into pieces of appropriate sizes. Prior to the SEM analyses and EDS measurements, the samples were gold-sputter-coated to facilitate electron conduction. The samples were then mounted on aluminium stubs with conductive double sticking tape. The tape is made of carbon material to facilitate the conduction of electrons and is double sticking in order to hold the sample on the one side and to stick on the sample holder stubs on the other. The morphology and particle size of the composites were observed by transmission electron microscopy (TEM). TEM images were recorded on a JEOL-JEM 200CX transmission electron microscope. To study the crystalline/amorphous structures of the products, XRD measurements were carried out at room temperature. XRD scans of the samples were performed with a Bruker AXS Discover diffractometer with CuK_{α} radiation of wavelength 1.5406 Å.

5.2.4 Photoluminescence measurements

PL measurements were made on a Carry Eclipse fluorescence spectrophotometer system, equipped with a 150 W xenon lamp as the excitation source. Samples were excited at 350 nm and emission observed in the wavelength range 400 to 600 nm at room temperature.

5.2.5 Thermal analysis

A Perkin-Elmer DSC 7 differential scanning calorimeter, under flowing nitrogen, was employed for the DSC analyses. The system was interfaced to a computer, which was used for calculations by means of the Pyris software. Calibration of the system was

based on the onset temperatures of melting of indium and zinc standards, as well as the melting enthalpy of indium. Samples of masses ranging from seven to ten milligrams were sealed in aluminium pans and heated from 25 to 160 °C at a heating rate of 10 °C min^{-1}, and immediately cooled at the same rate to 25 °C. For the second scan, the samples were heated and cooled under the same conditions. Peak temperatures of melting and crystallization, as well as melting and crystallization enthalpies, were determined from the second scan. Thermogravimetric analyses (TGA) were performed in a Perkin-Elmer TGA7 thermogravimetric analyzer in a flowing nitrogen atmosphere (flow rate 20 mL min^{-1}). The samples, each having a mass between 6 and 10 mg, were heated from 25 to 600 °C at a rate of 10 °Cmin^{-1}. For both DSC and TGA analyses three measurements were performed on each sample composition, from which average temperature and enthalpy values were calculated.

5.3. Results and discussion

Fig. 5.2 shows the SEM micrographs of the polymer composites. Two types of morphology can be observed. The first consists of large and small particles (lumps) superimposed on an otherwise smooth surface (Fig. 5.2a). Most probably, these lumps are non-dispersed phosphor particles. However, EDS point analysis confirmed the distribution of phosphor particles throughout the whole polymer surface for the different

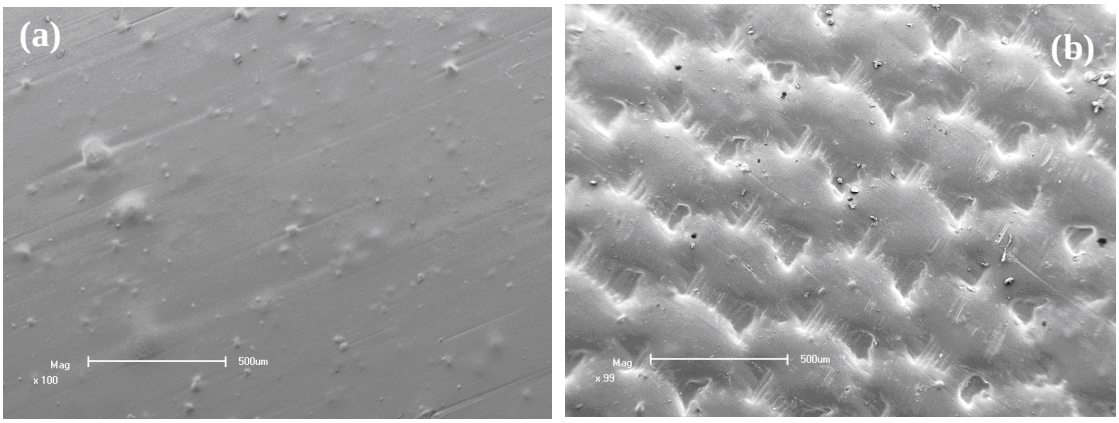

Figure 5.2: SEM images of (a) 97/3 v/v LDPE/$SrAl_2O_4$:Eu^{2+},Dy^{3+} [100× magnification], (b) 97/3 v/v PMMA/ $SrAl_2O_4$:Eu^{2+},Dy^{3+} [100× magnification]

concentrations. The second type of morphology observed consists of leaflet-like structures (Fig. 5.2b). Based on available results, these patterns are most probably the result of the mechanical sample manufacturing process. The EDS results, shown in Fig. 5.3, show the presence of the expected elements, i.e., strontium, aluminium, oxygen and carbon. On the basis of several spot analyses results on the samples, it was found that for each of the respective phosphor concentrations the distribution of the elements, strontium, aluminium, and oxygen, in the polymer matrices was fairly uniform.

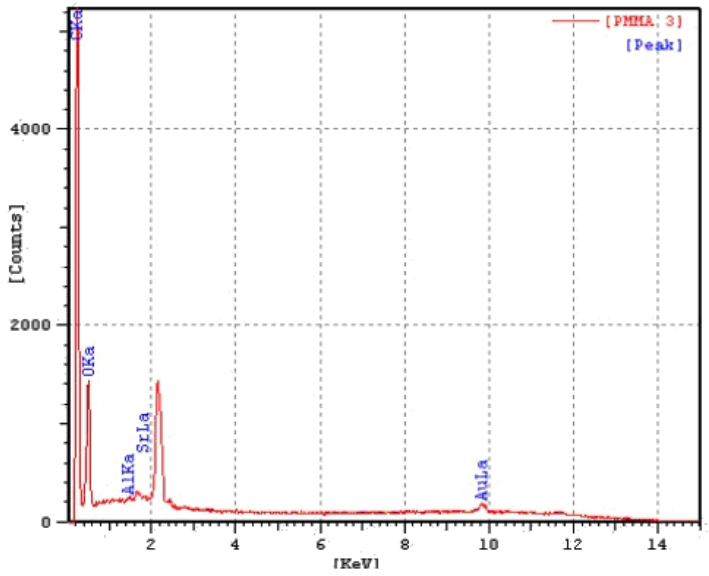

Figure 5.3: Point EDS results of 97/3 v/v LDPE/$SrAl_2O_4$:Eu^{2+},Dy^{3+}

Typical XRD patterns recorded for the composites of LDPE and PMMA, as well as the $SrAl_2O_4$:$Eu^{2+}Dy^{3+}$ powder, are displayed in Fig. 5.4. The $SrAl_2O_4$ crystal is characterized by planes having diffraction peaks of (011), (020), (-211), (220), (211), (031), and (400). The measurements displayed here have visible peaks at 20°, 30°, and 35°, corresponding to the planes (020), (220) and (031). The peaks indicate the presence of $SrAl_2O_4$. The absence of the other expected phosphor peaks in the XRD spectra may be due to the low concentration of the phosphor in the polymer matrix. It is observed that as the phosphor concentration in LDPE increases, there are no changes in either the peak

positions, sizes, or shapes. These results indicate that the introduction of the phosphor did not significantly change the general structure of the polymer. Crystallite sizes calculated from Scherrer's equation have a wide range, but in the nanometre range, averaging 70 ± 23 nm.

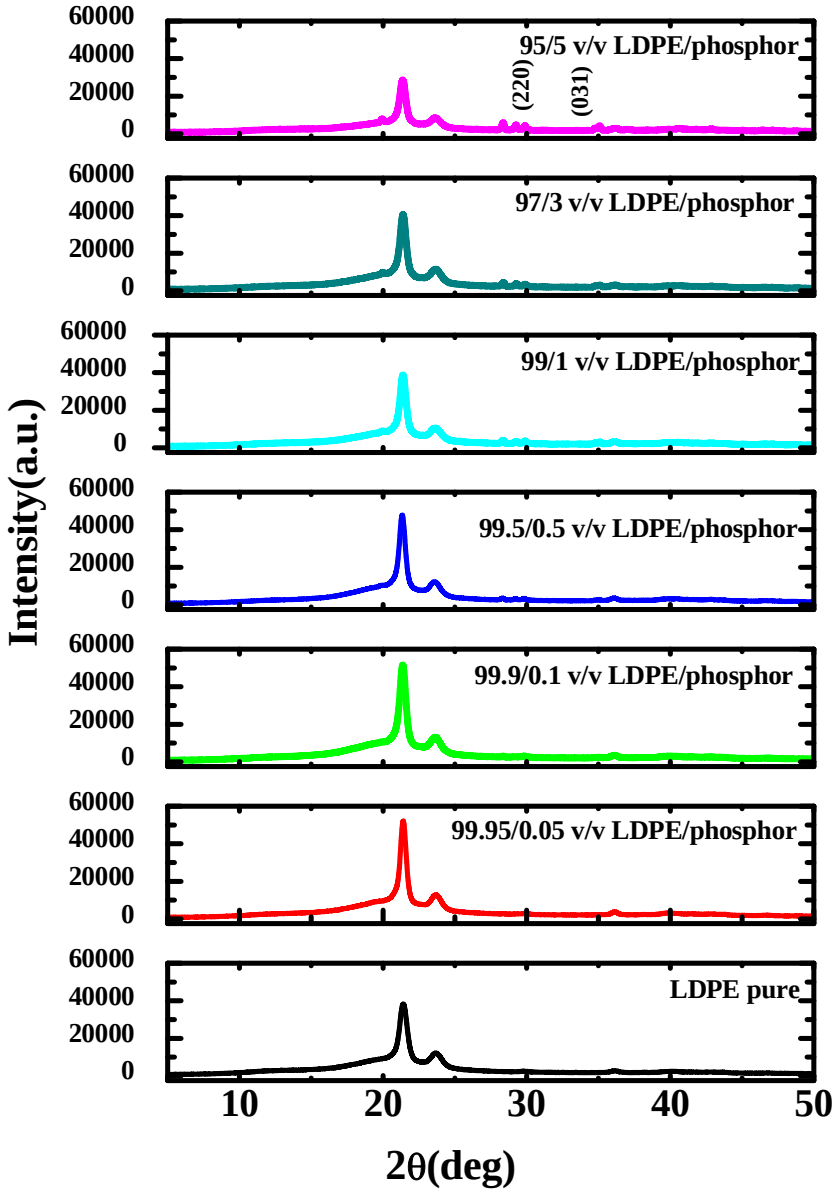

Figure 5.4(a): XRD spectra of LDPE and LDPE/$SrAl_2O_4$:$Eu^{2+}Dy^{3+}$

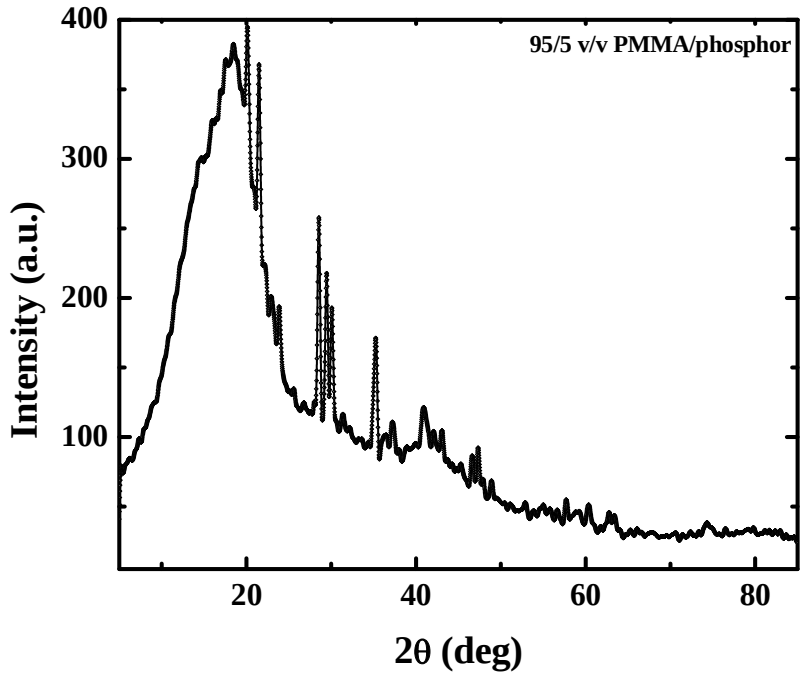

Figure 5.4(b): XRD spectra of PMMA/$SrAl_2O_4$:$Eu^{2+}Dy^{3+}$

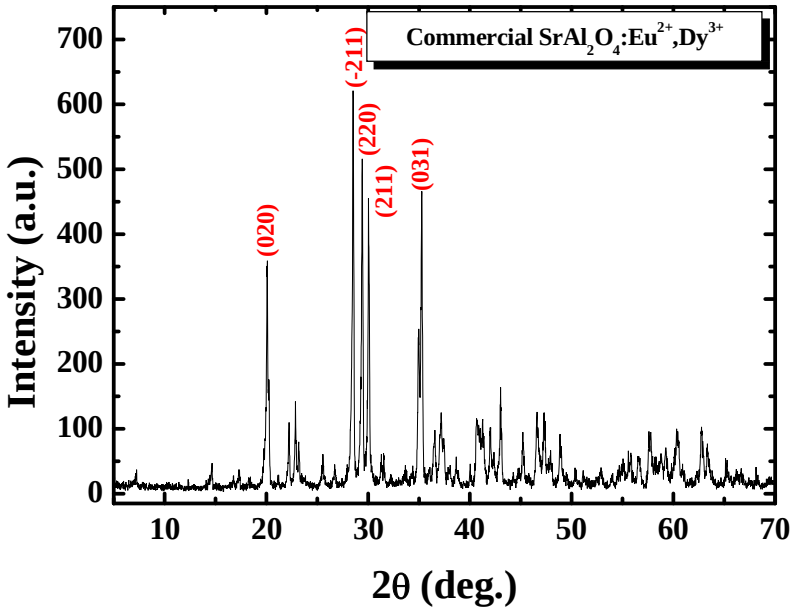

Figure 5.4(c): XRD spectrum of the green-emitting $SrAl_2O_4$:$Eu^{2+}Dy^{3+}$

Fig. 5.5 shows the TEM micrographs of the composites containing 5% phosphor in LDPE and PMMA.. The image shows the basic morphology of the phosphor particles and their distribution at the low phosphor concentration. The particles are fairly monodisperse in size and isotropic in shape.

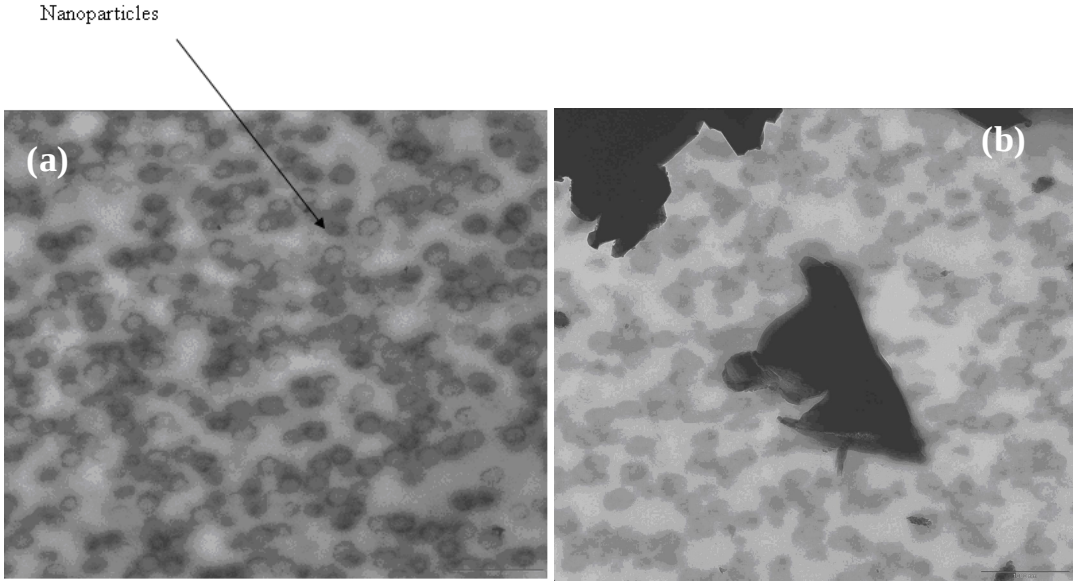

Figure 5.5: TEM micrographs of 5% $SrAl_2O_4:Eu^{2+},Dy^{3+}$ in (a) LDPE (b) PMMA

The LDPE composites with a phosphor concentration greater than 0.5% and PMMA composites with a concentration greater than 1.0% show an intense green emission, as seen in Fig. 5.6. The PL spectrum corresponding to each concentration is composed of a broad PL band peaking near 510 nm. This green photoluminescence has been attributed to the $4f^6 5d^1 \rightarrow 4f^7$ electronic transition of the divalent europium ion (Eu^{2+}) in the $SrAl_2O_4:Eu^{2+}$ bulk phosphors, as reported earlier [2,3]. The PL peaks for LDPE shift to higher wavelengths with increasing phosphor concentration. Higher phosphor concentration favours the excitation of the green luminescence wavelength (520 nm) which is attributed to the Eu^{2+} emission centre.

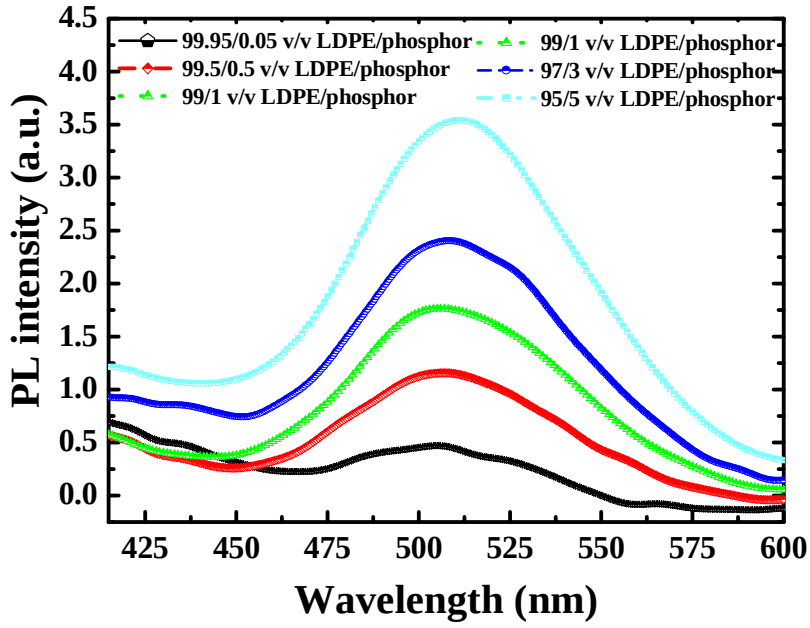

Figure 5.6(a): PL spectra for LDPE/$SrAl_2O_4$:Eu^{2+},Dy^{3+}composites

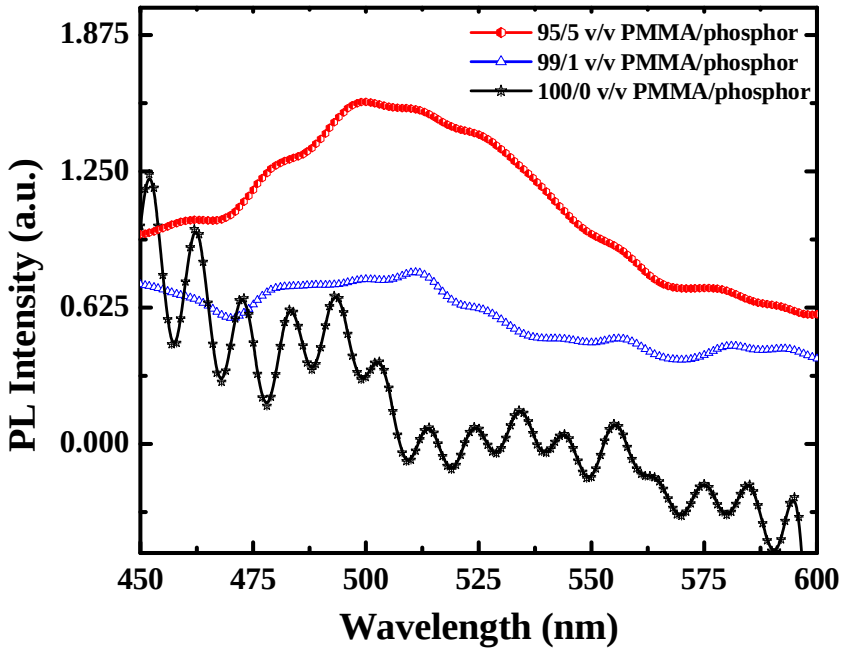

Figure 5.6(b): PL spectra for PMMA/$SrAl_2O_4$:Eu^{2+},Dy^{3+}composites

Fig. 5.7 correlates the photoluminescence intensity with the phosphor concentration. The superiority in luminescence displayed by LDPE is probably a consequence of a polaronic effect in which phosphor particles may be responsible for an

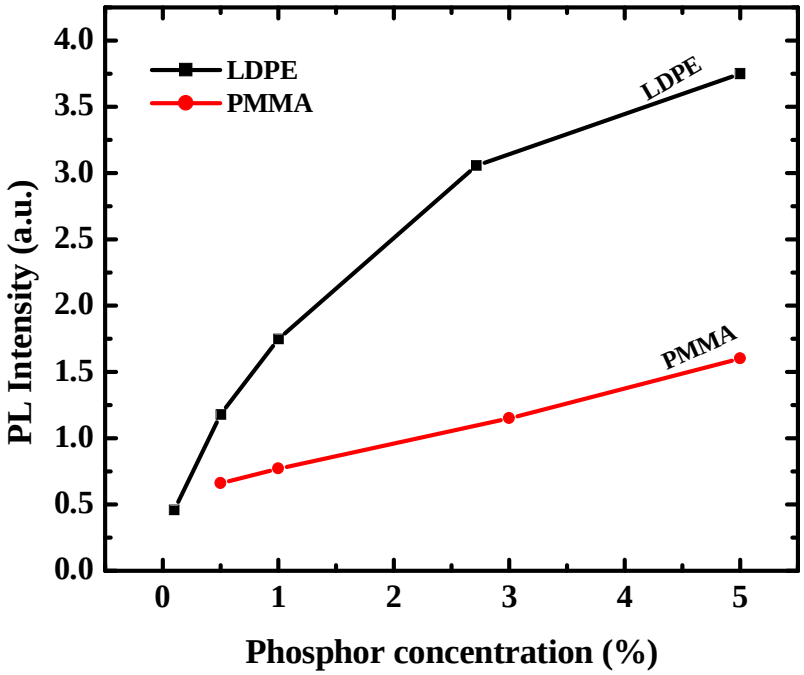

Figure 5.7: Concentration-dependence of the PL emission peaks of the LDPE- and PMMA/$SrAl_2O_4$: Eu^{2+},Dy^{3+} composites

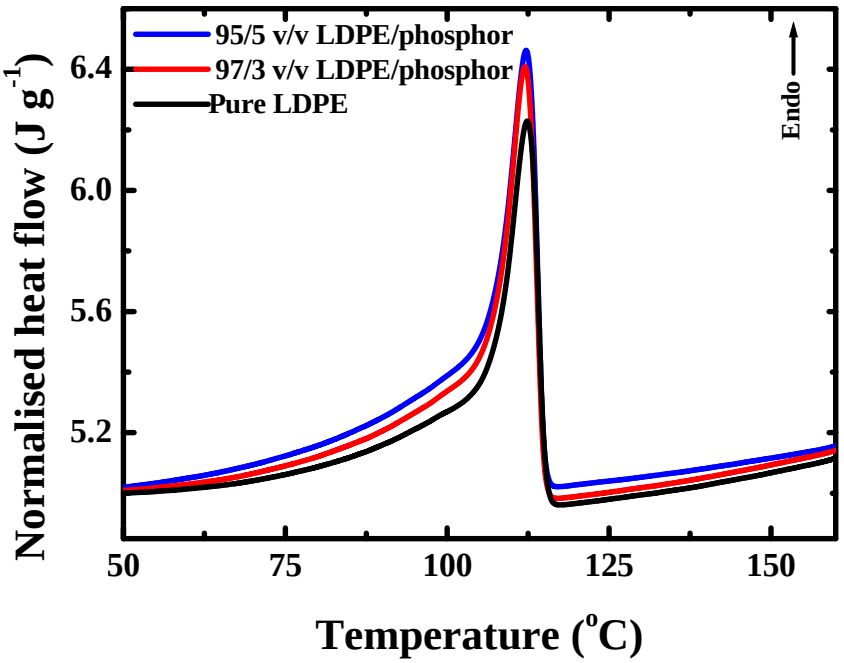

Figure 5.8(a): DSC heating curves of LDPE and LDPE/$SrAl_2O_4$:Eu^{2+},Dy^{3+}

alteration in the polymer bond geometry, giving rise to the creation of an “excited state” (polaron), which on being relaxed may lead to the energy being emitted radiatively. The transparency and resistance of the polymer matrix for UV radiation are also possible contributing factors.

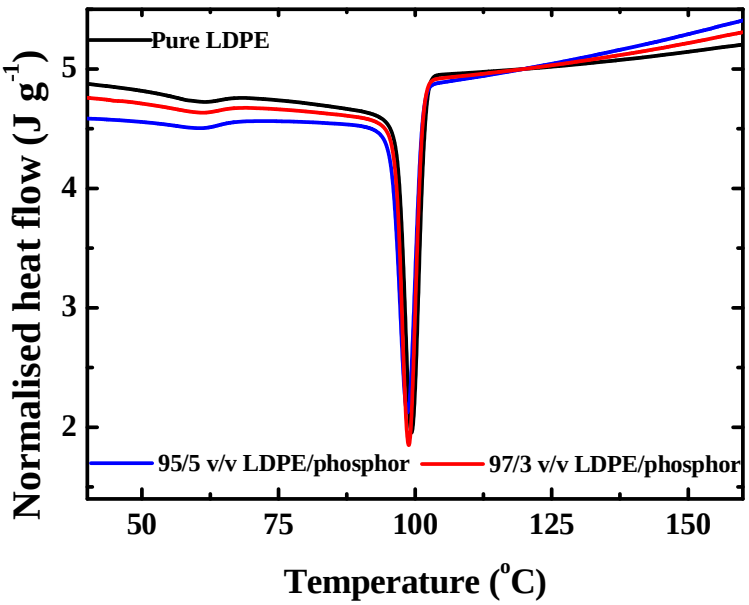

Figure 5.8(b): DSC cooling curves of LDPE and LDPE/$SrAl_2O_4$:Eu^{2+},Dy^{3+}

The DSC curves for LDPE and its composites are shown in Fig. 5.8. The average values of the peak temperatures of melting, as well as the melting and crystallization enthalpy values, are summarized in Table 1. The heating curves in Fig. 5.8(a) show endothermic peaks at about 112 °C, with no significant peak shifts, suggesting that the phosphor content did not have an appreciable effect on the melting temperature of LDPE. The comparison between the observed and expected enthalpies (calculated taking into account the weight fraction of LDPE in the samples, and assuming that the LDPE crystallization mechanism does not change in the presence of the phosphor particles) shows lower than expected enthalpies for the composites at low phosphor contents, but at higher phosphor concentrations the experimentally observed enthalpies are higher. This behaviour may be explained by the fact that the particles are not agglomerated at low contents, and therefore there are large interfacial areas between the nano-particles and the

Table 5.1: DSC data of LDPE and LDPE/$SrAl_2O_4$:Eu^{2+},Dy^{3+}

ΔH_m and ΔH_c - melting and crystallization enthalpies; T_m and T_c - peak temperatures of melting and crystallization

Vol.% phosphor	T_m / °C	ΔH_m^{obs} / J g^{-1}	ΔH_m^{cal} /J g^{-1}	T_c / °C	ΔH_m^{obs} / J g^{-1}	ΔH_c^{cal} / J g^{-1}
0.00	112.5 ± 0.3	80.7 ± 6.4	-	99.1 ± 0.1	-61.8 ± 4.5	-
0.05	112.5 ± 0.4	62.7 ± 2.0	80.5	99.2 ± 0.1	-52.9 ± 2.2	-61.7
0.10	112.3 ± 0.3	76. 6 ± 2.1	80.4	99.2 ± 0.4	-56.7 ± 2.7	-61.6
0.50	112.1 ± 0.0	72.2 ± 6.0	79.2	98.8 ± 0.0	-55.1 ± 6.7	-60.6
1.00	112.4 ± 0.2	70.6 ± 0.3	77.6	98.7 ± 0.1	-58.8 ± 3.5	-59.3
3.00	112.2 ± 0.6	75.5 ± 0.2	72.1	98.7 ± 0.2	-58.7 ± 6.4	-55.0
5.00	112.3 ± 0.3	75.9 ± 0.3	67.4	98.7 ± 0.9	-54.2 ± 4.3	-51.3

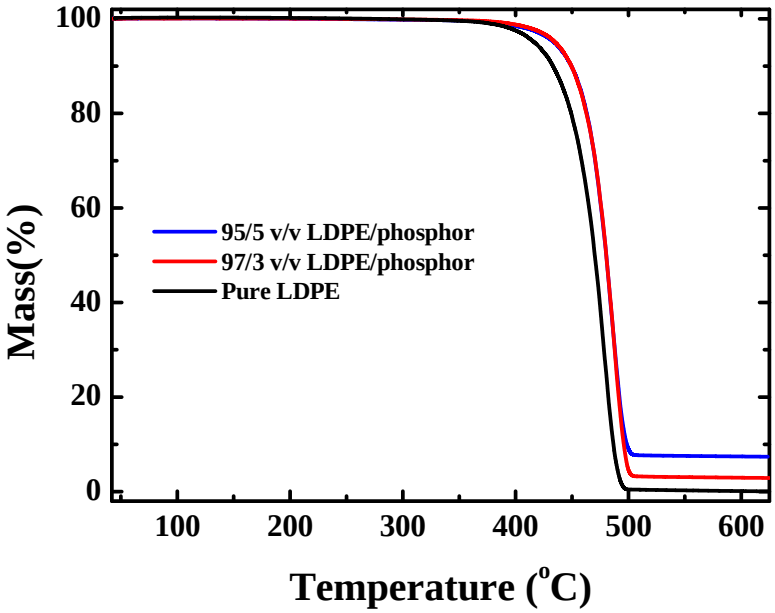

Figure 5.9: TGA curves for LDPE and LDPE/$SrAl_2O_4$:Eu^{2+},Dy^{3+}

polymer. This will result in immobilization of the polymer chains and accompanying decrease in crystallinity. At high phosphor contents there is particle agglomeration which probably gives rise to epitaxial crystallization of LDPE on the phosphor surfaces.

The TGA results (Fig. 5.9) show that the composites start decomposing at higher temperatures than pure LDPE. The main degradation for the pure polymer starts at about 380 °C and leaves a residue at 496 °C, while the corresponding values for the composites are 402 °C and 501 °C respectively. This indicates that the phosphor particles increased the thermal stability of the polymer. Considering values of the weight loss over the two temperature ranges, i.e. 380 °C to 496 °C and 402 °C and 501 °C, LDPE degrades over a wider temperature change (116 °C) compared to the composites (99 °C). Hence, the rates of degradation for the composites are higher than that of pure LDPE. The residual mass corresponds to the amount of phosphor initially mixed with the polymer. An observation similar to this, made for LDPE-copper composites [11], was attributed to the relatively higher heat capacity and thermal conductivity values of copper, which caused it to preferentially absorb the heat. In view of the higher values of the heat capacities and thermal conductivities for ceramics, the increased stability in the LDPE-phosphor composites may similarly be explained. However, extended heat absorption by the phosphor particles, may cause these particles to reach a higher temperature than the surrounding matrix resulting in a more rapid degradation of the polymer. Alternatively, the phosphor particles may temporarily trap the volatile degradation products, which will escape at a faster rate as soon as they acquire enough energy at higher temperatures.

5.4. Conclusions

This study has provided some insight into the ability to controllably mix nano- to micro-sized phosphor particles into, and to uniformly disperse them in both semi-crystalline and amorphous polymer matrices. To elucidate this information, the morphology, photoluminescence, and thermal properties of the polymer composites were investigated. SEM micrographs and EDS spectra showed generally smooth morphologies and a fairly uniform distribution of phosphor particles in the polymer matrices. XRD

peaks for the composites of the polymers are similar to those of the pure polymers, manifesting a close resemblance in the configurations of the pure polymers and their phosphor composites. TEM micrographs reveal monodispersed, nanosized phosphor particles. A characteristic green emission peak at about 505 nm wavelength was exhibited by the composites. Peak intensities of the PL emission spectra monotonously increased with an increase in phosphor concentration. The higher intensity values in LDPE are probably due to a polaronic effect. The DSC results for LDPE do not show a major influence of the phosphor content on either the melting temperature or enthalpy of the polymer. These results demonstrate that LDPE can be employed to create a suitable three-dimensional phosphor network for practical luminescence applications.

5.5 References

1. Murayama, Y. Takeuchi, N. Aoki, Y. Matsuzawa, T. *Phosphorescent Phosphor*. US Patent, **006:** 5, 424, (1995).
2. Matsuzawa, T. Aoki, Y. Takeuchi, N. Murayama, Y. *J. Electrochem. Soc.,* **143:** 2670, (1996).
3. Katsumata, T. Sakai, R. Komuro, V. Morikawa, T. *J. Electrochem. Soc*., **150:** H111, (2003).
4. Qiu, J. Gaeta, V. Hirao, V. *Chem. Phys. Lett.,* **333:** 236, (2001)
5. Fukuda, K. Fukushima, K.*J. Solid State Chem*., **178**: 2709, (2005).
6. Katsumata, T. Sakai, R. Komuro, S. Morikawa, T. Kimura, H. *J. Cryst. Growth*., **198/199:** 869, (1999).
7. Shionoya, S. Yen, W.M. (Eds.) *Phosphor Handbook*. CRC Press, Boca Raton, FL, USA, 651, (1999).
8. Nakamura, T. Kaiya, K. Takahashi, N. Matsuzawa, T. Rowlands, C.C. Beltran-Lopez, V. Smith, G.M. Riedi, P.C. *J. Mater. Chem.,* **10:** 2566, (2000).
9. Clabau, F. Rocquefelte, X. Jobic, S. Deniard, P. Whangbo, M.H. Garcia, A. Mercier, T.L. *Chem. Mater.*, **17:** 3904, (2005).
10. Tsutai, H. Shimizu, I. Kawakami, T. Shinbo, K. Kato, K. Kaneko, Ohta, F. M. *Tech. Rep. of IEICE CPM.,* **13:** 95, (1995).
11. Tsutai, T. Kamimura, I. Kato, K. Kaneko, F. Shinbo, K. Ohta, M. Kawakami, T. *Tech. Rep. of IEICE CPM.*, **55:** 97, (1997).
12. Luyt, A.S. Molefi J.A. Krump, H. *Polym. Degrad. Stab.*, **91:** 1629, (2006).

Chapter 6

Structural, Luminescent, and Thermal Properties of Blue $Sr_4Al_{14}O_{25}:Eu^{2+},Dy^{3+}$ Phosphor-Filled Low Density Polyethylene Composites

6.1 Introduction

Strontium aluminate phosphors activated by europium and dysprosium have attracted much attention because of their excellent properties [1-3]. Compared with classical sulfide phosphorescent materials, aluminates have several valuable properties [4-6]; high radiation intensity, colour purity, longer afterglow, chemically stable, safe and require no additional radiation from a radioactive source. The origin of the extremely long persistent luminescence has tentatively been attributed to alkaline earth metal vacancies [7].

One of the undesirable consequenses of producing nano-sized phosphors is the degradation resulting from accelerated rates of reaction with environmental factors such as water, oxygen, and CO_2. Consequently, in technological applications, protecting nanomaterials from degradation becomes one of the important considerations.

Passivating the surfaces of nanoparticles can be accomplished using chemical reactions to coat or disperse the particles in a polymer or glass matrix [8].

The purpose of the work done in this chapter was to investigate the mixing conditions, structural, luminescence as well as thermal properties of the $Sr_4Al_{14}O_{25}:Eu^{2+},Dy^{3+}$ phosphor introduced into a low-density polyethylene (LDPE) matrix. The properties are characterized for the purpose of elucidating information for identifying suitable materials for hybridization with phosphors to minimize their degradation rates while sustaining their luminance in practical applications.

6.2 Materials and methods

6.2.1 Materials

Commercially produced strontium aluminate powder from Phosphor Technology in the UK was used. It has a density of 3.67 gcm^{-3} and a melting point of 1200ºC. The average crystallite size of the powder, as determined from the Scherrer equation, is 48 ± 16 nm. LDPE has a melt flow index (MFI) of 2.0 g/10 min, which was determined by preheating a sample of the polymer at 190 ^{o}C for 5 minutes followed by a shear analysis on a 2.16 kg mass. It has a melting point of 110 ºC, and a density of 0.922 gcm^{-3}. The polymer was supplied by Sasol Polymers, South Africa.

6.2.2 Sample preparation

The phosphor was prepared by a conventional high temperature processing method [9]. Polymer/phosphor composites were produced by melt-mixing the blue-emitting strontium aluminate phosphor into low-density polyethylene at volume ratios ranging from 1% to 5%. Samples were weighed according to the required ratios and mixed using a volume of 50 cm^3 in a Brabender Plastograph mixing chamber at a speed of 30 rpm for 15 minutes. The mixing was carried out at 160°C. The samples were hot

melt-pressed into slabs of average thickness 0.98 ± 0.05 mm, at 160°C. This technique is different from the previous one (chapter 5) and was preffered due to its simplicity.

6.2.3 Morphology and structural analysis

To study the structure of the samples, XRD scans were performed at room temperature with a Bruker AXS Discover diffractometer with CuK_{α} radiation of wavelength 1.5406 Å.

6.2.4 Photoluminescence (PL) measurements

The phosphorescence spectra were measured on a SPEX 1870 0.5m spectrometer system, equipped with a He–Cd laser lamp as the excitation source. Samples were excited at 325 nm and emission observed in the wavelength range 350 to 700 nm at room temperature. The He–Cd laser is considered to excite the electrons to the 5d states of Eu^{2+} ions because the wavelength (325 nm) is close to the peak wavelength of a broadband absorption from 250 to 420 nm seen in the excitation spectra from $Sr_4Al_{14}O_{25}:Eu^{2+},Dy^{3+}$ crystals. The excitation energy of the He–Cd laser is thought to be smaller than the band gap energy of the specimen [10].

6.2.5 Thermal analysis

A Perkin-Elmer DSC7 differential scanning calorimeter, under flowing nitrogen (20 mL min^{-1}), was employed for the DSC analyses. The calculations were done by means of Pyris software. Samples of masses ranging from 7 to 10 mg were sealed in aluminium pans and heated from 25 to 160 °C at a heating rate of 10 °C min^{-1}, and immediately cooled at the same rate to 25 °C. For the second scan, the samples were heated and cooled under the same conditions. Peak temperatures of melting and crystallization, as well as melting and crystallization enthalpies, were determined from the second scan. Thermogravimetric analyses (TGA) were performed in a Perkin-Elmer TGA7 thermogravimetric analyzer in a flowing nitrogen atmosphere (20 mL min^{-1}). The

samples, each having a mass between 6 and 10 mg, were heated from 25 °C to 600 °C at a rate of 10 °C min^{-1}. For both DSC and TGA analyses three measurements were performed on each sample composition, from which average temperature and enthalpy values were calculated.

6.3 Results and discussion

6.3.1 X-ray diffraction (XRD)

The peaks of the (020), (-211), (220), (211), and (031) planes that characterize the $Sr_4Al_{14}O_{25}:Eu^{2+},Dy^{3+}$ crystal (JCPDS data No. 34-0379) [3] can be observed in Fig. 6.1 for LDPE. This indicates that LDPE is a suitable host for the phosphor. No other products are observed, implying that the $Sr_4Al_{14}O_{25}$ phase composition of the phosphor [11] is well preserved within the polymer.

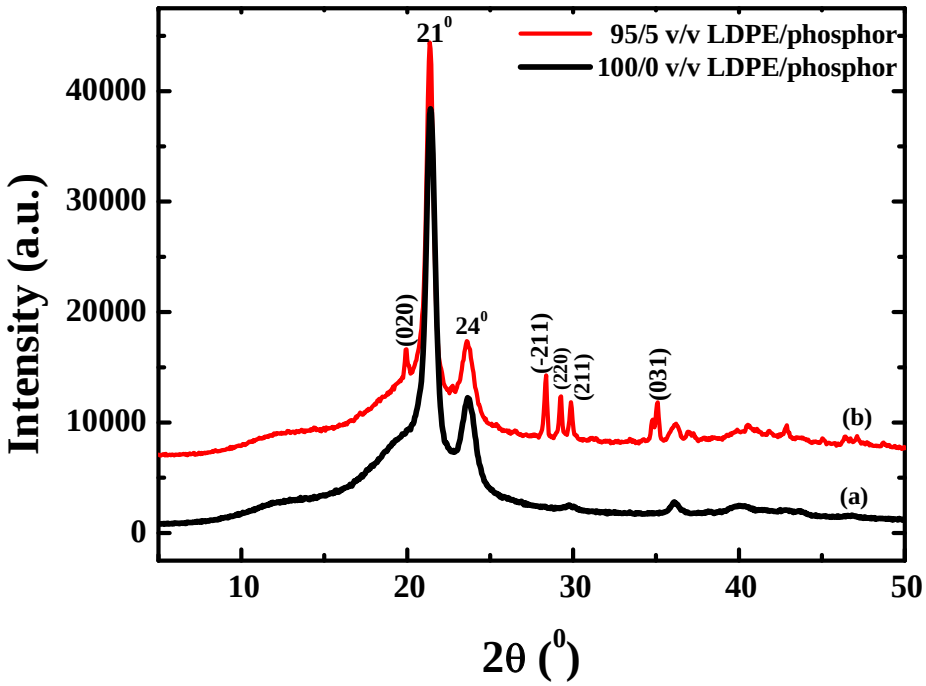

Figure 6.1: XRD spectra of (a) LDPE and (b) the composite sample with 5% $Sr_4Al_{14}O_{14}: Eu^{2+},Dy^{3+}$

6.3.2 Photoluminescence spectra

Phosphors based on aluminate hosts, e.g. $SrAl_2O_4:Eu^{2+}Dy^{3+}$, are among the most researched long-lasting phosphors that have been found to be the most efficient [7]. Hence, one of the phases, $Sr_4Al_{14}O_{25}:Eu^{2+},Dy^{3+}$, was chosen for this investigation. Fig. 6.2 shows the PL spectra for LDPE with its composites. The spectra have major broad PL bands peaking at about 485 nm and minor peaks at about 412 nm attributed to the 4f–5d transition of Eu^{2+} [12]. Though variations in the peak positions of both the prominent and minor peaks are observed, the shifts are only slight and may not be attributable to any significant change(s) in the composite properties. Fig. 6.3, which correlates the photoluminescence intensity of the composites with the phosphor concentration shows a fairly direct proportional relation.

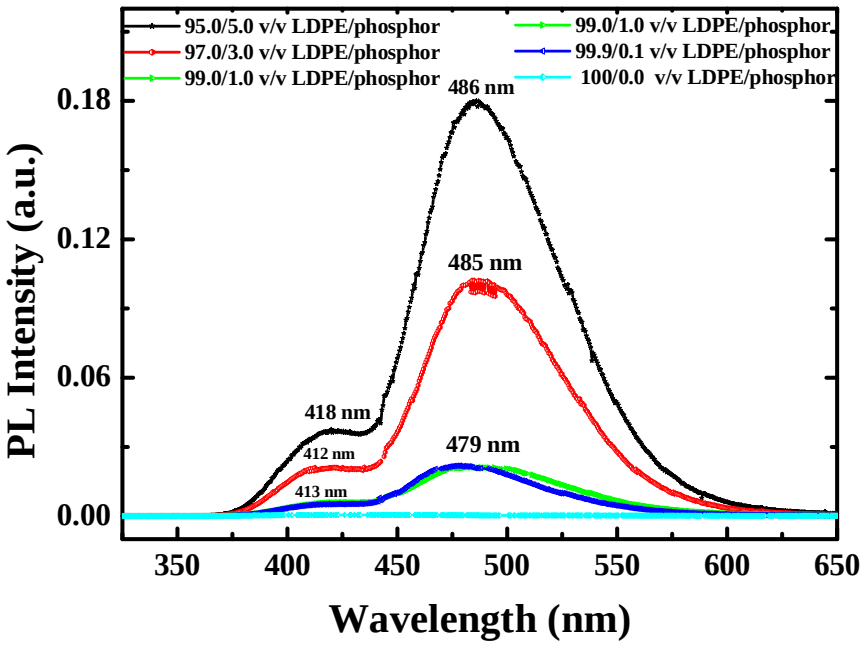

Figure 6.2(a): PL spectra for LDPE and LDPE/$Sr_4Al_{14}O_{14}:Eu^{2+},Dy^{3+}$

The phenomenon of persistent luminescence is based on the use of lattice defects for storing excitation energy and deals with very complicated mechanisms. Some of the mechanisms, which have been published, involve either a direct or valence band assisted

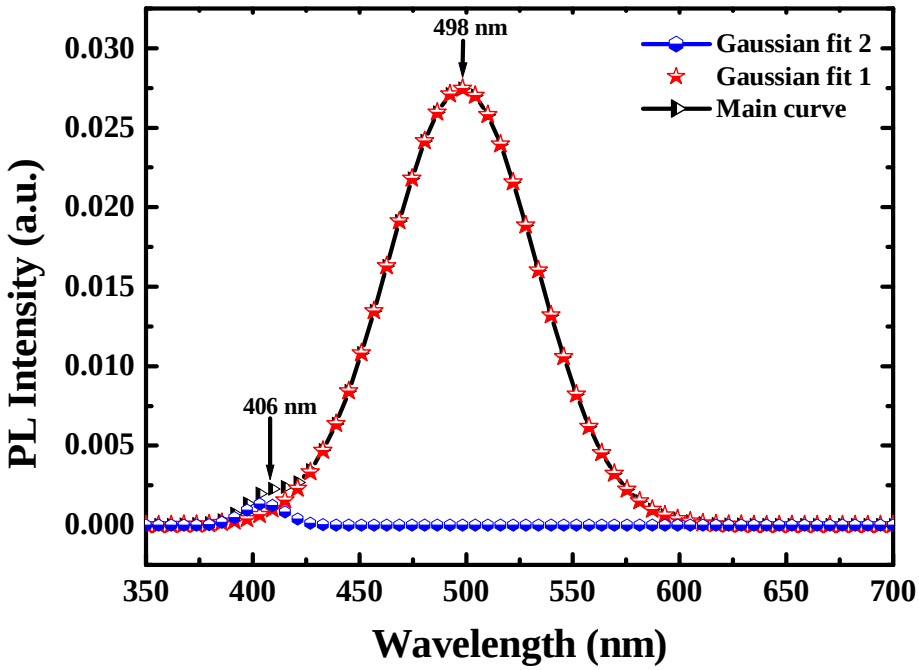

Figure 6.2(b): Deconvolution of the PL spectrum of the 99.0/1.0 v/v LDPE/$Sr_4Al_{14}O_{14}$: Eu^{2+},Dy^{3+} composite

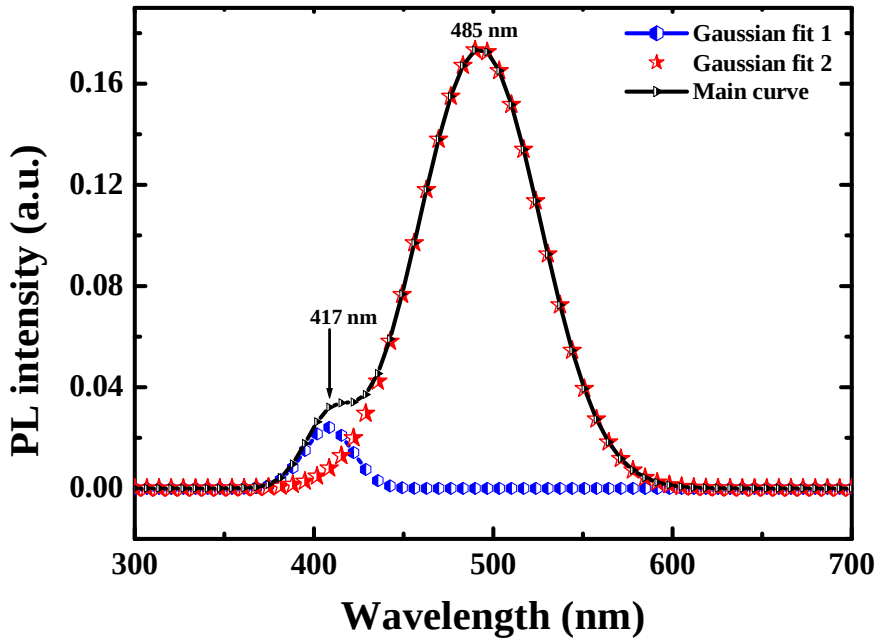

Figure 6.2(c): Deconvolution of the PL spectrum of the 95.0/5.0 v/v LDPE/$Sr_4Al_{14}O_{14}$: Eu^{2+},Dy^{3+} composite

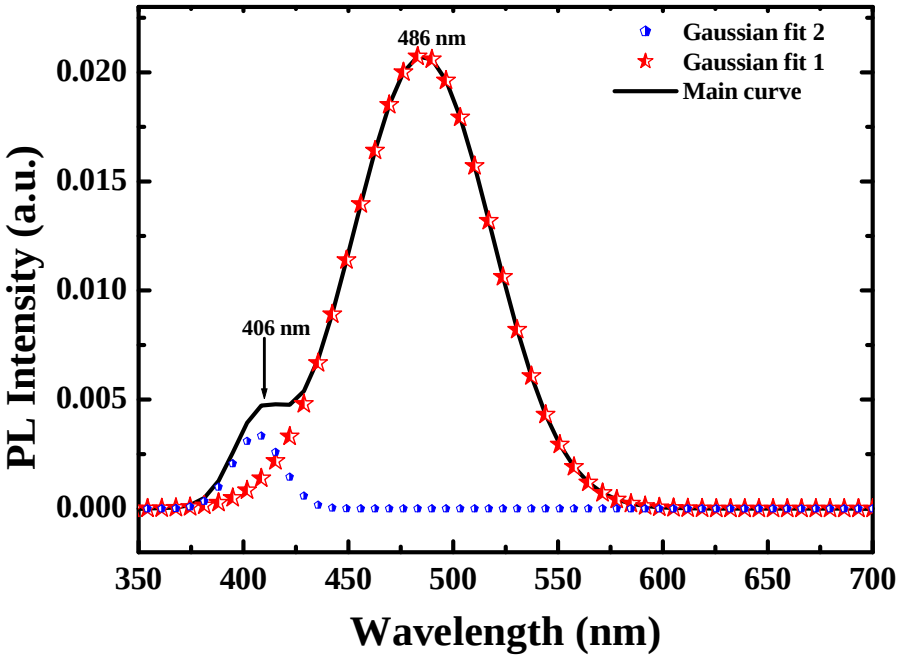

Figure 6.2(d): Deconvolution of the PL spectrum of 97.0/3.0 v/v LDPE/$Sr_4Al_{14}O_{14}$: Eu^{2+},Dy^{3+} composite

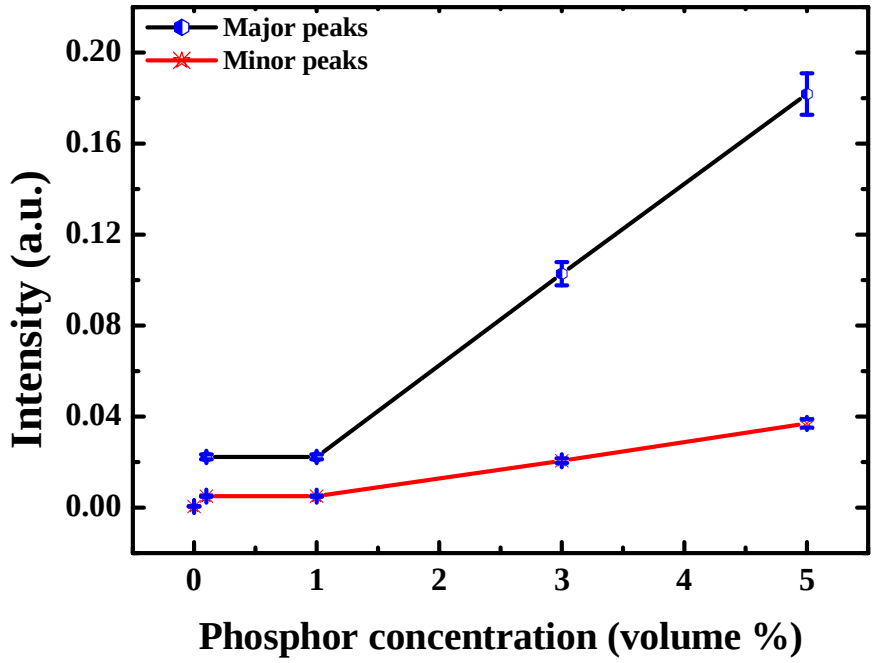

Figure 6.3: Concentration-dependence of the luminescence of LDPE/$Sr_4Al_{14}O_{14}$: Eu^{2+},Dy^{3+}

transfer of a hole from Eu^{2+} to a trap and its eventual recombination with the emitting Eu^{2+} centre after thermal excitation [13]. Lin et al. [14] reported two emissions from $Sr_4Al_{14}O_{25}$ and associated them with the two crystallographic sites occupied by Eu^{2+} in the host lattice. A model on similar lines for explaining the occurrence of the two emissions has been proposed by Clabau *et al.* [15]. However, on account of the chemical indistinguishability of the two sites as well as their similarity in abundance, their attribution of the two emissions to Eu^{2+} occupying the two Sr^{2+} sites has solicited a quest for more insight in the model by Ngaruiya *et al.* [16], who postulate the preferential alignment of one of the 5d-orbitals of the Eu^{2+} ion to modify the Clabau model.

6.3.3 Thermal properties

The DSC heating and cooling curves for the investigated samples are shown in Fig. 6.4. The values of the peak temperatures of melting and crystallization, as well as those of the melting and crystallization enthalpy, as obtained from the heating and cooling curves, are summarized in Table 6.1. All the results presented here are statistical averages of three sets of identical experiments and the errors reported are the standard deviation values of those measurements. It can be seen in Fig. 6.4 that both the melting and crystallization peaks slightly shift to lower temperatures with an increase in the phosphor content. The DSC data in Table 6.1 show that the melting enthalpy values are reduced by the presence of the filler. These results are an indication of reduced crystallinity in LDPE, which is probably the result of a reduction in chain mobility. Although nanostructured fillers usually act as nucleation centres [17], the crystallization in the present system is inhibited by a strong interaction between LDPE and phosphor particles, which immobilized the LDPE chains, giving rise to fewer and smaller crystallites. The reduction in crystallite size is manifested in the decrease in melting temperature, while the reduced crystallinity is explained by the decrease in melting enthalpy values in the presence of phosphor particles. The melting enthalpy is significantly lower, and the peak temperature of melting observably reduced, with only 0.1 v/v phosphor particles in the LDPE matrix, but there is no further decrease with increasing amounts of phosphor particles. This is probably caused by particle

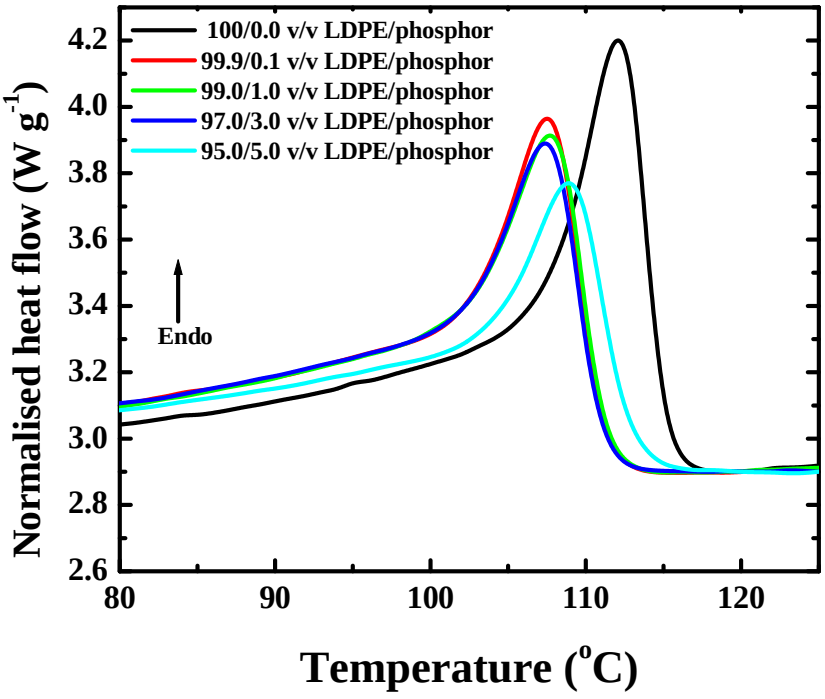

Figure 6.4(a): DSC heating curves of LDPE and LDPE/$Sr_4Al_{14}O_{14}$: Eu^{2+},Dy^{3+}

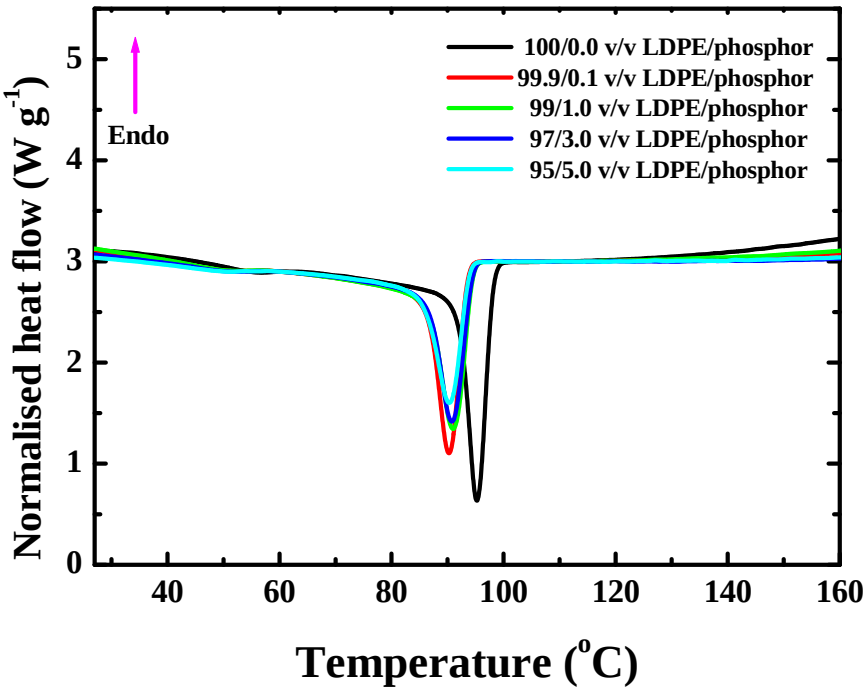

Figure 6.4(b). DSC cooling curves of LDPE and LDPE/$Sr_4Al_{14}O_{14}$: Eu^{2+},Dy^{3+}

agglomeration. The actual nature of the polymer/phosphor interaction may be rooted in the size effects of the nanoparticles. Phosphor synthesis methods that yield particles in the micro or nano range, i.e., solid-state reaction or combustion techniques, are usually high temperature procedures. Due to the high temperatures, many different agents are prone to condensation on the particle while they cool down and are exposed to different ambient atmospheres. These changes mean that complex surface chemical processes are to be expected.

Table 6.1: DSC data of LDPE and LDPE/$Sr_4Al_{14}O_{14}$: Eu^{2+},Dy^{3+}

ΔH_m and ΔH_c - melting and crystallization enthalpies; T_m and T_c - peak temperatures of melting and crystallization

Vol. % phosphor	T_m / °C	ΔH_m^{obs} / g^{-1}	ΔH_m^{cal} / J g^{-1}	$T_{p,c}$/ °C	ΔH_c^{obs} /Jg^{-1}	ΔH_c^{cal} / Jg^{-1}
0.0	112.7 ± 0.4	70.2 ± 3.3	70.2	99.2 ± 0.1	-60.7 ± 1.2	-60.7
0.1	108.2 ± 0.6	50.7 ± 0.6	70.0	95.6 ± 0.2	-54.5 ± 2.1	-60.5
1.0	109.1 ± 0.4	48.7 ± 0.5	67.4	96.2 ± 0.4	-50.8 ± 0.3	-58.3
3.0	108.2 ± 0.1	48.4 ± 3.4	62.5	96.4 ± 0.1	-47.2 ± 3.2	-54.0
5.0	108.4 ± 0.2	51.8 ± 2.1	58.3	96.4 ± 0.3	-48.7 ± 2.0	-50.4

The TGA curves of pure LDPE and the LDPE/$Sr_4Al_{14}O_{14}$: Eu^{2+},Dy^{3+} composites with different phosphor contents are shown in Fig. 6.5. The incorporation of the phosphor particles significantly improved the thermal stability of the LDPE matrix. The thermal decomposition of LDPE is shifted towards higher temperatures by about 33°C in the presence of the phosphor particles. For LDPE, the thermal degradation starts with free radical formation at weak points or chain ends. The radicals then induce further chain fragmentation processes followed by the transfer of the radicals to adjacent chains through interchain actions [18]. The improved thermal stability can be explained through the reduced mobility of the LDPE chains in the nanocomposite. Because of the reduced chain mobility, the chain transfer reaction will be suppressed, and consequently the

degradation process will be slowed and decomposition will occur at higher temperatures. Another possible reason is the difference between the thermal conductivity values of LDPE (0.3 $Wm^{-1}K^{-1}$) and ceramics (3-150 $Wm^{-1}K^{-1}$). This wide difference in thermal conductivity values, as well as the expected relatively higher heat capacities of ceramics, may provide an alternative explanation for the improved thermal stability in LDPE/phosphor composites similar to an observation made for LDPE/copper composites [19]. In that case the shift in decomposition to higher temperatures was attributed to the relatively higher heat capacity and thermal conductivity values of copper, which caused it to preferentially absorb heat. It was also observed that after decomposition of the composites, the residual mass is slightly higher than the original content of phosphor. This observation is characteristic of polymers filled with inorganic particles [20].

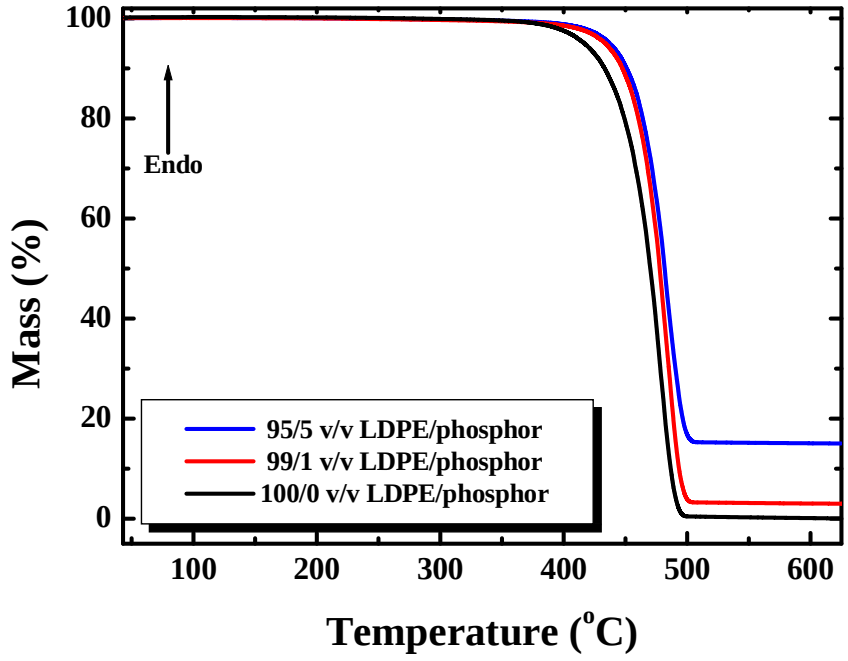

Figure 6.5: TGA curves for LDPE and LDPE/$Sr_4Al_{14}O_{14}$: Eu^{2+},Dy^{3+}

6.4 Conclusions

It has been demonstrated that various loadings of blue-emitting $Sr_4Al_{14}O_{25}$:Eu^{2+},Dy^{3+} phosphor can be incorporated into low density polyethylene (LDPE) matrices. The results have highlighted the capacity of the polymer to act as a host

for the purpose of addressing the sensitivity to environmental factors such as moisture, and hence enhancing the capability of the phosphor. The results are summarized as follows:

1. XRD peaks display planes corresponding to the $Sr_4Al_{14}O_{25}$ monoclinic phase.
2. The PL spectra have two sets of peaks, a major broad band peaking at about 486 nm and a minor one at a wavelength of about 412 nm, attributed to the 4f–5d transitions of Eu^{2+}.
3. The presence of phosphor particles in LDPE slightly reduced the crystallinity but strongly improved the thermal stability of the polymer, attributed to immobilization of polymer chains and the relatively higher thermal conductivity and heat capacity of the phosphor.

6.5 References

1. Jia, W. Yuan, H. Lu, L. *J. Cryst. Growth.*, **200:** 179, (1999).
2. Blasse, G. Wanmaker, W.L. Bril, A. *Philips Res. Rep.*, **23:** 201, (1968).
3. Haranath, D. Shanker, V. Chander, H. Sharma, P. *J. Phys. D: Appl. Phys.*, **36:** 2244, (2003).
4. Nag, A.T.R. Kutty, N.J. *J. Alloys Comp.*, **354:** 221, (2003).
5. Peng, M. Pei, Z. Hong, G. Su, Q. *Chem. Phys. Lett.*, **371**(1-2)**:** 1, (2003).
6. Holsa, J. Hogne, J. Lastusaari, M. Niittykoski, J. *J. Alloys Comp.*, **323-324:** 326, (2001).
7. Matsuzawa, T. Aoki, Y. Takeuchi, N. Murayama, Y. *J. Electrochem. Soc.*, **143:** 2670, (1996).
8. Yen, W.M. Shionoya, S. Yamamoto, H. *Practical Applications of Phosphors*, 2nd Ed., CRC, London, (2006).
9. Tsutai, I. Shimizu, H. Kawakami, T. Shinbo, K. Kato, K. Kaneka, F. Ohta, M. *Tech. Rep. of IEICE CPM.*, **13:** 95, (1995).
10. Katsumata, T. Kasajima, K. Nabe, T. Komuro, S. Morikawa, T. *J. Am. Ceram. Soc.*, **81:** 413, (1998).
11. Lin, Y. Zhang, Z. Zhang, F. Tang, Z. Chen, Q. *Mater. Chem. Phys.*, **65:** 103, (2000).
12. Geng, J. Wu, Z. *J. Mater. Synth. Proc.*, **10:** 245, (2002).
13. Kato, K. Tsutai, I. Kamimura, T. Kaneko, F. Shinbo, K. Ohta, M. Kawakami, T. *J. Lumin.*, **82:** 213, (1999).
14. Lin, Y. Tang, Z. Zhang, Z. *Mater. Lett.*, **51:** 14, (2001).
15. Clabau, F. Rocquefelte, X. Jobic, S.M. Deniard, P. Whangbo, M.H. Garcia, A. Mercier, T.L. *Chem. Mater.*, **17:** 3909, (2005).
16. Ngaruiya, J.M. Nieuwoudt, S. Ntwaeaborwa, O.M. Terblans, J.J. Swart, H.C. *Mater. Lett.*, **62:** 3192, (2008).
17. Ning, N.Y. Yin, Q.J. Luo, F. Zhang, Q. Du, R. Fu, Q. *Polym.*, **4:** 7374, (2007).
18. Allen, N.S. Edge, M. *Fundamentals of Polymer Degradation and Stabilization*, 2nd Ed., Elsevier, London, (1992).

19. Luyt, A.S. Molefi, J.A. Krump, H. *J. Polym. Degrad. Stab*., **91:** 1629, (2006).
20. Dragana, S. Zoran, V.S. Nikola, C. Milena, M. Jovan, M.N. *Chem. Phys. Lett.*, **329:** 168, (2000).

Chapter 7

Characterization of Luminescent and Thermal Properties of Long Afterglow $SrAl_xO_y:Eu^{2+},Dy^{3+}$ Phosphor Synthesized by Combustion Method

7.1 Introduction

The special long afterglow phenomena [1] in rare earth-doped phosphors as well as high quantum efficiency in the visible region [2] have significantly motivated research on this class of materials. The suitability of strontium aluminate ($SrAl_2O_4$) as a host is on account of its efficiency, as well as its capacity for broad band emissions [3]. Doped with Eu^{2+}, it provides typical emission bands in the blue and green regions of the electromagnetic spectrum. The phosphorescence of Eu^{2+} in most hosts is believed to be caused by the $4f^65d^1 \rightarrow 4f^7$ transition. The peak position in the emission spectra strongly depends on the nature of the Eu^{2+} surroundings, and therefore Eu^{2+} ion can emit different visible wavelengths in various crystal fields. Its luminescence spectra have emission wavelengths extending from the UV to the red portions of the spectrum [1,4]. The afterglow lifetime and intensity of these phosphors can be enhanced by co-doping with a second rare-earth ion [5] such as Dy^{3+}. These phosphors exhibit a rapid initial decay from the Eu^{2+} ion followed by a long persistence due to the Dy^{3+} ion when it acts as a trap for holes [6,7].

Over the years, the variety of methods that have been employed in the synthesis of $Sr_xAl_yO_z:Eu^{2+},Dy^{3+}$ phosphors have included co-precipitation [8], sol–gel [1] microwave [9] solid-state reaction [10], detonation [11], and combustion synthesis techniques [12].

The combustion process has distinguished itself as a safe, instantaneous and energy saving technique due to the possibility of using relatively low temperatures and the short duration of the reaction process. Its other advantages include the use of relatively simple equipment, formation of high-purity products, stabilization of metastable phases, and formation of virtually any size and shape of products.

The class of strontium aluminate phosphors has widely been investigated due to its several advantages over other phosphors. However, degradation of these phosphors due to weak resistance to water or even moisture remains an unresolved issue. This lack of resistance originates in the nature of the structure of the low temperature phase of $SrAl_2O_4$. $SrAl_2O_4$ belongs to the distorted stuffed tridymite type structure, which adopts the monoclinic structure (space group $P2_1$, a = 8.447, b = 8.816, and c = 5.163 Å) that consists of a three-dimensional network of corner-sharing AlO_4 tetrahedron containing connected open channels [13,14]. Water molecules can enter the channels, and the strong polarity of the water breaks the bonds of O–Sr–O [17]. Consequently, the $SrAl_2O_4:Eu^{2+},Dy^{3+}$ phosphor is inclined to hydrolyze and deteriorate. Various intervention techniques have been attempted, to varying degrees of success in terms of cost effectiveness and side effect on phosphor output. Currently, SiO_2 [16], Al_2O_3 [17], SrF_2 [18], BN [16] compounds, and organic ligands [19] are being used for encapsulation. Other efforts involve the use of inorganic layers for phosphor encapsulation and surface treatment using phosphoric acid (H_3PO_4) in ethanol [20]. These approaches involve complex processes that require elaborate equipment, but still tend to compromise the luminescence intensity of the phosphors.

In the work reported here, the combustion synthesis method was used to prepare nanophase $SrAl_xO_y:Eu^{2+},Dy^{3+}$ phosphor powders, which were subsequently mixed in low-density polyethylene (LDPE). Results indicate the dominance of the low-temperature monoclinic phase of $SrAl_2O_4$ in the synthesized phosphor powder. The photoluminescence intensity as well as afterglow of the obtained phosphor compares well with that of commercial powders.

The work presented in this chapter is intended to assess the performance of the polymer/phosphor composite system, as a precursor to the determination of a strong and stable composite network, with a view to addressing environmental factors, such as moisture, that may compromise phosphor potency.

7.2 Experimental

Strontium aluminate phosphor ($SrAl_xO_y:Eu^{2+},Dy^{3+}$) was prepared by a combustion synthesis method. High purity (Aldrich make, 99.99%) raw materials, strontium nitrate ($Sr(NO_3)_3.4H_2O$), aluminum nitrate ($Al(NO_3)_2.9H_2O$), europium nitrate ($Eu(NO_3)_3.6H_2O$), dysprosium nitrate ($Dy(NO_3)_3.5H_2O$) and urea ($CO(NH_2)_2$), were used for preparation of the charge. The materials were weighed in stoichiometric ratios and mixed thoroughly in an agate mortar. The precursors for each phosphor were mixed and milled in a mortar using a pestle and the resulting thick white paste was transferred into a china crucible, which was then introduced into a muffle furnace maintained at 500 ^oC. This synthesis technique makes use of the heat energy liberated by the redox exothermic reaction between metal nitrates and urea at a relatively low igniting temperature (500 ^oC). Urea serves as the source of carbon and hydrogen, which on combustion form carbon dioxide and water, and liberate heat. It also forms complexes with the metal ions facilitating homogeneous mixing of the cations. Urea's popularity as a fuel in combustion techniques is probably due to its ready availability and high exothermicity.

The surface morphology and elemental composition of the phosphor powders were investigated using a Shimadzu Superscan SSX-550 electron microscope (SEM) coupled with an energy dispersive x-ray spectroscope (EDS). For SEM measurements, the probe size was 3.0 nm, the probe current 0.02 nA, and the accelerating voltage 5.0 keV. The probe size for EDS analysis was 4 nm, specimen current 1.00 nA, and accelerating voltage 15.0 keV. Phase and crystallinity were investigated by powder XRD using a Bruker D8 (Bruker Co., Germany) x-ray diffractometer with CuK_α (λ = 1.5406 Å). For microstructure and crystallinity analysis using a transmission electron microscope (TEM), sample preparation involved suspending particles in ethanol by ultrasonification

and drying a drop of the suspension on a carbon-coated copper grid. A JEOL JEM-2100 transmission electron microscope operating at 200 kV was employed for this investigation. The system is available at the CSIR nanomaterials laboratory. The photoluminescence (PL) excitation and emission spectra were taken on a Cary Eclipse fluorescence spectrophotometer equipped with a monochromatic xenon lamp. Each sample was loaded into a circular holder and excited with 340 nm radiation from a pulsed xenon lamp. The emission spectra were scanned in the range of wavelengths from 360 to 750 nm. To measure the excitation spectra, the analyzer monochromator was set to the maximum wavelength of the emission spectra and then an excitation monochromator was scanned in the range of 250 to 450 nm. The same system (Cary Eclipse) was used to investigate the phosphorescence decay curves of the phosphors in air at room temperature.

Polymer/phosphor composites were prepared by mechanically mixing the synthesized phosphor powder with low-density polyethylene (LDPE) (supplied by Sasol Polymers, South Africa, melt flow index 2.0 g/10 min, melting point 110ºC, and density 0.922 g cm^{-3}). Samples, containing phosphor volume ratios ranging from 0.4% to 10%, were weighed according to the required ratios and mixed using a volume of 50 cm^3 in a Brabender Plastograph mixing chamber at a speed of 30 rpm for 15 minutes. The mixing was carried out at 160 °C. The samples were hot melt-pressed into slabs of average thickness 0.98 ± 0.05 mm, at 160 °C.

A Perkin-Elmer DSC7 differential scanning calorimeter, under flowing nitrogen (20 mL min^{-1}), was employed for the DSC analyses. The system is interfaced to a computer, which was used for calculations by means of Pyris software. Samples of masses ranging from 7 to 10 mg were sealed in aluminum pans and heated from 25 to 160 °C at a heating rate of 10 °C min^{-1}, and immediately cooled at the same rate to 25 °C. For the second scan, the samples were heated and cooled under the same conditions. Peak temperatures of melting and crystallization, as well as melting and crystallization enthalpies, were determined from the second scan. Thermogravimetric analyses (TGA) were performed in a Perkin-Elmer TGA7 thermogravimetric analyzer in a flowing

nitrogen atmosphere (20 mL min^{-1}). The samples, each having a mass between 6 and 10 mg, were heated from 25°C to 600°C at a rate of 10 °C min^{-1}. For both DSC and TGA analyses three measurements were performed on each sample composition, from which average temperature and enthalpy values were calculated.

7.3 Results and discussion

The representative SEM micrographs of $SrAl_xO_y:Eu^{2+}Dy^{3+}$ phosphor for 3000× and 6000× magnifications are shown in Fig. 7.1. The characteristic foamy

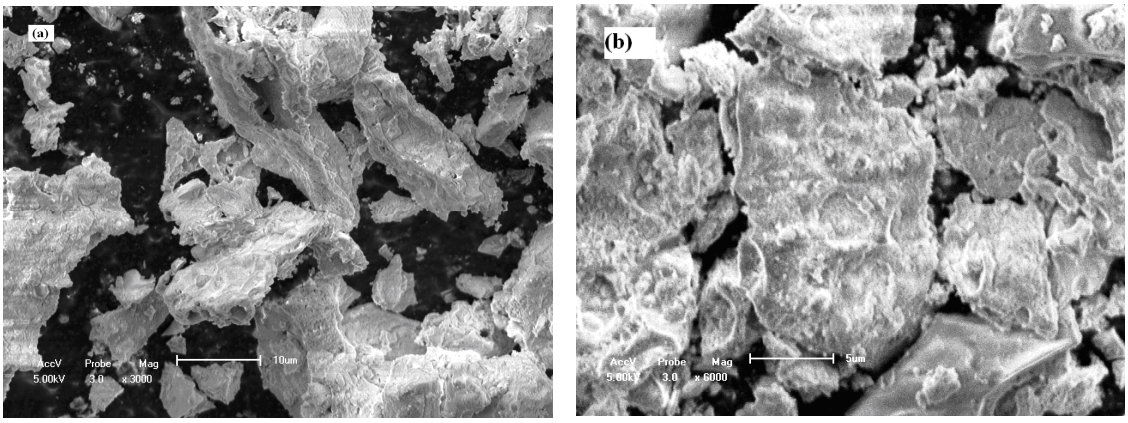

Figure 7.1: (a) SEM images of the $SrAl_xO_y:Eu^{2+},Dy^{3+}$ sample having a 1:2 molar ratio of $Eu^{2+}:Dy^{3+}$ with (a) 3000× magnification (b) 6000× magnification

structure that reflects the inherent nature of the reaction is clearly visible. Results for the elemental analysis by EDS are shown in Fig. 7. 2 which, apart from the carbon that originates from the sample-holding tape, displays the presence of the expected elements, i.e., oxygen, aluminum, and strontium, in proportions commensurate with the initially measured masses.

Fig. 7.3 shows the powder XRD patterns for the $SrAl_xO_y:Eu^{2+},Dy^{3+}$ with low and high $Dy(NO_3)_3$ concentrations. The monoclinic phase diffraction peaks of $SrAl_2O_4$ are dominant in these patterns and match well with $SrAl_2O_4$ standard values given in the International Centre for Diffraction Data (ICDD) No. 34-0379 files. However, there are also a few other peaks, which may be ascribed to impurities such as $SrAl_{12}O_{19}$, or

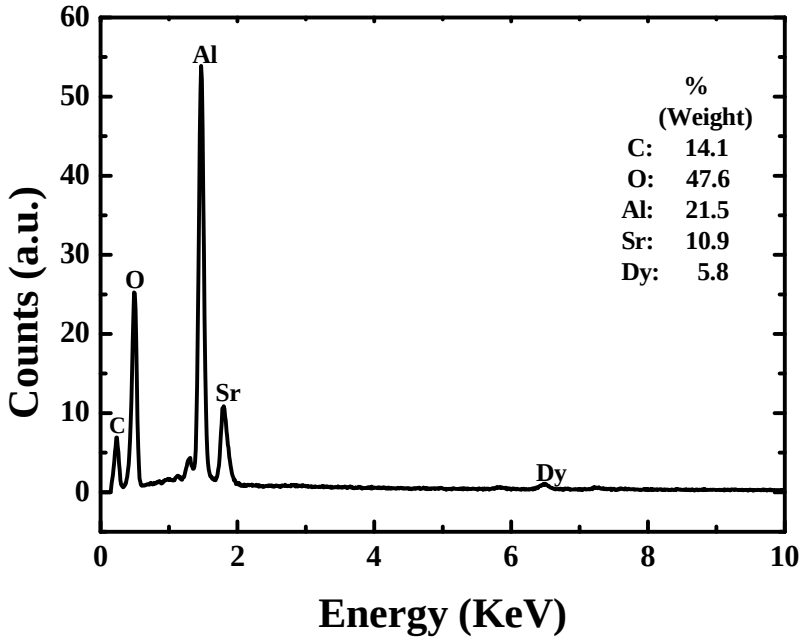

Figure 7.2: Point EDS results of the $SrAl_xO_y:Eu^{2+},Dy^{3+}$ sample having a 1:2 molar ratio of $Eu^{2+}:Dy^{3+}$

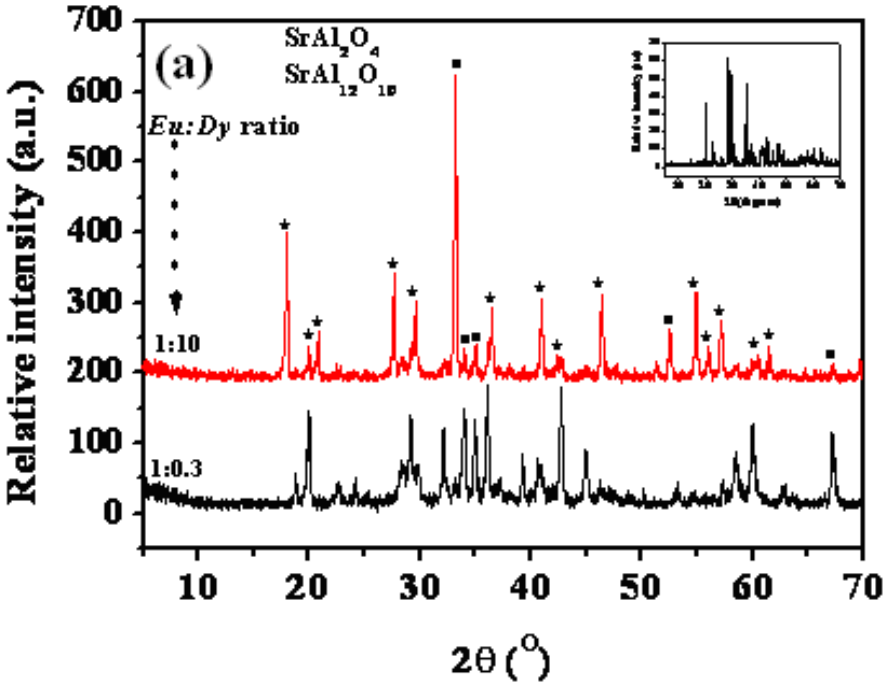

Figure 7.3(a): XRD patterns at two dopancy levels of the synthesized $SrAl_xO_y$: Eu^{2+},Dy^{3+} powder and [Inset: XRD pattern of a commercial phosphor]

unreacted precursor powders [21]. The effect of the doped rare-earth active ions Eu^{2+} and Dy^{3+} on the basic crystal structure of the end product is negligible. The average crystallite sizes were calculated using powder x-ray diffraction data by means of the Debye-Scherrer equation (6.1),

$$D = K\lambda/\beta\cos\theta, \qquad (6.1)$$

where D is the average diameter of the particles, K is the Scherrer constant equal to 0.89, λ is the wavelength of the CuK_α radiation = 1.5406 nm, β is the corrected full width at half-maximum (FWHM), and θ is the Bragg angle. The calculated average crystallite sizes of the phosphor powder vary between 34 ± 7 and 43 ± 7 nm. The XRD patterns of

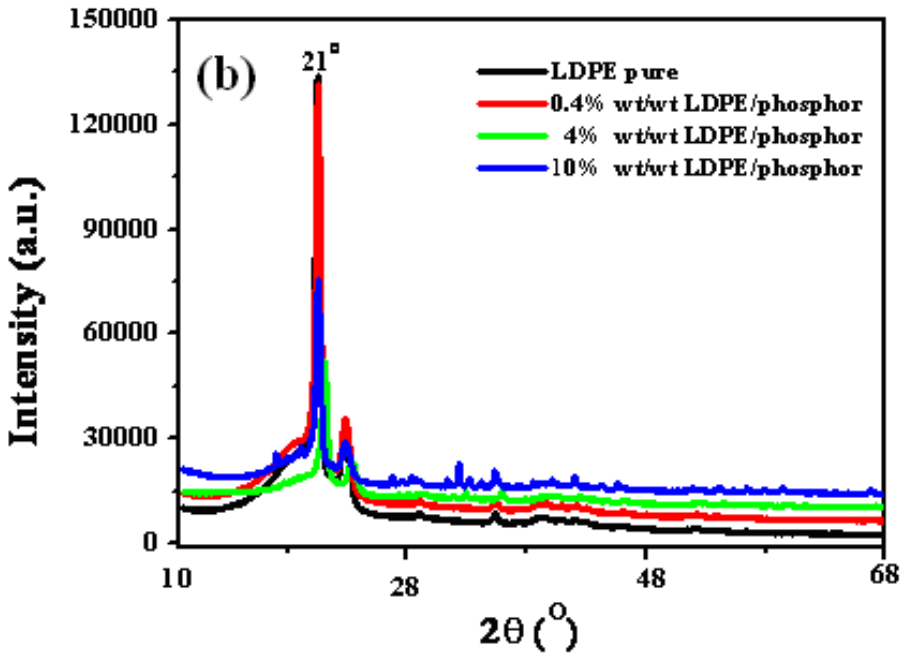

Figure 7.3(b): XRD patterns of LDPE/$SrAl_xO_y$:Eu^{2+},Dy^{3+} composites for the 1:2 molar ratio sample

the pure LDPE and LDPE/phosphor composites over diffraction angles of $10^o \leq 2\theta \geq 68^o$ are shown in Fig. 7.3(b). The origin of the prominent peak at 21^o, which dwarfs the peaks corresponding to the phosphor planes, is clearly that of the LDPE polymer matrix. Otherwise, and particularly for the 10% concentration spectrum, peaks corresponding to the planes of the phosphor are clearly discernible, indicating that the absence of the

expected phosphor peaks in the other spectra is due to their low concentrations. It is observed that as the phosphor concentration increases, there are no changes in the peak positions. Thus the introduction of the phosphor in LDPE did not alter the crystal structure of the polymer.

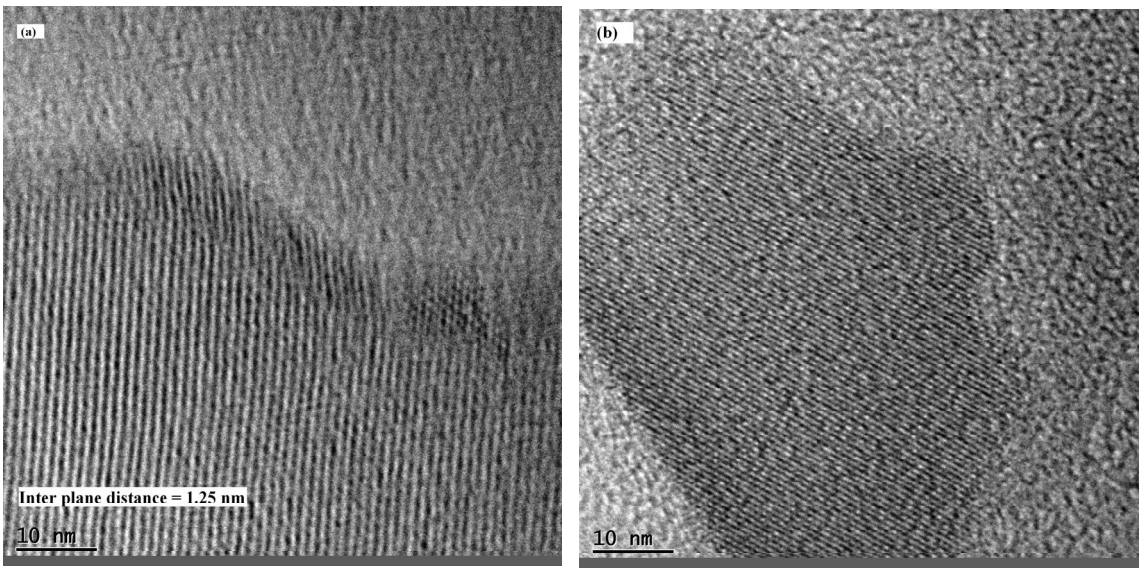

Figure 7.4: TEM micrographs of the $SrAl_xO_y:Eu^{2+},Dy^{3+}$ samples having, (a) 1:0.3 molar ratio (b) 1:10 molar ratio of $Eu^{2+}:Dy^{3+}$

Transmission electron microscopy is capable of providing useful information regarding the local structure and particle size of a material. It is therefore an apt tool for investigating the current material in view of the various possible aluminate phases that can result from the synthesis process, as well as the crystallographic transformation from the high temperature hexagonal phase to the low temperature monoclinic phase, which occurs at about 650 ^{o}C. The representative high-resolution transmission electron micrographs (HRTEM) for the low and high Dy concentration samples, are shown in Fig. 7.4(a) and (b). In HRTEM imaging the spacing of a set of fringes is proportional to the lattice spacing when the corresponding lattice planes meet the Bragg condition. In this study the value of the interplanar spacing, calculated from the visible fringes (Fig. 7.4(a)), was found to be 1.25 nm. The clarity of the micrographs shows that the

synthesized $SrAl_xO_y:Eu^{2+}Dy^{3+}$ phosphor crystallizes almost in single phase and the presence of secondary phases is minimal. This result is supportive of the XRD results, which point to the dominance of the monoclinic (α) phase in the synthesized product. The differences in intensity may be attributed to variations in particle sizes, which occur on the nanometre scale.

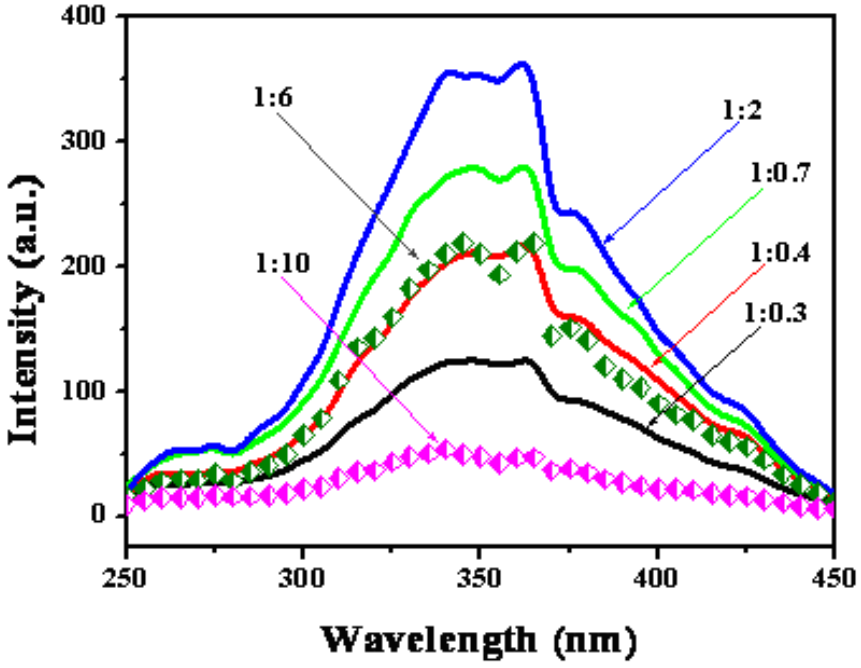

Figure 7.5: Excitation spectra of $SrAl_xO_y:Eu^{2+}$, Dy^{3+}, for the samples with 1:0.3 to 1:10 molar ratio of Eu^{2+}:Dy^{3+}

The excitation and emission spectra for $SrAl_xO_y:Eu^{2+},Dy^{3+}$ with various Dy^{3+} concentrations are shown in Figs. 7.5 and 7.6, respectively. The excitation spectra show one broad band from 255 to 375 nm with a shoulder at about 375 nm corresponding to the crystal field splitting of the Eu^{2+} d-orbital. The prepared phosphor compositions exhibit emission in the green region. This is a strong indication that the Eu ion is in a divalent (Eu^{2+}, green emission) rather than trivalent (Eu^{3+}, red emission) state. It is to be noted that this result was obtained in the absence of any deliberately designed reducing environment. The emission band is symmetrical at about 515 nm which is attributed to the typical $4f^65d^1 \rightarrow 4f^7$ transition of the Eu^{2+} ion. The 515 nm emission wavelength indicates the dominance of the monoclinic, green-emitting phase of the aluminate

phosphor. Two other, minor peaks, at 615 and 683 nm indicate the presence of more than one luminescent centre and may be due to remnants of Eu^{3+} ions as a result of incomplete reduction during sample preparation [22]. The emission spectra have the highest intensity for a Eu^{2+}:Dy^{3+} mole ratio of 1:2. According to Lin and Tang [23], under UV irradiation, an Eu^{2+} ion, which is placed at a specific energy level of the $4f^7(^8S_{7/2})$ ground state

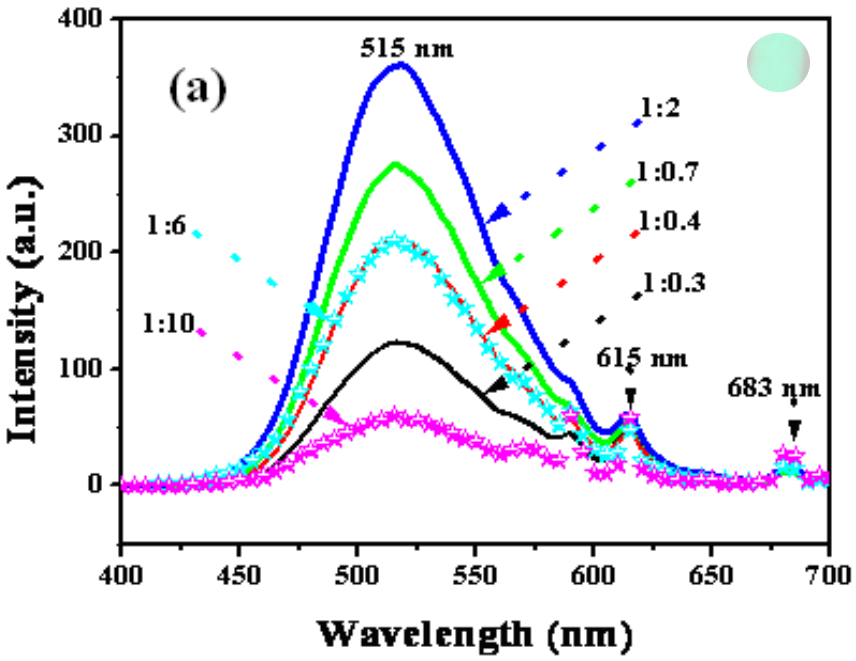

Figure 7.6(a): Emission spectra of $SrAl_xO_y:Eu^{2+},Dy^{3+}$, for the samples with 1:0.3 to 1:10 molar ratio of Eu^{2+}:Dy^{3+}

between the valence and conduction bands, is excited and an electron-hole pair is created. The excited electron is transferred to the $4f^65d^1$ excited state while the hole is transferred to the valence band. After removing the UV exposure source, the excited electron tends to stay at a lower energy level. Energy decrease may have occurred in two steps; firstly releasing part of the energy (usually thermally) after relaxing to the metastable state, followed by transferring electrons from the metastable state to the ground state while recombining with the hole accompanied with light emission. However, there is a probability that after the initial transition, energy can be trapped in lattice defects or impurities. The long-lasting persistence afterglow of the phosphors arises from these processes. The observed reduction in emission intensity above the 1:2 molar ratio may

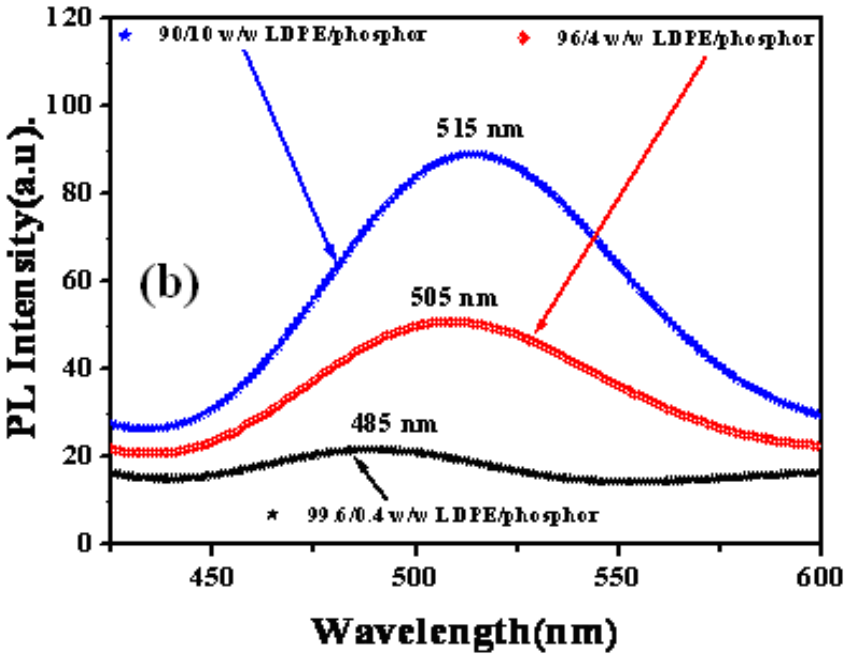

Figure 7.6(b): Emission spectra of LDPE/$SrAl_xO_y$:Eu^{2+},Dy^{3+} composites for different concentrations of the phosphor sample with 1:2 Eu^{2+},Dy^{3+} molar ratio

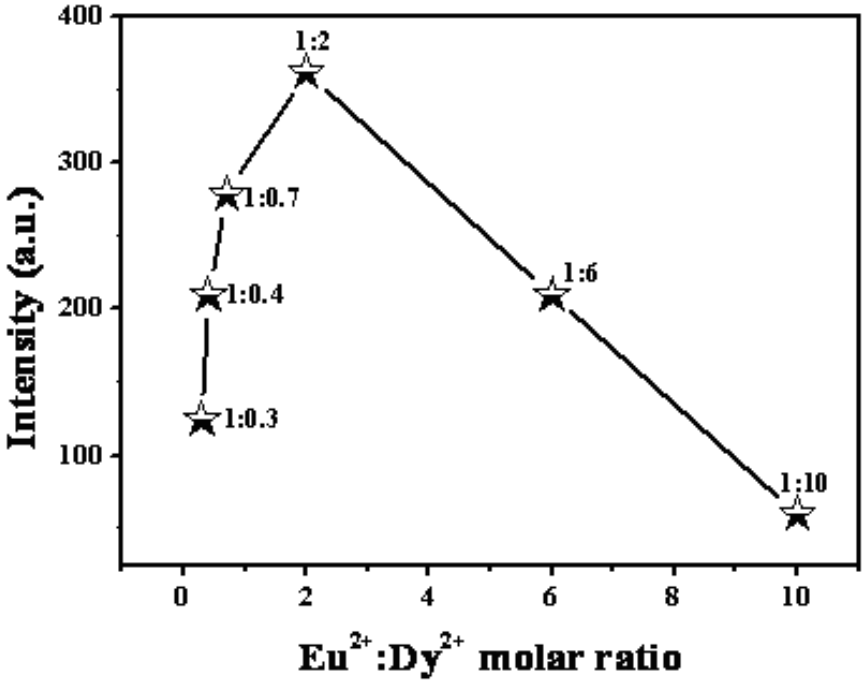

Figure 7.7: Emission intensity of the $SrAl_xO_y$:Eu^{2+},Dy^{3+} phosphor at 515 nm as a function of Eu^{2+}:Dy^{3+} molar ratio; $\lambda_{excitation}$ = 340 nm

be explained in terms of the existence of a critical (optimum) number of Dy^{3+} ions for luminescence emission. On exceeding this number, the ions produce more crystalline defects apart from the traps. These defects neutralize the electron-hole recombination processes, thereby reducing the emission intensity as well as traps responsible for the long persistence.

The PL emission spectra for three phosphor concentrations in LDPE are shown in Fig. 7.7. Except for a slight red-shift, as phosphor concentration increases, the emission spectra generally replicate the phosphor powder emission behaviour. At the higher phosphor concentration, particle agglomeration is possible and may lead to the reduction in the kinetic energy of the electrons, resulting in a reduced band gap. A smaller band gap would require less energy to excite the phosphor and hence lead to the emission maximum shifting to longer wavelengths [9].

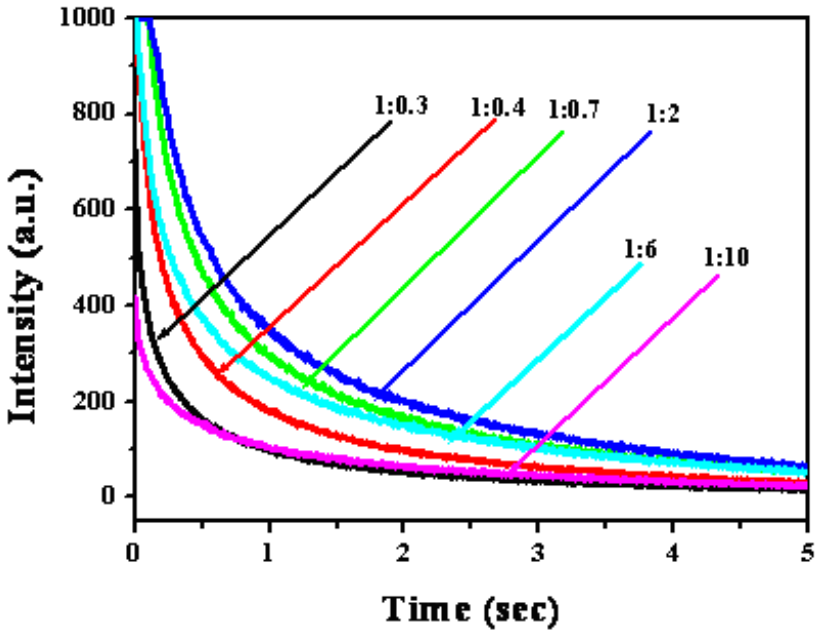

Figure 7.8: Decay curves for the phosphor $SrAl_xO_y:Eu^{2+},Dy^{3+}$ samples with 1:0.3 to 1:10 molar ratio of Eu^{2+}:Dy^{3+}

In similar work by Mothudi *et al.* [24], a broad emission spectrum of $SrAl_2O_4:Eu^{2+}$, Dy^{3+} phosphor powder, is observed to be symmetrical at 528 nm with an additional peak at 685 nm. Nsimama *et al.* [25], working on thin films of commercial $SrAl_2O_4:Eu^{2+},Dy^{3+}$ phosphor, also report the observation of two peaks, but at 517 and 630 nm respectively, while the maximum broad-band of the UV excited luminescence spectrum of the $SrAl_2O_4$:Eu, Dy sample, synthesized using the sol-gel process by Peng *et al.* [1] appears at 506 nm. These observations clearly illustrate the variability in the peak position that can be obtained for similar phases. These differences may be explained in terms of crystallite sizes. Due to the proximity of the 5d energy level to the conduction band, changes in particle size may change the size of the band gap such that there is a corresponding change in the 5d energy level. Since particle size seems to significantly influence the $4f^7–4f^6$5d electric dipole-allowed transitions originating from Eu^{2+}-doped alkaline-earth aluminate hosts [26], these transitions may form the basis for the variations in the emission wavelengths observed by the various authors.

The phosphorescence decay characteristics of the $SrAl_xO_y:Eu^{2+},Dy^{3+}$ phosphor samples for various Dy^{3+} concentrations are shown in Fig. 7.8. Results for fitted decay curves of the phosphor are recorded in table 7.1. The decay phenomenon is very useful in the study of traps. The results show that the initial luminescent intensity and the decay time of afterglow of the samples are different from each other. By increasing the Dy^{3+} concentration, the initial luminescent intensity changed such that the sample with the intermediate Dy^{3+} concentration (1:2 Eu^{2+}:Dy^{3+} ratio) has the highest initial intensity and longest decay time. The high initial intensity is attributed to the presence of a sufficient number of shallow traps and the ensuing rapid decay is ascribed to the short survival time of an electron in Eu^{2+}. The deep trap energy centres of Dy^{3+} [26] could be responsible for the very long-lasting decay times. Samples with lowest and highest concentrations of Dy^{3+} (10:3 and 1:10) have lower initial intensity values and short-lived afterglow due to a lack of adequate numbers of both shallow and deep traps. Other than for the sample with the highest Dy^{3+} concentration (1:10), whose curve may only be fitted by a second order equation, the other decay times can be calculated by a curve fitting technique based on the third order exponential decay equation (7.2),

$$I = A_1 \exp\left(-\frac{t}{\tau_1}\right) + A_2 \exp\left(-\frac{t}{\tau_2}\right) + A_3 \exp\left(-\frac{t}{\tau_3}\right), \qquad (7.2)$$

where I is the phosphorescence intensity at any time t after switching off the excitation illumination; A_1, A_2, and A_3 are constants; τ_1, τ_2, and τ_3 are decay times for the exponential components, corresponding to the fast, medium and slow afterglow processes, respectively. It is observed that the initial fast decay process is missing from the sample with the highest Dy^{3+} concentration (1:10 molar ratio) in line with the quenching results displayed in the PL spectra.

The DSC heating curves for LDPE and its phosphor composites are shown in Fig. 7.9. The curves show endothermic peaks at about 116 ^{o}C. There is a slight shift in melting peaks to lower temperatures with an increase in the phosphor content. The peak

Table 7.1: Results for fitted decay curves of the $SrAl_xO_y:Eu^{2+},Dy^{3+}$ phosphor

Sample (Eu^{2+}: Dy^{3+})	10:3	10:4	10:7	1:2	1:6	1:10
Component	Half life times (s)					
Fast (τ_1)	0.037	0.085	0.328	0.434	0.095	0.155
Medium (τ_2)	0.316	0.432	1.344	2.216	0.429	1.470
Slow (τ_3)	2.313	2.559	3.573	4.644	2.419	-

temperatures of melting ($T_{p,m}$), as well as the experimental (ΔH_m^{obs}) and calculated (ΔH_m^{cal}) melting enthalpies, are summarized in Table 7.2. The comparison between the observed and expected enthalpies shows higher than expected enthalpy values for all the composites except for the 0.4% sample. The relative difference between the experimental and calculated enthalpies increases with increasing phosphor content. This result may be explained in terms of the relatively amorphous nature of LDPE. Since the phosphor particles will be situated in the amorphous part of the polymer matrix, and because LDPE has a relatively low crystallinity, this may be explained through epitaxial crystallization on the phosphor surfaces giving rise to more crystallites in the presence of the phosphor.

Table 7.2: DSC and TGA data of pure LDPE and LDPE/$SrAl_xO_y:Eu^{2+},Dy^{3+}$

$T_{p,m}$ - peak temperature of melting; ΔH_m - melting enthalpy; T_{wl} – temperature at weight loss

Vol. % phosphor	$T_{p,m}$/°C	ΔH_m^{obs} /J g^{-1}	ΔH_m^{cal} /J g^{-1}	T_{wl}/ °C
0.0	112.8 ± 1.1	52.5 ± 1.6	52.5	385
0.4	111.5 ± 0.0	51.1 ± 1.2	52.3	280
4.0	111.5 ± 0.3	52.6 ± 1.9	50.5	386
10.0	110.3 ± 0.1	50.4 ± 2.0	47.6	329

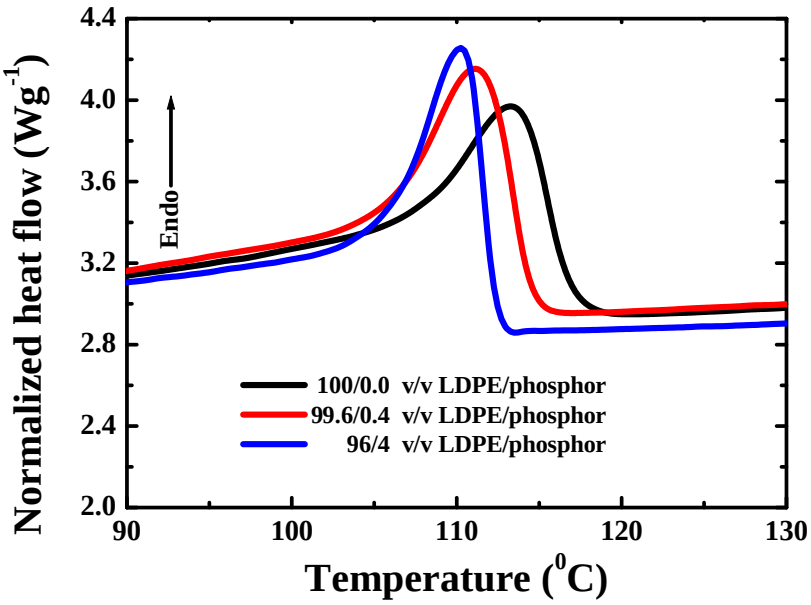

Figure 7.9: DSC heating curves of LDPE and LDPE/$SrAl_xO_y:Eu^{2+},Dy^{3+}$ composites

Overall, the DSC results indicate that, while the introduction of the phosphor nanoparticles in LDPE increased the total crystallinity of LDPE, the reduced peak temperature of melting values suggest that the nanofiller phosphor particles prevented lamellar growth resulting in smaller crystallites. These observations show that the

phosphor particles acted as nucleating agents in the LDPE/$SrAl_xO_y$:Eu^{2+},Dy^{3+} phosphor system.

The TGA curves (Fig. 7.10) of the pure LDPE and LDPE/$SrAl_xO_y$:Eu^{2+},Dy^{3+} phosphor composites show a one-step weight loss between 400 and 500 ^oC. The curves show residual masses that correspond well with the amounts of the initially added components. Changes in the thermal stability of LDPE, with increase in phosphor content, can be deduced from the slight shifts in the curves as well as the variation in the values of the temperature at 10% weight loss. These results show that the phosphor nanoparticles generally catalyzed the degradation of LDPE, which is contrary to the findings by other authors on the effect of inorganic fillers on the thermal stability of polymers. Luyt *et al.* [27] observed improved thermal stability of copper nanoparticles-filled LDPE nanocomposites. A similar conclusion was arrived at by Mbhele *et al.* [28] in their work on silver-filled polyvinyl alcohol.

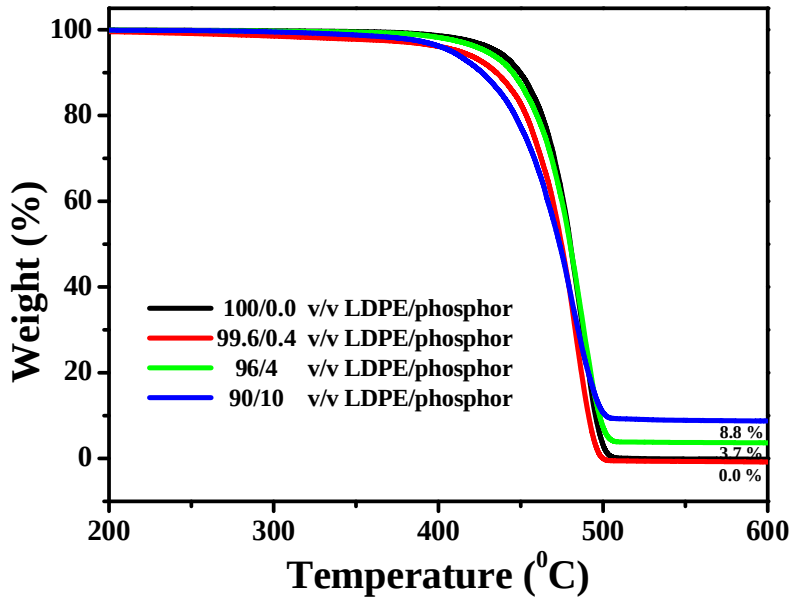

Figure 7.10: TGA curves for pure LDPE and LDPE/$SrAl_xO_y$:Eu^{2+},Dy^{3+}

7.4 Conclusions

$SrAl_xO_y:Eu^{2+},Dy^{3+}$ phosphor powders have been synthesized by a combustion synthesis method. The relative amounts of Eu^{2+} and Dy^{3+} affected the luminescence properties of the phosphor. Emission spectra at room temperature have a major broad band peaking at 515 nm and minor ones at 615 and 683 nm. The broad-band spectra manifest the occurrence of transitions between the 5d and 4f orbital gaps of Eu^{2+}. The broad emission spectra are indicative of the good quality of the samples. Investigation on the variation of emission intensity of different phosphor samples containing different amounts of Dy^{3+} revealed that after 2 mol% of Dy^{3+} concentration, a quenching process occurred. Dy^{3+} formed trap levels and the results demonstrated that the initial, relative intensity as well as decay time were optimized for the 2 mol% concentration of Dy^{3+}. Improvements in the initial brightness, quenching thresholds and the afterglow times, are attributed to the presence of both shallow and deep traps. The XRD peaks as well as the emission wavelength of the major peak (515 nm) are indicative of the dominance of the monoclinic crystal system in the phosphor powder. The introduction of the phosphor in LDPE did not structurally alter the polymer, but as the phosphor concentration increased. On the other hand, the polymer permitted replication of the emission PL peak positions of the phosphor. Thermal analysis shows that the phosphor nanoparticles acted as nucleating agents and improved the overall crystallinity in the LDPE matrix.

7.5 References

1. Peng, T. Huajun, L. Yang, H. Yan, C. *Mater. Chem., Phys.,* **85:** 68, (2004).

2. Fu, Z. Zhou, S. Yu, Y. Zhang, S. *Chem. Phys. Lett.,* **395:** 285 (2004).

3. Suematsu, H. Sengiku, M. Kato, K. Mitome, M. Kimoto, K. Matsui, Y. Jiang, W. Yatsui, K. *Thin solid Films.,* **407:** 136, (2002).

4. Aitasulo, T. Dereń, P. Hölsä, J. Jungner, H. Krupa, J.C. Lastusaari, M. Legendziewicz, J. Niittykoski, J. Strek, W. *J. Sol. State Chem.,* **171:** 114, (2003).

5. Sakai, R. Katsumata, T. Komuro, S. Morikawa, T. *J. Lumin.,* **85:** 149, (1999).

6. Katsumata, T. Toyomane, S. Sakai, R. Komuro, S. Morikawa, T. *J. Amer. Ceram. Soc.,* **89:** 932 (2006).

7. Ngaruiya, J.M. Nieuwoudt, S. Ntwaeaborwa, O.M. Terblans, J.J. Swart, H.C. *Mater. Lett.,* **62:** 3192, (2008).

8. Lin, Y.H. Zhang, Z.T. Zhang, F. Tang, Z.L. Chen, Q.M. *Mater. Chem., Phys.,* **65:** 103, (2000).

9. Ravichandran, D. Johnson, S.T. Erdei, S. Roy, R. White, W.B. *Displays.*, **19:** 197, (1999).

10. Sarkisov, P.D. Popovich, N.V. Zhelnin, A.G. *Glass Ceramics*, **60** (9-10)**:**, 309, (2003).

11. Li, X. Qu, Y. Xie, X. Wang, Z. Li, R. *Mater. Lett.,* **60:** 3673, (2006).

12. Chander, H. Haranath, D. Shanker, V. Sharma, P. *J. Cryst. Growth*., **271**: 307, (2004).

13. Han, S.D. Singh, K.C. Cho, T.Y. Lee, H.S. Jakhar, D. Hulme, J.P. Han, C.H. Kim, J.D. Chun, I.S. Gwak, J. *J. Lumin*., **128:** 301, (2008).

14. Glasser, F.P. Glasser, L.S.D. *J. Am. Ceram. Soc*., **46:** 377 (1963).

15. Lin, J. Huang, Y. Zhang, J. Shi, F.J. Wei, S.Y. Gao, J.M. Huang, Z.X. Ding, X.X. Tang, C.C. *Mater. Chem. Phys*., **108:** 440, (2008).

16. Masumi, I. Hidehiko, K. Takuya, O. Tomoya, S. *JP. Patent*, 316, 433 (1997).

17. Lu, X.D. Zhong, M.J. Shu, W.G. Yu, Q.M. Xiong, X.Q. Wang, R.Q. *Powder Technol*., **177**(2)**:** 83, (2007).

18. Guo, C.F. Luan, L. Huang, D.X. Su, Q. Lu, Y.H. *Mater. Chem. Phys*., **106:** 268, (2007).

19. Wu, S.L. Zhang, S.F. Liu, Y. Yang, J.Z. *Mater. Lett*., **61:** 3185, (2007).

20. Zhu, Y. Zeng, J. Li, W. Xu, L. Guan, O. Liu, Y. *Appl. Surf. Sci.*, **255:** 7580, (2009).

21. Park, J.K. Lim, M.A. Kim, C.H. Park, H.D. *Appl Phys Lett.*, **82:** 683 (2003).

22. Clabau, F. Rocquefelte, X. Jobic, S. Denieard, P. Whangbo, M.H. Garcia, A. Mercier, T. *Solid State Sci.*, **9:** 608, (2007).

23. Lu, Y. Li, Y. Xiong, Y. Wang, D. Yin, Q. *Microelectron, J.*, **35:** 379, (2004).

24. Mothudi, B.M. Ntwaeaborwa, O.M. Botha, J.R. Swart, H.C. *Phys. B.***, 404:** 4440, (2009).

25. Nsimama, P.D. Ntwaeaborwa, O.M. Coetsee, E. Swart, H.C. *Phys. B.*, **404:** 4489, (2009).

26. Chen, X.Y. Ma, C. Li, X.X. Shi, C.W. Li, X.L. Lu, D.R. *J. Phys. Chem. C*., **113:** 2685, (2009).

27. Luyt, A.S. Molefi, J.A. Krump, H. *Polym. Degrad. and Stab*., **91:** 1629, (2006).

28. Mbhele, Z.H. Salemane, M.G. Sittert, C.G.C.E. Nedeljkovic, J.M. Djokovic, V. Luyt, A.S. *Chem. Mater.*, **15:** 5019 (2003).

Chapter 8

Temperature Dependence of the Structural and Luminescent Properties of Long-lasting Afterglow $SrAl_xO_y:Eu^{2+},Dy^{3+}$ Phosphor

8.1 Introduction

Phosphors synthesized from rare-earth metal ions have continued to be deeply studied and put to wide applications since 1964, when europium doped yttrium vanadate ($YVO_4:Eu^{3+}$) was successfully proposed as a red phosphor for colour television tubes [1] and later also for luminescent lamps. This was the start of the nowadays overwhelming role of rare-earth ion luminescence in commercial phosphors [2]. This extensive interest has been inspired by both current and very promising potential applications of these phosphors due to qualities such as high quantum efficiency, anomalous long phosphorescence, and good stability [3,4].

For example, for scintillator applications, innumerable host lattices containing rare-earth ions as luminescent activators have been investigated because the 4f→5d transitions of these ions are parity-allowed, yielding fast optical transitions that are highly desirable in these applications. The fast relaxation is attributed to the ions' favourable energy configuration within the host lattice whereby the 4f and lowest 5d levels reside

within the normally forbidden crystalline band gap. Transfer of energy from radiation-induced electron-hole pairs to the luminescent ion is usually quite efficient, although quenching due to non-radiative electronic transitions may limit the overall luminescence efficiency of the phosphor [2]. A strong mechanoluminescent property, which can be utilized in the visualization of stress distribution and other mechano-optical devices, has also been reported by various authors [5]. In another example, thermographic phosphors have been extensively explored for remote temperature sensing measurements due to their accurate sensing capability over a wide range of temperatures, as well as their ability to withstand a harsh environment. This is exemplified in europium-doped yttrium oxide (Y_2O_3: Eu), which has been utilized for high temperature sensing within a rotating gas turbine [6,7], and managanese-doped magnesium fluorogermanate ($Mg_4(F)GeO_6$:Mn), which has been explored for thermal mapping of hotspots on the walls of a cryogenic fuel tank [8]. Problems associated with temperature-monitoring within a magnetic resonance imaging (MRI) scanner, particularly to an infant or a critical-care patient, has provided an impetus for the development of a phosphor-based optical sensor for human skin temperature sensing (27–37 ^{o}C) [9] within such an environment.

In particular, rare-earth metal ions doped strontium aluminate phosphors, e.g. $SrAl_2O_4$: Eu^{2+},Dy^{3+}, have attracted great interest for applications in the lamp, the cathode-ray tube (CRT), and the plasma display panel (PDP) due to their non-radiation and bright luminescence characteristics. One of the prominent applications of these phosphors is in the production of flat display panels (FDP), particularly plasma display panels (PDPs). FDP's are being successfully developed to replace the cathode-ray tube displays (CRTs) due to their capacity for faster response, wider viewing angle, larger screen, lower energy consumption, and higher scalability [10]. However, there still remain issues affecting operational parameters such as luminescence efficiency, stability against temperature, high colour purity, and perfect decay time that need to be resolved.

The solid-state reaction process has been used both intensively and extensively for phosphor synthesis, but this process often results in poor homogeneity and requires

high calcinating temperature. In addition, the slow diffusion processes in the solid-state reactions require the use of fluxing agents, like B(III) ions, to reduce the synthesis temperature in order to favour the formation of the monoclinic phase and avoid the stabilization of the hexagonal one. To increase the efficiency of light-emitting materials, new principles and methods of synthesis are used, in particular, the sol-gel method. Due to the easier composition control, better homogeneity, and low processing temperature, the sol–gel technique is a more suited approach for synthesizing fine phosphor powders. These advantages have led to greater use of this technique [11–13].

The great application potential of the temperature-dependence behaviour of aluminate luminescent materials gets compromised by the delicate nature of this property. Hence, it is imperative that a concerted effort is employed to better understand this important relationship. The aim of the work reported in this chapter was to use the sol-gel method for the synthesis of nanophase strontium aluminate phosphor powders activated by europium and dysprosium ions and to study the effect of annealing temperature on the phase composition and luminescence properties of the phosphor material. This line of research is interesting for two reasons: (1) It is known that various crystalline luminescent phases are formed in this system: $SrAl_2O_4$ [3,14], $SrAl_{12}O_{19}$ [15], $Sr_2Al_6O_{11}$ [16], and $Sr_4Al_{14}O_{25}$ [17]. (2) In the production of nano-phosphors by the sol-gel method, variations in annealing temperature are expected to have a profound effect on the degree of crystallization and transition of Eu^{3+} ions into Eu^{2+} state and vice versa.

8.2 Experimental procedure

The initial components for preparing homogeneous solutions were aluminium nitrate ($Al(NO_3)_2.9H_2O$), crystalline strontium nitrate ($Sr(NO_3)_2.4H_2O$), distilled water and nitric acid. It is important to state that other preparation conditions were fixed, so as not to contribute in any way. Gel formation and drying were performed at room temperature. Gels were heat-treated in a temperature interval of ambient – 1000 ^oC for 2 h in air, which is needed for the transition of europium ions into the bivalent state and strontium aluminates phase formation. Surface morphology and elemental composition of

the phosphor powders were investigated using scanning electron microscopy (SEM) and energy dispersive x-ray spectroscopy (EDS) on a Shimadzu Superscan SSX-550 coupled with an EDS system. Phase and crystallinity of the synthesized compositions were investigated by powder XRD using a Bruker D8 (Bruker Co., Germany) x-ray diffractometer (XRD) with CuK_α (λ = 1.5406 Å). The photoluminescence (PL) excitation and emission spectra were taken on a Cary Eclipse fluorescence spectrophotometer equipped with a monochromatic xenon lamp. Each sample was loaded into a circular holder and excited with 340 nm radiation from a pulsed xenon lamp. The emission spectra were scanned in the range from 360 to 750 nm.

8.3 Results and discussion

The results of the morphological studies along with chemical composition determination, which were determined using the SEM coupled with EDS, are shown in Fig. 8.1 and 8.2, respectively. Fig. 8.1 represents the SEM micrographs of the 1000°C sample at 500× and 5000×

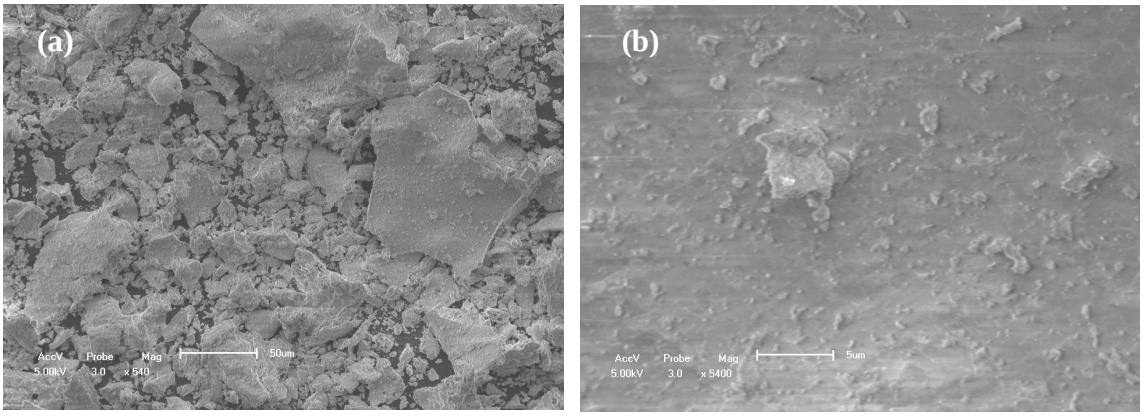

Figure 8.1: SEM images of the 1000˚C sample of $SrAl_xO_y:Eu^{2+},Dy^{3+}$ with (a) 500× magnification, (b) 5000× magnification

magnifications, respectively. The micrographs clearly indicate the presence of submicron crystallites. Fig. 8.1(a) shows irregularly sized and shaped grains with discernible micropores. The crystallite size distribution is wide. Fig. 8.1(b) shows a generally smooth

and shiny surface, containing encrustations of smaller particles. The smooth and shiny layer of the crystallites is indicative of the melting morphology generated by a solid-liquid reaction at high temperature. Fig. 8.2 illustrates the EDS results of the unannealed and the 1000 °C annealed samples, respectively. The chemical composition of the samples is relatively unaffected by the change in temperature.

The x-ray diffraction patterns of the as-prepared $SrAl_xO_y:Eu^{2+},Dy^{3+}$polycrystal specimens, sintered at different temperatures, 200, 500, and 1000 °C, are shown in Fig. 8.3(a). The crystal structure is not significantly different between all these samples, indicating that the pure monoclinic phase of $SrAl_2O_4$ has already formed in the first sol-gel process at room temperature. Although no flux is added to the starting materials, an $SrAl_2O_4:Eu^{2+},Dy^{3+}$ phase with high purity was obtained at room temperature through the

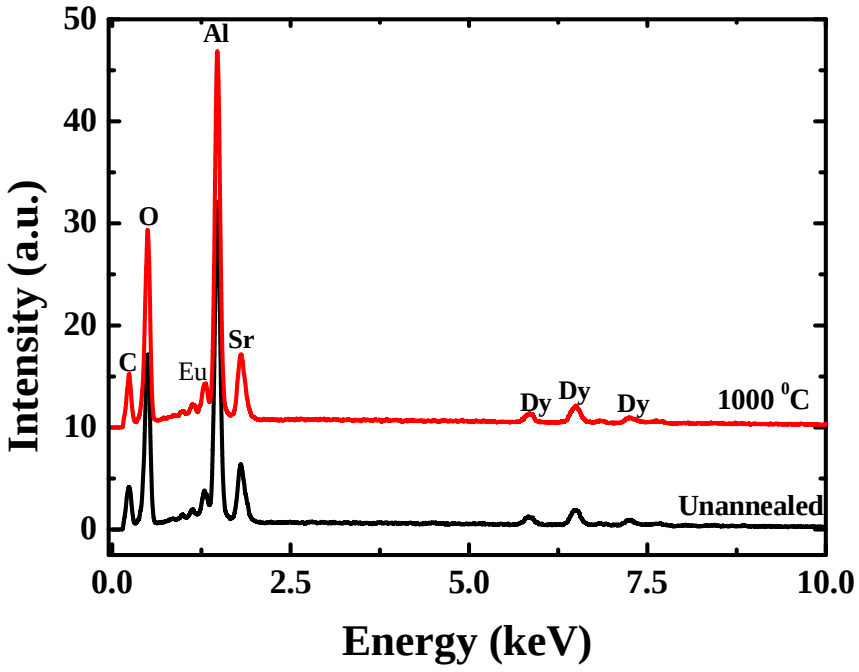

Figure 8.2: EDS results of the unannealed and 1000°C annealed samples of $SrAl_xO_y:Eu^{2+},Dy^{3+}$

sol-gel technique, which is not easily achievable by the solid-state reaction and combustion methods due to impurities that are formed at lower temperatures. As can be

seen from the XRD patterns, pure monoclinic phase diffraction peaks of $SrAl_2O_4$ are seemingly predominant. Other products or starting materials were also observed, implying that the phase compositions of the precursor powders do not consist of low-temperature monoclinic phase (α-phase) only. This mixed phase could be attributed to the ratio of Sr to Al used in the precursor. It is known that the presence of the little amount of doped rare-earth ions has almost no effect on the $SrAl_2O_4$ phase composition [18] but, of more

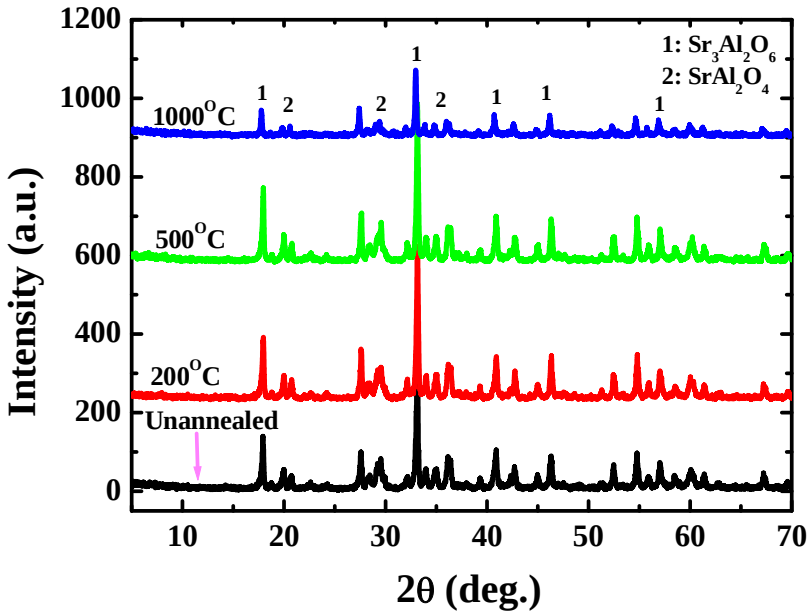

Figure 8.3(a): XRD spectra of the samples at the various temperature values

importance, the annealing temperature had a significant effect on the degree of crystallization. As the annealing temperature increased from ambient temperature to 200 °C, the intensity of the x-ray diffraction peak increased. After 200 °C the diffraction peaks, especially those of the low-temperature monoclinic phase (α-phase), were significantly reduced, therefore affecting the luminescent property of the samples. Also accompanying the increasing temperature, from ambient to 1000 °C, is the enlargement in the crystallite sizes. The Scherrer equation relates the width of the peaks in an x-ray powder diffraction pattern to crystal size. The average crystallite sizes of the phosphors, which were determined from the equation, vary between 42.2 ± 8 nm to 47.2 ± 10 nm.

Similar results (40–50 nm) were observed by Lu *et al* and Arturo *et al*. [19,20], who used the microemulsion method for synthesis, with post–annealeing treatment of their samples,

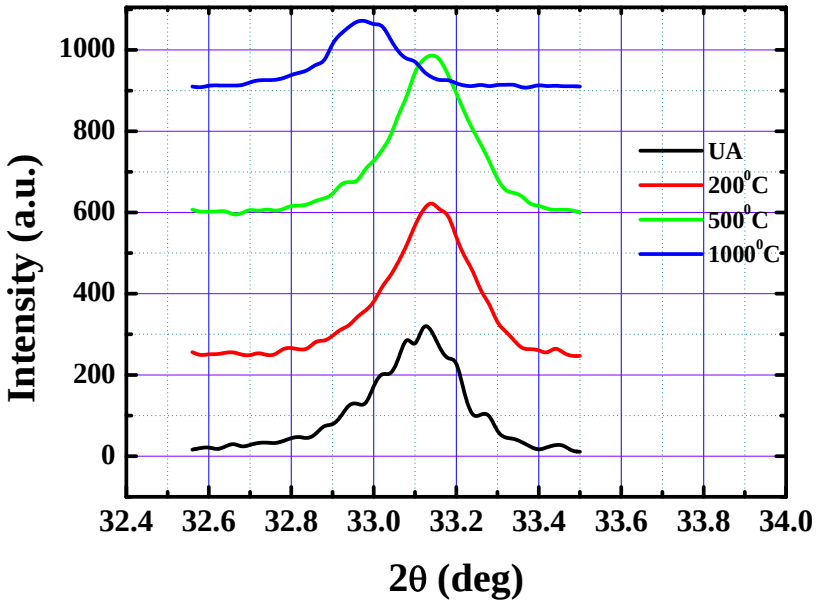

Figure 8.3(b): XRD maximum intensity peaks ($32.6^o<2\theta<33.6^o$)

between 800 and 1000 °C. They attributed the small particle sizes to a cage effect, in which the constituent cations are confined by nano-scaled micelles, which restricted the particle growth. Using the peak for the reflection plane at 33^o (Fig. 8.3(b) and Table 8.1), two features can be illustrated: the peak-narrowing due to crystallite growth and the shifting in peak position due to the increased crystallinity.

Table 8.1: Full width at half maximum (FWHM) values for the reflection at 33^o

Temperature (°C)	UA	200	500	1000
FWHM (degrees)	0.20	0.19	0.18	0.16

Fig. 8.4 shows the excitation spectra of the prepared $SrAl_xO_y:Eu^{2+},Dy^{3+}$ phosphor samples with the emission wavelength fixed at 515 nm, which is the characteristic wavelength for the energetic transitions of Eu^{2+}. Broad bands with varying maximum

values were observed. The unannealed and 200 °C samples, which had the relatively high intensities, the spectra peaked at around 350 nm. The broad bands correspond to the $4f^6 5d \rightarrow 4f^7$ energy level transitions of the Eu^{2+} electron lying in the band gap region of the host matrix [21]. The emission spectra, monitored with an excitation wavelength of 340 nm, are shown in Fig. 8.5. This wavelength is suitable for excitation of Eu^{2+} rather than Eu^{3+}. For temperatures below 600 °C, broad emission peaks were

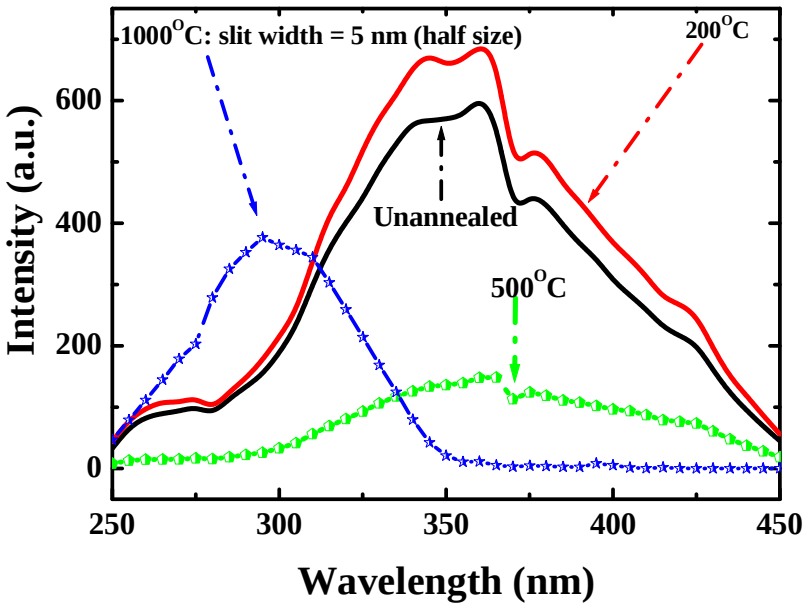

Figure 8.4: Excitation spectra of $SrAl_xO_y:Eu^{2+},Dy^{3+}$ at various annealing temperature values

observed at around 515 nm, revealing the characteristic emission of the Eu^{2+} activators ($4f^6 5d^1 \rightarrow 4f^7$ ($^8S_{7/2}$)) parity-allowed transition [22]. As the annealing temperature increases, not only a very broad emission band due to Eu^{2+}, but also relatively narrow lines ascribed to Eu^{3+}, are observed. The effect of annealing on photoluminescence emission intensity of as prepared phosphors is easily observable from the measurements. Annealing the phosphors at 200 °C slightly enhanced the luminescence, while further increase in temperature significantly quenches the luminescence. When annealed at around 1000 °C, the type of luminescence changes from broad to several sharp peaks. The relatively sharp emission lines at around 600 nm are attributable to the 4f–4f

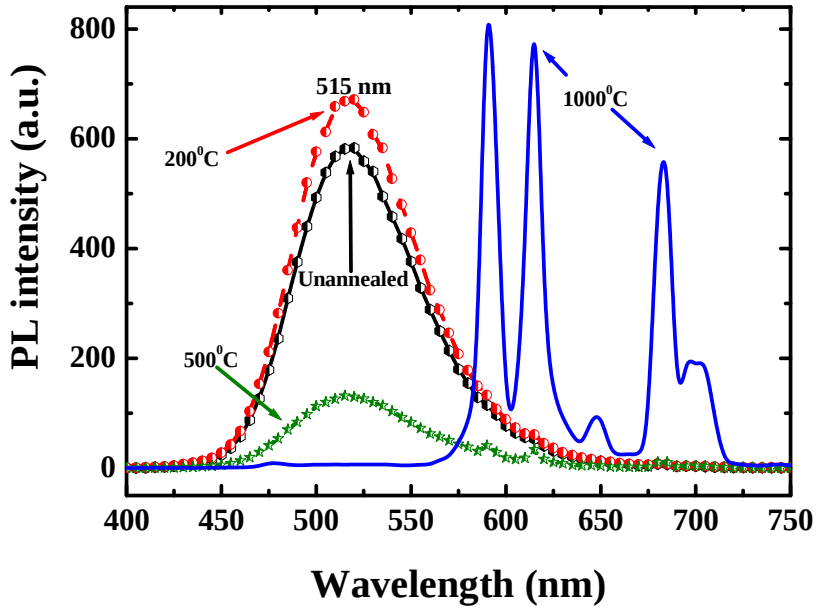

Figure 8.5: Emission spectra of $SrAl_xO_y:Eu^{2+},Dy^{3+}$ at the various annealing temperature values

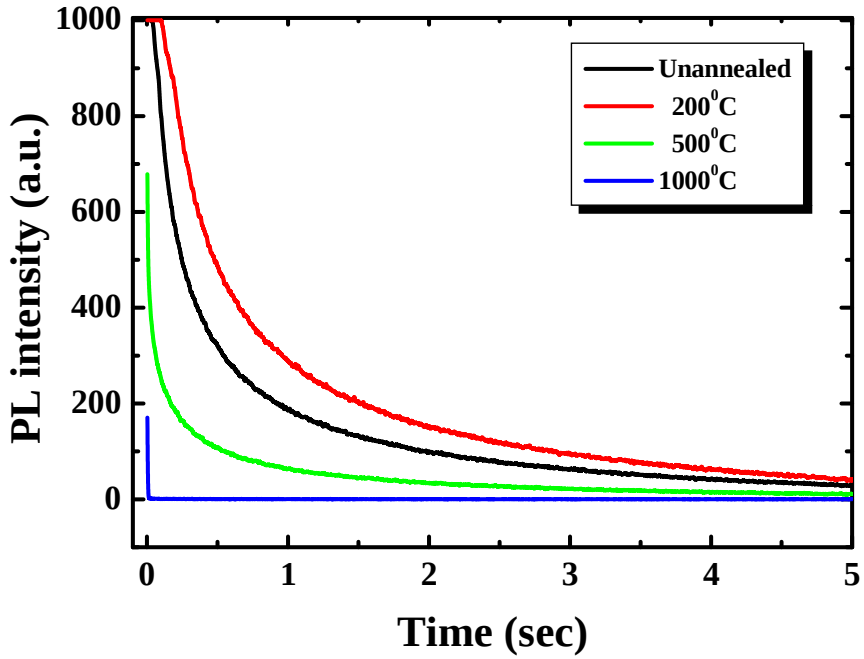

Figure 8.6: Decay curves of $SrAl_xO_y:Eu^{2+},Dy^{3+}$ phosphor samples annealed at different temperature values after exciting for 5 min

transitions of Eu^{3+}. The $^5D_0 \rightarrow {}^7F_0$, $^5D_0 \rightarrow {}^7F_1$, and $^5D_0 \rightarrow {}^7F_2$ transitions of Eu^{3+} are observed as emission lines at 585, 621, and 650 nm, respectively.

Significant variations in the light output as well as the quantum efficiency of some phosphor materials have been observed to occur with changes in temperature. These changes may result in degradation during processing or operation of certain devices. In the case of the blue-emitting $BaMgAl_{10}O_{17}:Eu^{2+}$ phosphor for PDP application, degradation due to temperature effects is considered to be related to its host lattice and the Eu^{2+} activator ion [23]. This degradation has been attributed mainly to the oxidation of the Eu^{2+} ion resulting in the production of a trivalent europium oxide ion, which is inefficient and is in some cases hardly visible in the emission spectrum [24]. The photoluminescence spectrum of a luminescent material shows characteristic temperature-dependence; as the temperature is increased the emission peak shifts to lower energy, the emission band is broadened, and the emission intensity is quenched at some temperatures [25]. The temperature dependence of the electron–phonon interaction in both the ground state and the excited state of the luminescence centre is the origin of these phenomena [26].

Fig. 8.6 shows the decay characteristics of the $SrAl_xO_y:Eu^{2+},Dy^{3+}$ phosphor annealed at different temperatures. The results show that both the initial luminescence intensity and decay time of afterglow of phosphors are enhanced when annealed at 200 °C. However, further increase in temperature reduces these two properties. The sample annealed at 1000 °C completely quenches the afterglow property of the phosphor. Except for the sample annealed at 1000 °C, all the samples show a rapid initial decay and subsequent long-lasting phosphorescence, which can be analyzed by a curve fitting procedure relying on the following triple exponential equation:

$$I = I_1 \exp\left(-\frac{t}{\tau_1}\right) + I_2 \exp\left(-\frac{t}{\tau_2}\right) + I_3 \exp\left(-\frac{t}{\tau_3}\right), \quad (1)$$

where I represents the phosphorescent intensity; I_1, I_2, and I_3 are constants; t is the time; τ_1, τ_2, and τ_3 are the decay constants deciding the decay rate for the rapid, medium, and

slow exponential decay components, respectively. The fitting results of the τ_1 and τ_2 parameters are listed in Table 8.2.

The decay constants have higher values for the 200 °C sample but completely vanish for the 1000 ˚C sample. It is known that trap depth greatly influences the recombination between the excited electrons and trapped holes. Consequently, the decay components are determined by the carriers, which are trapped at different trapping levels. The long afterglow property of the phosphor samples can be described in terms of these carriers, whose nature is considered to be holes [14,27]. Upon exposure of phosphors to the excitation radiation, direct excitation of the 4f–5d transition of Eu^{2+} happens and plenty of holes are created; some of the free holes are released thermally to the valence

Table 8.2: Results for fitted decay curves of $SrAl_xO_y:Eu^{2+},Dy^{3+}$ samples at different temperatures

Temperature (°C)	UA	200	500	1000
Component	Decay constants (s)			
Fast (τ_1)	0.19	0.19	0.02	-
Medium (τ_2)	0.88	0.88	0.22	-
Slow (τ_3)	3.31	3.31	2.01	-

band, meantime, one part of the released holes travel through the valence band, and are trapped by Dy^{3+} ions [28]. When the excitation source is removed, the excited Eu^{+1} ion is relaxed to the metastable state $(Eu^{+1})^*$. The trapped holes are released thermally to the valence band and move to recombine with the excessive electrons in the metastable state $(Eu^{+1})^*$ sites leading to the long afterglow [29].

8.4 Conclusions

In this work, the sol-gel procedure was successfully employed to synthesize nanophase $SrAl_xO_y:Eu^{2+},Dy^{3+}$ phosphor powders. The average crystallite sizes increased

from 42.2 ± 8 nm to 47.2 ± 10 nm as the heating temperature increased from room temperature to 1000°C, indicating an increase in crystallinity. The effect of annealing temperature on the transformation in phase composition is not conclusive but the dominance of the $SrAl_2O_4$ polymorph is evident from the reflections in the XRD results. Luminescent results show variations in the peak shapes, positions, and intensities of the excitation and emission spectra as well as the afterglow behaviour of the samples. This reflects the profound influence of annealing temperature on these properties, which may be traced to transitions between trivalent (Eu^{3+}) and divalent (Eu^{2+}) europium states that originate from changes in the crystal field around the ions.

8.5 References

1. Levine, A.K. Palilla, F.C. *Appl. Phys. Lett.*, **5:** 118, (1964).
2. Blasse, G. Grabmaier, B.G. *Luminescent Materials*, Springer, Berlin, (1994).
3. Palilla, F.C. Levine, A.K. Tomkus, M.R. *J. Electrochem. Soc.*, **115:** 642, (1968).
4. Blasse, G. Bril, A. *Philips Res. Rep*., **23:** 201, (1968).
5. Xu, C.N. Zheng, X.G. Akiyama, M. Nonaka, K. Watanabe, T. *Appl. Phys. Lett*., **76:** 179, (2000).
6. Ranson, R.M. Thomas, C.B. Craven, M.R. *J. Meas. Sci. and Tech*., **9:** 1947-1950, (1998).
7. Ranson, R.M. Evangelou, E. Thomas, C.B. *Appl. Phys. Lett*., **72:** 2663, (1998).
8. Beshears, D.L. Capps, G.J. Simmons, C.M. Schwenterly, S.W. *Laser-induced Fluorescence of Phosphors for Remote Cryogenic Thermometry*. (1990).
9. Jansky, L. Vavra, V. Jansky, P. Kunc, P. Knizkova, I. Jandova, D. Slovacek, K. *J. Therm. Biol*., **28:** 429, (2003).
10. Kim, C.H. Bae, H.S. Pyun, C.H. Hong, G.H. *J. Korean Chem. Soc*., **5/42:** 588, (1998).
11. Atkinson, A. Segal, D.L. *J. Sol–Gel Sci. Technol*., **13:** 133, (1998).
12. Chen, I.C. Chen, T.M. *J. Mater. Res.*, **16:** 644, (2001).
13. Chen, I.C. Chen, T.M. *J. Mater. Res*., **16:** 1293, (2001).
14. Abbruscato, V. *J. Electrochem. Soc*., **118**(6)**:** 930, (1971).
15. Singh, V. Rao, T.K.G. Zhu, J.J. *J. Solid State Chem*., **179:** 2589, (2006).
16. Smets, B. Rutten, J. Hoeks, G. Verlijsdonk, J. *J. Electrochem. Soc*., **136**(7)**:** 2119, (1989).
17. Kemenade, J.T.C. Hoeks, G.P.F. *The Electrochemical Society Extended Abstracts*, **83-1:** Abstract 607, San Francisco, CA, May 8–13, 914, (1983).
18. Lin, Y. Zhang, Z. Zhang, F. Tang, Z. Chen Q. *Chem. Phys*., **65:** 103, (2000).
19. Lu, C.H. Chen, S.Y. Hsu, C.H. *Mat. Sci. and Eng. B.*, **140:** 218, (2007).
20. Arturo, M. Quintela, L. *J. Colloid Interface Sci.*, **8:** 137, (2003).
21. Kim, J.S. *J. Cer. Proc. Res*., **10**(4)**:** 443, (2009).

22. Cordoncillo, E. Julian-Lopez, B. Martínez, M. Sanjuán, M.L. Escribano, P. *J. Alloys Comp*., **484:** 693, (2009).
23. Lange. H. *U.S. Patent*, No. 3, 294, 699, (1966).
24. Oshio, S. Kitamura, K. Nishiura, T. Shigeta, T. Horii, S. Matsuoka, T. *Nat. Tech. Rep*., **43:** 69, (1997).
25. Kamada, M. Muarakami, J. Ohno, N. *J. Lumin.*, **87–89:** 1042, (2000).
26. Matsushima, S. Nakamura, H. Arai, M. Xu, C.N. *Chem. Lett*., **7:** 700-701, (2002).
27. Matsuzawa, T. Aoki, Y. Takeuchi, N. Murayama, Y. *J. Electrochem. Soc*., **143:** 2670, (1996).
28. Swart, H.C. Terblans, J.J. Ntwaeaborwa, O.M. Coetsee, E. Mothudi, B.M. Dhlamini, M.S. *Nucl. Inst. Meth., B.*, **267:** 2630, (2009).
29. Chen, R. Wang, Y. Hu, Y. Hu, Z. Cheng, L. *J. Lumin.*, **128:** 1180, (2008).

Chapter 9

Characterization of Luminescent and Thermal Properties of Long-afterglow $BaAl_xO_y:Eu^{2+},Dy^{3+}$ Nanoparticles and Polymer Composites

9.1. Introduction

Although extensive research on aluminate phosphors has been undertaken over the years, the Eu^{2+},R^{3+} co-doped barium aluminates such as $BaAl_xO_y:Eu^{2+},Dy^{3+}$ [1,2] have been studied only infrequently, even though they have potential for persistent luminescence. The reasons may be attributed to the rather complicated structural chemistry of the MAl_2O_4 host as well as the considerable size mismatch between the host (Ba^{2+}) and the main dopant (Eu^{2+}) cations [3]. On the other hand, the crystal structures of the compounds studied in this work are all derivatives of the stuffed tridymite structure (Fig. 9.1). In this type of structure there are large open channels in the framework, which provide suitable sites for large cations to lodge themselves. These channels are sources of the structural weakness, which, can ultimately result in degradation.

The aim of the work reported in this chapter, was to prepare $BaAl_2O_4:Eu^{2+},Dy^{3+}$ phosphor materials at different Eu^{2+} and Dy^{3+} concentrations by means of a combustion method. The effects of the Eu^{2+}:Dy^{3+} molar ratio on the structure, homogeneity, persistent

luminescence as well as stability are presented and discussed based on the analyses of the x-ray powder diffraction, SEM imaging and photoluminescence studies. In addition to the

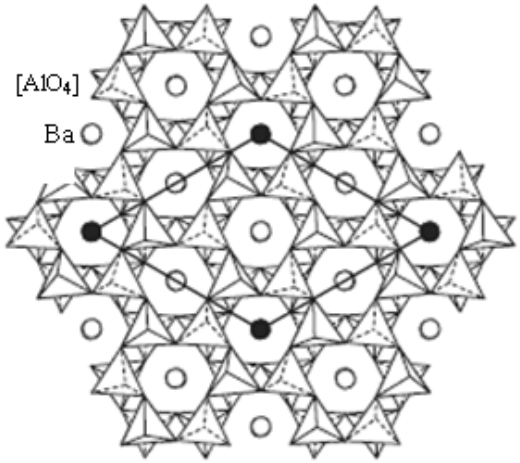

Figure 9.1: $BaAl_2O_4$ structure viewed along [0001]. The solid lines depict the unit cell. The closed circles indicate Ba atoms at the special position (2a) site [4].

synthesized $BaAl_xO_y:Eu^{2+},Dy^{3+}$. In addition to the synthesized $BaAl_xO_y:Eu^{2+},Dy^{3+}$ powder, polymer/phosphor composites of well-defined compositions were also prepared and studied. This second part of work was motivated by: (i) the possibility of combining the merits of organic and inorganic materials into systems with novel properties, (ii) the promising results from previous work by this group [5].

9.2 Experimental Section

9.2.1 Synthesis of the $BaAl_xO_y:Eu^{2+},Dy^{3+}$ phosphor samples

Barium aluminate samples were prepared by a combustion synthesis method. Powders of $Ba(NO_3)_2$ (A.R.), $Al(NO_3)_3{\cdot}9H_2O$ (A.R.), $Eu_2(NO_3)_3$ (4N), CH_4N_2O (A.R. added as fuel) were used as starting materials. Eu^{3+} was introduced in the form of $Eu(NO_3)_3.5H_2O$. A homogeneous, thick, white solution was obtained after thoroughly milling the precursor mixture in a mortar using a pestle. Formation of the solution was facilitated by the water of crystallization present on the metal nitrates. The solution was then introduced into a muffle furnace maintained at 500 °C. Initially, the paste boiled and underwent dehydration, followed by decomposition with large amounts of gases

escaping. Spontaneous ignition then occurred and the material underwent smouldering combustion with enormous swelling. The whole process was over in about 5 minutes. The voluminous and foamy combustion ash was easily milled to obtain the final $BaAl_xO_y:Eu^{2+},Dy^{3+}$ phosphor powder.

9.2.2 Preparation of $BaAl_xO_y:Eu^{2+},Dy^{3+}$/LDPE nanocomposites

Linear low-density polyethylene (LDPE) was supplied by Sasol Polymers, South Africa. It has a melt flow index (MFI) of 2.0 g/10 min, which was determined by preheating a sample of the polymer at 190 °C for 5 minutes followed by a shear analysis on a 2.16 kg mass. It has a melting point of about 110ºC, and a density of 0.922 gcm^{-3}. The polymer/phosphor composites were produced by melt-mixing the synthesized barium aluminate phosphor powder into LDPE at volume ratios ranging from 0.4% to 10%. Samples were weighed according to the required ratios and mixed using a volume of 50 cm^3 in a Brabender Plastograph mixing chamber at a screw speed of 30 rpm for 15 minutes. The mixing was carried out at 160 °C. The samples were hot melt-pressed into slabs of average thickness 0.98 ± 0.05 mm, at 160 °C.

9.2.3 Morphology and structural analysis

Microstructural and elemental composition characterization of the $BaAl_2O_4:Eu^{2+},Dy^{3+}$particles were performed on a Shimadzu model ZU SSX–550 Superscan scanning electron microscope (SEM), coupled with an energy dispersive x-ray spectrometer (EDS). For SEM measurements, the probe size was 3.0 nm, the probe current 0.02 nA, and the accelerating voltage 5.0 keV. The probe size for EDS analysis was 4 nm, specimen current 1.00 nA, and accelerating voltage 15.0 keV.

Crystalline phases were characterized by an x-ray diffractometer (Bruker D8 diffractometer, Bruker Corporation of Germany, operating at 40 kV and 40 mA, and using Cu K_α = 1.5406 Å) with a scan step of 0.02° in 2θ and a scan speed of 4°/min. The divergence slit (DS), scatter slit (SS), and receiving slit (RS) are 1°, 1°, and 0.15 mm,

respectively. The average crystallite size of the materials was calculated from the diffraction data by using the Scherrer equation (Eq. 1) [6].

$$D = \frac{0.9\lambda}{\beta \cos\theta} \qquad (1)$$

where D is the average crystallite size in metres, λ the x-ray wavelength in metres, β the full width at half maximum (FWHM) of the selected reflection in radians, and θ (in degrees) is half of the Bragg angle (2θ). The calculation is based on the measurement of full-width at half-maximum (FWHM) values in the corresponding XRD pattern.

9.2.4 Photoluminescence (PL) measurements

The excitation, emission, and decay spectra were measured at room temperature on a Varian Cary Eclipse Fluorescence spectrophotometer (Model: LS 55) with a built-in 150 W Xe flash lamp as the excitation source and a grating to select a suitable wavelength for excitation. Each sample was loaded into a circular holder and excited with 340 nm radiation.

9.2.5 Thermal analysis

For thermal analysis, differential scanning calorimetry (DSC) and thermogravimetric analysis (TGA) were performed using the the same measurement systems as well as procedures as described in the previous chapters.

9.3 Results and discussion

9.3.1 SEM micrographs and EDS spectra

The microstructures of $BaAl_xO_y:Eu^{2+},Dy^{3+}$ powders are shown in the SEM micrographs in Fig. 9.2. Figs. 9.2(a) and (b) depict the SEM images of the as-synthesized phosphor powders for low (a) and high (b) Dy^{3+} concentrations, respectively. The magnification is 10000× in both images. An inspection of the morphology of the samples

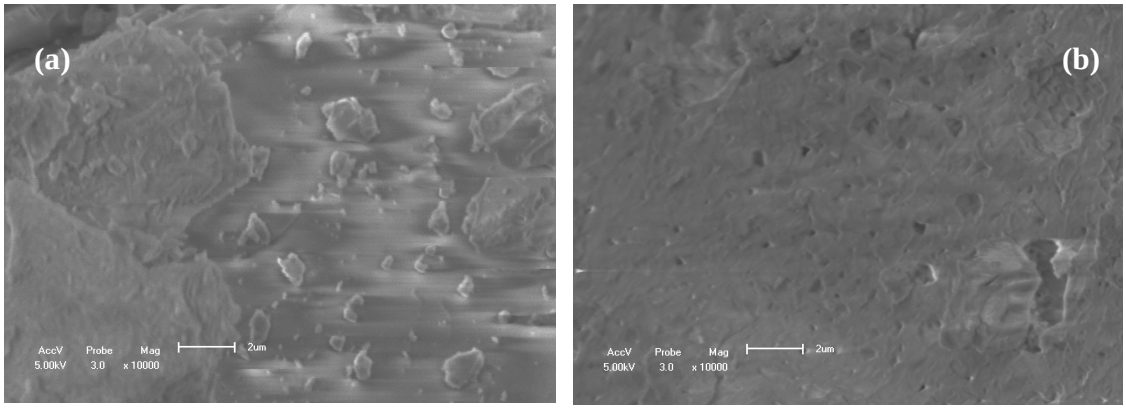

Figure 9.2: 10000× magnification SEM micrographs of as-synthesized $BaAl_xO_y$: Eu^{2+},Dy^{3+} with Eu^{2+}:Dy^{3+} ratio = (a) 10:1 and (b) 1:10.

reveal that the powders are characterized by flakes up to 10 μm diameter. The surfaces of the samples show voids and pores formed by the escaping gases during the combustion process. When a gas is escaping under high pressure, pores are formed with the formation of small particles near the pores. The formed gas transports heat away from the forming product, thus limiting the particle growth. The wide particle-size distribution as well as irregular shapes of the particles is probably due to the nonuniform distribution of temperature and mass flow in the combustion wave.

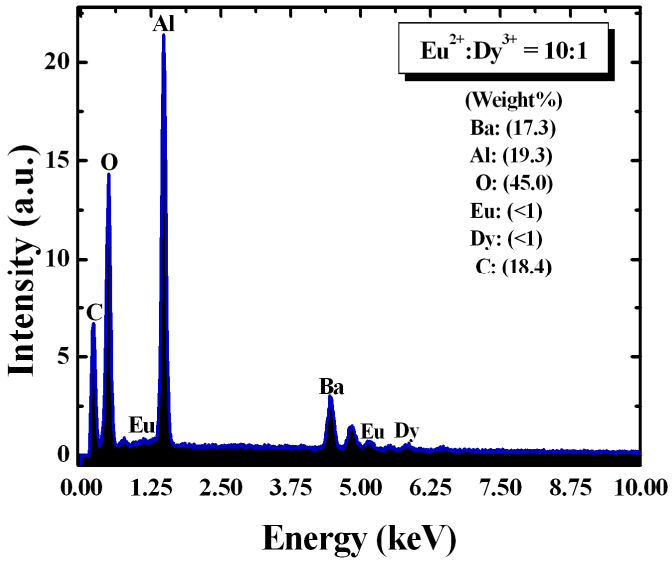

Figure 9.3: EDS spot analysis results for the $BaAl_xO_y$:Eu^{2+},Dy^{3+} powder sample with 10:1 Eu^{2+}:Dy^{3+} ratio

Energy dispersive spectroscopy (EDS) is a standard procedure for identifying and quantifying elemental composition of sample areas as small as few micrometres [7]. Fig. 9.3 shows the EDS spectra of the sample with 10:1, Eu^{2+}:Dy^{3+} molar ratio. The existence of Eu in the samples is clear in the corresponding EDS spectra. No other elements were detected in the EDS emissions apart from Ba, Eu, O, Dy, Al, and C. The elements appear in ratios concomitant with the proportions mixed in the starting materials, which shows the advantage of the combustion method in controlling chemical components.

9.3.2 X-ray diffraction (XRD)

Generally, it is well known that the luminescence properties of phosphor particles are strongly dependent upon the characteristics of the prepared phosphors such as particle size [8], surface morphology [9], concentration quenching [10], and crystallinity [11]. Crystallinity is one of the most important parameters to obtain phosphor particles with high luminescence efficiency.

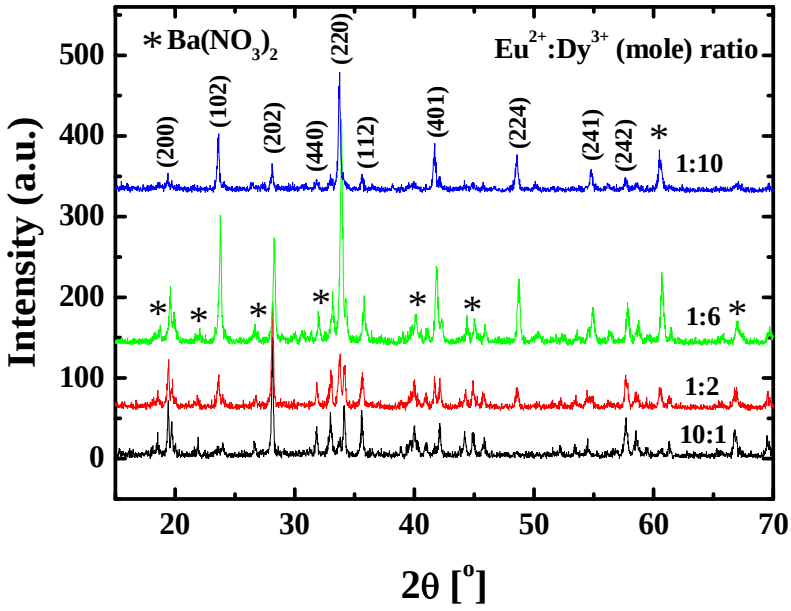

Figure 9.4(a): XRD spectra of $BaAl_xO_y$:Eu^{2+},Dy^{3+} powder samples for various Eu^{2+}:Dy^{3+} ratios

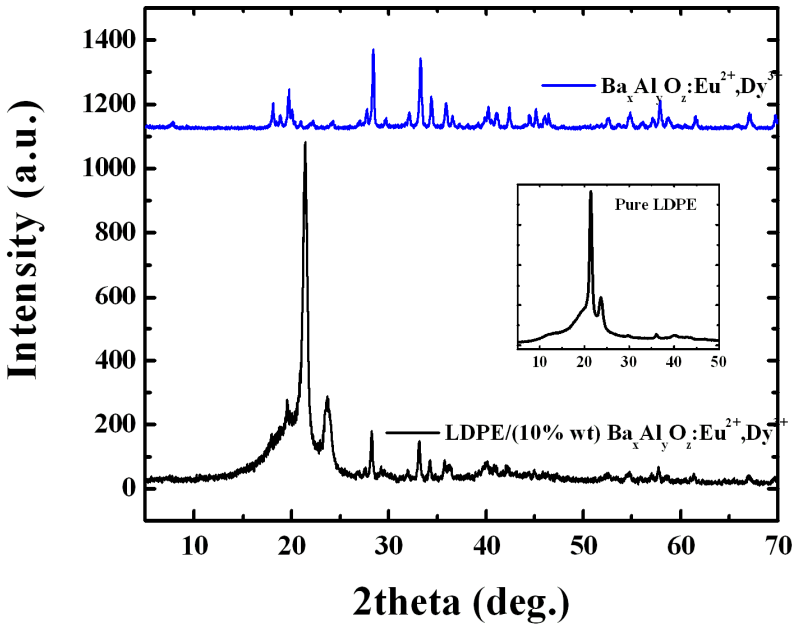

Figure 9.4 (b): XRD spectra of $BaAl_xO_y:Eu^{2+},Dy^{3+}$ phosphor samples with $Eu^{2+}:Dy^{3+}$ molar ratio = 2:1, and composite of LDPE with 10% $BaAl_xO_y:Eu^{2+},Dy^{3+}$. [Inset – XRD spectrum of pure LDPE].

The x-ray powder diffraction (XRPD) technique is an effective tool for determining the phase, crystallinity, and purity of samples prepared under various conditions. Fig. 9.4 is a display of the XRD results for the $BaAl_xO_y:Eu^{2+},Dy^{3+}$ nanophosphor samples. The broad peaks clearly indicate that nanoparticles were obtained. The spectra clearly show the presence of the expected hexagonal crystalline phase for the nanopowders. The main diffraction peaks index well with the card file (JCPDS:17-0306) in agreement with other reports [12,13]. Crystallite size estimation based on the Scherrer analysis yielded values ranging between 34 and 41 ± 4 nm.

9.3.3 Photoluminescence spectra

PL measurements were carried out in order to determine the luminescent properties of the as-prepared aluminate phosphor samples as well as those of the LDPE/$BaAl_xO_y:Eu^{2+},Dy^{3+}$ nanocomposites. Figs. 9.5 and 9.6 display the excitation and emission spectra for the phosphors and the nanocomposites, respectively. The

photoluminescence spectra exhibit different shapes and broadband peaks. The wavelength bands in the excitation spectra are broad with wavelengths ranging from 275 to 445 nm while the corresponding blue-green emissions consist mainly of symmetrical

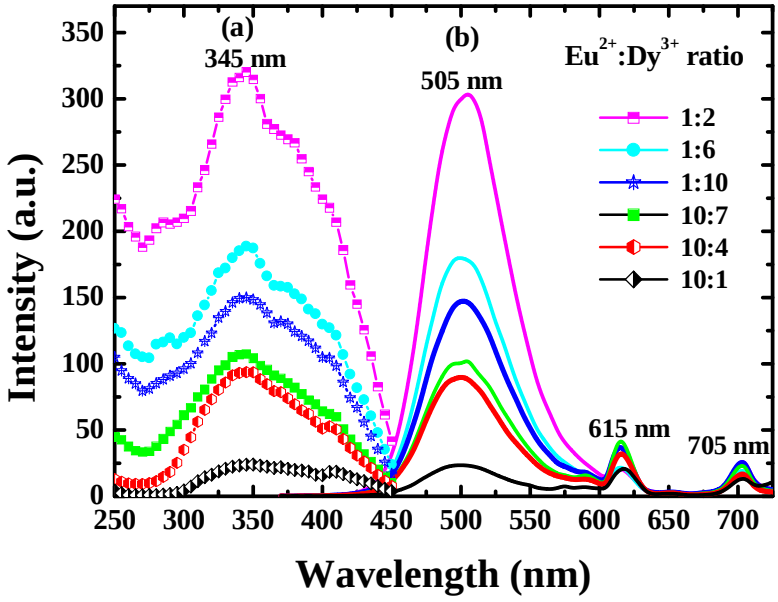

Figure 9.5: PL (a) excitation (λ_{em}= 505) nm and (b) emission (λ_{exc}= 340 nm), spectra of $BaAl_xO_y:Eu^{2+},Dy^{3+}$ phosphor for $Eu^{2+}:Dy^{3+}$ ratio = 10:1 – 1:10.

bands with major peaks having maxima at 505 nm that originate from the energy transitions between the ground state ($4f^7$) and the excited state ($4f^65d^1$) of the Eu^{2+} ions [14]. The minor peaks at 615 and 705 nm arise from the f-f transitions of the remnant, unreduced Eu^{3+} ions.

The photoluminescence in rare earth-doped alkaline earth aluminates originates in the electronic transitions in the rare-earth ions. The luminescence may be attributed to one of three possible processes as a result of transitions in either 4f energy levels, $4f^{n-1}5d^1$ states or charge-transfer states. In the case of doping with Eu^{2+} ions, luminescence is due to $4f^7 \rightarrow 4f^65d^1$ transitions in Eu^{2+}. $4f \leftrightarrow 5d$ transitions are electric dipole allowed optical transitions and correspond to strong optical absorption. During excitation, 4f electrons get transferred to the 5d orbital, which is split into a number of levels due to the crystal field. The 4f electrons of Eu^{2+} are not sensitive to the lattice environment due to the shielding

function of the outer shell, but the 5d electrons may couple strongly to the lattice. Consequently, the mixed states of 4f5d will be split by the crystal field and will couple strongly to the lattice phonons, resulting in broadband absorption and emission. On the other hand, it is known that different host structures and crystallographic distortions will influence the crystal field environment of rare-earth ions in the host structure [15]. Since the crystal field splitting varies considerably depending upon the host material, the spectral position of the excitation band would also change. In this work the excitation spectrum at each concentration is broad with a peak at around 340 nm. A concentration-dependent shoulder also appears at 275 nm.

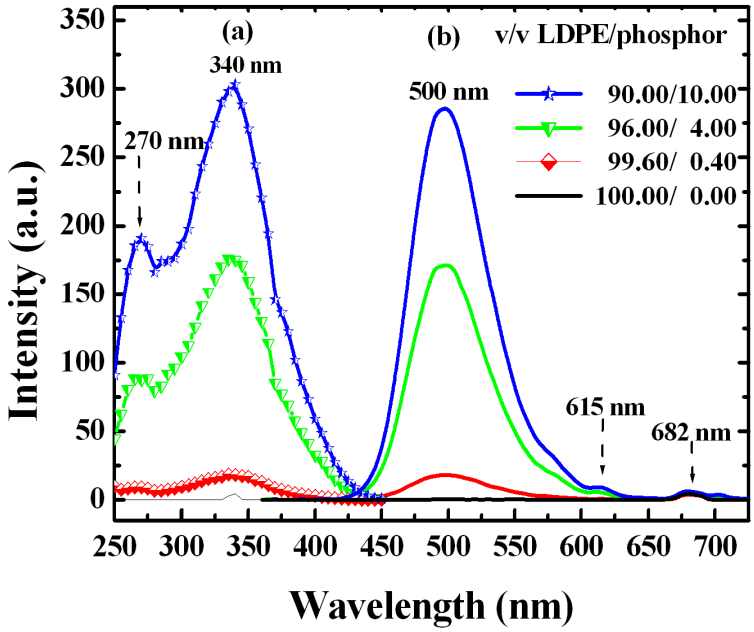

Figure 9.6: PL (a) excitation (λ_{em} = 500 nm), and (b) emission (λ_{exc} = 340 nm), spectra of LDPE/$BaAl_xO_y$:Eu^{2+},Dy^{3+} composites for Eu^{2+}:Dy^{3+} ratio = 1:2.

The PL curves for the phosphor materials (Fig. 9.5) show that the peak wavelength of the phosphorescence does not vary significantly with the concentration of the dopants. This implies that the crystal field, which affects the 5d electron states of the Eu^{2+} ions, is not changed dramatically by the concentration variations in the phosphors. Unlike the excitation bands, the emission bands do not only depend on the crystal field splitting of the 5d level and the 4f→5d de-excitations. In a given host, the emission of Eu^{2+} is also significantly influenced by the size of the host cation (Ba^{2+} in this case),

which is replaced by Eu^{2+}. The ionic size of Eu^{2+} (1.20 Å) is smaller than the radius of the Ba^{2+} ion (1.38 Å). Hence, when Eu^{2+} substitutes for Ba^{2+} in $BaAl_xO_y$, the Eu^{2+} ion experiences a reduced attraction owing to shrinkage of the crystal lattice. Anamorphic crystal lattices result when the surroundings of Eu^{2+} are changed and so the emission wavelengths change correspondingly [2,16].

Two Ba^{2+} sites are believed to exist in the $BaAl_2O_4$ crystal structure. However, the symmetry of the emission bands in the observed results illustrate the presence of one kind of luminescent centre in the $BaAl_xO_y:Eu^{2+},Dy^{3+}$, where the Eu^{2+} ions are substituted with the nine-coordinated Ba^{2+} sites [17]. Of the two expected Ba^{2+} sites, the first one (2a) has a multiplicity of two and a site symmetry of C_3 while the second one (6c) has a multiplicity of six and a site symmetry of C_1. Both the Ba^{2+} sites have nine-coordination and the sites are similar in average size (d(Ba–O)Ave = 2.86 and 2.87 Å). However, the lower symmetry site has also shorter Ba–O distances (2.69 Å) corresponding to those typical of Eu^{2+}–O (2.68 Å [18]). These differences imply that the 6c site will be filled preferentially leading to a corresponding higher PL intensity as a result of a contribution from six instead of two Eu^{2+} ions. The emission wavelength (505 nm) is consistent with the result derived from the ceramic method by Lin *et al.* [19] but slightly higher than the 500 nm obtained by Stefani *et al*., who also observed a minor peak at 435 nm using the solid state reaction method [20], and the 496 nm by Qiu *et. al.* (microemulsion) [21].

Though the mechanism of persistent luminescence in lanthanide ions-doped alkaline earth aluminates is not fully understood, it is agreed that the Eu^{2+} ion is the luminescent centre, while the R^{2+} and R^{3+} ions have been suggested to trap holes and electrons, respectively [22]. The mechanism is considered to include the photoionization of the Eu^{2+} ions and a subsequent transfer of the electrons to traps formed by the lattice defects as oxide ion vacancies and possibly also the auxiliary R^{3+} ion co-dopants. The thermal bleaching of the electrons from the traps followed by the process reverse to the storage of the excitation energy leads to the Eu^{2+} emission [23].

The mechanisms explaining the enhanced luminescence emission, as well as the photoluminescence quantum efficiency when nanoparticle-filled polymer composites act as the active emitting layer, are not particularly clear. Initially, optical scattering from the nanoparticle surfaces was believed to be a factor but was excluded since it could not explain some phenomena such as the observed radiance enhancement in LEDs [24]. An alternative possible explanation was in terms of an increase of the recombination at the polymer-nanoparticle interfaces, but this was also discounted. A more plausible mechanism suggests that the change in morphology, arising from the significant increase in surface area, may be responsible for the observed enhanced luminance [24,25]. The high surface reactivity of a nanostructure with a polymer may provide interactions that can modify polymer properties in a positive way, leading to novel luminescent properties of the composite. These interactions may yield new radiative recombination mechanisms, that may be utilized for broadband light emission or wavelength tunable emission. The mechanisms may be influenced by factors such as the individual properties of the organic and inorganic components as well as their relative concentration. In some nanocomposites, the presence of new recombination mechanisms is suggested by the generation of new PL emission lines [26], which may be attributed to the formation of interfacial states termed exciplex [27].

9.3.4 Decay curves

Fig. 9.7(a) depicts the typical afterglow decay curves of the phosphor samples after the powders were activated using a pulsed xenon lamp. The curves show that the $BaAl_xO_y:Eu^{2+},Dy^{3+}$ phosphor material emits light far longer than the typical microsecond lifetime of Eu^{2+} [28]. This indicates the presence of persistent luminescence. The origin of this long persistence is associated with the second activator ion Dy^{3+}. The Dy^{3+} incorporation creates deep traps in the energy band gap of the $BaAl_xO_y:Eu^{2+},Dy^{3+}$. These traps are in the form of hole-trapping levels near the valence band. After excitation by the light photons, electrons of the Eu^{2+} ion in the 4f level are transferred to the 5d level, and holes are produced in the valence band. Some holes created are captured by the Dy^{3+} hole

traps, then thermally released slowly to the valence band, and return to the ground state of Eu^{2+} accompanied with the emission of light photons.

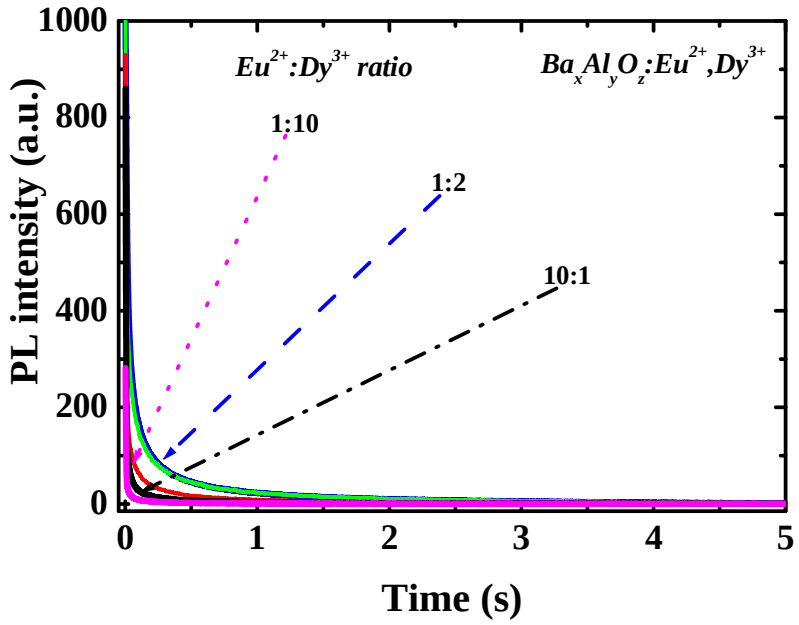

Figure 9.7(a): Decay curves of $BaAl_xO_y:Eu^{2+},Dy^{3+}$ phosphor for the samples with $Eu^{2+}:Dy^{3+}$ molar ratios = 10:1–1:10

Table 9.1(a): Results for fitted decay curves of the phosphor powders

Sample ($Eu^{2+}:Dy^{3+}$)	10:1	1:2	1:10
Component	Half life times (s)		
Fast (τ_1) [$\times 10^{+4}$]	3.3	3.4	0.4
Slow (τ_2)[$\times 10^{+3}$]	7.8	8.8	2.6

It can be clearly seen that all the afterglow decay curves are composed of two regimes, i.e., the initial rapid decay followed by a much slower process. The initial luminescent intensity and decay speed of afterglow of phosphors are different from each other. Decay times can be calculated by a curve fitting technique based on the following equation:

$$I = A_1 \exp\left(-t/\tau_1\right) + A_2 \exp\left(-t/\tau_2\right), \qquad (9.2)$$

where I is the phosphorescence intensity, A_1 and A_2 are constants, τ_1 and τ_2 are decay times for the exponential components, and t is time [29]. The results recorded in Table 9.1(a) indicate that the $BaAl_xO_y:Eu^{2+},Dy^{3+}$ phosphor samples had different decay times.

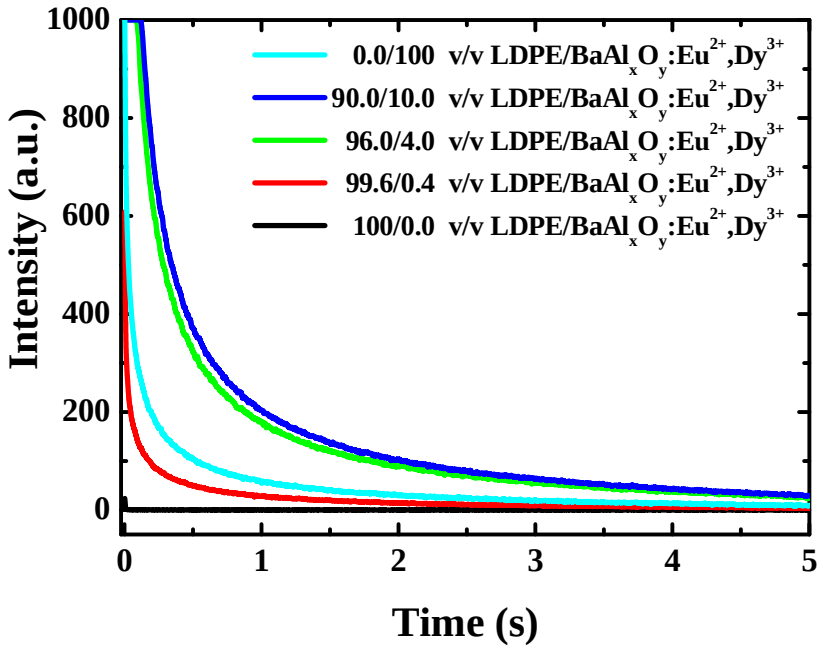

Figure 9.7(b): Decay curves of pure LDPE, LDPE/$BaAl_xO_y:Eu^{2+},Dy^{3+}$ nano-composites for phosphor vol.% = 0.4–10 and $BaAl_xO_y:Eu^{2+},Dy^{3+}$ phosphor sample with Eu^{2+}:Dy^{3+} molar ratio = 2:1

The role of Eu^{2+} ions as well as Dy^{3+} ions as luminescent centres and trap centres, respectively, in aluminate phosphors is well established. The lifetime of afterglow is related to the energy stored, and the number of electrons, which stay, in the trap level. The intensity of the afterglow is related to the velocity, including the velocity of electrons escaping from the trap level and the velocity of energy transfer. The rapidly-decaying process is due to the short survival time of the electrons in Eu^{2+} while the slow-decaying process arises from the deep trap energy centre of Dy^{3+} [30]. The magnitude of the afterglow intensity and decay time depend on the type of the host structure, which influences the nature of traps formed.

The curves for the polymer/phosphor nanocomposites, displayed in Fig. 9.7(b), reveal very interesting observations. At a phosphor content of only 0.4 vol.%, the polymer matrix seems to alter the decay mechanism from second order to third order as

the corresponding decay curves could be fitted with the third order exponential (equation 9.3),

$$I = A_1 \exp\left(-\frac{t}{\tau_1}\right) + A_2 \exp\left(-\frac{t}{\tau_2}\right) + A_3 \exp\left(-\frac{t}{\tau_3}\right). \qquad (9.3)$$

Table 9.1(b): Results for fitted decay curve of the 0.4 vol.% LDPE/$BaAl_xO_y$:Eu^{2+},Dy^{3+} composite – taken from 1:2, Eu^{2+}:Dy^{3+} sample

Component	Fast (τ_1) [$\times 10^{+2}$]	Medium (τ_2)[$\times 10^{+2}$]	Slow (τ_3)[$\times 10^{+2}$]
Half life times (s)	0.7	13.53	155.28

In addition, further increase of the phosphor content above 0.4% appears to progressively slow the rate of decay. Such elongation in afterglow characteristics would be very appropriate for applications such as lighting, among others. As mentioned earlier on (PL section), the origin of the influence of the polymer on phosphorescence behaviour may be rooted in the morphological changes that arise from the increased surface area [24,25].

The contribution of hole mobility in this process may be significant and is worth considering. It has been proposed that when nanoparticles are introduced into a polymer, probable causes for the improvement in hole mobility may be either a reduction in the density of traps or reduction in charge trapping due to the superposition of several transport mechanisms in the nanocomposite, which may include percolation through polymer nanoparticle interface network [31]. A low rate of hole mobility and electron-hole recombination will increase the re-trapping probability and further slow down the decay process [32].

9.3.5 Thermal properties

The DSC heating and cooling curves of the pure LDPE and the LDPE/$BaAl_xO_y$:Eu^{2+}, Dy^{3+} nanophosphor composites obtained from the second heating and cooling cycles,

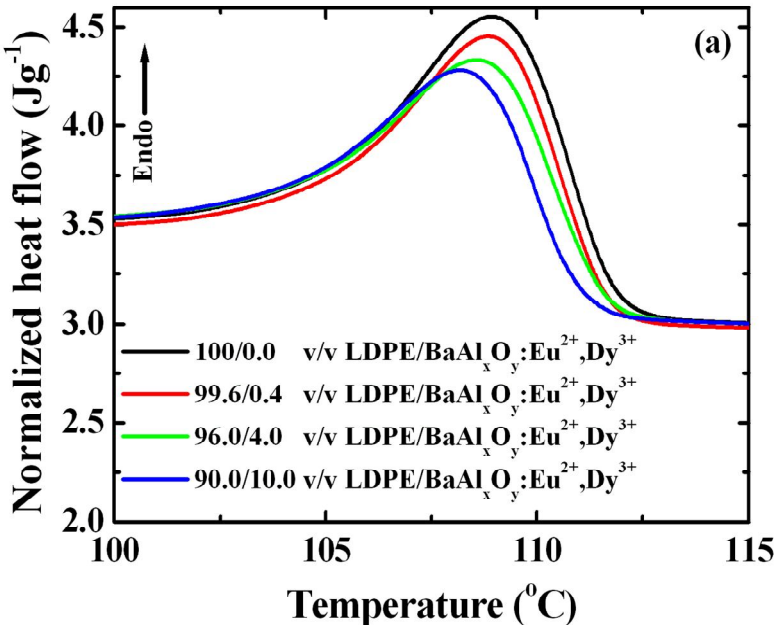

Figure 9.8(a): DSC heating curves of LDPE and LDPE/$BaAl_xO_y$:Eu^{2+},Dy^{3+} nanocomposites

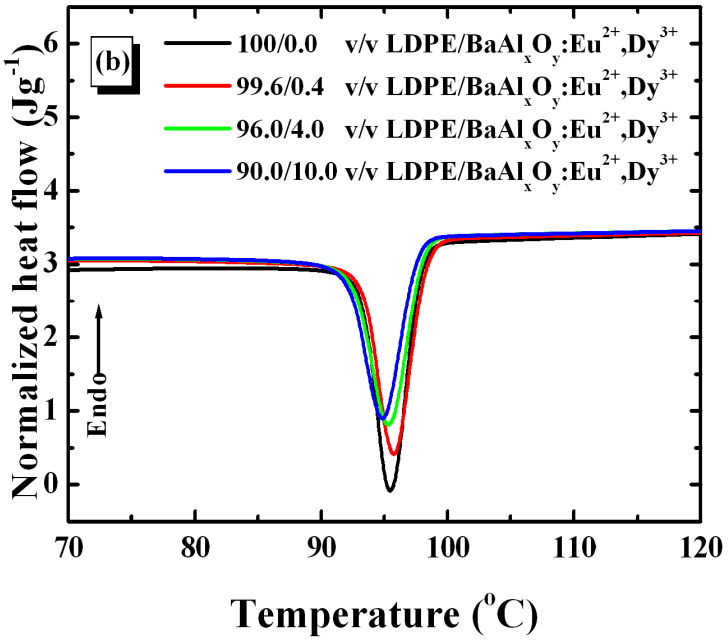

Figure 9.8(b): DSC cooling curves of LDPE and LDPE/$BaAl_xO_y$:Eu^{2+},Dy^{3+} nanocomposites

Table 9.2: DSC data of pure LDPE and LDPE/$BaAl_xO_y:Eu^{2+},Dy^{3+}$ composites

T_m: melting peak temperature; T_c: crystallization peak temperature; ΔH_m and ΔH_c: melting and crystallization enthalpies, respectively; σ: standard deviation.

Filler content (Vol.%)	T_m/°C ± σ	ΔH_m^{obs} /Jg^{-1} ± σ	ΔH_m^{cal} /Jg^{-1}	T_c/°C ± σ	ΔH_c^{obs} /Jg^{-1} ± σ	ΔH_c^{cal} /Jg^{-1}
0.0	109.2 ± 0.0	52.3 ± 7.9	-	95.4 ± 0.1	-64.16 ± 6.5	-
0.4	109.2 ± 0.2	57.1 ± 7.5	52.1	95.6 ± 0.1	-63.9 ± 2.7	-63.9
4.0	109.2 ± 0.7	53.3 ± 1.3	50.3	95.2 ± 0.2	-64.7 ± 2.6	-61.7
10.0	108.3 ± 0.3	48.6 ± 5.5	47.4	95.1 ± 0.2	-57.4 ± 5.5	-58.2

respectively, are shown in Fig. 9.8. The observed as well as expected parameters corresponding to these DSC curves are recorded in Table 9.2. The curves show that as the phosphor content is increased, both the melting and crystallization temperatures decrease slightly. The reduced temperature values are an indication of a reduction in crystallite sizes in LDPE. This result is similar to our previous observations on the effect of the commercial $SrAl_2O_4:Eu^{2+},Dy^{3+}$ phosphor in LDPE [5]. However, in contrast to the same work, values of the expected melting enthalpy values (normalized with respect to the mass fraction of the LDPE in the composite), are lower than the experimentally determined ones. Although the difference in the two values progressively decreases as the phosphor content increases, it is clear that the $BaAl_xO_y:Eu^{2+},Dy^{3+}$ particles acted as nucleating centres and enhanced the overall crystallinity in the LDPE nanocomposite while preventing lamellar growth. This is in line with some documented results [33] for the effect of nanostructured fillers.

Previous studies have shown that the thermal stability of LDPE can be enhanced to various extends following the introduction of phosphor nanoparticles [5]. In this work, TGA measurements were made in order to investigate the effect of the combustion-synthesized $BaAl_xO_y:Eu^{2+},Dy^{3+}$ phosphor nanoparticle fillers on the thermal stability of LDPE. The curves obtained from the measurements are depicted in Fig. 9.9. The curves

show that $BaAl_xO_y:Eu^{2+},Dy^{3+}$ significantly increased the thermal stability of LDPE, shifting the onset temperature of degradation from about 324 ^oC to 400 ^oC (for the nanocomposite with 4 vol.% of $BaAl_xO_y:Eu^{2+},Dy^{3+}$). Two probable reasons may account

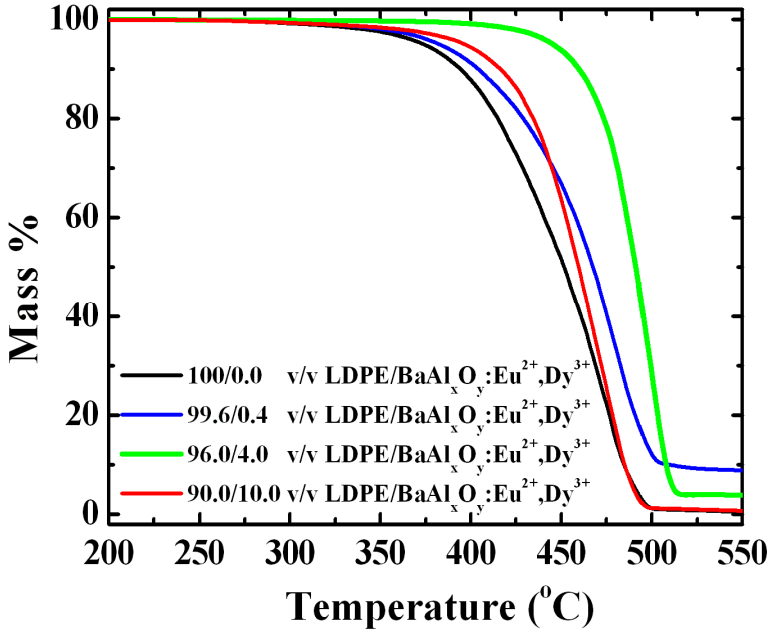

Figure 9.9: TGA curves for LDPE and LDPE/$BaAl_xO_y:Eu^{2+},Dy^{3+}$ nanocomposites

for the improved stability. Firstly, a strong interaction between the nanofiller particles and the polymer chains may result in reduced chain mobility, which then suppresses the chain transfer reaction that is responsible for the degradation in LDPE [34], ultimately delaying the onset temperature of mass loss. The 10 vol.% sample shows that there is a filler loading threshold for improved stability. However, the afterglow curves indicate that this particular concentration does not perform much better than the 4 vol.% one, indicating that the threshold filler content for optimum persistence luminescence ans stability of the polymer matrix is less than 10%.

9.4 Conclusions

Nanostructured $BaAl_xO_y:Eu^{2+},Dy^{3}$ powders were prepared by a combustion method, and ultimately mixed in an LDPE matrix. EDS analysis confirmed the elemental

composition in the phosphor. The average crystallite sizes determined from XRD measurements, using the Scherrer formula, ranged between 34 and 41 nm. The powders exhibited high brightness luminescence with major peaks having maxima at 505 nm, which were nicely replicated by the nanocomposite samples. Of particular interest, was the persistence luminescence behaviour of the phosphor/polymer composites, which were observed to be profoundly enhanced compared to the as-prepared $BaAl_xO_y:Eu^{2+},Dy^{3+}$ samples. The enhancement probably originated in the change in morphology, arising from the significant increase in surface area. DSC results show that the $BaAl_xO_y:Eu^{2+},Dy^{3+}$ particles acted as nucleating centres and enhanced the overall crystallinity in LDPE while preventing lamellar growth. The LDPE/$BaAl_xO_y:Eu^{2+},Dy^{3}$ nanocomposites had higher thermal stability with respect to that of the pure LDPE. The improved stability may be attributed to a strong interaction between the nanofiller particles and the polymer chains, which led to reduced chain mobility, ultimately delaying the onset of degradation.

9.5 References

1. Kuang, J. Liu, Y.L. *Chem Lett*., **34**(4)**:** 598, (2005).
2. Mothudi, B.M. Ntwaeaborwa, O.M. Botha, J.R. Swart, H.C. *Phys. B: Phys. Cond. Matt.*, **404**(22)**:**, 4440, (2009).
3. Katsumata, T. Sakai, R. Komuro, S. Morikawa, T. Kimura, H. *J. Cryst. Growth*., **198-199**(I)**:** 869, (1999).
4. Fukuda, K. Fukushima, K. *J. Solid State Chem*., **178**: 2709 , (2005).
5. Bem, D.B. Luyt, A.S. Dejene, B.F. Botha, J.R. Swart, H.C. *Phys. B: Phys. Cond. Matt.,* **404:** 4504, (2009).
6. Klug, H.P. Alexander, L. E. *X-ray Powder Diffraction Procedures*. Wiley: New York, (1959).
7. Galvan, D.H. Hirata, G.A, Adem, E. *Mat. Sci. Eng. B.*, **126:** 28, (2006).
8. Kang, Y.C. Lenngoro, I.W. Park, S.B. Okuyama, K. *Mat. Res. Bul.*, **35**(5)**:** 789, (2000).
9. Chang, H. Lenggoro, I.W. Okuyama, K. Kim, T.O. *Jpn. J. Appl. Phys.*, **43:** 3535, (2004).
10. Jacobsohn**,** L.G. Bennett**,** B.L. *Radiat. Meas.*, **42**(4-5)**:** 675, (2007).
11. Lee, S.K. Yoon, H.H. Park, S.J. Kim, K.H. Choi, H.W.J. *J. Appl. Phys*., **46:** 7983, (2007).
12. Ryu, H. Singh, B.K. Bartwal, K.S. *Phys. B.,* **403:** 126, (2008).
13. Chen, X.Y. Ma, C. Li, X.X. Shi, C.W. Li, X.L. Lu, X.D.R. *J. Phys. Chem., C.***, 113:** 2685, (2009).
14. Lu, C.H. Chen, S.Y. Hsu, C.H. *Mater. Sci. Eng. B.*, **140:** 218, (2007).
15. Lin, Y. Zhang, Z. Tang, Z. *Mat. Chem. Phys.*, **70:** 156, (2001).

16. Chen, Y.J. Qiu, G.M. Sun, Y.B. *J. Rare Earths*., **20**: 50, (2002).

17. Park, Y.J. Kim, Y.J. *Mater. Sci. Eng. B*., **146:** 84, (2008).

18. Shannon, R.D.. *Acta Cryst.*, **A32:** 751, (1976).

19. Li, Y.L. Zhang, Z. Tang, Z. Zhang, J. Zheng, Z. Lu, X. *Mat. Chem. Phys.*, **70**: 156, (2001).

20. Stefani, R. Rodrigues, L.C.V. Carvalho, C.A.A. Felinto, M.C.F.C. Brito, H.F. Lastusaari, M. Hölsä, J. *Opt. Mat.*, **31:** 1815, (2009).

21. Ryu, H. Singh, B.K. Bartwal, K.S. *J. Lumin*., **85:** 149, (1999).

22. Guanming, Q. Yongjie, C. Xiujuan, G. Linjiu, X. Yiguang, T. Yanbin, S. *J. Rare Earths.*, **23:** 5, (2005).

23. Aitasalo, T. Deren, P. Holsa, J. Jungner, H. Krupa, J.C. Lastusaari, M. Legendziewicz, J. Niittykoski, J. Strek. W. *J. Solid State Chem.*, **171:** 114, (2003).

24. Aitasalo, T. Hölsä, J. Jungner, H. Lastusaari, M. Niittykoski, J. *J. Phys. Chem. B*., **110:** 4589, (2006).

25. Blom, P.W.M. Schoo, H.F.M. Matters, M. *App. Phys. Lett.,* **73**(26)**:** 3914, (1998).

26. Aleshin, A. Alexandrova, E. Shcherbakov, I. *J. Phys. D: App. Phys.,* **42**(10)**:** 1361, (2009).

27. Morteani, A. Ho, P.K.H. Friend, R. Silva, C. *App Phys Lett.,* **86:** 1077, (2005).

28. Poort, S.H.M. Meijerink, A. Blasse, G. *J. Phys. Chem. Solids*., **58**: 1451, (1997).

29. Matsuzawa, T. Nabae, T. Katsumata, T. Sasajima, T. *J. Electrochem. Soc*., **144:** L243, (1997).

30. Katsumata, T. Nabae, T. Sasajima. K. *J. Cryst. Growth*., **183:** 361, (1998).

31. Aleshin, A.N. Shcherbakov, I.P. Alexandrova, E.L. Lebedev, E.A. *Solid State Comm.*, **146(**3-4)**:** 161, (2008).

32. Jia, W. Yuan, H. Lu, L. Liu, H. Yen, W.M. *J. Lumin.,* **76-77:** 424, (1998).

33. Ning, N.Y. Yin, Q.J. Luo, F. Zhang, Q. Du, R. Fu, Q. *Polym.,* **4**(25)**:** 7374, (2007).

34. Luyt, A.S. Dramicanin, M.D. Antic, Z. Djokovic, V. *Polym. Test.*, **28**(1)**:** 1, (2009).

Chapter 10
Summary and Outlook

10.1 Summary

The global objectives of the experimental studies presented in this thesis focused on factors, which may lead to the enhancement in the qualities of luminescent materials. The approach adopted involved an analysis of the morphological, structural, photoluminescent, and thermal characteristics of both commercial and self-synthesized phosphors as well as phosphor/polymer composites.

Two types of aluminate-based commercial phosphors; the green-emitting $SrAl_2O_4:Eu^{2+},Dy^{3+}$ and the blue-emitting $Sr_4Al_{14}O_{25}:Eu^{2+},Dy^{3+}$, were initially investigated, firstly in their pristine forms and secondly as composites after incorporation in PMMA and LDPE polymers. The set of PL emissions for the major peaks in $SrAl_2O_4$ and $Sr_4Al_{14}O_{25}$-based samples, were broad and occurred at about 505 nm and 418 nm, respectively. The DSC and TGA results for the corresponding LDPE/$SrAl_2O_4:Eu^{2+},Dy^{3+}$ and LDPE/$Sr_4Al_{14}O_{25}:Eu^{2+},Dy^{3+}$ composites, showed that the phosphor had no major influence on either the crystallinity or stability of the former composites. In the latter composite samples, the phosphor influence on the crystallinity in LDPE was not significant, but it strongly improved the stability. This first phase of the study provided

some insight into the relevant characteristics of phosphors as well as phosphor/polymer composites, which led to the elimination of PMMA from further investigations and paved the way for further investigations of these materials.

The second phase of these investigations concerned the synthesis of two types of phosphors; aluminates of strontium and barium. The preparation of strontium aluminate was carried out by two methods; combustion and sol-gel. The combustion-synthesized phosphor powder samples were initially analyzed for the effect of the ratio of Eu^{2+} to Dy^{3+} on the photoluminescence and thermal properties. The emission intensity had a major peak at 515 nm and was observed to be optimum for a 1:2 mol% ratio of Eu^{2+}:Dy^{3+} concentration: Higher concentrations of Dy^{3+} quenched the intensity of the phosphor. The 1:2 mol% ratio was also found to be the optimal value for the initial, relative intensity, as well as the after-glow decay time. Improvements in these characteristics were attributed to the presence of both shallow and deep traps. Thermal analysis showed that the phosphor nanoparticles improved the overall crystallinity in LDPE by acting as nucleating agents.

One of the attractive features of the aluminate systems is the ability to form luminescent phases of various forms. In the specific case of the strontium aluminate systems, some of the prominent crystallographic polymorphs are $Sr_3Al_2O_6$, $SrAl_2O_4$, $SrAl_4O_7$, $Sr_4Al_{14}O_{25}$, and $SrAl_{12}O_{19}$. This aspect was investigated by studying the effect of temperature on the structural and photoluminescent properties of sol-gel derived samples of strontium aluminate, doped and co-doped with Eu^{2+} and Dy^{3+}, respectively. The PL results clearly show red-shifted excitation and emission spectra as temperature increased. At temperatures above 500 ^{o}C, the broad bands, which originate from f-d transitions of Eu^{2+} are reduced to several sharp lines that are characteristic of the f-f transitions of the Eu^{3+} ions, which originate from $^5D_0 \rightarrow {}^7F_J$ transitions (J = 0,1-6). These changes are attributed to the variation in the crystallite sizes, whose average values increased from about 42 to 47 nm as the temperature rose from 0 to 1000 ^{o}C. The presence of the $SrAl_2O_4$ and $Sr_2Al_3O_6$ phases was detected from XRD spectra.

The final set of experiments consisted of the study of the structural and photoluminescent properties of a combustion synthesized $BaAl_xO_y:Eu^{2+},Dy^{3+}$ phosphor as well as $BaAl_xO_y$: Eu^{2+}, Dy^{3+}/LDPE composites. In addition, the composite samples were thermally analyzed. The intention here was two-fold: (1) To produce a good quality phosphor. (2) To assess the performance of the phosphor in an LDPE matrix. Photoluminescence emission and excitation spectra, obtained at room temperature, are of high intensity and consist of broad bands, which are attributed to the transition between the excited state ($4f^65d^1$) and the ground state ($4f^7$). PL results indicate that the LDPE/phosphor interface, which is considered to have an influence on the composite behaviour, did not significantly change the spectral positions of the phosphor materials, whose major emission peaks occurred at about 505 nm; which was a desirable result. The improved afterglow results for the composites may have been caused by morphological changes due to increased surface area and defects. Thermal results indicate that the $BaAlxOy:Eu^{2+},Dy^{3+}$ particles acted as nucleating centres and enhanced the overall crystallinity in the LDPE nanocomposite while preventing lamellar growth, hence reducing the crystallite sizes in LDPE.

10.2 Outlook

Issues which may inform future research work in the development and application of luminescent materials revolve around the ability to; (1) produce high brightness persistent phosphors of high efficiency, (2) develop comprehensive mechanisms to explain persistence luminescence as well as luminescence in nanocomposite (hybrid) materials, (3) clarify the size-induced effects in nanophosphors, (4) develop strategies to control the location, distribution, or segregation of dopant ions in nanoparticles and nanocomposites.

With regard to producing persistent luminescent compounds, the intense research in this area has resulted in only a handful of phosphors that are bright enough to consider their use in practical applications. In addition, these materials almost exclusively fall into two main categories, the aluminates and the silicates, i.e. the number of hosts used is

relatively low. Besides the limited host compounds, so far there has not been any serious alternative for Eu^{2+} activators as the emitting centre. Consequently, the price of Eu^{2+} is sky-rocketing due to its almost exclusive use as a dopant in most luminescence applications, including as security markers in Euro bank notes. The most noteworthy problem in the preparation Eu^{2+}-doped persistent luminescent compounds is the lack of yellow, orange and red phosphors. The paucity in the search for, particularly bright red persistent luminescent compounds, has been ascribed to two causes: (1) The difficulty in obtaining a high enough crystal field in oxides for Eu^{2+} to emit radiation in the red region of the visible spectrum. (2) The existence of the so called Purkinje effect, which basically refers to the natural weakness in the human eye to perceive red (and blue) wavelengths light.

Quite a number of mechanisms have so far been postulated to explain the persistent luminescence phenomenon in phosphors. They generally involve charge carriers getting trapped in long-lived energy levels inside the band gap. However, these mechanisms are not yet fully understood since many details remain unclear. Clarity is needed on issues such as: (1) The origin of the charge carriers. (2) The conduction process of the energy from the traps to the luminescent centres. (3) The influence of codopants and lattice defects in the neighbourhood of the activators. Future experiments are necessary to unravel these mysteries.

Nanocrystalline systems constitutes a relatively young field of research. Improved performance in phosphors is expected when phosphor particles are formed at the nanometre scale. The anticipated improvement is on account of the reduced sizes of the particles. Phosphors having a small particle size and high efficiency would be most useful, since this would ideally enable the preparation of practical phosphors, which can form a dense, pinhole-free coating on a substrate. However, key issues regarding size-dependent optical properties still persist. The particle size dependence of the luminescence efficiency is obscure. Consequently, the potential to prepare high efficiency and robust phosphors for diverse applications, will require strategies to control the size,

location, distribution, or segregation of dopant ions in nanoparticles and multiple phases in nanocomposites.

Nanocomposite (hybrid) materials represent one of the most fascinating emerging developments in materials chemistry. The tremendous possibilities of combining different properties in one material initiated an explosion of ideas about potential materials and applications. However, the basic science is sometimes still not understood. Therefore investigations in this field in particular, to understand the structure/property relationships are crucial.

Against this backdrop, prospects for future research work, derived from the work presented in this thesis, are many. These include, but are not limited to the following specific areas:

- The opportunity to fine-tune (optimize) the conditions for sample preparation, following the successful synthesis of the phosphor powders; intensity comparable to (sometimes surpassing) that of commercial phosphors (see Appendix).
- Detailed investigation of some of the influencing parameters such as temperature, fluxing and reducing agents, as well as TL studies, in order to build on the currently inadequate experimental (and theoretical) databases.
- Due to time constraints, it was not possible to carry out adequate TEM analysis. For most of the investigations undertaken, TEM analysis would go a long way in concretizing many of the conclusions arrived at. This is an imperative tool to further gather valuable information on the crucial parameters like, crystallinity, crystallite size and shape.
- The polymer/phosphor interface is a virtually unexplored region that is pregnant with the information, which will provide answers to the interesting observations (e.g. the improved decay times reported in chapter 9). These composites deserve to be further investigated.

Publications:

1. *"Luminescent properties of long-lasting $BaAl_xO_y$: Eu^{2+},Dy^{3+} nanocomposites"* – To be published in: *Journal of Applied Polymer Science*. DOI 10.1002/app.
2. *"Temperature dependence of the structural and luminescent properties of long-lasting afterglow $SrAl_xO_y$: Eu^{2+},Dy^{3+} phosphor"*. Submitted to: *Journal of Rare Earths.*
3. *"Characterization of Luminescent and Thermal Properties of Long Afterglow $SrAl_xO_y$:Eu^{2+},Dy^{3+}. Phosphor Synthesized by Combustion Method"*. To be published in; *Polymer Composites*. DOI 10.1002/pc.21036.
4. *"Properties of Green $SrAl_2O_4$: Eu^{2+},Dy^{3+} Phosphor in LDPE and PMMA Polymers"*. Published in: *Journal of Applied Polymer Science,* Vol. 117, Issue 5, pp. 2635–2640, (2010).
5. *"Structural, Luminescent and Thermal Properties of Blue $Sr_4Al_{14}O_{25}$: Eu^{2+}, Dy^{3+} Phosphor in LDPE and PMMA Polymers"*. Published in the *Journal, Physica B*, pp. 4504–4508, (2009).

Appendix: PL intensities for the commercial and the as-synthesized phosphors